



**HAL**  
open science

# Optomechanical probe for high-speed AFM

Lucien Schwab

► **To cite this version:**

Lucien Schwab. Optomechanical probe for high-speed AFM. Micro and nanotechnologies/Microelectronics. Institut national des sciences appliquées de Toulouse, 2020. English. NNT: . tel-03030399v1

**HAL Id: tel-03030399**

**<https://laas.hal.science/tel-03030399v1>**

Submitted on 30 Nov 2020 (v1), last revised 30 Mar 2021 (v2)

**HAL** is a multi-disciplinary open access archive for the deposit and dissemination of scientific research documents, whether they are published or not. The documents may come from teaching and research institutions in France or abroad, or from public or private research centers.

L'archive ouverte pluridisciplinaire **HAL**, est destinée au dépôt et à la diffusion de documents scientifiques de niveau recherche, publiés ou non, émanant des établissements d'enseignement et de recherche français ou étrangers, des laboratoires publics ou privés.

# THÈSE

En vue de l'obtention du  
**DOCTORAT DE L'UNIVERSITÉ DE TOULOUSE**  
Délivré par l'Institut National des Sciences Appliquées de  
Toulouse

---

Présentée et soutenue par  
**Lucien SCHWAB**

Le 25 septembre 2020

**Sonde opto-mécaniques pour la microscopie AFM rapide**

---

Ecole doctorale : **GEET - Génie Electrique Electronique et Télécommunications :  
du système au nanosystème**

Spécialité : **MicroNano Systèmes**

Unité de recherche :  
**LAAS - Laboratoire d'Analyse et d'Architecture des Systèmes**

Thèse dirigée par  
**Bernard LEGRAND et Ivan FAVERO**

Jury

M. Ludovic BELLON, Rapporteur  
M. Tarik BOUROUINA, Rapporteur  
Mme Béatrice DAGENS, Examinatrice (Présidente)  
M. Jean-Paul SALVETAT, Examineur  
M. Ignacio CASUSO, Examineur  
M. Bernard LEGRAND, Directeur de thèse  
M. Ivan FAVERO, Co-directeur de thèse

## Acknowledgements

First of all, I would like to thank my PhD director Bernard Legrand aka the MEMS Master, aka "Bernard il est trop fort". The living proof that experience is way better than youth. Thanks for always having answers to my questions, your encouragements, I worked partially for them. It was a real pleasure to enjoy moments with the (ultra)skilled, humble and friendly person that you are.

The second person I must absolutely thank is Pierre Allain, my optomechanics mentor (not in a Greek way). You taught me everything about optomechanics with your finger pointing up: "et la raison est ..." starting from: "Le mieux est l'ennemi du bien" especially when you are working with the last sample. Your curiosity is very contagious. You are like a precious treasure of interesting things.

Then comes Ivan Favero. I did not interact a lot with you but what struck me is your analyzing capability to find the pertinent view on everything.

Thanks to Rose-Marie Sauvage, my DGA supervisor.

Thanks also to the people participating in the Olympia project. Without their work, this optomechanical AFM probe would not have been. Many thanks to Guillaume Jourdan, Sébastien Hentz, Marc Faucher, Benjamin Walter and more which I did not met.

Thanks to Laurent Mazonq, Denis Lagrange and Nicolas Mauran. Laurent thanks for the fabrication explanations and your report on fast AFMs. Nicolas this LabView project is a masterpiece, I tried to mess it up but you kept it clean. You are so friendly it is hard to not become your friend. Denis, you are so strong in electronics and signal processing, jumping seamlessly between temporal and frequency explanations. Thanks for your insights. I would say your only flaw is your lack of tact, the other side of the coin being that you are an extremely sincere and genuine person, which I enjoyed.

Thanks to Samuel Charlot and Benjamin Reig for their precious help in the substrate etching of our devices.

Thanks to Xavier Dollat for the mechanical pieces, your good mood always had me, I will terribly miss reading your emails.

Thanks to all the friends I made in LAAS: Vincent my soulmate, I love you (a very manly love), I personally think you should write schools programs in physics. Matthieu my besta, growing worms in your office, I wish to walk in your musical steps; Gabriel, I don't know what to say but you deserve to be at least in the top 3 of this list. Cécile, we had so much fun, you were the greatest singer of the LAAS (for what it's worth I don't know). Maréva, you put glitters in my life, we were not lost in Prague. Aarushee, you grow old now, you used to be more fun (but starting from a big fun reservoir so it's still okay). Eirini, I wish you were already there at the beginning of my thesis so we could have talked for 2 years more. Kata, I believe all Hungarians are racists and being semi-poor is not an excuse 😊, keeping Argos was one of the best moments in my thesis I hope he has not forgotten. Douglas, you make such a good Trump 😊, I was always sincerely impressed by your will in the hikes even if you were dying (almost)

at the one before, wish you the best in Tours. Ali, I hope I will see you at one of my parties inchAllah. Pierre (Moritz), I hope you will tell me your climbing secrets, I will tell you my skiing ones in exchange, deal? Asma, your last name suits you so well, I think I had my biggest laughs with you in those 3 years, thanks. Dolores, arre borriquito, arre burro are, anda más deprisa que llegamos tarde. Kayum, I enjoy your sensitive company. Elise, you are the sweetest person I know, wish you the best. Benjamin, I take you for a one-on-one fight anytime you want. Adrian, I told you already, you should publish a book: "coffee bits". François, Luca, Pierre (Joseph) and Antonio, I was glad to cross your path in the music room, may the groove of Marvin Gaye be with you.

Thanks to all the friends I made in MPQ, my second home: Samantha, you are a smiling ray of light. Carlo, do your plants auto-water themselves now? Evelio, I have never been to Cuba but I know you are its best ambassador, olympiquement. Medhi, Oud-ini, aka the golden coupling hands. Natalia, is there any chance you teach me you skating technique? Valerio, the funniest person I know, remember when I told I do not know what to Samantha's grandparents? Giuseppe the neat, I hope to hear you sing soon. Will, tell me when you come back to France. Cherif, I do not know how you function but anyway many thanks for the help in clean room. Marco, I need surfing lessons from you. Thanks to Biswarup. Iannis, thanks for the effective index script.

Thanks also to my thyroid, you stole 1 year of my life but made me a more comprehensive person.

Thanks to the Jury members who accepted to review my work. In particular thanks to Ignacio Casuso, I really enjoyed your questions. Special thanks to Ludovic Bellon who gave me back an annotated pdf manuscript, that was super appreciated.

Thanks for the French Agence Nationale de la Recherche (ANR) and the French Direction Générale de l'Armement (DGA) for the funding of this PhD.



# Contents

<b>GLOSSARY</b> .....	<b>9</b>
<b>TABLE OF PARAMETERS</b> .....	<b>11</b>
<b>GENERAL INTRODUCTION</b> .....	<b>15</b>
<b>OUTLINE</b> .....	<b>16</b>
<b>I. STATE OF THE ART OF AFM TECHNOLOGY</b> .....	<b>17</b>
I.1 POSITION OF AFM AMONG MICROSCOPY METHODS - HISTORY .....	17
I.2 PRINCIPLE OF THE AFM .....	19
I.2.1 Interactions between a tip and a surface .....	20
I.2.2 Historical AFM operation .....	24
I.2.3 Operating modes and controls .....	27
I.3 RECENT DEVELOPMENTS OF THE AFM INSTRUMENT .....	32
I.3.1 Reaching higher speed/bandwidth .....	32
I.3.2 Reaching higher resolution .....	33
I.3.3 Reaching easier and cheaper AFM .....	39
I.3.4 AFM probe performance figure of merit (bandwidth over force resolution) .....	39
I.4 STATE OF THE ART AFM PROBES AND THEIR ELECTRO-MECHANICAL TRANSDUCTIONS .....	40
I.4.1 Actuation .....	40
I.4.2 Detection .....	43
<b>II. OPTOMECHANICAL SILICON MICRO-RING THEORY, DESIGN FOR AFM AND FABRICATION</b> .....	<b>47</b>
II.1 HISTORY OF CAVITY OPTOMECHANICS .....	47
II.2 OPTICAL RESONATOR .....	49
II.2.1 Straight waveguide: effective index .....	49
II.2.2 Curved waveguide: ring cavity .....	54
II.2.3 Intrinsic losses .....	56
II.2.4 Evanescent coupling .....	60
II.2.5 Optical inputs/outputs: coupled mode theory (CMT) .....	61
II.2.6 CW and CCW degeneracy lifting: mode splitting .....	65
II.2.7 Thermo-optic shift/optical bi-stability .....	66
II.3 MECHANICAL RESONATOR .....	67
II.3.1 Mechanical modes, AFM considerations .....	67
II.3.2 Position of the tip relative to the spokes .....	68
II.3.3 Damped harmonic oscillator mass-spring model, losses .....	70
II.4 OPTOMECHANICAL COUPLING, EQUATIONS, RESONANCE .....	71
II.4.1 Optical sensing of the mechanical motion $gO \leftarrow M$ .....	72
II.4.2 Optical actuation of the mechanical motion $gO \rightarrow M$ .....	73
II.4.3 Capacitive/electrostatic actuation of the mechanical motion .....	74
II.4.4 Optomechanical coupling model .....	75
II.5 FORCE SENSING/CONTACT OPERATION MODEL AND CONSIDERATIONS .....	77
II.6 FABRICATION .....	79
II.7 OPTOMECHANICAL FIGURE-OF-MERIT: TOWARDS THE IDEAL OM PROBE .....	81
<b>III. CHARACTERIZATION OF THE OPTOMECHANICAL PROBE: SET-UP AND PERFORMANCES</b> .....	<b>83</b>
III.1 OPTICAL CHARACTERIZATION SET-UP .....	83
III.2 OPTICAL PERFORMANCES STUDY .....	85
III.2.1 Gap length influence on coupling .....	85
III.2.2 Spokes and tip width scattering effect .....	86
III.2.3 Losses beyond scattering, roughness or absorption? .....	88
III.2.4 Study of doublet mode quality factor discrepancy due to symmetry .....	88

III.3 MECHANICAL MOTION CALIBRATION WITH BROWNIAN MOTION .....	90
III.4 NOISE/STABILITY .....	92
III.4.1 Detection noise .....	92
III.4.2 Stability and drifts.....	98
III.5 ACTUATION AND BACKGROUND .....	101
III.5.2 Data post processing .....	104
III.5.3 Saving reference traces and subtraction .....	107
III.5.4 RF Interferometry in the electrical domain.....	107
III.5.5 Using 2 lasers for actuation and detection.....	107
III.5.6 Using an alternative actuation (capacitive):.....	109
III.6 DETERMINATION OF THE OM PROBE'S MECHANICAL BANDWIDTH.....	111
<b>IV. A FAST AFM ENVIRONMENT TO OPERATE THE OPTOMECHANICAL SENSOR .....</b>	<b>115</b>
IV.1 COMPUTER INTERFACE .....	115
IV.2 HIGH-BW FEEDBACK CONTROL .....	116
IV.2.1 High-BW detection .....	117
IV.2.2 Better surface tracking: dynamic PID.....	117
IV.3 HIGH-BANDWIDTH Z PIEZO ACTUATOR.....	118
IV.3.2 Mechanical design.....	119
IV.3.3 Signal processing.....	123
IV.4 HIGH-SPEED SCANNING .....	124
IV.5 TRANSPOSITION .....	127
IV.6 INTEGRATION OF THE PROBE INTO THE AFM.....	128
IV.6.1 Protruding tip: getting rid of the substrate under the tip.....	129
IV.6.2 Sensor integration: optical and electrical interconnects .....	135
IV.6.3 Mounting.....	137
<b>V. TOWARDS OM AFM .....</b>	<b>139</b>
V.1 MECHANICAL INTERACTION DETECTION IN POINT MODE .....	139
V.1.1 Approach-retract curves.....	139
V.1.2 Feedback control operation.....	148
V.2 PSEUDO OM AFM IMAGE .....	150
<b>CONCLUSION.....</b>	<b>153</b>
<b>PERSPECTIVES .....</b>	<b>155</b>
<b>APPENDIX A: RESULTS TABLE .....</b>	<b>157</b>
<b>APPENDIX B: ELECTROMAGNETIC WAVE PROPAGATING IN A SLAB .....</b>	<b>158</b>
<b>APPENDIX C: INSTRUMENTS.....</b>	<b>161</b>
C.1. OPTICS .....	161
C.2. RF ELECTRONICS .....	166
C.3. POSITIONERS .....	168
C.4. MISCELLANEOUS .....	168
<b>APPENDIX D: THERMOMECHANICAL NOISE SPECTRUM .....</b>	<b>169</b>
<b>APPENDIX E: CALIBRATION VIA ACQUISITION CHAIN .....</b>	<b>171</b>
<b>APPENDIX F: DELAY LINE PHASE SLOPE EFFECT .....</b>	<b>173</b>
<b>APPENDIX G: CLEAVED FACET SIDE-INJECTION AND FABRY-PEROT EFFECT .....</b>	<b>174</b>
<b>APPENDIX H: CONTRAST AND FWHM DEFINITION .....</b>	<b>176</b>
<b>APPENDIX I: THERMO-OPTICAL SAW-TOOTH SHIFT.....</b>	<b>179</b>

<b>APPENDIX J: ACQUISITION AND GENERATION DIGITAL INTERFACE .....</b>	<b>181</b>
<b>APPENDIX K: EFFECTIVE INDEX CORRECTION ON THE FREE SPECTRAL RANGE.....</b>	<b>182</b>
<b>DISSEMINATION .....</b>	<b>185</b>
<b>BIBLIOGRAPHY .....</b>	<b>187</b>
<b>RESUME .....</b>	<b>201</b>
<b>ABSTRACT .....</b>	<b>202</b>

“The principle of AFM is comparable to a blind person’s use of a stick to probe the environment” [1]. In this thesis work, we try to improve the stick to a more sensitive & faster optomechanical one.





## Glossary

1PA: One-Photon Absorption.  
2PA: Two-Photon Absorption.  
AFAM: Atomic Force Acoustic Microscope.  
AFM: Atomic Force Microscope.  
AM (AM-AFM): Amplitude Modulation.  
APC: Angled Physical Contact.  
BOx: Buried Oxide.  
BW: Bandwidth.  
CCW: Counter Clock-Wise.  
CMT: Coupled Mode Theory.  
CNT: Carbon Nano-Tube.  
CW: Clock-Wise.  
DFM: Dynamic Force Microscope.  
DMT: DeJarguin-Muller-Toporov.  
DR: Dynamic Range.  
DRIE: Deep Reactive Ion Etching.  
DUT: Device Under Test.  
EBD: Electron Beam Deposition.  
EDFA: Erbium Doped Fiber Amplifier.  
EOM: Electro-Optical Modulator.  
FCA: Free Carrier Absorption.  
FEM : Finite Element Method.  
FFM: Friction Force Microscope.  
FIB: Focused Ion Beam.  
FM (FM-AFM): Frequency Modulation.  
FSR: Free Spectral Range.  
FWHM: Full Width at Half Maximum.  
FWHm: Full Width at Half Minimum.  
HOPG: Highly-Oriented Pyrolytic Graphite.  
HSA: High-Speed Actuator.  
JKR: Johnson-Kendall-Roberts.  
LDV: Laser Doppler Vibrometer.  
LER: Length Extensional Rod.  
LFM: Lateral Force Microscope.  
LIA: Lock-In Amplifier.  
LNA: Low-Noise Amplifier.  
LO: Local Oscillator.  
LOD: Limit Of Detection.  
LPF: Low-Pass Filter.  
MEMS: Micro-Electro-Mechanical Systems.  
MF-AFM: Multi-frequency AFM.  
MFD: Mode Field Diameter.  
MNOEMS: Micro-Nano-Opto-Electro-Mechanical Systems.  
MOEMS: Micro-Opto-Electro-Mechanical Systems.  
MST: Maxwell Stress Tensor.  
NEP: Noise-Equivalent Power.

OBD: Optical Beam Deflection.  
OM: Optomechanical.  
PC: Polarization Controller.  
PD: Photodiode.  
PDH: Pound-Drever-Hall.  
PID: Proportional Integral Derivative.  
PLL: Phase-Locked Loop.  
PM (PM-AFM): Phase Modulation.  
RIN: Relative Intensity Noise.  
SEM: Scanning Electron Microscope.  
SNFUH: Scanning Near-Field Ultrasound Holography.  
SNOM: Scanning Near-field Optical Microscope.  
SNR: Signal-to-Noise Ratio.  
SOI: Silicon On Insulator.  
SPM: Scanning Force Microscope.  
STED: STimulated Emission Depletion microscope.  
STEM: Scanning Transmission Electron Microscope.  
STM: Scanning Tunneling Microscope.  
TCF: Temperature Coefficient of Frequency.  
TE: Transverse Electric.  
TEM: Transmission Electron Microscope.  
TIR: Total Internal Reflection.  
TLS: Two-Level System.  
TM: Transverse Magnetic.  
UHV: Ultra-High Vacuum.  
VdW: Van der Waals.  
VSB: Variable Shape Beam.  
WGM: Whispering Gallery Mode.  
WGR: Whispering Gallery Resonator.

Table of parameters

Name	Symbol	Unit	Equation	Typical value
<i>Mechanics</i>				
Mechanical resonance frequency	$f_m$	Hz	$\frac{1}{2\pi} \sqrt{\frac{k_{eff}}{m_{eff}}}$	$130 \times 10^6$
Mechanical resonance angular frequency	$\omega_m$	rad.s <sup>-1</sup>	$2\pi f_m$	$817 \times 10^6$
Static stiffness	$k_{static}$	N.m <sup>-1</sup>		100
Effective (or dynamic) stiffness	$k_{eff}$	N.m <sup>-1</sup>		$40 \times 10^3$
Effective mass	$m_{eff}$	kg		$30 \times 10^{-15}$
Mechanical quality factor	$Q_m$	-	$f_m/\Delta f$	$10^3$
Mechanical susceptibility	$\chi(\omega)$	m.N <sup>-1</sup>	cf. eq. (D-3)	
Zero point fluctuation	$z_{ZPF}$	m	$\sqrt{\frac{\hbar_p \times f_m}{k_{eff}}}$	$1.5 \times 10^{-15}$
Probe tip displacement	$z$	m		$1 \times 10^{-12}$
Vibration amplitude	$A$	m		$1 \times 10^{-12}$
Spectral density of the thermomechanical force exerted on OM probe tip	$NF_{th}$	N.Hz <sup>-1/2</sup>	$\sqrt{\frac{4k_B T k_{eff}}{Q_m \omega_m}}$	$1.38 \times 10^{-15}$
Thermal bath-induced displacement noise	$Nz_{th}$	m.Hz <sup>-1/2</sup>	$F_{th} \times \chi(\omega)$	$712 \times 10^{-18}$
Phase slope at mechanical resonance	$p_\phi$	rad.Hz <sup>-1</sup>	$\frac{2Q_m}{f_m}$	$2.4 \times 10^{-6}$
Mechanical figure-of-merit of an AFM probe	$\mathcal{F}_m$	Hz.m.N <sup>-1</sup>	$\frac{A f_m^{3/2}}{\sqrt{Q_m k_{eff}}}$	
<i>Tip-sample interaction</i>				
Lennard-Jones 6-12 energy potential	$U(z)$	J	cf. eq. (1)	
Energy depth of the Lennard-Jones potential, <i>i.e.</i> maximum attraction energy	$U_0$	J		
Equilibrium distance between the tip and the surface	$z_0$	m		$2 \times 10^{-9}$
Force exerted by the sample on the tip of an AFM probe	$F_{ts}(z)$	N	cf. eq. (66)	
Force gradient felt by the an AFM probe tip when close to a sample	$k_{ts}$	N.m <sup>-1</sup>	$\partial F_{ts}(z)/\partial z$	
Viscous damping coefficient added by the surface	$c_{ts}$	kg.s <sup>-1</sup>		

<i>Optics</i>				
Laser wavelength	$\lambda_{laser}$	m		$1.55 \times 10^{-6}$
Optical resonance wavelength	$\lambda_0$ or $\lambda_{cav}$	m	cf. eq. (18)	$1.55 \times 10^{-6}$
Optical resonance angular frequency	$\omega_{cav}$ or $\omega_0$	rad.s <sup>-1</sup>	$2\pi c/\lambda_0$	$1.2 \times 10^{15}$
Propagation constant	$\beta$	rad.m <sup>-1</sup>	$k_0 n_{eff}$	$9.7 \times 10^6$
Wavenumber	$k_0$	rad.m <sup>-1</sup>	$2\pi/\lambda_0$	$4.1 \times 10^6$
Optical FWHm in angular frequency	$\Delta\omega$	rad.s <sup>-1</sup>	$2\pi c \Delta\lambda/\lambda_0^2$	$24 \times 10^9$
Optical FWHm in wavelength	$\Delta\lambda$	m		$30 \times 10^{-12}$
Optical quality factor	$Q_{opt}$	-	$\lambda_0/\Delta\lambda$	$40 \times 10^3$
Optical contrast	$C$	-	cf. eq. (H-15)	50 %
Optical extrinsic quality factor	$Q_e$	-	$\frac{\omega_0}{\gamma_e}$	$10^5$
Optical rate of the waveguide to cavity evanescent coupling	$\gamma_e$	rad.s <sup>-1</sup>	cf. eq. (H-17)	$1.2 \times 10^9$
Optical intrinsic quality factor	$Q_{int}$	-	$\frac{\omega_0}{\gamma_{int}}$	$10^6$
Optical loss rate of the cavity only	$\gamma_{int}$	rad.s <sup>-1</sup>	cf. eq. (H-19)	$1.2 \times 10^9$
Optical linear loss coefficient	$\alpha$	m <sup>-1</sup>	$\frac{\beta\gamma}{\omega_0}$	194
Optical cavity length	$L$ or $L_{cav}$	m	$2\pi R n_{eff}$	$147 \times 10^{-6}$
Optical index (material)	$n$	-		3.47
Effective optical index (waveguide)	$n_{eff}$	-		2.4
Free spectral range	$FSR$	m	$\lambda_0^2/2n_{eff}L$	$8 \times 10^{-9}$
Angle	$\theta$	rad		
Azimuthal order	$m$	-		100
Insertion Loss	$L_{oss}$	-		8 dB
Transmission	$T(\lambda)$	W	cf. eq. (26)	$200 \times 10^{-6}$
Laser power	$P_{laser}$	W		$10 \times 10^{-3}$
Optical power injected in the waveguide	$P_{in}$	W		$1 \times 10^{-3}$
Power drop on optical transmission spectrum	$P_{drop}$	W		$100 \times 10^{-6}$
Optical field in the cavity	$a$	J <sup>-1/2</sup>		
Time for a photon to complete a lap in the cavity	$T_0$	s	$m\lambda_0/c$	$500 \times 10^{-15}$
Optical energy in the cavity	$E_{stored}$	J	cf. eq. (25)	
Optical power in the cavity	$P_{stored}$	W	$E_{stored}/T_0$	$160 \times 10^{-3}$

Optical figure-of-merit of an OM AFM probe	$\mathcal{F}_{opt}$		$\frac{g_{O \leftarrow M} Q_{opt} C}{L_{oss}}$	
<i>Opto-mechanics</i>				
Optomechanical frequency-pull factor	$g_{O \leftarrow M}$	Hz.m <sup>-1</sup>	$\frac{g_0}{Z_{ZPF}}$	$7.7 \times 10^{18}$
Optomechanical actuation factor	$g_{O \rightarrow M}$	N.W <sup>-1</sup>	$\frac{k_{eff} A}{P_{st} Q_m}$	$8 \times 10^{-10}$
Normalized optomechanical frequency-pull factor	$g_0$	Hz		$1.15 \times 10^4$
Optomechanical figure-of-merit of an OM AFM probe	$\mathcal{F}_{OM}$		$\mathcal{F}_m \times \mathcal{F}_{opt}$	
<i>Dimensions</i>				
Cavity radius	$R$	m	$R_{ext} - \frac{w_{ring}}{2}$	$9.75 \times 10^{-6}$
External radius of a OM probe ring	$R_{ext}$	m		$10 \times 10^{-6}$
Radius of a OM probe pedestal	$R_{ped}$	m		$2.5 \times 10^{-6}$
Ring thickness	$h$	m		$220 \times 10^{-9}$
Ring width	$w_{ring}$	m		$500 \times 10^{-9}$
Width of the waveguide close to the ring	$w_{taper}$	m		$500 \times 10^{-9}$
Width of the spokes of the OM probe	$w_{spk}$	m		$100 \times 10^{-9}$
Width of the tip of the OM probe at its base	$w_{tip}$	m		$100 \times 10^{-9}$
Coupling distance between the waveguide and the ring cavity	$d_{gap}$	m		$150 \times 10^{-9}$
OM tip's apex radius of curvature	$R_{tip}$	m		$50 \times 10^{-9}$
Roughness	$\sigma_{rms}$	m		$10^{-9}$
Surface of the electrostatic electrodes	$S$	m <sup>2</sup>	$h \times 3 \times 10^{-5}$	$7 \times 10^{-12}$
<i>Constants</i>				
Temperature	$T$	K		293
Light celerity	$c$	m.s <sup>-1</sup>		$3.0 \times 10^8$
Hamaker constant	$H$	J		$3.5 \times 10^{-19}$
Planck constant	$h_p$	J.s <sup>-1</sup>		$6.63 \times 10^{-34}$
Boltzmann constant	$k_B$	J.K <sup>-1</sup>		$1.38 \times 10^{-23}$
Imaginary number	$i$ or $j$	-	$j^2 = i^2 = -1$	
Vacuum permittivity	$\epsilon_0$	F.m <sup>-1</sup>		$8.85 \times 10^{-12}$
Impedance	$r$	$\Omega$		50
Electron charge	$e$	C		$1.6 \times 10^{-19}$

<i>Miscellaneous</i>				
Working frequency, <i>i.e.</i> the frequency of the LIA	$f_{LIA}$	Hz		$130 \times 10^6$
Operating tension of the EOM	$V_{\pi/2}$	V		1.5
Amplitude of the electrical signal applied to the EOM	$V_{OM}$	V		$100 \times 10^{-3}$
Electrostatic force	$F_{elec}$	N		
Tension applied on capacitive electrodes	$V$	V		$100 \times 10^{-3}$
Capacitive modulation angular frequency	$\omega_{mod}$	rad.s <sup>-1</sup>		$817 \times 10^6$
Power spectral density of electrical thermal noise	$S_{thermal}$	W.Hz <sup>-1</sup>		-174 dBm
Amplifier gain	$G$	-		20 dB
Photodiode responsivity	$R_{esp}$	A.W <sup>-1</sup>		1
Current	$I$	A		
Allan deviation (operator)	$\sigma_y$			
Phase-shift	$\varphi$	rad		

## General introduction

Nano-world, atom-sized-world, was given 40 years ago a new class of tools to interact with: local probe microscopes also known as scanning probe microscopes (SPM). They consist in micrometer-sized sharp tips put in close vicinity of the surface to analyze. The tip is locally probing the surface through electronic, mechanical or even optical near-field interaction and scanners then move it over the surface in a raster fashion. They also allowed atoms manipulation<sup>1</sup>. The first of these tools was the Scanning Tunneling Microscope (STM) invented in 1982 by Binnig *et al.* [2], recording the electrical current flowing between a sharp tip and the surface to analyze. This microscope was followed 4 years later by the Atomic Force Microscope (AFM)[3], recording the force exerted by the surface on the sharp tip. But those local probe microscopies have one inherent drawback: slowness. Indeed, to obtain a full image of a surface, the sharp tip needs to be displaced over every pixel. In today commercially available AFMs, it takes in the order of one minute to acquire a full image. Scientific community had to wait another 24 years to reach video-rate AFM [4], unlocking information on rapid biological phenomena. This achievement was reached thanks to impressive technical improvements of each building block of the instrument architecture. It however faces fundamental limits on acquisition speed as the sensing sharp tip bandwidth is governed by its resonance frequency. To reach higher frequencies (*i.e.* higher acquisition speed), AFM probe dimensions were shrunk until two locks were met: fabrication capability and detection sensitivity thus calling for new probe architecture and new detection schemes (p. 422 in [5]). Parallel to that development, teams tried to find integrated and sensitive measurements of the sharp tip motion, to name a few: piezoelectrical [6], piezoresistive [7], capacitive [8] and optomechanical [9]. This thesis work is focused on the latter.

Through optomechanical coupling, optical resonators provide an ultra precise, quantum limited displacement sensor<sup>2</sup>, whose most recent achievement is the detection of gravitational waves [10] with a 4-km cavity. On the other side of the size-scale, benefiting the growing silicon photonics capability, optical micro-resonators pushed frontiers in nonlinear optics [11], quantum optics [12] and sensing [13]. This micro-cavity optomechanical detection was applied to local probe microscopy in 2017 with promising results [14][15] but lacking actuation to achieve dynamic AFM operation. The new AFM probe presented in this thesis work is an optical micro-cavity acting as the sensing sharp tip, providing integrated ultra-sensitive and high bandwidth actuation and detection. This thesis work is included in the Olympia ANR project and is part of a four labs and one start-up collaborative work: MPQ, LAAS, IEMN, LETI and Vmicro.

---

<sup>1</sup> See the “A Boy And His Atom” movie made out of atoms by IBM in 2013, url: <https://youtu.be/oSCX78-8-q0>.

<sup>2</sup> Down to  $10^{-19}\text{m}/\sqrt{\text{Hz}}$  [199].



## Outline

The first chapter of this manuscript introduces the AFM instrument and its operation, with a focus on recent developments and in particular its probes. The second chapter is dedicated to the new optomechanical (OM) probe developed, from theory to design and fabrication. The third chapter presents experimental instrumentation and optical as well as mechanical characterization of those probes. The fourth chapter is dedicated to the fast-AFM instrument built to host the OM probe. The fifth and last chapter presents our results: feedback control and AFM imaging. My thesis work was mainly characterization and experiments with the OM probe.

## I. State of the art of AFM technology

In this chapter, the Atomic Force Microscope (AFM) is first placed among its optical and electron counterparts. We then introduce force interaction framework at the nanoscale. We identify the AFM five building blocks and detail its operating regimes. Then its recent developments, mainly towards higher speed and higher resolution, are presented. Finally an overview of the AFM probes is given to position our new OM probe concept among them.

### I.1 Position of AFM among microscopy methods - History

History of microscopies can roughly break down in four parts<sup>3</sup>: optical, electron, local probe and super-resolved optical. Main invention dates are displayed on Figure 1. AFM comes nearly last, in the local probe category.

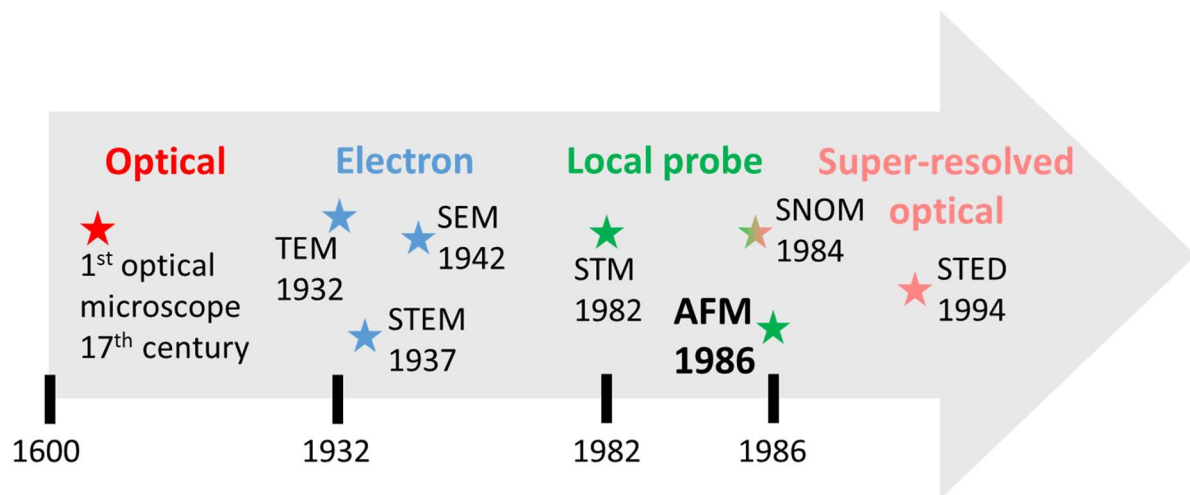


Figure 1: Timeline of major advances in microscopy. Invention references in chronological order: 1<sup>st</sup> optical microscope [16], Transmission Electron Microscope (TEM) [17], Scanning Transmission Electron Microscope (STEM) [18], Scanning Electron Microscope (SEM) [19], Scanning Tunneling Microscope (STM) [2], Scanning Near-field Optical Microscope (SNOM) [20], AFM [3], STimulated Emission Depletion (STED) [21].

Interests and drawbacks of each type is briefly presented:

- **Optical** (classical to super-resolved): light sources and glass lenses magnification are light-speed, simple and inexpensive. The optical microscope has a resolution fundamental limit determined by photon wavelength ( $\lambda_{purple} = 400 \text{ nm}$ ) which practically limits lateral resolution to 200 nm.
- **Electron** (Transmission electron microscope TEM, Scanning electron microscope SEM): Electron gun, electrostatic and magnetic lenses provide a fast scanning. The electron microscope resolution is limited by the electron/ion spot size, practically limiting lateral resolution to a routinely few nanometers<sup>4</sup>. It must be used in vacuum, almost completely excluding living biological imaging<sup>5</sup>. Its main feature is its large range, allowing to observe small and large patterns in the same experiment.

<sup>3</sup> The reality is indeed infinitely richer with crossed domains between those categories.

<sup>4</sup> Down to atomic resolution for the TEM.

<sup>5</sup> Environmental SEM allows wet sample imaging.

- **Local probe** (STM, AFM): Sharp tips provide the best resolution among all microscopies with a 0.1 nm resolution [22], mainly limited by the tip's apex size in first approach. Imaging speed is slow but it can be applied to any material (only electrically conductive ones for STM).
- **Super-resolved optical** (SNOM, STED): One can overcome the photon wavelength limit by using more expensive and slower local probes, near-field techniques and/or fluorescence. Scanning near-field optical microscope (SNOM<sup>6</sup>) and fluorescence microscope STED thus reach a 20 nm resolution [23].

Specs Type	Lateral resolution	Application field	Imaging Rate	Cost/ Complexity
Optical microscope	Diffraction limit: 200 nm	Everything	1 ms/frame	5 k€
SEM	Focusing limit: 0.4 nm	Except bio*	1 ms/frame	100 k€
STM	Tip-size limit: 0.1 nm	Only conducting and semi-conducting materials	10 s/frame	100 k€
AFM	Tip-size limit: 0.1 nm	Everything	10 s/frame	150 k€
SNOM	Aperture size limit: 20 nm	Everything	100 ms/frame	150 k€

Table 1: Specifications comparison among different microscopies. Every number in this table is more of a magnitude order than a precise value. \*Actually environmental SEM allows wet sample imaging.

A brief operating overview of each microscope is given in Figure 2.

---

<sup>6</sup> As a sharp sensing tip is used, SNOM also belongs to the local probe category.

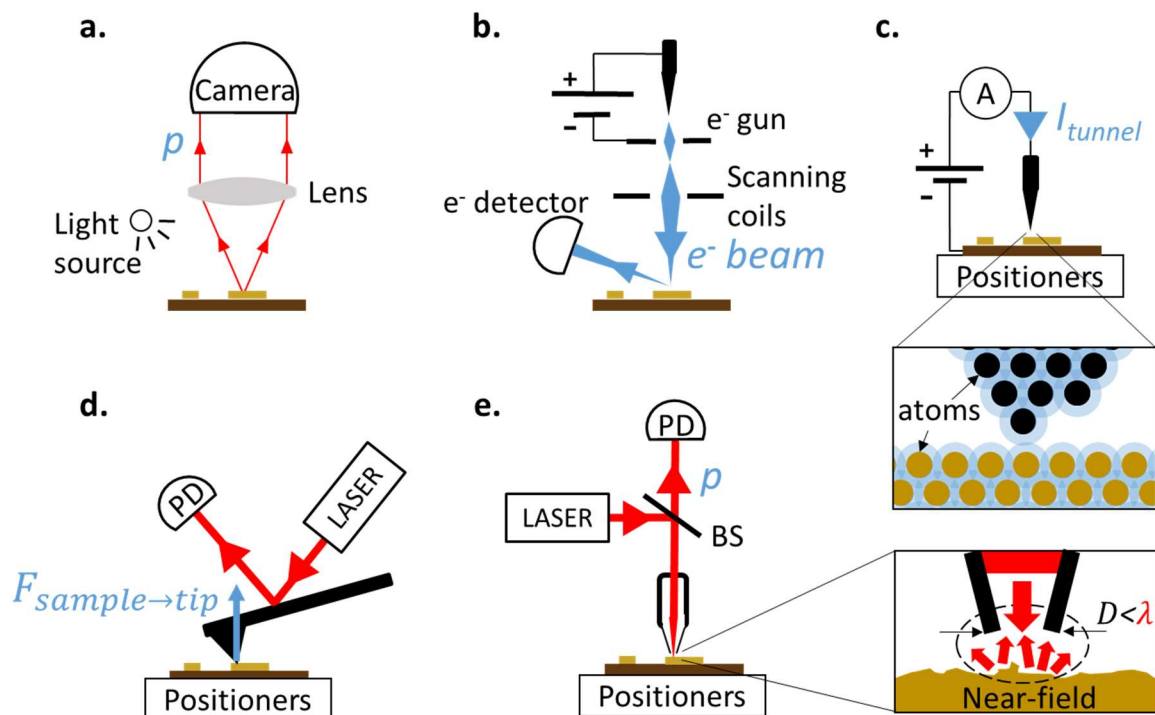


Figure 2: Operating schemes of different microscopies. (a.) Optical microscope, (b.) Scanning Electron Microscope (SEM), (c.) Scanning Tunneling Microscope (STM), (d.) Atomic Force Microscope (AFM) and (e.) Scanning Near-field Optical Microscope (SNOM). (a.) Optical microscope: the light emitted by the source is reflected by the sample. The lens modifies the path of the light so that a camera (PD) or a viewer's eye can see a magnified view of the sample. No scanner is needed to capture one image: it is called a full-field technique. (b.) SEM: an electron gun shoots electrons at a surface. The sample either scatters the incoming electrons or re-emits electrons that are then recorded by an electron detector. Scanning coils then deviate the beam in order to map electrons scattered or re-emitted over the sample. (c.) STM: when the conductive tip is brought close to the conductive sample, it closes the electrical circuits. As a potential is applied between the two, a current appears as electronic clouds of the atoms overlap in inset. Positioners then move in order to map current over the sample. (d.) AFM: the sample exerts either attractive or repulsive force onto the tip, bending it. The laser reflected on the tip is deflected according to the bending. The deflection sensitive photodiode (e.g. 4-quadrant PD) records thus the force at this location. Positioners then move in order to map force over the sample. (e.) SNOM: laser light is focused on a sample via a tiny hole ( $\sim 20\text{nm}$ ) at the end of a tip. The sample modifies the light-field locally. Reflected light is then collected through the same aperture, is separated from the source via a beam splitter (BS) and is collected by a photodiode. Positioners then move in order to map optical reflection over the sample.

Among microscopies, AFM is versatile, has the best resolution with STM [24][25] but is far slower than its full-field or electron counterparts, mainly because moving bulky mechanical parts is slow. We will now see in details how this microscope works and where those characteristics stem from.

## 1.2 Principle of the AFM

Before describing the different blocks composing the microscope, we glance at what feels the probe: the interactions between the AFM probe's tip and the surface.

## 1.2.1 Interactions between a tip and a surface

### 1.2.1.1 Mechanical interaction from a static picture

The interactions between a tip and the surface can be of magnetic, electrostatic and mechanical<sup>7</sup> nature<sup>8</sup>. They become significant when the tip is brought in the 100 nm range apart from the sample [26]. If the materials from both sides are at the same electrical potential, not chemically reactive, not magnetic and considering a condensed matter tip and surface in vacuum, the interaction can be broken down in 2 forces:

1. Long-range attractive Van der Waals (VdW): they arise from electrostatic interactions between dipoles (atoms, polarized molecules) and polarization (electrostatic dipole density). For an atom-atom interaction, those forces vary as  $z^{-6}$  [27],  $z$  being the distance between the dipoles.
2. Short-range repulsive atomic force, exchange interaction of electrons or Pauli repulsion: for an atom-atom interaction, those forces approximately vary as  $z^{-12}$ .

The widely used semi-empirical 6-12 Lennard-Jones energy potential (p. 26 in [28] and equation (1)) accounts for the two forces between two atoms.

$$U(z) = 4U_0 \left\{ \left( \frac{z_0}{z} \right)^{12} - \left( \frac{z_0}{z} \right)^6 \right\} \quad (1)$$

Where  $U_0$  is the depth of the energy potential (*i.e.* maximum attraction energy) and  $z_0$  is the equilibrium distance in contact.

However, considering a usual AFM tip apex of 10 nm of curvature radius [29], tens or hundreds of atoms participate in the contact interaction. One thus needs to consider integrated interaction in a macroscopic picture as Hamaker did for a sphere-plane configuration [30]. Integrating VdW interaction leads to a  $1/z^2$  force profile (equation (2)),  $z$  being the distance between the tip and the sample.

$$F_{VdW/sphere-plane}(z) = -\frac{HR_{tip}}{6z^2} \quad (2)$$

Where  $H$  is the Hamaker constant in Joules ( $H$  is about 1 eV for solids [26]) and  $R_{tip}$  is the tip's curvature radius.

Alike the macroscopic treatment of VdW forces, short range interaction will scale as a lower inverse power  $1/z^{n<1}$  depending on the contact geometry. Another similar potential used for chemical interactions is the Morse potential [26][31].

Depending on the size-scale of the chosen contact picture, other phenomena come at play as bulk elasticity of materials or adhesion/contact energy. Among contact mechanics models,

---

<sup>7</sup> Mechanic here refers to Pauli electronic cloud repulsion.

<sup>8</sup> We neglect gravity as the tip and surface are fixed.

one can cite the Hertz [32], JKR [33], DMT [34] and Bradley [35] models, which main features are represented in Figure 3. To know which model to use, the reader is referred to [36].

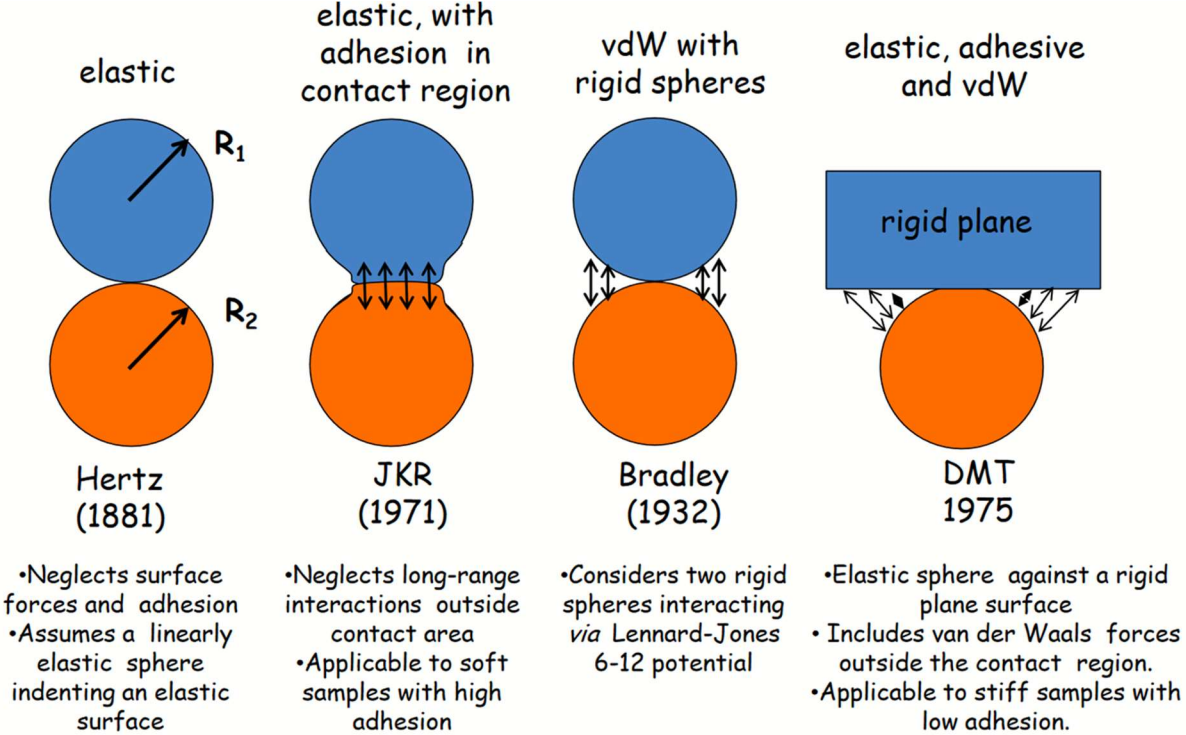


Figure 3: Scheme of different contact mechanics models. From the online course [37], itself from [38].

Applying those models, one can find the force profiles felt by the tip. A standard scheme of the contact is presented in Figure 4a. It presents the different force profiles felt by the tip, for increasing complexity models Figure 4b, c and d.

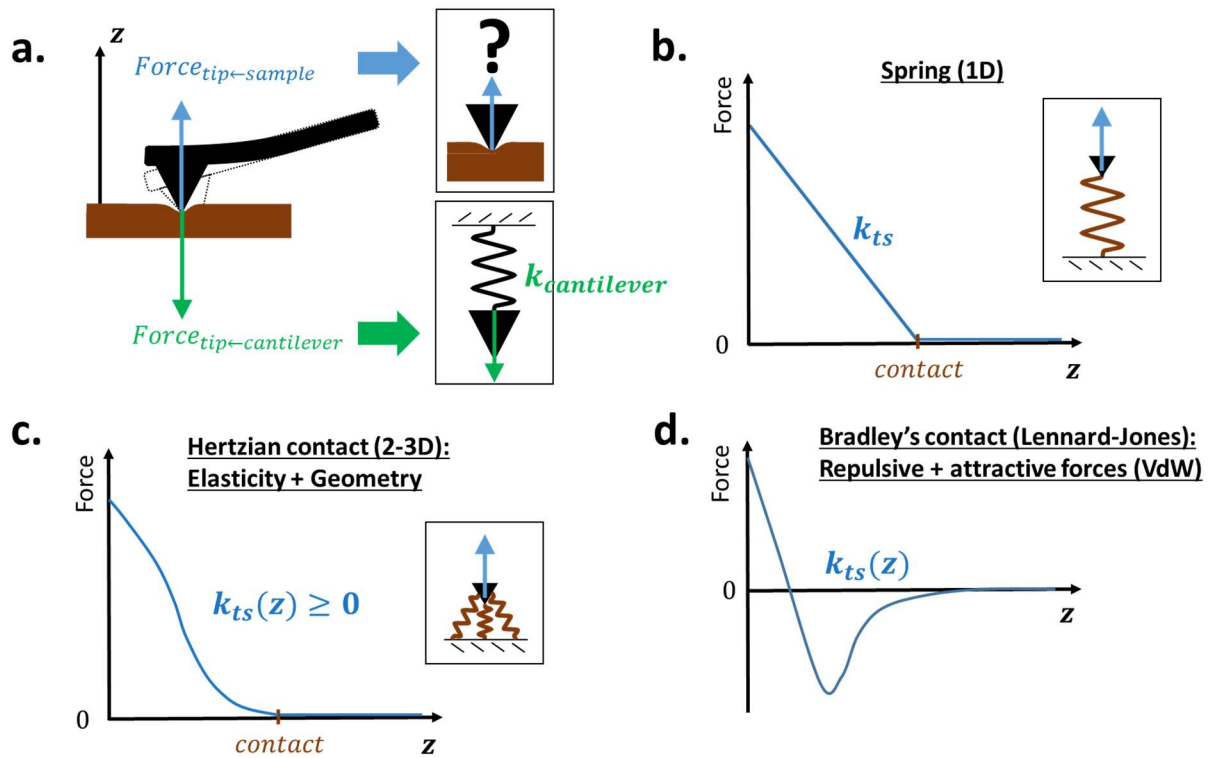


Figure 4: (a.) Scheme of the contact with (b.), (c.) and (d.) different contact/force profile models with increasing complexity.  $k$  represents a force gradient or stiffness. (b.) The simplest contact model represents the contact by a spring of stiffness  $k_{ts}$ . (c.) Hertzian contact model represents the contact by a stiffness that varies with the distance. (d.) Bradley contact model represents the contact between two rigid materials interacting via the Lennard-Jones potential.

We will use the more precise Bradley model of contact. As it considers an attractive regime of forces, it induces a dynamic effect: jump-to-contact.

### 1.2.1.2 Jump-to-contact phenomenon

The attractive interaction can cause the so-called “jump-to-contact” and “jump-off-contact” dynamic phenomena (green arrows in Figure 5). Indeed, if a tip is slowly brought close to a surface, due to attractive forces, there is a brutal increase of the force applied to tip and it goes to the equilibrium position between attractive and repulsive forces, in the 4-7 Å range [39][40]. The brutal shift appears as the force gradient felt by the tip becomes greater than its stiffness, resulting in a bending of the cantilever as it slips in the potential well. As a consequence, for a high-stiffness  $k_{high}$  cantilever, there is no jump-to-contact (Figure 5).

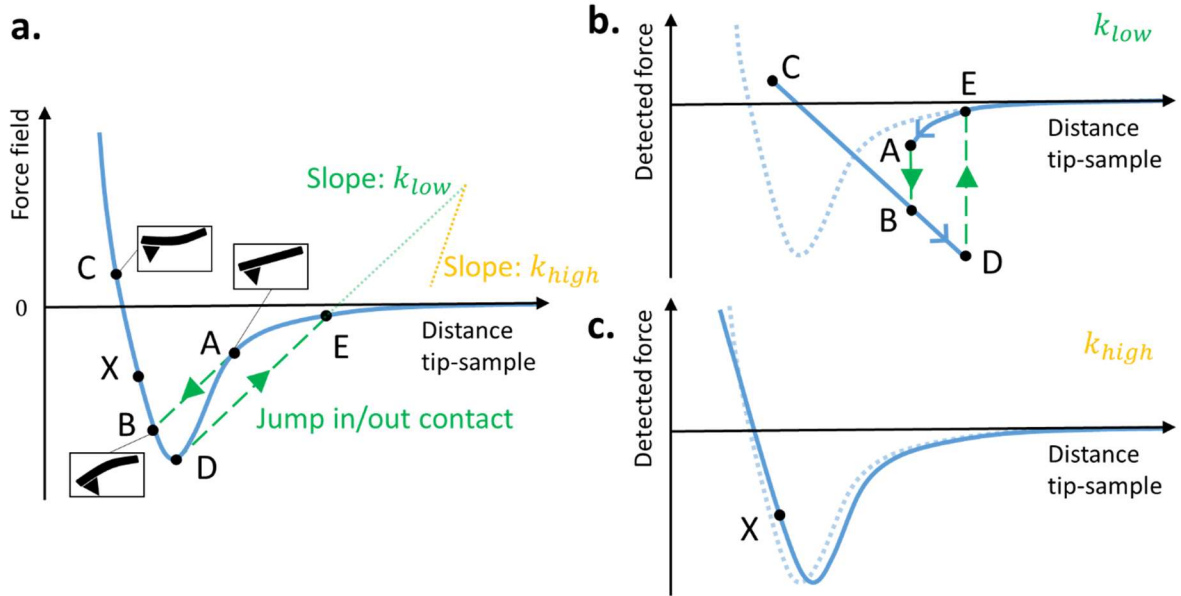


Figure 5: Schemes of (a.) the force field profile and the detected force profile with (b.) a low stiffness  $k_{low}$  and (c.) a high stiffness  $k_{high}$  stiffness cantilever. (a.) When the attractive force gradient is stronger than the cantilever stiffness  $k_{ts} \geq k_{cantilever}$  (i.e. when  $F_{ts} > F_{cantilever}$ ), the cantilever bends down leading to the jump-to-contact phenomenon. Interestingly, one can note that here the condition on  $k_{ts}$  depends on  $k_{cantilever}$  because it is considered the lowest stiffness (over the sample bending one for example). (b.) Constructed from [41]. The detected force profile differs from the force field if the cantilever stiffness is too low. (b.) and (c.) The slope in the left-hand-side of trace is the cantilever's stiffness.

The non-jump condition writes itself  $k_{cantilever} > |dF_{ts}/dz|$ . If the cantilever is vibrating with an amplitude  $A$ , one can rewrite the non-jump condition (p. 3 in [42], [43]):

$$k_{cantilever}A > F_{ts} \quad (3)$$

Typical stiffness to prevent jump-to-contact is in the order of  $1 \text{ kN.m}^{-1}$ .

In practice, other effects of different nature, that were not considered here, appear and modify the interaction. For example, environment effects come to play in the interaction.

### 1.2.1.3 Environment effects

In air, a water layer is often present at material surface. So when the tip approaches the surface, a meniscus forms between the tip and the surface [44]. Thus a capillary force appears<sup>9</sup> [45], adding to the attractive forces.

In most used AFM imaging modes, the tip is vibrating. It then experiences viscous damping in air and to greater extent in liquid.

For a comprehensive report on forces and phenomena at play in AFM interaction, one can read [26] and [46] for different models application. Now that interactions are clear, we will see how one detects the tip movement in response to the interaction and which instruments and what signal processing is used.

<sup>9</sup> Obvious but to have in mind: in water this meniscus effect disappears.



### 1.2.2 Historical AFM operation

The first AFM idea, by Binnig *et al.* in 1986 [3], is described as a mix of the stylus profilometer and the tunneling microscope: basically an improved detection profilometer allowing to detect atomic forces. It consisted of a tunnel current detection (STM on top of cantilever) of a golden foil cantilever with a diamond tip (Figure 6). The tunnel current is detected and compared to a setpoint and the difference feeds the piezoelectric positioner of the sample. It therefore keeps the force exerted on the cantilever constant. As the feedback loop is closed, the sample is then scanned to give a force/topography image. In this initial publication, the cantilever is not actuated (*i.e.* static mode), however oscillating operation (*i.e.* dynamic mode) is described and as this mode is widely used nowadays, we will only consider the latter. Brief comparison of the two modes is given in the beginning of next part. So, the cantilever is put in vibration at its resonance frequency. This resonant detection allows a better sensitivity, compromising on the bandwidth as detailed in next part.

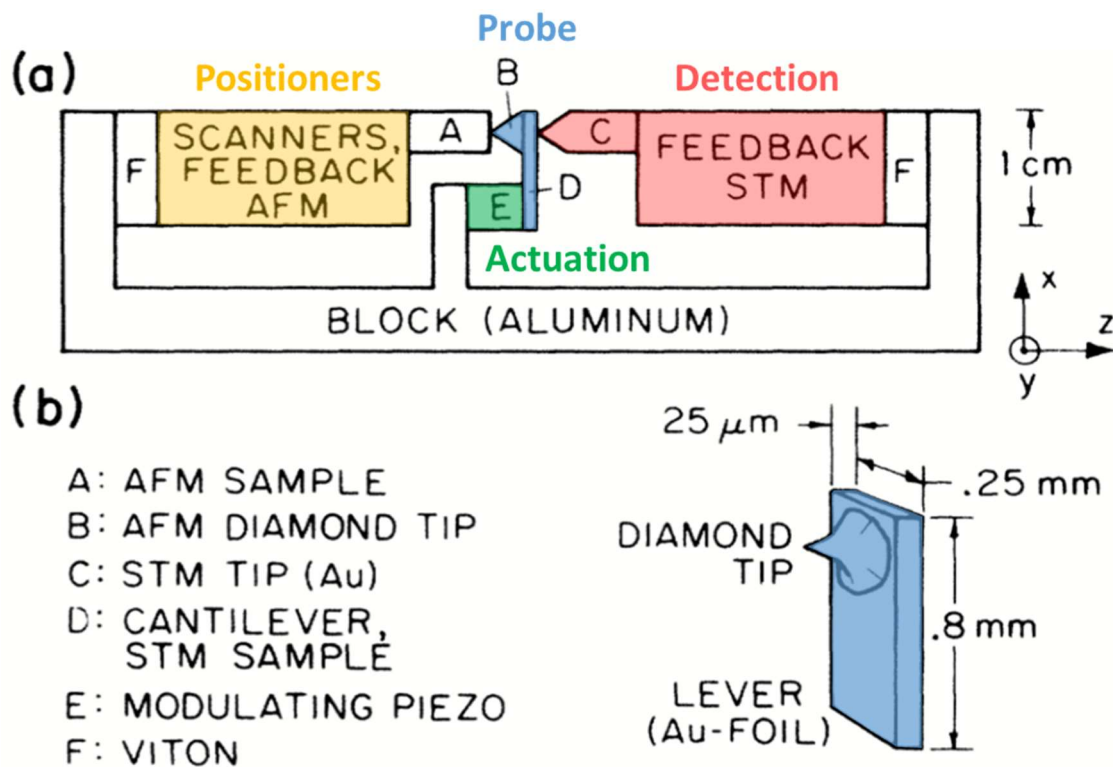


Figure 6: Scheme of the first AFM, from [3]. The essential blocks of the instruments are highlighted in color: (blue) probe, (red) detection, (yellow) positioners, (green) actuation. The last essential block considered is the feedback control, here included in the positioners and detection blocks.

From Figure 6, we can identify five essential blocks in the AFM apparatus:

- Probe
- Probe's mechanical motion detection
- Signal processing and feedback control
- XYZ scanners
- Probe actuation

### 1.2.2.1 Probe

The purpose of the probe is to transduce the interaction force between the tip and the sample into a mechanical motion, the latter being easier to detect. The tip must be the sharpest possible to have the best lateral force resolution. Its apex is generally considered as a half sphere and characterized by its radius of curvature. Today, classical radius of curvature is about 10 nm [29], yielding a nanometric resolution. Its mass, among other parameters, defines its dynamical behavior. The lower the mass, the quicker the response to an applied force. The latter is discussed in next part.

### 1.2.2.2 Mechanical motion detection

How can the mechanical motion of the tip be transduced to an electrical signal, in order for it to be processed and recorded by a computer? The first chosen detection of the tip, STM seen above in Figure 6, is a complex and inconvenient apparatus [47]. Rapidly, optical deflection detection [48] was preferred for the sake of simplicity (Figure 7). It consists in shooting a laser onto a reflective probe, the reflected laser's angle carries the deflection, and thus force, information. A 4-quadrant photodiode, that is angle-sensitive, then records the laser signal. Today, most commercially available AFMs rely on this "optical lever" or optical beam deflection (OBD) detection (as AFMs from Bruker, Asylum research or JPK). This OBD technique reaches a typical limit of detection of about  $10^{-14} \text{ m}/\sqrt{\text{Hz}}$ . A fundamental limit of detection (LOD) is thermomechanical noise: thermal bath excites mechanical motion of the probe. This thermal limit is quantified in next part.

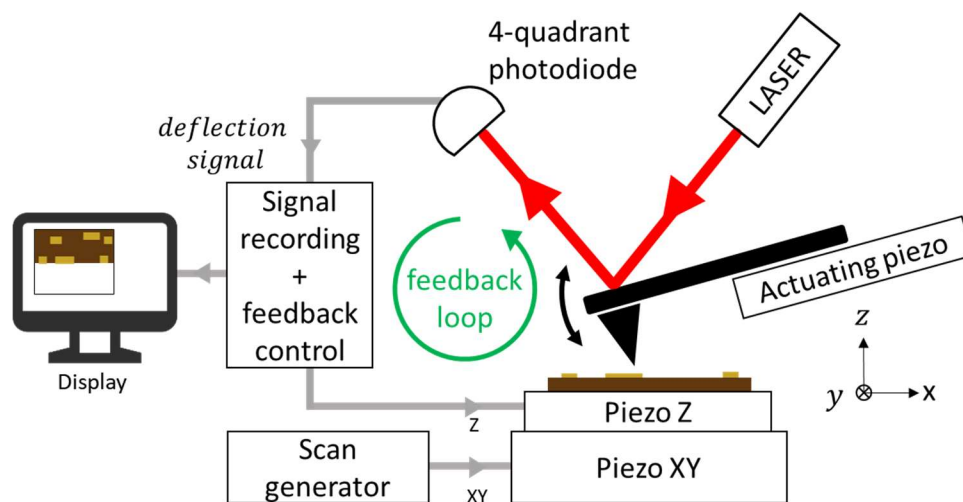


Figure 7: Scheme showing the typical operation of an AFM.

Other detection-actuation method/transductions are studied and used in research groups, those methods are discussed in Sec. 1.4.

### 1.2.2.3 Scanners

To scan all the sample, SPMs use either sample or tip scanning, the latter having the advantage of being independent of the sample's size and mass but usually complicates the detection. Usual scan pattern is the rectangular raster scan (Figure 8).

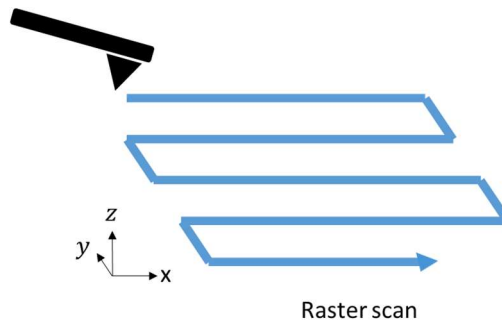


Figure 8: Scan pattern scheme: raster scan.

- Scanners' type

Typically, piezoelectric ceramic scanners, as Lead Zirconate Titanate (LZT<sup>10</sup>), are mainly used in AFM and more generally in SPM. This is because they routinely reach a below angstrom precision, necessary to achieve atomic resolution. Indeed, in crystals, atoms are separated from each other of a few angstroms (0.1 nm). Their main disadvantages are creep, which is the displacement drift for a constant applied voltage, and hysteresis [49]. Teams also exceptionally use magnetic [50], and MEMS electrothermal scanners [51].

- Scanning speed/bandwidth

In the usual raster-scan pattern, we refer at Y direction as slow axis and the X as the fast axis. In terms of bandwidth this means that, if the image has 100 lines, the speed of the X scanner must be 100 times higher than the Y one. Equally, in feedback loop operation, if each line has 100 measurement points, the feedback loop Z-positioner must have a 100 times higher speed than the Y one to accurately probe a surface's topography. Varying at each location point, the Z-positioner is thus fundamentally the limiting one in the image acquisition. Therefore, its speed and the feedback loop speed must be the highest possible to reach fast imaging in feedback operation.

#### *1.2.2.4 Signal processing and feedback control*

The probe signal acquired by the photodiode is compared to a set-point reference. The difference is then fed in a proportional-integral PI controller that commands an amplifier that

---

<sup>10</sup> Or PZT in French.

drives the piezo positioner (Figure 9). Those operations are done by either analog or digital electronics, the latter being more versatile.

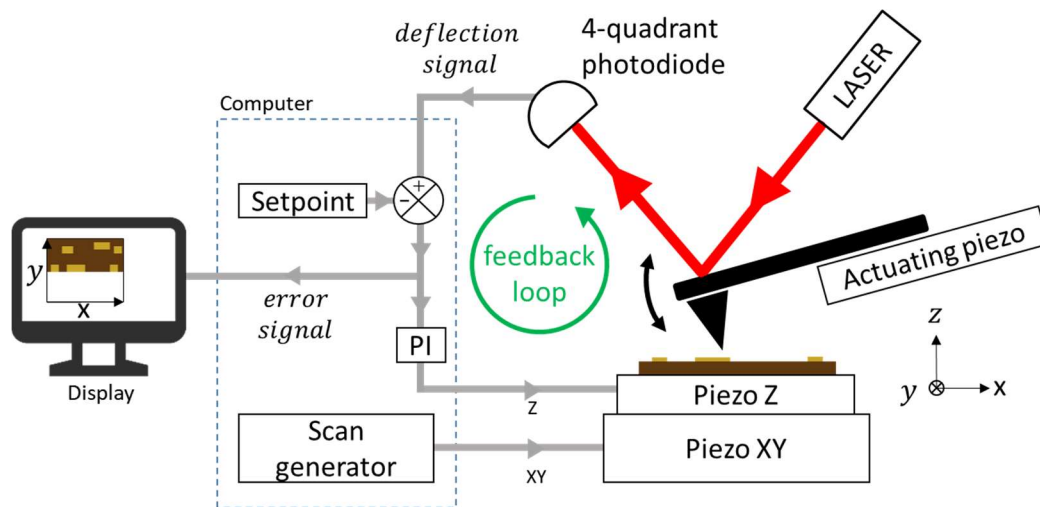


Figure 9: Scheme of the signal processing in the servo loop.

**Feedback Bandwidth:** The imaging speed of the instrument is limited by the feedback bandwidth. Indeed, due to delays in the feedback loop, the feedback system has not an instantaneous time response. Those delays can induce instabilities and oscillations that can damage the tip and the sample. The feedback bandwidth is defined as the first resonance reached by this system. The global feedback bandwidth is hence limited by each feedback loop component's bandwidth (*i.e.* delays). Feedback bandwidth limitation thus stem from piezo controller delay, cantilever mechanical delay and/or from signal processing digital latency. It is detailed in Sec. 1.3.1.

In practice, when scanning, the operator raises both PI gains until resonance appears (sine deflection signal) and reduces the gains just before the resonance point (p. 93 in [52] or Ziegler-Nichols method [53]).

#### 1.2.2.5 Tip actuation

As it is detailed in next section, AFM can be operated in different dynamic modes, where the tip must be actuated. This actuation must have the highest bandwidth, stability and dynamic range. This function is generally performed by a piezoelectric transducer on which the tip is mounted. Other techniques are detailed in Sec. 1.4.1. The tip vibration amplitude is typically of a few nanometers. It has to be significantly higher than the limit of detection to obtain a quality measurement. For a standard OBD limit of detection (LOD) of  $10^{-1} \text{ m}/\sqrt{\text{Hz}}$ , with a feedback bandwidth of 10 kHz and taking a 40 dB signal margin, the lower limit of tip vibration amplitude is 100 pm.

#### 1.2.3 Operating modes and controls

AFM tool can be used to perform imaging, *e.g.* topography of a sample but also to perform force spectroscopy, *e.g.* extract the local force profile. Those two modes are described after a static versus dynamic mode consideration.

### 1.2.3.1 Static versus dynamic modes

Although the first AFM imaging modes used were static ones [3], dynamic modes (*i.e.* when the tip oscillates) now prevail, referred as Dynamic Force Microscopy (DFM) in biological studies. Indeed, in static mode, if the tip is scanned without oscillation, it exerts lateral forces that can damage the sample or the tip. Furthermore, dynamic modes provide a more sensitive force detection as if they detect force with an equivalent softer cantilever:  $k_{dyn} = k_{eff}/Q_m$ <sup>11</sup>,  $Q_m$  being the mechanical resonance quality factor. Actually, bandwidth is traded for force sensitivity. Bandwidth goes up to  $f_m$  in static mode and up to  $f_m/Q_m$  in dynamic modes, *i.e.* the response is integrated during the average resonance decay time  $Q_m/f_m$ . In dynamic mode, measuring signal at the cantilever's frequency also implies less noise as, for low frequencies,  $1/f$  noise dominates. For the next paragraphs, only dynamic modes are considered.

### 1.2.3.2 Force spectroscopy (or Z-spectroscopy)

The force profile normal to the sample surface is extracted in one point, moving the tip to the sample. To acquire a force-distance curve, a force or distance set-point is given by the user. The cantilever then approaches the surface until it reaches the set-point and then retracts while deflection is recorded. This technique allows to obtain mechanical information from the surface. In particular, it gives insights in biological studies on meniscus [45], molecular bonds and cell's mechanical properties [54].

### 1.2.3.3 Imaging-Scanning (dynamic)

AFM imaging modes can be separated in 2 overlapping categories. The first category is the force regime of operation: repulsive, attractive or both. The second category is the type of servo operation: AFM can detect amplitude (AM), phase (PM) and frequency (FM) signals to control the tip-sample distance and thus obtain topography.

#### **Modes depending on the force regime (Figure 10):**

- **Non-contact:** the tip oscillates in the attractive regime. It is the least damaging imaging mode but the least sensitive one. Compared to other modes, it needs a stiffer cantilever to prevent jump-to-contact, *i.e.* to prevent the cantilever from slipping into the potential well [46]. Cantilever stiffness necessary to prevent jump-to-contact is in the 100 N/m range, depending on the tip size and material involved.
- **Tapping:** the tip oscillates in the attractive and repulsive regime. The tip intermittently « taps » by feeling the repulsive forces. In this mode, tip can exert higher peak force however on a briefer time. As it oscillates between the attractive and repulsive regime, it reduces lateral forces appearing when the sample is scanned.
- **Contact:** the tip oscillates in the repulsive regime [55]. This mode is *a priori* the mode in which the tip-sample interaction is the strongest. As the tip oscillates in the high repulsive slope, in order not to damage the sample, the vibration amplitude needs to be low (about a few angstroms maximum). It therefore is a more sensitive mode thanks to the higher repulsive slope but also potentially more damaging to the sample.

---

<sup>11</sup> This is shown in Sec. 1.3.2.1. However to be truly valid, this reasoning considers  $k_{eff} = k_{static}$ , which is not the case.

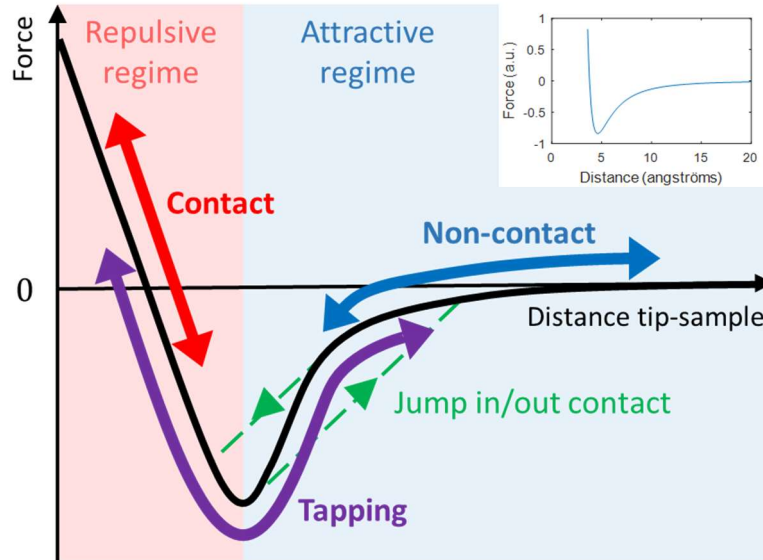


Figure 10 : Scheme of the different operating modes of AFM with regards to the sample's force profile. Inset shows a simulated force profile from Bradley's contact model (p. 18 in [46]).

In practice, the force regime is chosen by the AFM user, setting the vibration amplitude of the probe and the force gradient set-point, within the limits of the probe itself. That being said, a widely used mode is tapping, a sweet spot between sensitivity and sample damage. We will now see what servo operation can be chosen to scan the sample.

### Modes depending on the type of servo operation (Figure 11):

- **AM** (amplitude modulation), fixed actuation frequency mode: as the cantilever is oscillating, its vibration amplitude is recorded, compared to a set-point and the difference feeds the Z positioner. Typically, if the cantilever enters in a dissipative contact, its vibration amplitude will diminish. The Z scanner will then retract and thus augment tip-sample distance until the amplitude comes back to its initial value. In a simple spring-viscous damping contact model, the amplitude is inversely proportional to the viscous damping coefficient added on the cantilever.
- **PM** (phase modulation), fixed actuation frequency mode similar to **AM**: as the cantilever is oscillating, its phase is recorded, compared to a set-point and the difference feeds the Z positioner. Typically, if the cantilever enters in a repulsive contact, its phase will go up. The Z scanner will then retract and thus augment tip-sample distance until the phase comes back to its initial value. In a simple spring-viscous damping contact model, the frequency shift is proportional to the force gradient (or stiffness/spring) applied on the cantilever.
- **FM** (frequency modulation): to decouple the two components (force and damping) of surface interaction, one can fix the resonance's amplitude to a set-point with a feedback loop. Then use the cantilever frequency shift (which, now that the amplitude is set, reflects only the interaction force gradient) to feed the Z positioner. To know the frequency shift of the cantilever and thus actuate the cantilever at its varying

resonance frequency, a Phase-Locked-Loop (PLL) is generally used<sup>12</sup>. PI controller are generally used to control the amplitude excitation and the Z positioner. In this last scheme, there are thus three control loops: the detected amplitude controls the excitation amplitude, the detected frequency controls the excitation frequency and the frequency shift from the initial value controls the tip-sample distance.

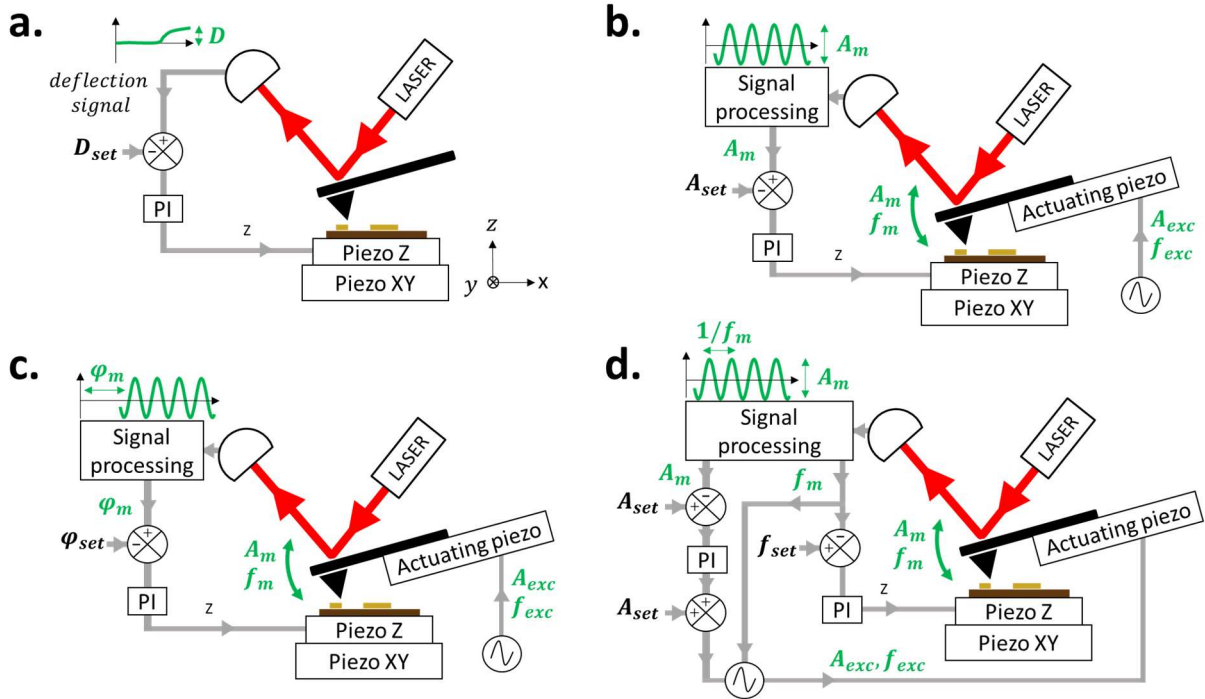


Figure 11: Schemes of AFM imaging modes: (a.) Constant force, (b.) AM-AFM, (c.) PM-AFM and (d.) FM-AFM.  $D$ : deflection,  $\varphi_m$ : vibration phase,  $A_m$ : vibration amplitude,  $f_m$ : vibration frequency,  $A_{set}$ : amplitude setpoint,  $f_{set}$ : frequency set-point,  $A_{exc}$ : cantilever drive amplitude and  $f_{exc}$ : cantilever drive frequency.

To summarize, FM-AFM is more complex to set up (3 control loops) but it provides an easier reading of the interaction information with the surface by projecting the interaction force on the conservative and dissipative forces (frequency shift/stiffness and drive signal/damping), assuming the contact as a spring + dissipation system. PM and FM mode are more stable modes because the loop is on the frequency, a typically less drifting value than amplitude. Whereas in AM and PM, the limit is  $f_m/Q_m$ , in FM-AFM mode bandwidth can extend beyond this limit, theoretically up to  $f_m$  [56][57].

**Bandwidth definitions:** A global definition of the bandwidth is the inverse of the minimal time the system will take to follow the command signal's value. Its meaning however varies depending on the system studied:

- **For a quasi-static system:** It represents the frequency span from 0 Hz in which the displacement of the system follows the command applied with a constant multiplying factor and a limited delay. In mechanical systems, it is limited by the first resonance frequency of the system (Figure 12). At the resonance, the response is amplified so the

<sup>12</sup> A PLL basically is a PID fed with phase and which controls a frequency.

multiplying factor is not constant anymore, and after it, response is delayed. In practice, if one tries to use the system faster than what it is supposed to, the system will barely move or oscillate at a resonance frequency.

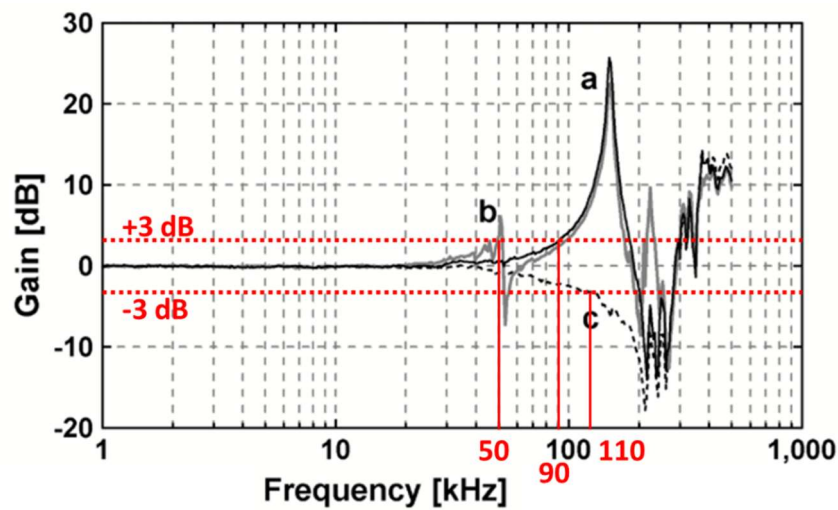


Figure 12: Responses of 3 different system versus frequency. For the “b” system, bandwidth is 50 kHz. For the “a” system bandwidth is 90 kHz and for the “c” system, 110 kHz. From [58].

- **For a resonating system:** When using a system at resonance, the bandwidth is defined as the resonance frequency divided by the quality factor  $f_m/Q_m$  or put in other words as the width of the resonance peak in the frequency domain (Figure 13). It represents the rate at which the system can change its output. Indeed, as the system resonates, it takes a few oscillations for it to change its energy. Bandwidth in AC mode is thus the minimal time the system will take to follow the command signal’s frequency.

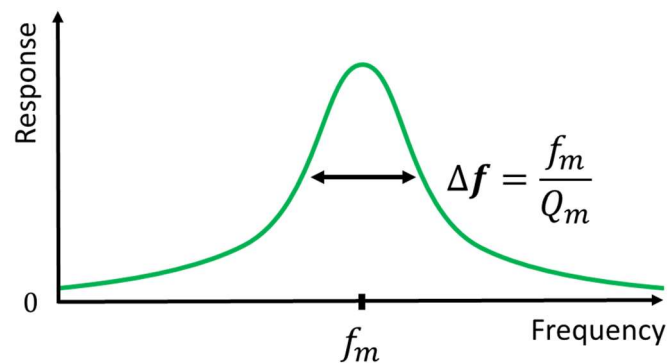


Figure 13: Response of a resonating system versus frequency, the resonance frequency being  $f_m$ . The bandwidth of the resonator is defined by the width of the resonance peak  $\Delta f$ .

#### 1.2.3.4 Other AFM configurations

In the past years, new feedback schemes/modes appeared. Among them one can note Multi-frequency-AFM (MF-AFM)[59], in which information on higher resonance modes of the cantilever are recorded or also the Lateral/Friction Force Microscope (LFM or FFM). The AFM apparatus as it is also allows Atomic Force Acoustic Microscopy (AFAM) where another lock-in amplifier puts the Z positioner in vibration or Scanning near-field ultrasound holography



(SNFUH), (See p. 424 [5]). Another mode consisting in mapping force spectroscopy is known as the “peak-force” mode [60].

### 1.3 Recent developments of the AFM instrument

Since its invention in 1986 and apart from the derived-techniques developments discussed above, AFM developments can be broken down in 3 directions: **speed** since an image in AFM takes a few minutes to take, **resolution** to achieve true atomic resolution in vacuum and other environments and **ease of use / cost cuts** to allow routine experiments and widen its user pool. In this part, the specific developments made on the positioners, signal processing and tip will be broached, leaving actuation and detection to the next part.

#### 1.3.1 Reaching higher speed/bandwidth

The idea is to chase each limiting block of the servo-loop chain to increase its bandwidth. In standard AFM, speed-limiting blocks are positioners, signal processing and the cantilever mechanical delay. This part is largely inspired from the global review [5].

##### 1.3.1.1 Positioners

From the positioners’ point of view, what limits scanning speed are the whole (or parts of the) structure’s lowest frequency mechanical resonances. In piezoelectric positioners, the main solutions are to increase those mechanical frequencies to the maximum and then to damp them. To increase mechanical frequency one can lower the size and increase the stiffness of the positioners. Indeed, as size is reduced, mass also is and following the harmonic oscillator’s resonance frequency formula  $f_m = \frac{1}{2\pi} \sqrt{k_{eff}/m_{eff}}$ , the resonance frequency is increased. But decreasing the size leads to a positioning range decrease. In a reversed reasoning,  $f_m$  is almost determined by the required maximum displacement. To date, the highest bandwidth Z-positioner reaches  $f_m = 150$  kHz [58][61], *i.e.*  $BW = 150$  kHz, thanks to a  $3 \times 3 \times 3$  mm<sup>3</sup> piezoelectric ceramic stack. Those results are made possible by suppressing/damping lower resonance frequencies of the positioner apparatus by design or signal processing pre-scanners (*i.e.* feed-forward). Those techniques are discussed in the description of our homemade AFM apparatus in Sec. IV.3 and IV.4.

##### 1.3.1.2 Detection signal processing

In practice in dynamic AFM, amplitude, phase or frequency of the probe’s vibration, needed for the feedback-loop control, are generally extracted with a Lock-In Amplifier (LIA)<sup>13</sup> in several cycles. To date, the best commercial digital LIA can demodulate signals up to 600 MHz with a 5 MHz demodulation bandwidth [62] with a typical few microseconds latency. Alternative synchronously triggered detections can give the same information in only one cycle, but come with more noise [63].

##### 1.3.1.3 Cantilever’s mechanical time response

As a resonator, the cantilever mechanical time response is not instantaneous. For example if initially excited, its vibration amplitude will then decay with a time constant depending on its

---

<sup>13</sup> A lock-in amplifier demodulates a signal of known frequency. It multiplies the signal with a reference signal of the same frequency and then filters it with a low-pass filter, hence filtering out all the frequencies different from the carrier.

quality factor  $\tau = Q_m/f_m$ . This time constant limits the cantilever's bandwidth, used in AM or PM mode, which is thus given by  $BW = f_m/Q_m$ . For example a  $f_m = 100$  kHz cantilever with  $Q_m = 100$  has a bandwidth of  $BW = 1$  kHz. There is thus a twofold path to improve its bandwidth: raising its mechanical resonance frequency or lowering its quality factor.

- Raising the resonance frequency can be done by using a higher frequency mechanical mode or by increasing stiffness and lowering mass. The latter is the route followed by Ando's team, who used small, lightweight and thus high frequency,  $7 \times 2 \times 0.1 \mu\text{m}$  cantilevers from Olympus<sup>14</sup> with  $f_m = 1.5$  MHz in air. Main limitation to size reduction is the optical deflection detection. Indeed, when the size of the cantilever becomes smaller than the laser spot, detection becomes less sensitive.
- To lower the quality factor, using cantilever in liquids contributed to attain higher bandwidth thanks to viscous damping. For example a BL-AC10DS-A2 cantilever in water with  $f_m = 400$  kHz and  $Q_m = 2$  has a bandwidth  $BW = 200$  kHz [64]. As for size reduction, lowering the quality factor improves the bandwidth but implies less sensitivity (equation (10)).

Note: To overcome the bandwidth limitation of one cantilever, more information can be obtained in less time with parallel operation of a cantilever array. That is the idea followed in [65] and more recently in [66]. In the latter, they demonstrate the parallel use of 14 cantilevers. This technique is suitable for large area studies as whole wafers. Here, the improvement is not exactly on the AFM speed but rather on the information throughput.

Briefly put, to reach higher speed in dynamic AFM, one needs the highest bandwidth positioners, signal processing and cantilever. State-of-the-art instruments reach an overall 100 kHz bandwidth (RIBM Ando-type and Cypher VRS AFMs), yielding an imaging speed of 1 to 10 frames per second.

### 1.3.2 Reaching higher resolution

Resolution can be broken down in 3 types: absolute **force resolution** of the probe, the **lateral (or in-plane) spatial resolution**, which is dependent on the tip's size, and **vertical (or out-of-plane) spatial resolution**, which is dependent on the imaging mode and specifically on the mechanical vibration amplitude of the tip.

#### 1.3.2.1 Force resolution

In this part, we first explicit the parameters of the AFM probe that define the AFM force resolution and then quantify the detection noises. We will use the notion of Limit Of Detection (LOD) to quantify the lowest detectable value of a given parameter. In the end, one wants the LOD to be dictated by the parameter's noise and not the detection noise given by the instrument.

In static mode, the tip-sample interaction force detected by the cantilever is given by:

$$F_{ts} = k_{static}Z \quad (4)$$

---

<sup>14</sup> Olympus BL-AC10DS-A2 is a commercially available small cantilever.

Introducing  $z_{lod}$  as the displacement limit of detection (*i.e.* the smallest displacement detectable), the force limit of detection  $F_{lod}$  (*i.e.* the smallest force variation detectable) is then straightforwardly given by:

$$F_{lod} = k_{static} z_{lod} \quad (5)$$

Thus its static stiffness must be the lowest to feel the lowest forces.

In dynamic mode, we consider  $z(t) = A \cos(\omega_m t + \varphi)$  with  $A$  the vibration amplitude and  $\varphi$  the phase shift between the driving signal and the detected motion signal of the probe. In dynamic mode, instead of a force, a force gradient  $k_{ts}$  is detected. The interaction force is then obtained using:

$$F_{ts} = \int_0^A k_{ts}(z) dz \quad (6)$$

Assuming small amplitudes and thus a constant force gradient, one can re-write  $F_{ts} = A k_{ts}$ .

In dynamic operation of the AFM, this force gradient  $k_{ts}$  is sensed by a shift  $\Delta f$  of the resonance frequency:  $k_{ts} = 2k_{eff}/f_m \times \Delta f$  (from harmonic perturbation limited development, assuming small frequency shifts, detailed in Sec. II.5). For a given frequency detection limit  $f_{lod}$  (*i.e.* the lowest frequency variation detectable), we can thus derive a force gradient limit of detection  $k_{ts\_lod} = 2k_{eff}/f_m \times f_{lod}$ . Thus, to improve the AFM performances, the probe's effective stiffness  $k_{eff}$  must be the lowest and its frequency  $f_m$  must be the highest to feel the lowest force gradients. For a resonator, the resonance frequency shift is usually obtained via its amplitude  $A$  or phase  $\varphi$  variations (Figure 14).

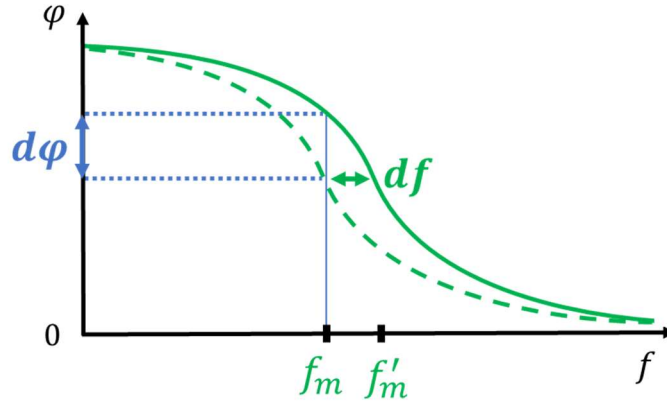


Figure 14: Phase versus driving frequency of a resonator. The phase experiences a  $\pi$ -rotation associated to the mechanical resonance.

As the frequency shift is extracted from the phase of the oscillator via the slope factor  $d\varphi/df$  and the slope factor being maximal at resonance  $f_m$  (Figure 14), we can further write:

$$f_{lod} = \frac{1}{\left| \frac{d\varphi}{df} \right|_{f_m}} \varphi_{lod} \quad (7)$$

For a damped harmonic oscillator calculation, one can find the slope at the resonance:

$$\left| \frac{d\varphi}{df} \right|_{f_m} = \frac{2Q_m}{f_m} \quad (8)$$

Injecting the two precedent equations in the force gradient one leads us to:

$$k_{ts\_lod} = \frac{k_{eff}}{Q_m} \varphi_{lod} \quad (9)$$

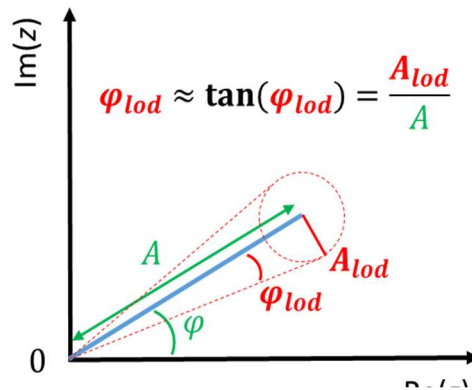


Figure 15: Complex representation of the tip position  $z$  in blue, placing ourselves in the rotating picture at  $f_m$ . In the small amplitude approximation, one can find that  $\varphi_{lod} = A_{lod}/A$ . One can note that  $A_{lod}/A$  is the inverse of the Signal-to-Noise Ratio (SNR). The lowest LOD is logically reached for the highest SNR.

Considering the signal as a complex vector as in Figure 15, one can re-write:

$$k_{ts\_lod} = \frac{k_{eff}}{Q_m A} A_{lod} \quad (10)$$

To compare with the static case, one can finally write, integrating the force gradient on the vibration amplitude  $F_{lod} = A \times k_{ts\_lod}$ :

$$F_{lod} = \frac{k_{eff}}{Q_m} A_{lod} \quad (11)$$

Comparing equations (5) and (11), and considering that  $A_{lod} = z_{lod}$ , dynamic mode emerges as being a factor  $1/Q_m$  more precise than static mode<sup>15</sup>. Or similarly, in dynamic mode, one can work with the same force limit of detection but with higher-stiffness AFM probe.

**Note:** Looking only at the quality factor, there is a fundamental incompatibility between looking for better resolution  $F_{lod} = \frac{k_{ef}}{Q_m} A_{lod}$  and higher bandwidth  $BW = f_m/Q_m$ . To

<sup>15</sup> Considering  $k_{static} = k_{eff}$ , which is not true. However considering the first resonance of a typical cantilever, the Rayleigh approximation gives  $k_{static} \approx k_{eff}$ . As a guideline, for higher order modes  $k_{eff} > k_{static}$ .

diminish the force LOD, one wants to increase  $Q_m$  whereas to reach higher bandwidth one wants to decrease it. To reach better performances in both, one wants to max out the ratio  $f_m/k_{eff}$ : “The usefulness and limitation of small cantilevers having a large  $f_m/k_{eff}$  in dynamic AFM is described in Section 8.2” (p. 352 in [5]).

The  $z_{lod}$  introduced is often limited either by spectral densities of detector noise  $N_{z_{det}}$  or by cantilever thermomechanical noise  $N_{z_{th}}$ .

- **Detector noise:** This noise depends on the detection scheme. For a standard optical beam deflection scheme, the noise is:  $N_{z_{det}} = 10 \text{ fm}/\sqrt{\text{Hz}}$ . For a 1 kHz BW, this gives a  $z_{det} = 300 \text{ fm}$ . From its invention, plethora of detecting transductions have been tried out to overcome existing constraints and most recent AFM achievements were obtained with non-cantilever probes. Other AFM probes structures and transducers are detailed in Sec. 1.4.
- **Thermomechanical noise:** When working at room-temperature, the cantilever is excited by a white noise force stemming from coupling to thermal bath. This gives rise to a fundamental noise limiting the measure. From a damped harmonic oscillator picture and equipartition theorem considerations (see Appendix D:), one can find:

$$N_{z_{th}} = \sqrt{\frac{2k_B T Q_m}{\pi f_m k_{eff}}} \quad (12)$$

Where  $N_{z_{th}}$  is the noise of the thermally-excited motion amplitude of the cantilever at resonance.  $k_{eff}$ ,  $f_m$  and  $Q_m$  are respectively the stiffness of the cantilever, its resonance frequency and its associated quality factor.  $k_B T$  is the thermal energy,  $k_B$  being Boltzmann’s constant and  $T$  the temperature. For a typical cantilever [29]:  $k_{eff} = 35 \text{ N/m}$ ,  $f_m = 190 \text{ kHz}$  and assuming  $Q_m = 1000$  in air at  $T = 293 \text{ K}$ , we find  $N_{z_{th}} = 622 \text{ fm}/\sqrt{\text{Hz}}$ . One can see in equation (12) that a cantilever with a higher resonance frequency and higher stiffness is less affected by thermal noise.

To summarize, for a typical AFM using a cantilever with a OBD detection,  $N_{z_{det}} = 10 \text{ fm}/\sqrt{\text{Hz}} < N_{z_{th}} = 622 \text{ fm}/\sqrt{\text{Hz}}$ . Taking the limiting noise, here  $N_{z_{th}}$ , as  $A_{lod}$  in equation (11), we obtain a force limit of detection  $F_{lod} = 22 \text{ fN}/\sqrt{\text{Hz}}$ , or similarly a force gradient limit of detection taking a 100 nm vibration amplitude  $k_{ts_{lod}} = \frac{k_{eff}}{Q_m A} N_{z_{th}} = 218 \text{ nN/m}/\sqrt{\text{Hz}}$ .

### 1.3.2.2 Lateral spatial resolution

Lateral resolution is dependent on the tip’s **geometry** in first place, then on **materials** involved and on the **environment** in which the experiment is conducted.

#### Tip geometry

Generally speaking, the tip must have a high aspect ratio and its apex must be the smallest to reach the best lateral resolution. To this end, a MEMS cantilever is typically micro-fabricated with a tip-end radius of about tens of nanometers. From now on, if one wants a sharper tip, one can either etch the tip or attach/grow a sharper tip on the initial one. Among the techniques used, one can cite Focused Ion Beam (FIB) etching [67], plasma etching leading to

an apex of a few nanometers radius of curvature (p. 353 in [5]), Electron-Beam Deposition (EBD)[68] and attachment/growth of carbon nano-tubes (CNT) [69]. The latter is interesting in the high aspect ratio of the provided tips, unlocking imaging of steep surfaces. But size<sup>16</sup> is not the only parameter and resolution also depends on the materials involved in the contact.

### Tip and sample Materials

Chemical bonds can form between tip and sample, leading to adhesion. Inert tips are thus preferred [22]. For example Howald *et al.* only managed to image Si surface by coating their Si tip with Teflon [70]. In [24], Gross *et al.* functionalized their tip with different materials, leading to different resolutions (Figure 16).

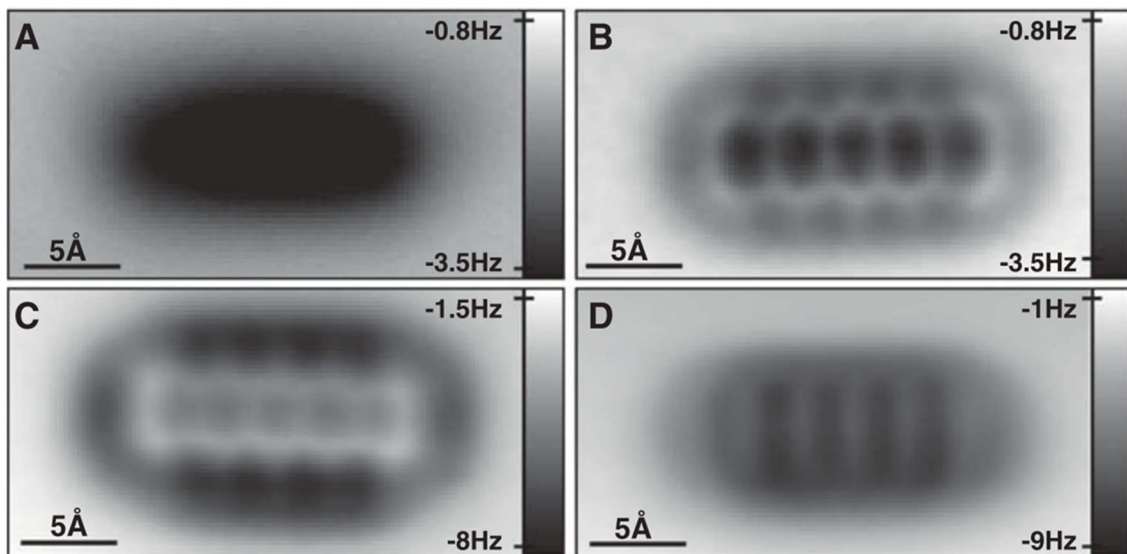


Figure 16: AFM images of a pentacene molecule with four different tips modifications: (A) Ag tip, (B) CO tip, (C) Cl tip and (D) pentacene tip. Best resolution was obtained with the most inert tip (CO). From [24].

In practice, the resolution attained also depends on the environment and conditions in which is conducted the experiment.

### Environment

In Ultra-High Vacuum (UHV), atomic resolution is routinely achieved thanks to high  $Q_m$  and high  $k$  probes in non-contact FM-AFM.

In air, water on surfaces and thus presence of a meniscus (Figure 17) [44][71] limits the resolution to the characteristic length of the meniscus.

<sup>16</sup> In practice, the lateral resolution changes while scanning as it highly depends on the foremost atoms of the tips [22] and their configuration can change while scanning.

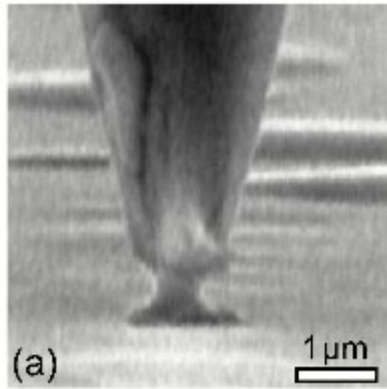


Figure 17: SEM image of a water meniscus between a tungsten tip and a Pt/C coated mica sample. From [71].

As the meniscus typically forms at a few angströms range, at every oscillation of the cantilever, the meniscus will form and break, shadowing the force profile. This limitation can be avoided using small-amplitude, within-meniscus oscillations of the probe (about 0.1 nm vibration amplitude) (Figure 18).

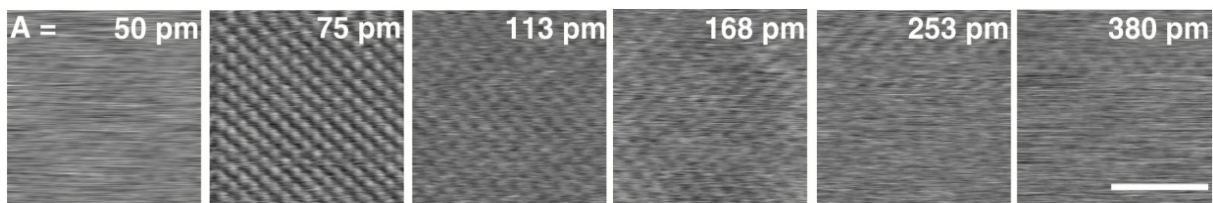


Figure 18: Amplitude dependence in AFM images of a KBr surface in ambient conditions. Scale bar 3nm. Atomic resolution is reached for a probe amplitude of 75 pm. As the water orders in 250 pm layers over the surface, authors reach atomic resolution thanks to in-layer oscillations. From [72], itself from [73].

In liquids, atomic resolution is achievable on stiff surfaces [74], [75]. On soft ones (Young's modulus  $E < 100$  MPa), the tip presence becomes invasive and buffers can be used to decrease tip-sample interaction yielding submolecular resolution (about 60 nm) [76].

### 1.3.2.3 Vertical spatial resolution

To reach the best vertical resolution in dynamic mode, one needs a low amplitude vibration to better select forces, as said by Gross in [24]: "For atomic resolution with the AFM, it is necessary to operate in the short-range regime of forces, where chemical interactions give substantial contributions. In this force regime, it is desirable to work with a cantilever of high stiffness with oscillation amplitudes on the order of 1 Å, as pointed out by Giessibl". But the low amplitude vibration lowers the signal-to-noise ratio (SNR) and hence the contrast of the image. There thus exists an optimal vibration amplitude depending on the decay-constant length of the observed forces, in practice around 1 angström [43] (p. 125 in [77]).

Briefly put, to reach higher resolution in AFM one needs to have the thinnest inert tip, operated at 100 pm amplitude with the lowest detection noise and thermomechanical noise. Furthermore to reach higher resolution and higher bandwidth, one wants to maximize the  $f_m/k_{eff}$  ratio of the AFM probe.

### 1.3.3 Reaching easier and cheaper AFM

Most commercial AFMs as JPK, Bruker and Asylum research ones come with many software automated features/modes. This makes instruments more user-friendly but is generally accompanied with high costs, about 300 k€. On the other side of the price scale, single chip AFM was demonstrated in 2011 [51], leading to few k€ commercial AFM now available. The latter has integrated electro-thermal actuators so no need for piezoelectric positioners, it however only functions in static mode. This last achievement was made possible by different positioners and detecting transducers. Those different transducers are discussed in next part.

### 1.3.4 AFM probe performance figure of merit (bandwidth over force resolution)

To resume the last discussion in terms of probe only, if one is looking for better performances in dynamic AFM, namely speed and force resolution, one needs a high bandwidth probe with the thinnest inert tip operated at 100 pm and with the smallest possible force gradient detection limit  $k_{ts\_lod}$ . We define a mechanical figure-of-merit as:

$$\mathcal{F}_m = \frac{BW}{k_{ts\_lod}} \quad (13)$$

Assuming  $z_{det}$  is not limiting  $z_{lod}$  but  $z_{th}$  is ( $z_{lod} = z_{th}$ ), we can further write:

$$\mathcal{F}_m = \frac{BW}{k_{ts\_lod}} = \frac{f_m/Q_m}{\frac{k_{eff}}{Q_m A} \sqrt{\frac{2k_B T Q_m}{\pi f_0 k_{eff}}}} = \frac{A f_m^{3/2}}{\sqrt{4k_B T Q_m k_{eff}}} \quad (14)$$

As temperature is not related to the probe, we re-write the mechanical figure-of-merit  $\mathcal{F}_m$ , removing the constants:

$$\mathcal{F}_m = \sqrt{\frac{f_m^3}{Q_m k_{eff}}} \quad (15)$$

Equation (15) provides a route towards high performance dynamic AFM, mainly through high frequency probes (or low-mass<sup>17</sup> probes as  $f_m^2 = k_{eff}/m_{eff}$ ). This conclusion led AFMists to develop new architecture of probes using vibration modes different from the cantilever's flexural mode (Figure 20). Those new architectures need new detection and actuation schemes. A review of those is given in next part. Among them, this thesis work is focused on a new optomechanical ring, high-frequency AFM probe, with high-bandwidth and ultra-sensitive detection.

---

<sup>17</sup> Here mass refers to the effective mass.



### 1.4 State of the art AFM probes and their electro-mechanical transductions

The drive to higher frequency probe to reach higher bandwidth and resolution led people to modify the initial AFM cantilever (800  $\mu\text{m}$  x 250  $\mu\text{m}$  x 25  $\mu\text{m}$  [3] with tens of kHz resonance frequencies), by using smaller cantilevers of 6  $\mu\text{m}$  for the smallest (Figure 20a).

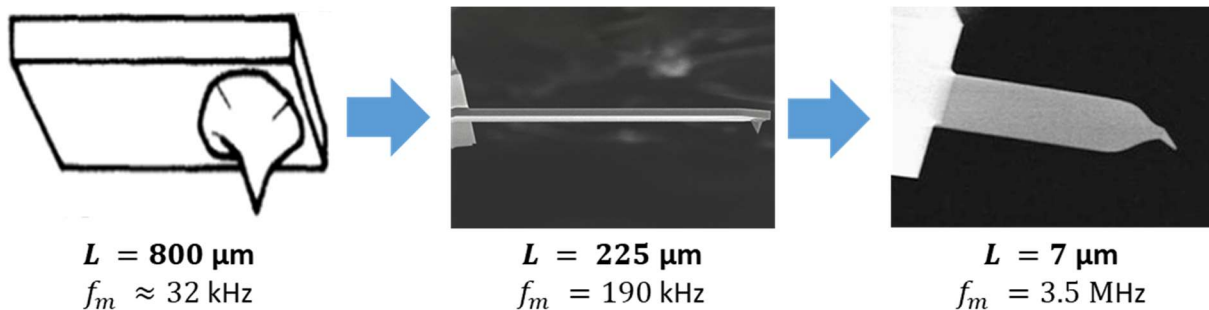


Figure 19: Images of three cantilevers. The left one is the initial AFM cantilever from the invention paper [3]. The middle one is a standard cantilever [29]. The right one is a small and high-frequency cantilever [78].

However, with such small dimensions, the optical beam deflection (OBD) detection method becomes less sensitive. Indeed, the laser spot is then wider than the cantilever and not all the beam is reflected. This limitation pushed new detection methods, using other integrated transductions (piezoelectric, piezoresistive, capacitive, etc.). To benefit from those different detections methods, new probes shapes with different resonance modes were developed (Figure 20b).

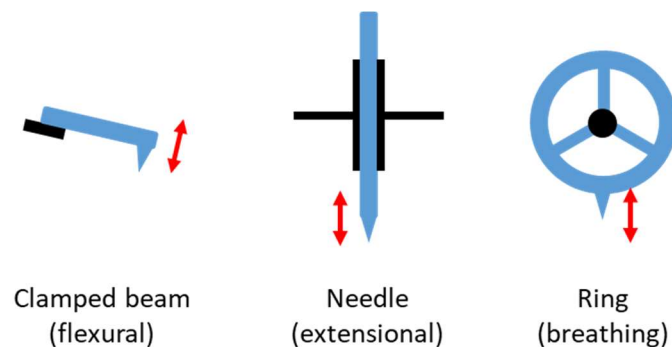


Figure 20: Schemes of different vibration modes of AFM probes. In black are the anchoring points. The tip movement is represented in red. Clamped beam is usually associated with low stiffness (roughly in the 1 N/m range) whereas Needle and Ring shapes are associated with higher stiffness (roughly in the 100 kN/m range).

Those modifications were made possible by micro opto-electro-mechanical systems (MOEMS) development, through integrated transductions. I will first list **actuation** and then **detection** transductions among different shapes of MOEMS probes to compare their performances and position our OM ring probe among them.

#### 1.4.1 Actuation

In dynamic AFM, actuation is needed to excite the cantilever's resonance. The ideal actuation has the highest dynamic range (DR: from the smallest to the highest amplitude), the highest

bandwidth, is the most stable, the easiest implemented, costless, easy of use and working in every environment.

#### 1.4.1.1 Piezoelectric actuation : far (initial AFM) to integrated

As in the initial AFM, cantilever mounted on a piezoelectric transducer provides an easily-implemented actuation and is the most used to date (Figure 22f). It however is “leaky” as the vibration propagates through the support and can perturb scanning or detection, exciting spurious resonances [79]. MEMS provided probes in piezoelectric material, mainly quartz, the probe thus being the transducer. This is the principle of the tuning fork “qPlus sensor” and the extensional “needle sensor” (Figure 22a and b). They work with higher spring constants (respectively in the kN/m and MN/m range [42]) and at smaller (sub-nanometric) amplitudes than usual cantilevers (Figure 21), providing a better force selectivity [80].

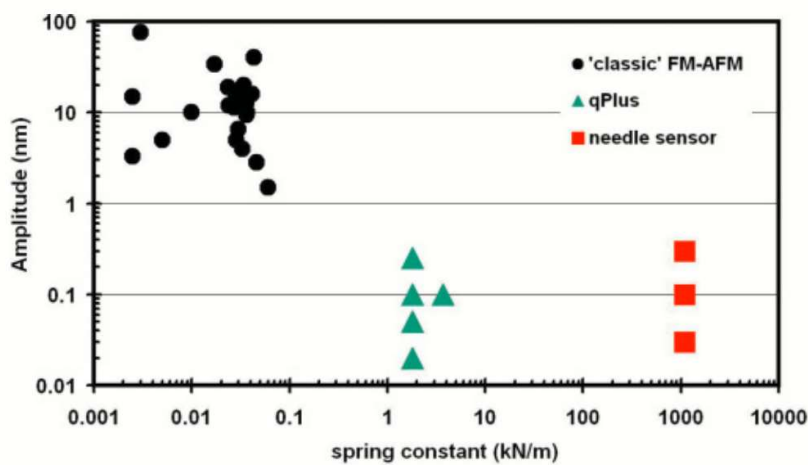


Figure 21: Parameter fields of cantilever spring constants  $k$  and oscillation amplitudes  $A$  for classic Si cantilevers, qPlus sensors, and needle sensors. From [80].

#### 1.4.1.2 Capacitive (or electrostatic) actuation

Using capacitive actuation provides an integrated transduction, allowing the use of different mechanical resonators as rings with higher frequencies. Capacitive detection needs large and close areas to gain actuation amplitude, without snapping, which represents a technological challenge (Figure 22c). Amplitude reached in capacitively actuated rings is about tens of pm [55], reaching nanometers in [81]. A detailed capacitive actuation explanation can be found in Sec. II.4.3.

#### 1.4.1.3 Magnetic actuation

Using Lorentz force, teams were able to actuate a cantilever up to 900 nm [82] and bandwidth attainable was proven to be at least 100 kHz [83]. Drawback to this transduction is the cantilever heating induced by the current, heating the cantilever by a few degrees. The magnitude of the magnetic actuation is dependent on the volume of magnetic material on the AFM probe. The magnitude would then diminish rapidly when using small probes to reach high frequency vibrations. In addition, the magnetic field generated can modify the sample.

#### 1.4.1.4 Electro-thermal, photo-thermal actuation

Electro-thermal (Joule heating) transduction through a thermal expansion mismatch can provide hundreds of nanometers actuation amplitude [84][85] (Figure 22d). Photo-thermal

actuation has been demonstrated, shooting a laser on a cantilever, the laser intensity being modulated at the cantilever resonance frequency (as blueDrive technology developed by Asylum Research). It displays up to 100  $\mu\text{m}$  actuation on gold-coated cantilevers [86], however its efficiency decreases rapidly with frequency after 10 kHz. It was proven viable still at 10 MHz in [79] with lower amplitudes in the 100 pm range. Both electro-thermal and photo-thermal actuations are theoretically limited in bandwidth by heating conduction slow time constant. Thermal diffusivity of silicon is  $100 \mu\text{m}^2/\mu\text{s}$  and recent work proved electro-thermal actuation effective up to a few MHz [85].

#### *1.4.1.5 Optomechanical (OM) actuation in cavity*

It consists in three phenomena: radiation pressure, electrostriction and photo-thermal forces. Photo-thermal forces are already discussed in the precedent paragraph. Indeed, as the two first effects are weak, they need an important optical power modulation to actuate a motion; optical cavities allow to reach high powers, at the expense of bandwidth. OM actuation in rings is detailed in Sec. II.4.2 of this manuscript and demonstrates a 1 pm actuation amplitude, up to 130 MHz (see Sec. III.5.4). Its actuation bandwidth is then limited by the optical cavity bandwidth, *i.e.* the rate at which optical power in cavity can vary. The bandwidth of optical interferometers is given by the linewidth of the cavity, for a  $\lambda = 1.55 \mu\text{m}$  and  $Q_{opt} = 40\,000$  cavity, the detection bandwidth is  $BW = \frac{c}{\lambda \times Q_{opt}} = 4 \text{ GHz}$ .

To resume, magnetic actuation is experimentally complex. Electro-thermal and photo-thermal actuations decreases rapidly for high frequencies as thermal effect are slow, however they still work up to a few MHz as those effect have important magnitudes. Piezoelectric actuation needs stiff piezoelectric materials that lower the force sensitivity. Capacitive actuation needs large and close areas that represent a technological fabrication challenge and lastly OM actuation needs a high-quality cavity to enhance the low-magnitude transduction.

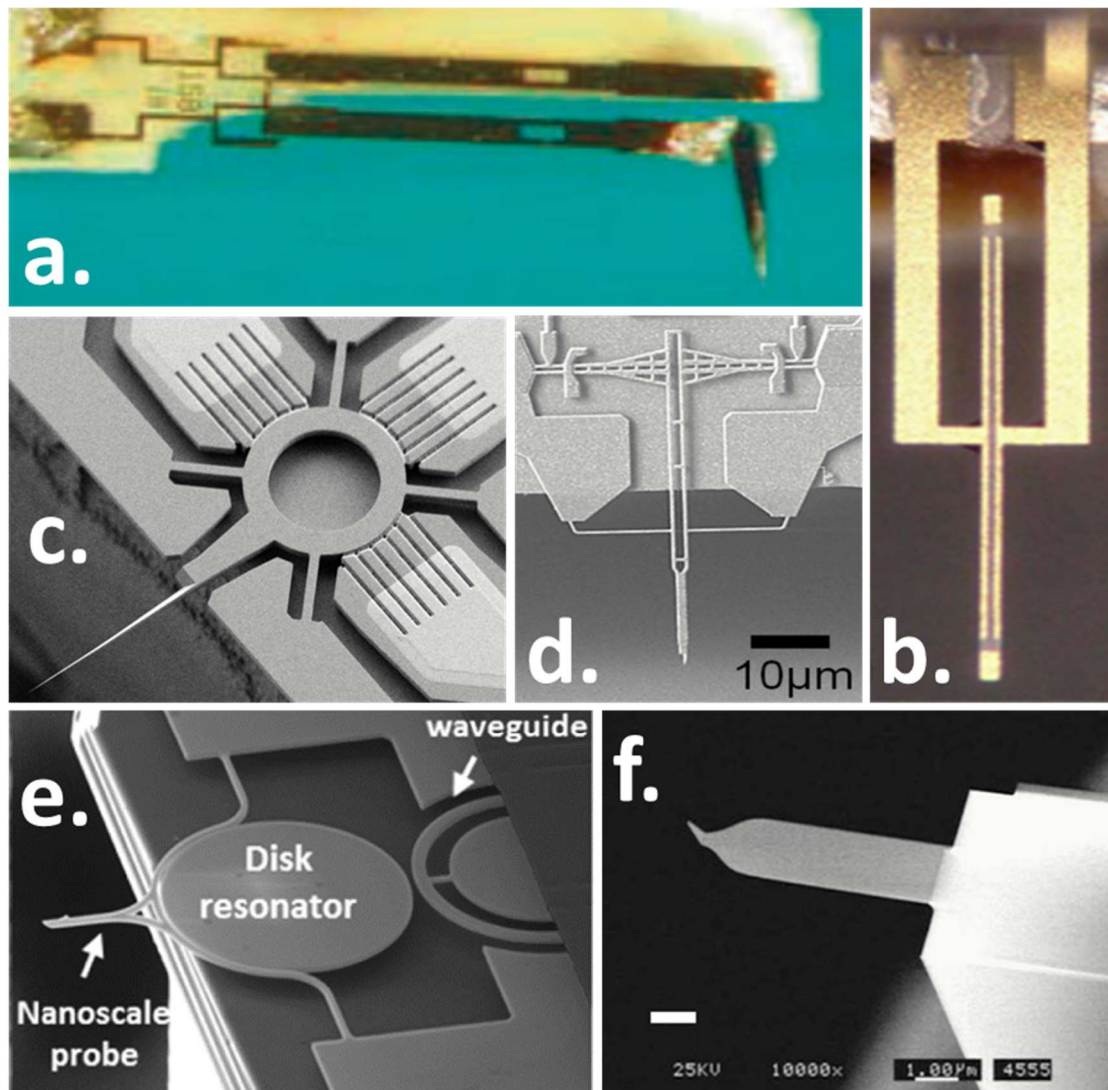


Figure 22: Pictures and SEM images of AFM probes. (a.) 2 mm long piezoelectrical tuning fork [77], (b.) 2 mm long length extensional piezoelectrical resonator [80], (c.) 60  $\mu\text{m}$ -diameter capacitive ring [8], (d.) Electrothermally driven, piezoresistively detected probe [85], (e.) 10  $\mu\text{m}$  diameter optomechanical probe [14] and (f.) 7  $\mu\text{m}$  long cantilever piezoelectrically or photothermally driven and detected with the OBD technique [5].

#### 1.4.2 Detection

As for actuation, the ideal detection has the lowest LOD, highest dynamic range (DR: from the lowest to the highest amplitude), the highest bandwidth, is the most stable, the easiest implemented, costless, easy of use and working in every environment.

##### 1.4.2.1 Optical laser deflection detection (or OBD, or optical lever)

The most used detection to date is Optical Beam Deflection (OBD). A laser reflects on the cantilever and its deflection is recorded via a 4-quadrant photodiode (Figure 22f). This technique is cheap and easily implemented. Due to diffraction (or Abbe, Rayleigh factor) limit, the cantilever must be wider than 1  $\mu\text{m}$ . The initial detection montage theoretically reaches a  $4 \times 10^{-14} \text{ m}/\sqrt{\text{Hz}}$  LOD [48], and in practice reaches a  $2 \times 10^{-1} \text{ m}/\sqrt{\text{Hz}}$  LOD (p. 391 in [5]).

#### 1.4.2.2 Piezoresistive detection

Piezoresistive detection has the same noise level as OBD [87] but provides an integrated measure (Figure 22d). Piezoresistive transduction has shown a  $1 \times 10^{-12} \text{ m}/\sqrt{\text{Hz}}$  LOD in [84] with a  $1.4 \times 10^{-3} \text{ N/m}$  spring constant and more recently  $8 \times 10^{-1} \text{ m}/\sqrt{\text{Hz}}$  LOD [85]. Contrary to optical laser deflection, piezoresistive detection impose little constraints on the cantilever shape and thus really flexible one can be used. The challenging part in piezoresistive readout is the fabrication of shallow piezoresistors necessary to keep signal-to-noise performance [87].

#### 1.4.2.3 Capacitive detection

Early tries of capacitive read-out in 1992, featuring  $1.5 \mu\text{m}$  air gap, didn't led to any image [88]. Thanks to growing MEMS fabrication capability, authors demonstrated a  $80 \text{ nm}$  air gap over a  $5 \mu\text{m} \times 23 \mu\text{m}$  surface, leading to a  $5 \times 10^{-1} \text{ m}/\sqrt{\text{Hz}}$  LOD in [89]. Capacitive sensitivity was later improved with a RF-interferometry scheme in [55], with a  $45 \text{ nm}$  air gap, leading to a  $1.5 \times 10^{-15} \text{ m}/\sqrt{\text{Hz}}$  LOD (Figure 22c).

#### 1.4.2.4 Piezoelectric detection

Piezoelectric detection was used in needle (or Length Extensional Rod LER) and tuning fork structures (Figure 22a and b). For a detailed comparison of their noises, see [80]. A  $6.2 \times 10^{-14} \text{ m}/\sqrt{\text{Hz}}$  LOD was obtained from a tuning fork in [80]. It was demonstrated in the imaging of soft things in aqueous environment in [90].

#### 1.4.2.5 Optical interferometry detection

Different interferometry configurations are used as detection. Using the cantilever as the mirror of one arm of a Michelson interferometer [91] allows motion detection of the cantilever. But people also used Fabry-Pérot interferometer with the cantilever as one mirror, using a fiber optic, to assess its deflection, leading to a  $5.5 \times 10^{-14} \text{ m}/\sqrt{\text{Hz}}$  LOD [92]. Integrated Fabry-Pérot interferometer was used in the form of a disk cavity in the vicinity of the cantilever (Figure 22e). Motion detection is done through evanescent optical field perturbation, leading to a  $3 \times 10^{-15} \text{ m}/\sqrt{\text{Hz}}$  LOD [14].

In this thesis work, an integrated interferometer in the form of a ring cavity, that acts as a cantilever, is demonstrated. This technique reaches a  $4.5 \times 10^{-1} \text{ m}/\sqrt{\text{Hz}}$  LOD. It is detailed in Sec. II. As for actuation, the bandwidth of optical interferometers is given by the linewidth of the cavity, for a  $\lambda = 1.55 \mu\text{m}$  and  $Q_{opt} = 40\,000$  cavity, the detection bandwidth is  $BW = \frac{c}{\lambda \times Q_{opt}} = 4 \text{ GHz}$ .

In Doppler interferometry technique (or Laser Doppler vibrometry (LDV)), a laser is modulated, then shot over the cantilever and then interferes with itself and then is demodulated. It was proven effective until  $10 \text{ MHz}$  [79]. Compared to classical interferometry, it has the advantage of being insensitive to low-frequency noise [91][93], and velocity measurements are still possible on  $100 \text{ nm}$  reflective surfaces [94]. As the tip velocity increases with the resonance frequency, the displacement sensitivity behaves has  $1/f_m$ , reaching  $1 \times 10^{-15} \text{ m}/\sqrt{\text{Hz}}$  LOD in p. 352 of [77].

The different detection performances are summarized in Table 2.

Transductions	Optical beam deflection (OBD)	Optical interferometry (and Doppler)	Capacitive interferometry	Piezoresistive	Piezoelectrical
Limit of detection (LOD) in $m/\sqrt{Hz}$	$2 \times 10^{-14}$	$2 \times 10^{-15}$	$1 \times 10^{-15}$	$8 \times 10^{-14}$	$6 \times 10^{-14}$

Table 2: Comparison of transduction's limit of detection in AFM probes. For comparison, our OM probe LOD is  $4.5 \times 10^{-17} m/\sqrt{Hz}$  (see Sec. III.3).

As a note, systems using several parallel actuation/detection schemes were also developed as Optical Beam Deflection (OBD) and Laser Doppler Vibrometry (LDV) [95].

Having in mind the conclusions of the last section I.3, we can map the performances of the different types of AFM probes presented above (Figure 23).

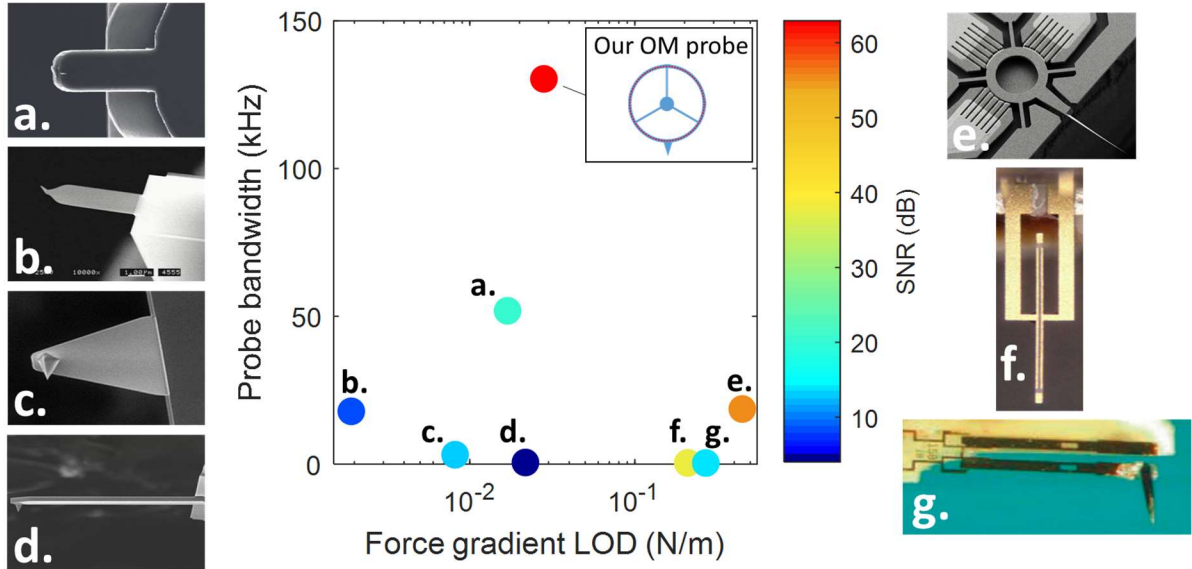


Figure 23: Graph of the performances of several state of the art AFM probes. Force gradient LOD is calculated from  $k_{ts\_lod}$ , taking  $A_{lod} = \sqrt{A_{det}^2 + A_{th}^2}$ . SNR is calculated from  $SNR = 20 \times \log(A / (NA_{lod} \times \sqrt{BW}))$ ,  $A$  being the vibration amplitude and  $BW$  being the detection bandwidth. For this calculation, a 100 pm vibration amplitude in air and a detection bandwidth of 10 kHz were considered. The quality factors used for this comparison are taken in air. (a.) Small SU-8 cantilever [96], (b.) ultra-small cantilever [78], (c.) Bruker A-probe [97], (d.) typical cantilever [29], (e.) ring probe [8], (f.) length extensional resonator [80] and (g.) tuning fork [77].

On Figure 23, the (e.), (f.) and (g.) AFM probe appear not really competitive. This is because their main advantage is in their low-amplitude of oscillations allowed by their high SNR, leading to better spatially-resolved imaging. This last point highlights the advantage of our OM probe: it has low-amplitude of oscillations, thanks to the highest SNR, without compromising too much on the force sensitivity and with the highest bandwidth. Thus an optomechanical AFM probe could provide a new operating window in investigating matter, namely high-

frequency, high-bandwidth and small-amplitude operation thanks to its ultra-sensitive OM detection. From a spectroscopic picture to a scanning one, this can unlock the visualization of fast processes at the nanoscale. This thesis work is focused on the characterization and proof-of-concept experiments of such a probe.

In this chapter, we introduced the AFM, its 5 essential blocks (namely probe, probe's mechanical motion detection, signal processing and feedback control, XYZ scanners and probe actuation) and its operation modes (namely contact, tapping, non-contact and AM, PM and FM). We then depicted current AFM challenges: higher resolution and higher speed. We saw that this challenges pushed high frequency probes to emerge and we finally compared different probe architectures' performances to position the new OM probe presented in this manuscript. The next chapter is dedicated to our OM probe, from theory to design and fabrication.

## II. Optomechanical silicon micro-ring theory, design for AFM and fabrication

This chapter, after a brief history of optomechanics, begins with an introduction on optical guiding in silicon and on the effective index. Then, the constructive-interference condition is written to present the silicon micro-ring cavity and the intrinsic optical losses of the cavity are listed. The cavity is optically addressed with an evanescently-coupled waveguide, this coupling dependencies are discussed. The expected behavior of the optical resonance, seen on the device transmission, is described in the coupled mode theory formalism. After this optical study, the mechanical resonances and mechanical design to form the AFM probe are discussed. Then the coupling between optics and mechanics is detailed, as well as the expected behavior of the OM probe when used in AFM. Finally, the fabrication of such a probe is illustrated.

### II.1 History of cavity optomechanics

The field of optomechanics is devoted to the study of reciprocal effects between optics and mechanics. The most direct form of it being radiation pressure. In the 17<sup>th</sup> century Johannes Kepler, observing that comets' tails were in the opposite direction of the sun, postulated that sunlight was exerting pressure on it (Figure 24a). Maxwell mathematically deduced this effect from electromagnetic equations in 1873. Another common optomechanical (OM) coupling is through photo-thermal effect (absorption and thermal expansion), which is usually much larger than radiation pressure. A famous historical misconception was Crookes' radiometer (in 1873, Figure 24b). A light-mill supposed to be powered by radiation pressure but where thermal effects were the true motor of the mill. First true light-mill demonstrations were given in 1901 [98][99].

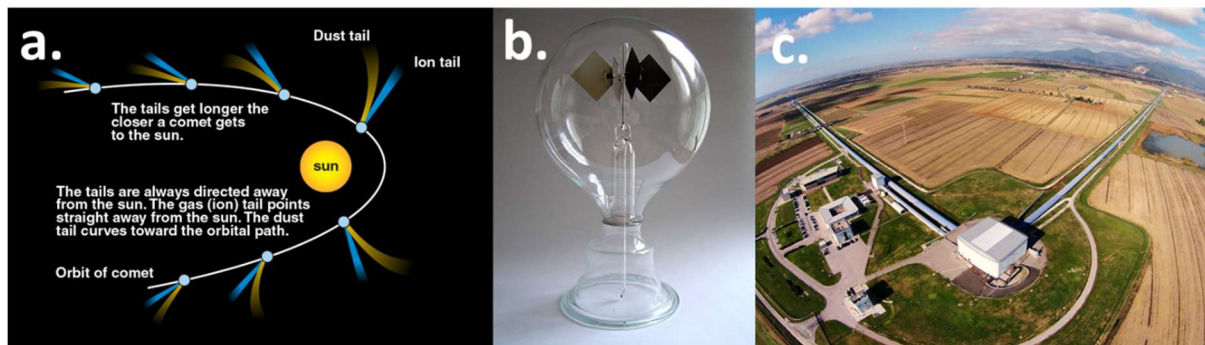


Figure 24: (a.) Scheme of a comet orbiting around the sun [100]. The comet's tail is always in the opposite direction of the sun. (b.) Crookes' radiometer picture [101]. The mill's wings have a reflective face and an absorbing face. (c.) Gravitational wave detector VIRGO picture [102], the two arms are two 4 km Fabry-Pérot cavities.

The optical cavity interferometers then provided an enhanced displacement sensitivity as Fabry-Pérot's interferometer (1899). Braginsky began investigating microwave optomechanics in cavities in the late 1960s. A recent achievement of optomechanical principles is gravitational wave detection with a 4 km-long Fabry-Pérot-Michelson optical interferometer [10] (Figure 24c). At small size scale, optomechanical effects were demonstrated in micro-cantilever cavities [103] by Karrai in 2004, in micro-toroids [104] by



Vahala in 2005 and expected in phoXonic<sup>18</sup> crystal cavities [105] in 2006 [106] (Figure 25). This led to more research on, OM mode cooling of macroscopic objects [107][108][109][110] and sensing [13] with OM devices. To get extended information on cavity optomechanics, the user is referred to reviews [111][112]. Optically addressing those devices remains a non-trivial task. However, thanks to the growing MNOEMS (Micro-Nano-Opto-Electro-Mechanical-Systems) fabrication capability, they have been increasingly integrated on semiconductor technological platforms, which can benefit to the sensing field.

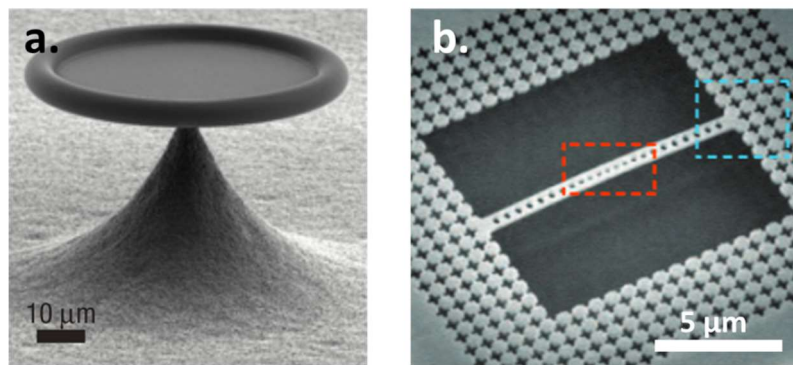


Figure 25: SEM images of  $\mu\text{m}$ -sized optomechanical cavities. (a) Micro-toroid featuring an optical mode circulating in the torus, coupled with its motion from [113]. (b) PhoXonic crystal with co-localized optical and mechanical modes in the red area; the blue area is a phononic shield [114].

In this thesis work, we use optomechanical micro-rings that have similarities with the micro-toroid shown in Figure 25a. To use it as an AFM probe, it needs a tip for spatial resolution. A tip is added to the design of such a micro-ring as in Figure 26.

---

<sup>18</sup> PhoXonic crystal refers to a patterned layer having coupled, engineered, photonic and phononic behavior.

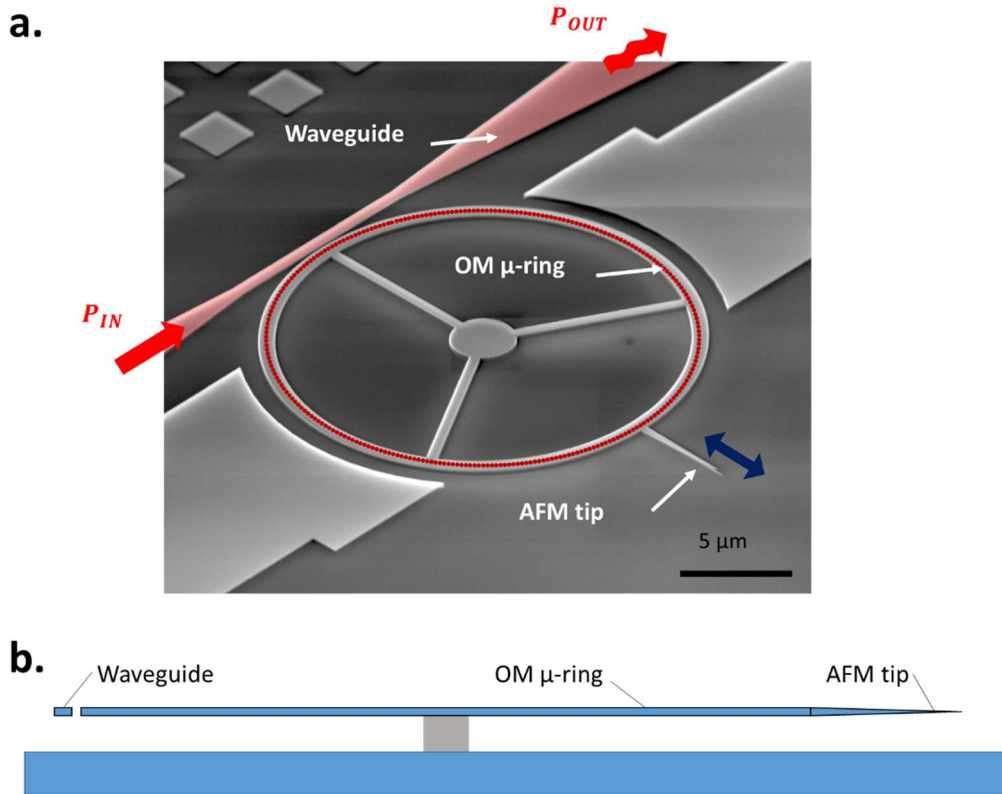


Figure 26: (a) Colored SEM image of an OM AFM probe used in this thesis work. In plain red is the waveguide optically coupled to the ring. The optical resonance mode of the OM ring is represented in dotted red. Motion of the tip is highlighted by a dark blue double arrow. The motion modulates the ring cavity length and is thus detected by a modulation of the transmitted optical power. (b) At scale scheme of the cross-section of the OM probe. Pedestal height is  $1\ \mu\text{m}$  and ring's radius is  $10\ \mu\text{m}$ <sup>19</sup>.

Following this brief description of the origins of such OM sensors, the design of our OM AFM probe is detailed in the next parts, from optical cavity considerations to mechanics and their mutual coupling.

## II.2 Optical resonator

How optical electromagnetic waves are guided in the ring? We will introduce the optical effective refractive index and guiding considerations<sup>20</sup> to build the ring optical cavity. Next, intrinsic optical cavity losses are detailed, defining the overall quality factor  $Q_{opt}$ . Then the coupled mode theory is written, introducing the optical cavity coupling factor  $\gamma_e$  to the neighboring waveguide.

### II.2.1 Straight waveguide: effective index

#### II.2.1.1 Geometrical approach

To understand how light can be guided, from the point of view of geometrical optics, let us consider an optical fiber consisting of a material 1 core in a material 2 sleeve. Material 1 refractive index is higher than the one of material 2 ( $n_1 > n_2$ ). Considering light rays with different incident angles (Figure 27), the condition for total internal reflection (TIR) is:

<sup>19</sup> Contrary to what the OM probe's shape might suggest, this thesis work was unfortunately not funded by Mercedes-Benz.

<sup>20</sup> The waveguide considerations presented in the following are largely inspired from [115] and [130].

$\cos(\theta_c) = n_2/n_1$ . Therefore, the condition on  $n_2$  for a ray with a given angle  $\theta$  to be guided is:

$$n_2 \leq n_1 \cos(\theta) \quad (16)$$

In other words, the lower the ratio  $n_2/n_1$ , the better guided optical modes will be (*i.e.* more acceptable insertion angle).

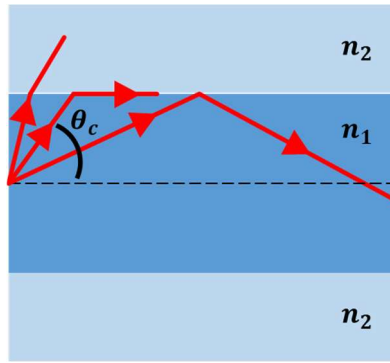


Figure 27: Total internal reflection (TIR) scheme.  $\theta_c$  is the maximum angle for the ray to be totally reflected and thus guided.

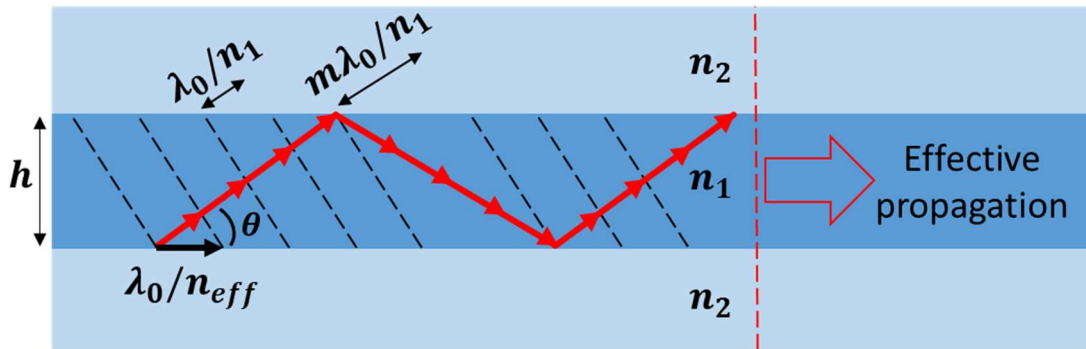


Figure 28: Geometrical optics scheme of an optical mode propagating in a slab waveguide.  $\lambda_0$  is the laser wavelength in vacuum.  $m$  is a positive integer representing the mode order, *i.e.* the electric field amplitude profile in the waveguide. From this picture, we can understand that for a thinner waveguide, the order  $m$  of the modes guided will decrease. However, this representation cannot fully account for waveguides smaller than the wavelength, where the outer material refractive index  $n_2$  will have an impact as the mode is also guided in the outer part. From p. 22 in [115].

Now considering the propagation of the modes, as the optical wave is reflected, its path is longer than the waveguide length: its overall propagation in the waveguide is slowed down. An effective refractive index  $n_{eff}$  is thus defined to account for this retardation. Consequently, this effective refractive index is lower than the material's refractive index. Looking at Figure 28, one can write that:

$$n_{eff} = n_1 \cos(\theta) \quad (17)$$

Combining equations (16) and (17), one can find a frame for any guided mode characterized by its  $n_{eff}$ :

$$n_2 \leq n_{eff} \leq n_1 \quad (18)$$

If the waveguide is thin enough (approximately the wavelength), higher order modes are not guided anymore (Figure 28) and only the fundamental is: single-mode waveguide. When reducing the thickness again, effective wavelength  $\lambda_{eff} = \lambda_0/n_{eff}$  continues to decrease. In this case, the light wave will also expand in the outer medium (Figure 31). To account for and assess this effect, one needs a more detailed electromagnetic description.

### II.2.1.2 Electromagnetic approach

From a standard electromagnetic picture of propagation of a monochromatic light wave of wavelength  $\lambda_0$  in vacuum, in a slab of thickness  $h$  as in Figure 28 (detailed in Appendix B:), using boundary conditions for a transverse electric (TE) mode, one can find that:

$$\tan(hk_0\sqrt{n_1^2 - n_{eff}^2}) = \frac{\sqrt{(n_1^2 - n_{eff}^2)(n_{eff}^2 - n_2^2)}}{k_0(n_1^2 - n_2^2)} \quad (19)$$

Where the wave number is  $k_0 = 2\pi/\lambda_0$ .

Setting the light wavelength, and thus its wave vector  $k_0$ , numerical calculations or drawings can then provide approached values of the effective index with implicit equation (19). One can find a discrete number of solutions, corresponding to fundamental and higher guided modes.

If the slab is thin enough, only the fundamental mode is guided, it is then called a monomode waveguide. The monomode condition on the height  $h_{monomode}$  in a slab waveguide is [116][117]:

$$h_{monomode} \leq \frac{\lambda_0}{2\sqrt{n_1^2 - n_2^2}} \quad (20)$$

Considering a silicon waveguide ( $n_{Si} = 3.47$  [118]) surrounded by air ( $n_{air} = 1$ ), we find  $h_{monomode} \leq 233$  nm for a  $\lambda_0 = 1.55$   $\mu\text{m}$  light wave. For the rest of this thesis manuscript, we will only consider monomode waveguides as we work with silicon rings of cross-section  $0.5$   $\mu\text{m}$  x  $0.22$   $\mu\text{m}$  thick silicon layer<sup>21</sup>.

But our structure is no slab, it is a ring, so we have to find the effective index for a strip waveguide.

---

<sup>21</sup> Actually the waveguide is monomode in the thickness direction but not strictly monomode in the width direction ( $w = 500$  nm > 233 nm). According to simulations and experimental results, a “snake-like” bouncing mode appears (see Figure 60 in Sec. III.2.2).

### II.2.1.3 Waveguide along z: Marcatili's method

For a strip, the electromagnetic field is confined in both  $x$  and  $y$  directions, there is no analytical solution to the problem. To know the effective index, one can choose numerical simulations or approximate analytical methods as the effective index method or Marcatili's method. We use the latter, introduced in 1969 [119], and later extended for high index contrast materials in [120]. This method consists in a separation of variables  $x$  and  $y$ , *i.e.* to consider 2 independent 1D slabs as in the paragraph before. So it neglects fields in the grey corners as shown in Figure 29, assuming that fields are low there.

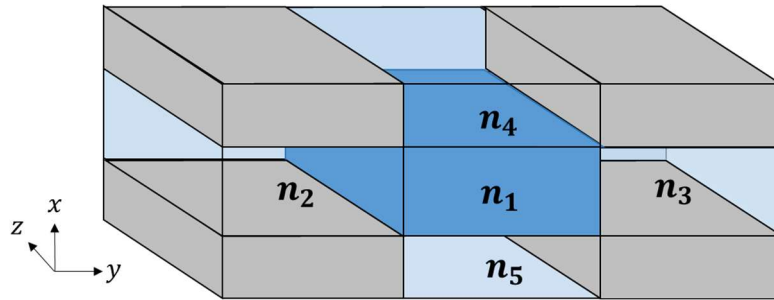


Figure 29: Scheme of the rectangular waveguide and the zones used in Marcatili's method. It separates the waveguide in five areas of distinct refractive index. Fields in grey areas are neglected.

In this case, since not all electromagnetic boundary conditions can be verified, one needs to make several hypothesis on the fields. This is where the derived method we used diverged from Marcatili's original method. From an open-source MATLAB implementation of it [120], we find the effective index for a  $\lambda_0 = 1.55 \mu\text{m}$  light wave propagating in a rectangular waveguide surrounded by air, with dimensions  $0.5 \mu\text{m} \times 0.22 \mu\text{m}$ , to be  $n_{eff} = 2.37$  (Figure 30). For comparison bulk silicon's refractive index is 3.47 at room temperature [118]. In other words, in an intuitive fashion from the bouncing wave picture, when one confines the light wave in the transverse direction in a smaller waveguide, its effective wavelength in the propagation direction increases (effective wavelength  $\lambda_{eff} = \lambda_0/n_{eff}$  and phase velocity  $v = c/n_{eff}$  go up).

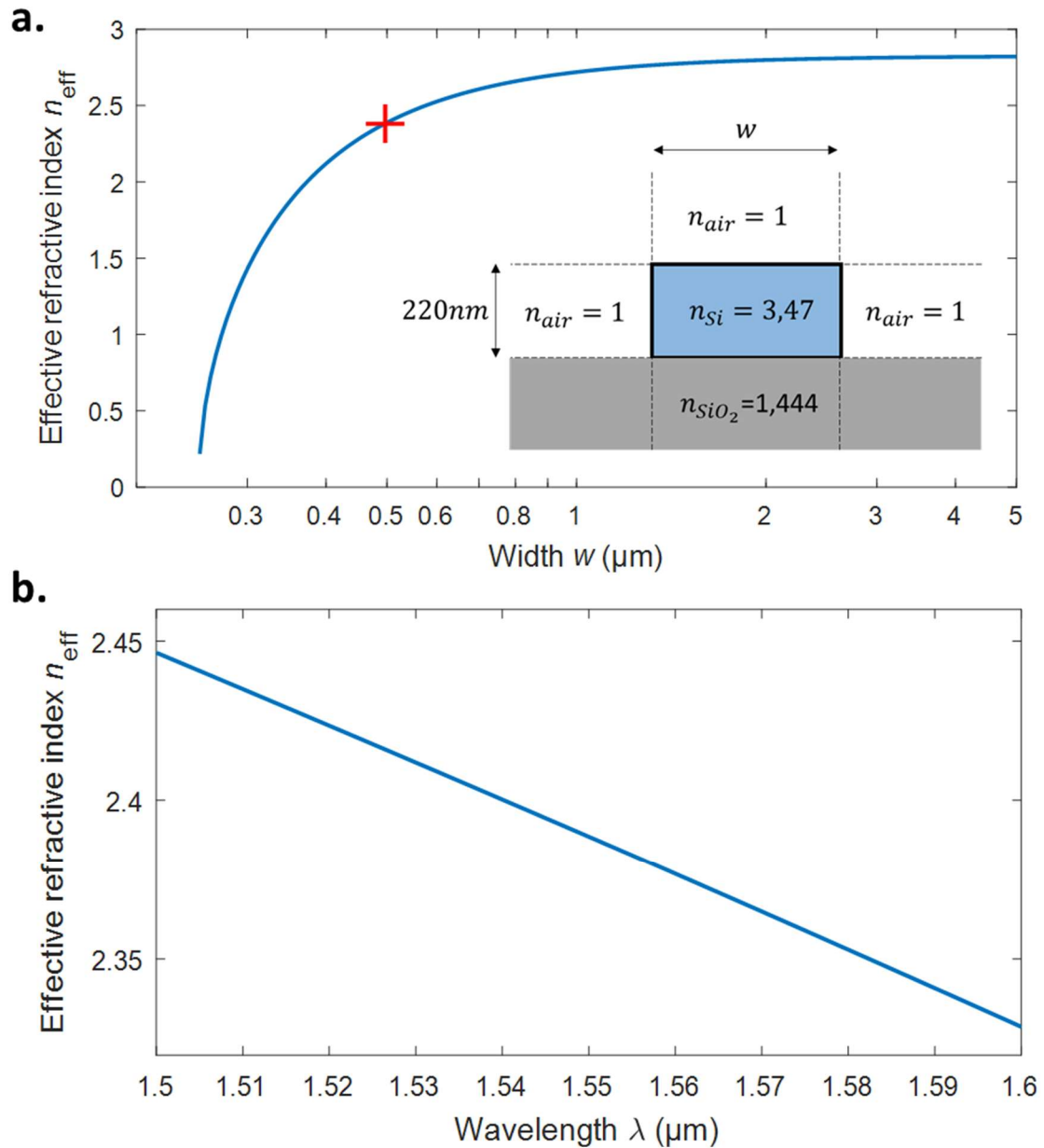


Figure 30: (a.) Plot of the effective refractive index versus the width of a 220 nm-thick SOI waveguide via the Marcatili's method. Inset shows the waveguide architecture taken for this calculation, the structure considered is a silicon waveguide (blue) lying on a silica substrate. Notably, if we take a  $0.47 \mu\text{m} \times 0.22 \mu\text{m}$  waveguide indicated by the red cross, the effective index is  $n_{eff} = 2.33$ . The silica layer was considered infinite in thickness to ease the calculation. The full stack features silicon under the  $1 \mu\text{m}$  silica layer which was neglected. (b.) Plot of the effective refractive index versus the wavelength in a 220 nm-thick silicon waveguide of width 500 nm surrounded by air, via the Marcatili's method. Both figures were done with help of the MATLAB code in [120].

On Figure 30, another dependency of the effective index is shown: the dependency on the wavelength. Indeed, the intrinsic refractive index of silicon diminishes when the wavelength increases. We will see in Figure 39 that this effect must be taken into account to predict the wavelength of the optical cavity modes.

Due to the rectangular geometry, the light propagating in the waveguide has a fixed polarization *i.e.* its electric and magnetic field remain aligned in one direction along the

propagation. TE and TM modes are thus defined as transverse electric mode and transverse magnetic mode. For example, Figure 31 shows the electric field map of a quasi-TE mode:

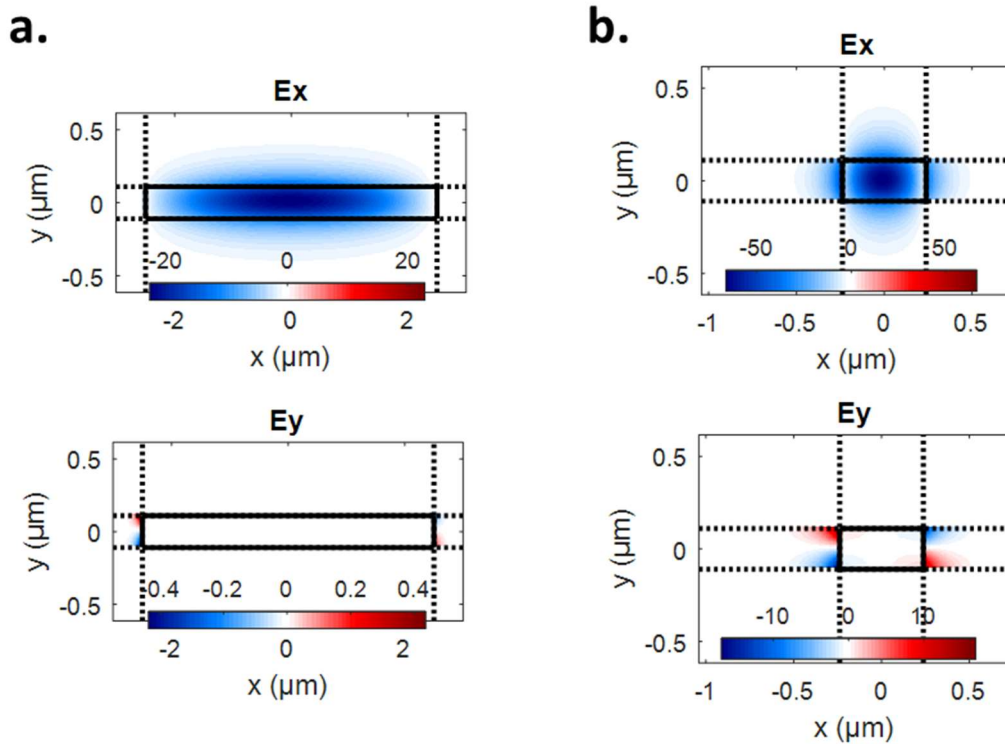


Figure 31: (a) Analytical simulation of the each electromagnetic field component (in a.u.) in a  $5\ \mu\text{m} \times 0.22\ \mu\text{m}$  SOI waveguide represented by a plain black contour (b) Same scheme in a  $0.47\ \mu\text{m} \times 0.22\ \mu\text{m}$  SOI waveguide. Both waveguides have the same stack structure as in Figure 30. Effective index in this  $0.47\ \mu\text{m} \times 0.22\ \mu\text{m}$  SOI waveguide is 2.3. This figure was done with help of the MATLAB code in [120].

One can observe that the  $E_y$  (and actually also  $E_z$  and  $H_x$ ) component is negligible compared to  $E_x$  as expected in a quasi-TE mode. One can observe in Figure 31b that the  $E_x$  component of the optical mode in the  $0.47\ \mu\text{m}$  wide guide is less confined than in the  $5\ \mu\text{m}$  width waveguide in Figure 31a. Unlike metal waveguides, dielectric waveguides provide a loose confinement of the field, this is actually what allows evanescent coupling to our device, as we will see in next part II.2.4.

Now that we introduced the effective refractive index and its dependencies, we will see what happens when you loop a waveguide on itself to form a ring cavity.

## II.2.2 Curved waveguide: ring cavity

### II.2.2.1 Geometrical approach

In terms of light guiding, a curved waveguide can be considered as a straight one (with the same effective refractive index) if the effective wavelength is negligible over the radius of curvature. The device we use has a radius of  $10\ \mu\text{m}$ , to be compared with the effective wavelength of the guided wave. As a reminder, in a  $0.5\ \mu\text{m} \times 0.22\ \mu\text{m}$  SOI waveguide, effective refractive index is 2.37 giving us  $\lambda_{eff} = 654\ \text{nm}$ . We will hence consider that the Marcatili's method calculation of the effective index is still valid.

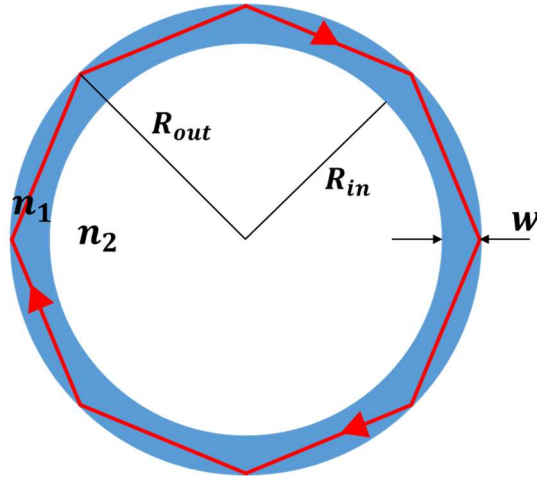


Figure 32: Scheme of an optical ring cavity. For our structures, typically  $R_{out} = 10 \mu\text{m}$  and  $w_{ring} = 0.5 \mu\text{m}$ . What is not shown in this scheme is the case where the light bounces also on the inner limit of the ring. The latter is shown in a simulation in Figure 60.

A waveguide looped on itself<sup>22</sup> forms a cavity. The condition for a harmonic wave to resonate being that it constructively interferes with itself after one lap. This condition gives, for a ring as in Figure 32:

$$m\lambda_0 = 2\pi R n_{eff}(\lambda_0) \quad (21)$$

$2\pi R n_{eff}$  being the optical path length.  $m$  being the azimuthal order of the mode<sup>23</sup>. As most of our structure are  $0.5 \mu\text{m} \times 0.22 \mu\text{m}$  ring section, leading to  $n_{eff} = 2.4$  [120] for a quasi-TE mode, with  $R_{out} = 10 \mu\text{m}$  ( $R = R_{out} - w_{ring}/2$ ) and with infra-red light  $\lambda_0 = 1.55 \mu\text{m}$ , we find  $m = 95$ . Meaning that there are  $2m = 190$  field maxima all around the ring.

### 11.2.2.2 Electromagnetic approach

Performing a Finite Element Method (FEM) simulation, using Maxwell formulas and boundary conditions, can be time consuming. To gain a significant amount of time, one can simplify the 3D ring problem to a 2D flat ring by taking an effective refractive index  $n_{eff\_slab220nm}$  for the ring material. This new refractive index is the effective index of a silicon slab of thickness 220 nm sandwiched by two layers of air for a quasi-TE mode (electrical field mostly in the plane of the ring). The result of such a simulation is given in Figure 33 for a  $10 \mu\text{m}$ -radius ring of width  $w_{ring} = 0.5 \mu\text{m}$ .

<sup>22</sup> A waveguide looped on itself is also called a “whispering gallery mode” waveguide similarly to acoustic reflection along a concave surface. One can thus hear someone whisper more than 30-meters apart as in the Saint-Paul cathedral in London. This has nothing to do with the two cups one string apparatus.

<sup>23</sup> If we had considered wider rings, we would also have to take higher order radial guided modes into account



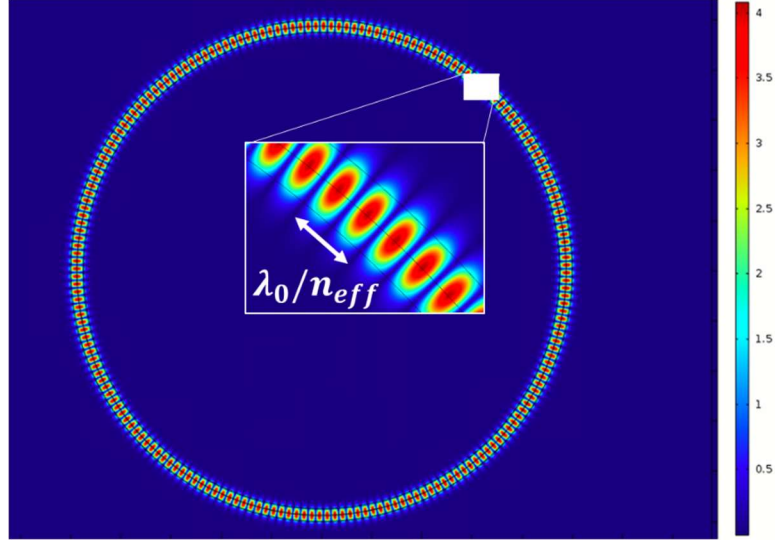


Figure 33: FEM (Finite Element Method) simulation of the electric field norm in a  $R = 10 \mu\text{m}$  and  $w_{ring} = 0.5 \mu\text{m}$  ring surrounded by air. The optical Whispering Gallery Mode (WGM) displayed is  $\text{TE}_{m=99}$ . This simulation is done with the Comsol software. Similar results can be found using the simple online simulator “wgms” [121].

With the simulation, we find an  $m = 99$ , a result close to our precedent geometrical approach giving  $m = 95$ .

### II.2.3 Intrinsic losses

If we imagine optical power circulating in the real ring-cavity made of silicon, it will experience losses due to defects in silicon or non-perfection of the waveguide. We define a loss rate  $\gamma_{tot}$  to quantify how much energy is lost over time and a loss coefficient  $\alpha_{tot}$  to quantify how much energy is lost over distance. We can thus write, assuming linear losses:

$$E_{EM}(z, t) = E_{EM}(0, t)e^{-\alpha_{tot}z} \text{ and } E_{EM}(z, t) = E_{EM}(z, 0)e^{-\gamma_{tot}t} \quad (22)$$

$E_{EM}(z, t)$  being the electromagnetic energy circulating in the cavity (not to be mistaken with the electromagnetic field).

To further differentiate the different independent loss channels  $n$ , each is attributed its own parameters  $\gamma_n$  and  $\alpha_n$ . We hence write:

$$\alpha_{tot} = \sum_n \alpha_n \text{ and } \gamma_{tot} = \sum_n \gamma_n \quad (23)$$

The losses of a cavity are often quantified with their optical quality factor  $Q_{opt}$ . It allows us to link the time and space pictures through their associated quality factor:

$$Q_n = \frac{\beta}{\alpha_n} = \frac{\omega_0}{\gamma_n} \quad (24)$$

$\beta = k_0 n_{eff}$  being the effective propagation constant in the ring azimuthal direction.

Three optical loss channels were identified from earlier studies ([122], p. 75 in [123]):

- **Curvature (or radiative) losses  $\alpha_{rad}$**

The wave circulating in the cavity has an evanescent tail outside of the cavity. So due to the curvature, the cavity is radiating to the outside tangentially to the disk: the resonance mode is leaky or radiative. Those losses are independent of the fabrication process and inherent to the structure. The losses decay exponentially when increasing ring radius  $R$  as seen in an approximate analytical formula (22) (from formula 26<sup>24</sup> in [124],[125]).

$$\alpha_{rad} = \left(1 - \frac{w}{2R_{out}}\right) \frac{\alpha_x^2}{2\beta \left(1 + \frac{w}{2}\alpha_x\right)} \frac{\beta_x^2}{\beta_x^2 + \alpha_x^2} e^{w\alpha_x} e^{-R \times 2(\alpha_x - \beta \tanh^{-1}(\frac{\alpha_x}{\beta}))} \quad (25)$$

Where  $w$  is the width of the waveguide,  $\beta$  is the propagation constant in the corresponding straight waveguide of same section.  $\beta_x$  and  $\alpha_x$  are defined in equation (B-5) in Appendix B:. For example, the TE mode  $m = 40$  of a  $R = 5 \mu\text{m}$  radius GaAs disk has an associated, radiation limited, quality factor  $Q_{rad} = 10^9$  (p. 76 in [123]). For our  $R_{out} = 10 \mu\text{m}$ ,  $w_{ring} = 500 \text{ nm}$ ,  $n_{Si} = 3.47$ ,  $n_{air} = 1$ ,  $n_{eff} = 2.4$  and  $\lambda_0 = 1.55 \mu\text{m}$ , we find  $\alpha_{rad} = 4.5 \times 10^{-7} \text{ m}^{-1}$ , limiting the intrinsic quality factor to  $Q_{rad} = \frac{2\pi n_{eff}}{\lambda_0 \alpha_{rad}} = 2 \times 10^{13}$ . We will see that those losses are negligible over the next loss sources in our structures of  $R_{out} = 10 \mu\text{m}$ .

- **Absorption losses  $\alpha_{1PA}$ ,  $\alpha_{2PA}$**

According to silicon's energy bandgap of 1.14 eV [126], it is transparent for  $\lambda_0 \geq 1.09 \mu\text{m}$ . As silicon wafers fabrication has a well-controlled procedure nowadays, the initial silicon layer has very little defects as impurities of crystalline defects. While linear photon absorption  $\alpha_{1PA}$  is almost negligible, absorption still occurs as non-linear two photon absorption (2PA)  $\alpha_{2PA}$ , which is proportional to the power circulating in the ring, *i.e.* the number of photons [127]. In crystalline bulk silicon at  $\lambda_0 = 1.55 \mu\text{m}$ , we have a negligible  $\alpha_{1PA} = 10^{-6} \text{ m}^{-1}$  [128]. As  $\alpha_{2PA}$  depends on laser power in the cavity which itself depends on the optical quality factor, one can express the quality

factor limit from which 2PA will dominate<sup>25</sup>:  $Q_{tot\_2PA} = \pi \sqrt{\frac{n_{eff} w_{ring} h m}{\lambda_0 \beta_{2PA} P_{in}}}$ . For a typical injected laser power of  $P_{in} = 1 \text{ mW}$ , we find  $Q_{tot\_2PA} = 145\,000$ , *i.e.* a  $\alpha_{2PA} = 33 \text{ m}^{-1}$ . This being said, another absorption seems to appear on the surfaces of the

<sup>24</sup> The sign in the last exponential had to be changed in order to retrieve the publication's results [124].

<sup>25</sup> From reference [198], we have the 2PA loss value for silicon of  $\beta_{2PA} = 0.8 \text{ cm/GW}$ . For a  $0.5 \mu\text{m} \times 0.22 \mu\text{m}$  waveguide section with a  $P_{stored} = 0.13 \text{ W}$  power circulating power as in our structures, we find  $\alpha_{2PA} = \beta_{2PA} P_{stored} / w_{ring} h = \frac{0.8 \times 10^{-2} \times 0.13 \times 10^{-9}}{0.5 \times 10^{-6} \times 0.22 \times 10^{-6}} = 9.4 \text{ m}^{-1}$ . But as the  $P_{stored}$  calculation is dependent on the optical quality factor of the cavity (see Appendix I:), we can further write the 2PA quality factor:  $Q_{2PA} = \frac{2\pi n_{eff}}{\lambda_0 \alpha_{2PA}} = \frac{2\pi n_{eff} w_{ring} h}{\lambda_0 \beta_{2PA} P_{stored}} = \frac{2\pi n_{eff} w_{ring} h \pi m}{\lambda_0 \beta_{2PA} P_{in} Q_{tot}}$ . Hence, the 2PA will dominate when  $Q_i = Q_{2PA}$ , assuming critical coupling (*i.e.*  $Q_{2PA} = 2Q_{tot}$ ). Leading us to the  $Q_{tot}$  from which 2PA will dominate:  $Q_{tot\_2PA} = \pi \sqrt{\frac{n_{eff} w_{ring} h m}{\lambda_0 \beta_{2PA} P_{in}}}$ .

waveguide (for example in GaAs structures in [122] and p. 57 in [127]). Indeed, it appears that electronic mid-gap states appear in between the valence and conduction band of silicon. Thus photons can be, linearly or not, absorbed in those regions, bolstering absorption coefficients in small dimensions waveguides. This seems to be the predominant loss factor in GaAs disks (p. 68 in [127])<sup>26</sup>.

This absorption leads to heating of the device, also triggering thermal effects as the thermo-optic shift that is discussed in Sec. II.2.7, or photo-thermal forces.

- **Scattering losses  $\alpha_{rough}$ ,  $\alpha_{geom}$**

Any obstacle in the light's path will scatter it: from large anchoring arms (about 100 nm in our structures) to surface roughness (about 1 nm) and lattice defects. The last effect is neglected owing to the high quality of silicon wafers.

- Roughness scattering

Due to fabrication considerations (see Sec. II.6), the roughness  $\sigma_{rms}$  is higher for etched walls on the sides of the ring than its top and bottom surfaces. The Payne-Lacey model accounts for these losses, giving an upper limit (choosing the exponential autocorrelation function in [129]):

$$\begin{aligned}\alpha_{rough} &\leq \frac{\sigma_{rms}^2 k_0 \beta_x^2 (n_1^2 - n_2^2)}{2n_1 \left(1 + \frac{W}{2} \alpha_x\right)} \\ &= \frac{\sigma_{rms}^2 k_0^3 (n_1^2 - n_{eff}^2)(n_1^2 - n_2^2)}{2n_1 \left(1 + \frac{W}{2} k_0 \sqrt{n_{eff}^2 - n_2^2}\right)}\end{aligned}\quad (26)$$

This gives for our  $w = w_{ring} = 0.5 \mu\text{m}$ ,  $n_1 = 3.47$ ,  $n_2 = 1$ ,  $n_{eff} = 2.4$  and with a roughness  $\sigma_{rms} = 1 \text{ nm}$ , for  $\beta_x$  and  $\alpha_x$  defined in Appendix B: and for a  $\lambda_0 = 1.55 \mu\text{m}$  light wave propagating:  $\alpha_{rou} \leq 207 \text{ m}^{-1}$ , limiting  $Q_{rou}$  to  $Q_{rough} \geq \frac{2\pi n_{eff}}{\lambda_0 \alpha_{rough}} = \frac{2\pi \times 2.4}{1.55 \times 10^{-6} \times 207} = 47\,000$ .

This model gives a coarse approximation due to the roughness and the roughness correlation that are not exactly known. To seek a more detailed analysis, the reader is referred to [122].

- Geometrical scattering

The large anchoring arms or geometrical obstacles contribution is noted  $\alpha_{geom}$ . For our structures, experiments will show (see Sec. III.2.2) that the main loss source is the scattering due to anchoring arms with about  $\alpha_{geom} = \frac{2\pi n_{eff}}{\lambda Q_{geom}} = \frac{2\pi \times 2.4}{1.55 \times 10^{-6} \times 80\,000} =$

---

<sup>26</sup> Free carrier absorption is also named in absorption studies, it was not considered here as it is considered negligible over 2PA.

$121 \text{ m}^{-1}$  (for 100 nm-wide anchoring arms in a 500 nm-wide ring waveguide)<sup>27</sup>. Two ways of improvement were tested in this thesis: shrink the spokes width and widen the width of the ring waveguide to have a "bouncing mode" that avoids spokes (to see this last phenomena, the reader can refer to Figure 60).

Table 3 resumes the different loss channels' magnitudes.

Loss channel	Radiation	Absorption		Scattering	
	$\alpha_{rad}$	$\alpha_{1PA}$	$\alpha_{2PA}$	$\alpha_{rough}$	$\alpha_{geom}$
Loss coefficient ( $\text{m}^{-1}$ )	$4.5 \times 10^{-7}$	$10^{-6}$	33	$\leq 207$	121
Quality factor	$2 \times 10^{13}$	$10^{13}$	$1.45 \times 10^5$	$\geq 4.7 \times 10^4$	$8 \times 10^4$

Table 3: Different loss channels and their associated loss coefficient and quality factor.

To resume, in our  $w_{spk} = 100 \text{ nm}$  and  $w_{ring} = 500 \text{ nm}$  ring, geometrical scattering by the spokes is the dominant optical loss source. But 2PA has nearly the same magnitude order, as well as roughness losses of which only the upper bound is known. The different loss sources are pictured in Figure 34.

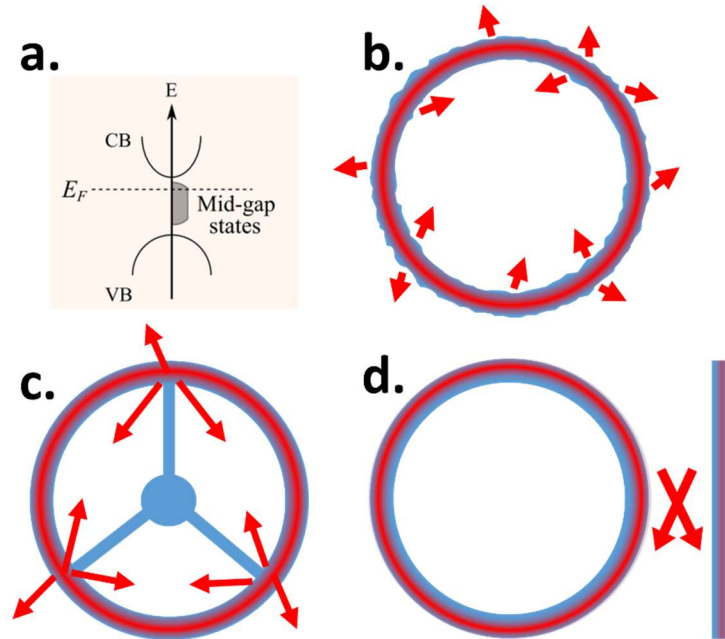


Figure 34: Scheme of the different loss sources in ring cavities. (a.) Absorption as an energy level scheme from p. 56 in [127]. (b.) Scattering due to roughness. (c.) Scattering due to anchoring arms and tip. (d.) Losses through coupling.

Another source of losses arises from the waveguide used to inject and collect light in and from the optical cavity. It is quantized by the extrinsic quality factor  $Q_e$ . This coupling is a loss from the cavity point of view but useful to extract sensing signal. We will see in next paragraphs how to balance this loss source in particular.

<sup>27</sup> Dispersion effect is neglected considering our laser's spectral width ( $FWHM = 400 \text{ kHz}$  [200]) negligible over our cavities' one ( $FWHM = 3.1 \text{ GHz}$ ).

## II.2.4 Evanescent coupling

The most used technique<sup>28</sup> to inject light into a Whispering Gallery Resonator (WGR) to date is to put an optical waveguide (a fiber taper for example) in the vicinity of the cavity (Figure 34d). To couple effectively, one can consider 2 aspects of the coupling problem: phase-matching and critical coupling.

- **Phase-matching:** coupling is best when fields of the waveguide's guided mode and the cavity's guided mode overlap. As the cavity is a curved waveguide, its coupling wavelength is larger when coupling from further (Figure 35). As a consequence, with fixed guide and ring thickness,  $w_{taper} \leq w_{ring}$  is required to ensure that the effective wavelength of the waveguide mode is slightly longer than that of the cavity. This condition can be set by numerical simulations with Lumerical or COMSOL softwares. Previous calculations for thicknesses of 220 nm and a 10  $\mu\text{m}$  ring radius, aiming at an effective index agreement between the straight guide and the curved guide led to:  $w_{ring} = 500 \text{ nm}$  and  $w_{taper} = 475 \text{ nm}$  or  $w_{ring} = 750 \text{ nm}$  and  $w_{taper} = 620 \text{ nm}$ . From this picture, one understands that for a thinner waveguide (*i.e.* with larger effective wavelength), the phase matching condition will impose the waveguide to be further apart from the cavity.

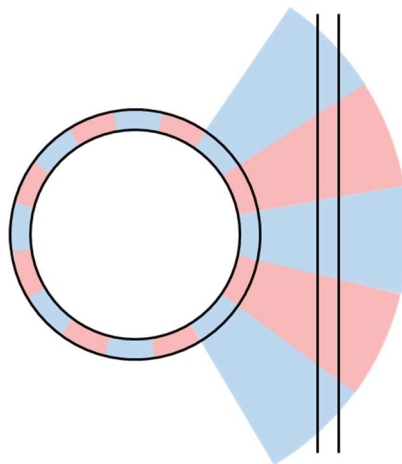


Figure 35: Scheme of a ring cavity (black circle) and its associated waveguide on the right. The electric optical field is represented in red and blue. When the wavelengths in the ring and in the waveguide matches, the phase matching condition is fulfilled. From p. 35 in [130].

- **Critical coupling:** the waveguide in the vicinity of the cavity acts as an injector and collector of light, with the same coupling factor in first approximation. To inject and collect more light, one wants to approach the guide of the cavity. But if the collection is too effective, it will act as a too strong loss for the cavity and thus lower its sensing performance. As discussed in more details in the next paragraphs, a sweet spot (*i.e.* critical coupling) has to be found, namely when losses due to coupling (*i.e.* extrinsic losses) match the losses of the cavity (*i.e.* intrinsic losses). From this picture, one understands that for a high intrinsic quality factor cavity (*i.e.* with low losses), the critical coupling condition will impose the waveguide to be further apart from the

---

<sup>28</sup> Other techniques, albeit less effective, were demonstrated as free-space grating coupling [201].

cavity. As the evanescent fields decay exponentially with the distance, the gap distance between the optical cavity and the waveguide is a crucial parameter. In practice, the critical coupling is therefore sensitive to fabrication variability and difficult to predict.

In addition to the phenomena discussed above, fabrication proximity effects hinder the optical performances when the waveguide is too close of the cavity. Typically, this happens for gaps lower than 150 nm in our structures (see Sec III. 2)).

In practice for single laboratory device (here opposed to integrated sensor devices), this is mainly done through placing a fiber or a fiber taper laterally or vertically with respect to the cavity [131][132]. For a more integrated and stable operation (in a sensing aim), monolithic SOI waveguide (or taper) are used to assess the WGR. We used the latter as this thesis work aims at creating consumables OM-AFM tips. Experimentally, having a mobile fiber allows one to adjust the coupling distance whereas for monolithic structures, many devices are needed to find the optimally coupled one. The straight waveguide coupling to the ring cavity is one of some evanescent coupling configurations. One can cite the pulley coupling [133][134], ring-ring coupling [14], straight waveguide-straight cavity [115] as seen in Figure 36. They can provide achromatic coupling or more selectivity.

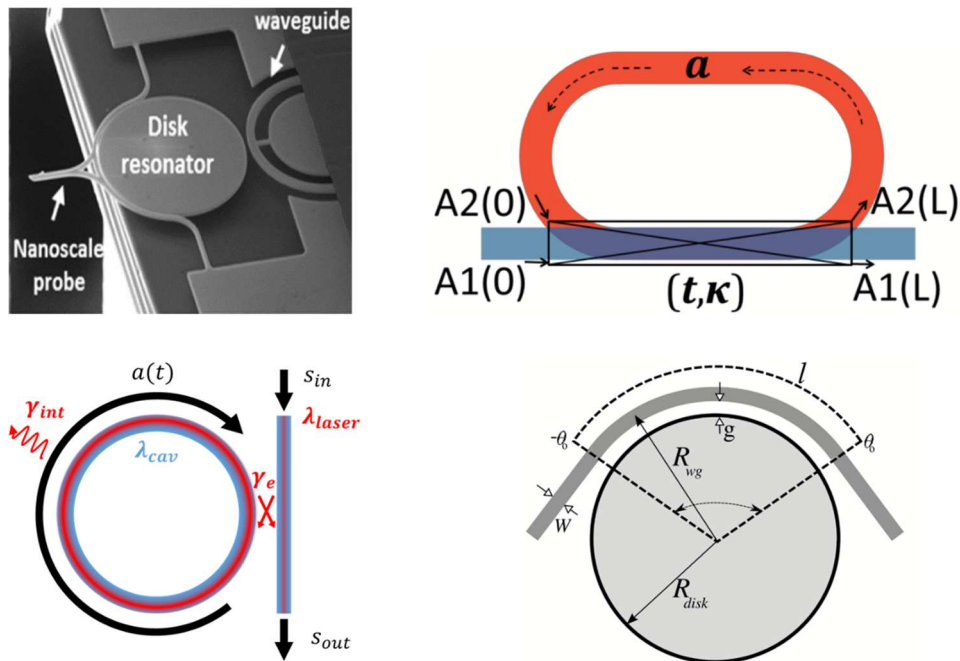


Figure 36: Schemes and pictures of different evanescent coupling configurations. From top left [14] to right p. 110 in [115] then to bottom left and right [134].

### II.2.5 Optical inputs/outputs: coupled mode theory (CMT)

To account for evanescent coupling between a ring and a waveguide, we will place ourselves in the time (here opposed to “space”) coupled mode theory, which provides insights on the optical cavity, in an analytical and intuitive fashion. This framework was extended to quantum behavior as the “input-output” formalism [135]. We introduce the cavity field amplitude  $a(t)$  as  $|a(t)|^2 = E_{stored}$ , the electromagnetic energy stored within the cavity mode. If we now consider that we inject light in the waveguide it will couple to the cavity with a coefficient  $\gamma_e$ . The situation is depicted in Figure 37.

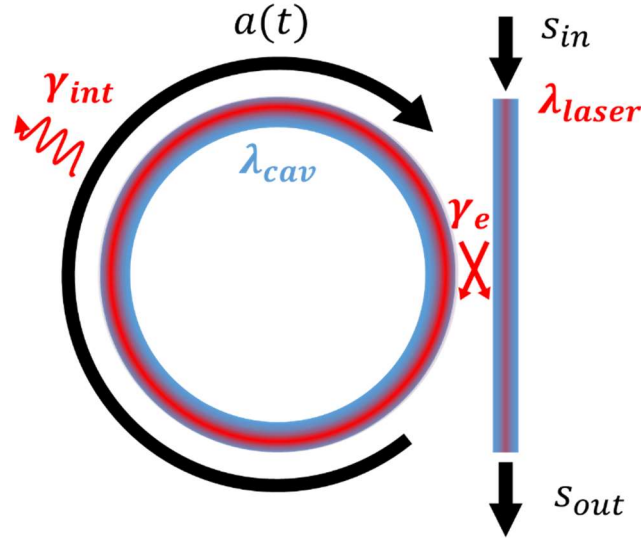


Figure 37: Scheme presenting elements of the input/output formalism (or coupled mode theory) applied to micro-rings.  $\gamma_e$  is the coupling rate with respect to time and  $\gamma_{int}$  is the loss rate associated to the ring only with respects to time. We define  $\gamma_{tot} = \gamma_{int} + \gamma_e$ .

From temporal input-output point of view, the cavity is losing energy through  $\gamma_{tot}$  losses and gaining energy with the light coupled in. One can thus write, in laser rotating picture<sup>29</sup> (similar to equation 4 in [112], equation 2.13 in [136], in [137], from equation 7.28 in [138]):

$$\frac{da}{dt} = -\left(\frac{\gamma_{tot}}{2}\right)a + i(\omega_{cav} - \omega_{laser})a + \sqrt{\gamma_e}S_{in} \quad (27)$$

Where  $\omega_{laser} - \omega_{cav}$  is the detuning of the injected laser in regard to the cavity's optical resonance,  $P_{in} = |s_{in}|^2$  is the input power injected in the waveguide<sup>30</sup> and  $i$  is the imaginary number.

#### II.2.5.1 Reflection/ Transmission versus wavelength: lorentzian optical mode

From the equation above, one can retrieve the energy stored and the transmission of the cavity in steady state ( $da/dt = 0$ ):

$$E_{stored}(\omega_{laser}) = |a(\omega_{laser})|^2 = \frac{\gamma_e P_{in}}{\left(\frac{\gamma_{tot}}{2}\right)^2 + (\omega_{laser} - \omega_{cav})^2} \quad (28)$$

Which is lorentzian-shaped. Where  $P_{in} = |s_{in}|^2$ .  $\omega_{laser} - \omega_{cav}$  is the detuning between the laser and the cavity angular frequency.

The transmission of the cavity is then<sup>31</sup>, assuming  $s_{out} = s_{in} - \sqrt{\gamma_e}a$ :

$$T(\omega_{laser}) = \left|\frac{s_{out}}{s_{in}}\right|^2 = \frac{\left(\frac{\gamma_{int}}{2} - \frac{\gamma_e}{2}\right)^2 + (\omega_{cav} - \omega_{laser})^2}{\left(\frac{\gamma_e}{2} + \frac{\gamma_{int}}{2}\right)^2 + (\omega_{cav} - \omega_{laser})^2} \quad (29)$$

<sup>29</sup> Replacing  $a$  in the original paper by  $ae^{i\omega_{laser}t}$ .

<sup>30</sup> For coherence with literature, the  $s_{in}$  notation was chosen. We consider  $\gamma a$  homogenous to  $\sqrt{\gamma}s_{in}$ .

<sup>31</sup> The opposite of reflection in p. 204 in [138]

Which looks like a lorentzian (Figure 38).

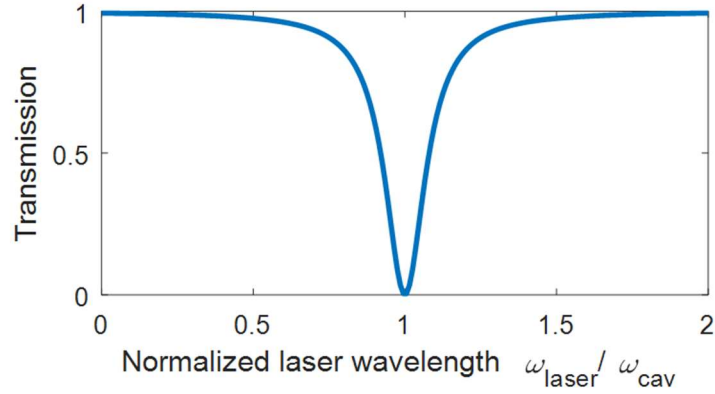


Figure 38: Transmission of a waveguide coupled to a cavity as in Figure 37. For this graph we chose  $\gamma_{int} = \gamma_e$  i.e. the critical coupling condition.

From equation (29), one can extract the two values  $T(\omega_{cav})$  and the full width at half minimum (FWHM)  $\Delta\omega$  (calculation in Appendix H):

$$T(\omega_{cav}) = \left( \frac{\gamma_e - \gamma_{int}}{\gamma_e + \gamma_{int}} \right)^2 \quad (30)$$

$$\Delta\omega = \gamma_e + \gamma_{int} \quad (31)$$

But depending on laser wavelength, many resonance modes of the cavity with different azimuthal numbers can be observed. A wide transmission spectrum is depicted in Figure 39.

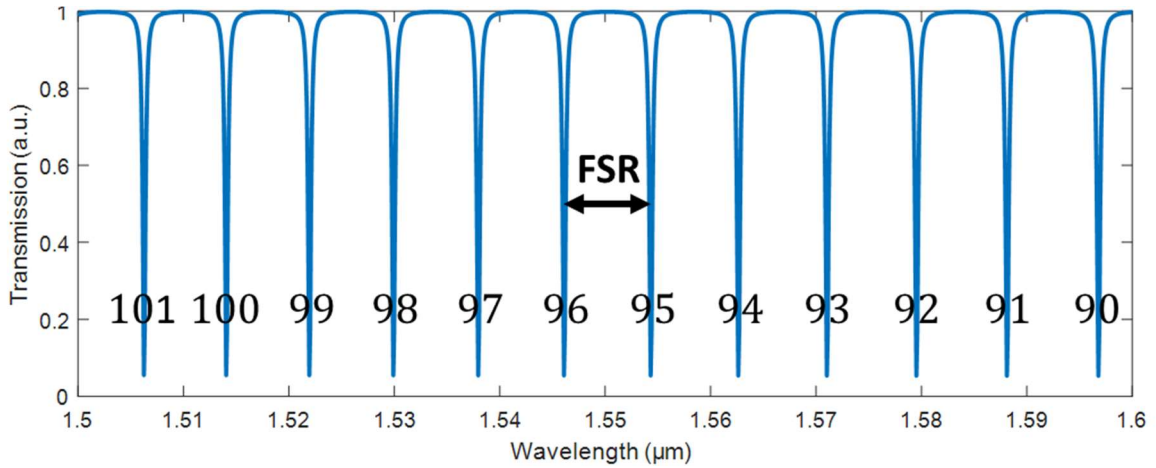


Figure 39: Transmission spectrum of one  $R = 10 \mu\text{m}$  ring cavity. Each lorentzian drop is an optical resonance of the ring, characterized by its azimuthal number  $m$  written on each resonance.  $m$  goes down with rising wavelengths (as less wavelengths can fit in the cavity). The free spectral range (FSR) is defined in Appendix K: Its value is about 9 nm for our 10  $\mu\text{m}$  radius ring cavities of cross-section  $0.5 \mu\text{m} \times 0.22 \mu\text{m}$ .

In practice, optical modes width is characterized by their quality factor, the narrower the resonance, the higher the optical quality factor. The total (or loaded) quality factor is then defined as  $\frac{1}{Q_{tot}} = \frac{\gamma_{int} + \gamma_e}{\omega_0} = \frac{1}{Q_{int}} + \frac{1}{Q_e}$ . For comparison sake, optical cavities are often described



with their finesse  $F = \frac{\Delta\lambda}{FSR_\lambda} = \frac{Q_{tot}}{m} = 2\pi Nb_{laps}$ . Where  $Nb_{laps}$  is the statistically-relevant number of laps a photon completes in the cavity before being emitted, absorbed, scattered or coupled out of the cavity  $Nb_{laps} = \frac{1}{\gamma_{tot} \times T_0}$ ,  $T_0$  being the time for a photon to complete a lap.

### II.2.5.2 Over/under-coupled waveguide

As we will see in Figure 49, to have the best optomechanical transduction<sup>32</sup>, one seeks for the highest transmission versus wavelength slope, that is to say highest contrast  $C$  (as defined in Figure 40) and narrowest width (*i.e.* highest  $Q_{opt}$ ). From equation (29), one can see that the only parameters that govern the lorentzian shape are  $\gamma_{int}$  and  $\gamma_e$ . One can show that the highest slope is obtained close to  $\gamma_{int} = \gamma_e$  named critical coupling<sup>33</sup>, or in words when the losses in the ring equal the losses due to coupling. To better grasp this fact, the influence of the ratio  $\gamma_e/\gamma_{int}$  on the transmission and the optical resonance is depicted in Figure 40.

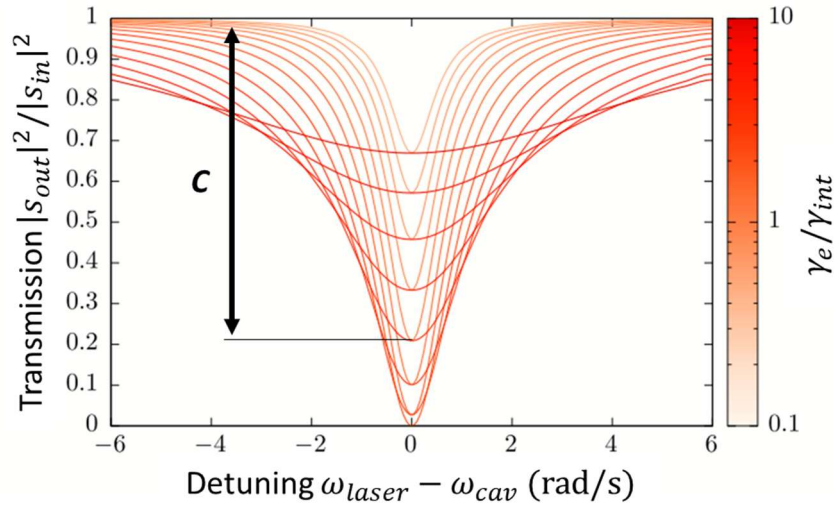


Figure 40: Numerical plots illustrating the under-coupled (light orange) and over-coupled (plain red) regimes. The curves are calculated from equation (29). The WGM resonance has a lorentzian profile. The ratio  $\gamma_e/\gamma_{int}$  successively takes the value from 0.1 to 10.  $C$  is the contrast of the mode. From p. 48 in [139].

One can see that, indeed, the highest slopes are obtained around  $\gamma_{int} = \gamma_e$ .

From a sensing point of view, one wants to reach the lowest, and equal,  $\gamma_{int}$  and  $\gamma_e$  (or the highest and equal  $Q_{int}$  and  $Q_e$ ). In practice, the fabrication process or design chosen define the intrinsic losses  $\gamma_{int}$  for a given cavity. The gap distance (*i.e.* the distance between the cavity and the waveguide) is adjusted in order for the extrinsic losses  $\gamma_e$  to match the intrinsic one  $\gamma_{int}$ <sup>34</sup>. Indeed, the coupling losses vary exponentially with gap distance  $d_{gap}$  (see Sec. III.2.1). For example to attain critical coupling, a  $Q_{int} = 100\,000$  cavity needs a wider gap distance

<sup>32</sup> In the bad-cavity regime relevant to this thesis ( $f_m \ll \gamma_{tot}$ ).

<sup>33</sup> Theoretically, the maximum  $Q_{opt} \times C$  is actually obtained for an under-coupled contrast of 89%, that is to say with  $\gamma_{int}$  lightly superior to  $\gamma_e$ .

<sup>34</sup> As the gap distance is fixed at the design definition, many device are fabricated, with the same design but different coupling gap distances. This allows one of the probe to be critically coupled.

than a  $Q_{int} = 10\,000$  one. Typical coupling gap distances in our experiments vary from 100 nm to 300 nm.

### II.2.6 CW and CCW degeneracy lifting: mode splitting

When characterizing optical cavities with about  $Q_{tot} > 10\,000$ , cavity mode splitting appears, where each optical mode appears split in a doublet (Figure 41).

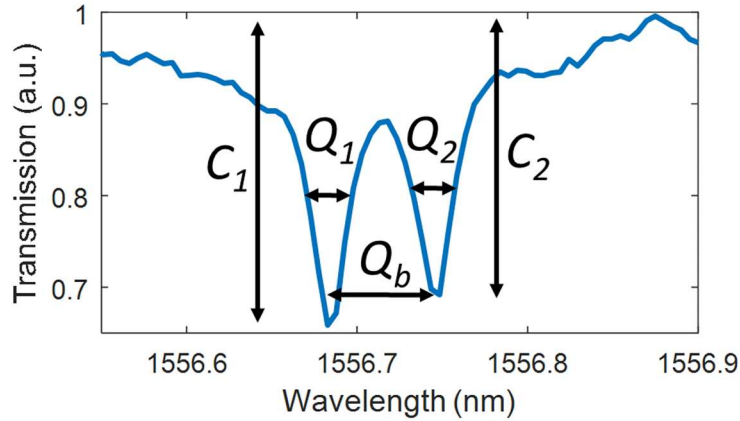


Figure 41: Transmission spectrum of a  $Q_{tot} > 10\,000$  OM cavity of this thesis. Two drops are visible separated by a few tens of picometers in wavelength, far below the  $FSR$  (about 10 nm).  $Q_1$  and  $Q_2$  are defined for each drop from their respective full width at half minimum  $\Delta\lambda$  (FWHM).

The clockwise (CW) and counter-clockwise (CCW) propagating modes are not always degenerated. This degeneration lifting phenomenon is due to non-perfect-symmetry of the two paths arising from the spokes and tip scattering features of the ring [140]. Back scattering occurs from one mode to the other and some of the optical power is reflected back in the ring (p. 167 in [123]). To account for those two modes, one can use an updated Coupled Mode Theory (CMT), taking into account a coupling rate between the two modes CW and CCW (Figure 42).

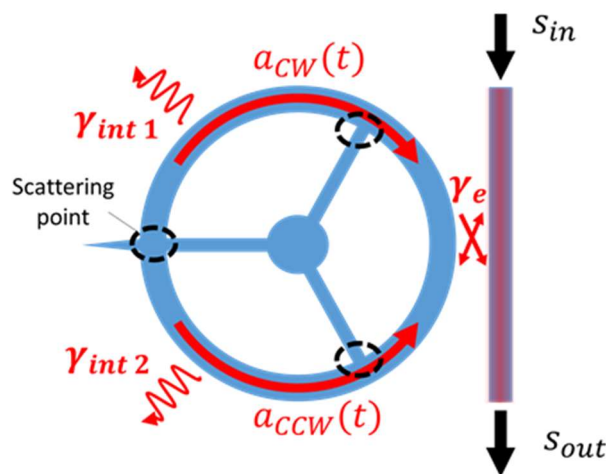


Figure 42: Scheme of the CMT updated with mode splitting. An exchange quality factor  $Q_b$  is defined between the two contra-propagating modes CW and CCW. Similar scheme can be found in [141] or p. 168 in [123].

The behavior of this optical resonance doublet is detailed in Sec. III.2.4.

## II.2.7 Thermo-optic shift/optical bi-stability

When injecting strong optical power in the ring ( $P_{in} > 10 \mu\text{W}$ ), the optical resonance in experiments appears not lorentzian anymore but rather a saw-tooth shaped drop (Figure 43). This is at least true if acquiring an optical spectrum with a slow scan of the laser wavelength.

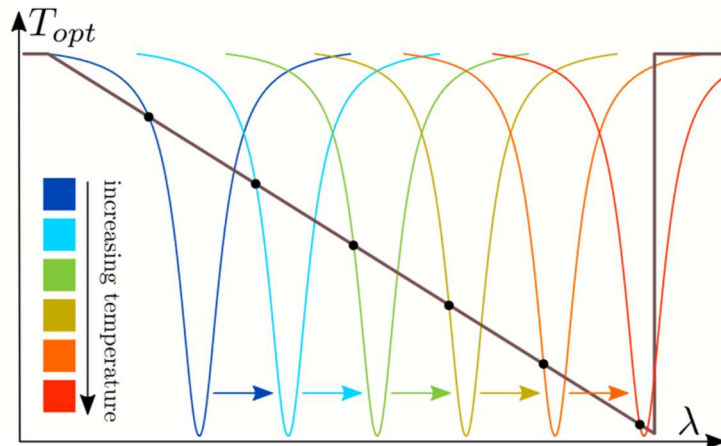


Figure 43: Transmission (in black) of an OM ring when probing laser is swept in increasing wavelength. It displays a saw-tooth-shaped, thermo-optic distortion of the cavity. The implicit optical resonance drop is represented in colors for increasing temperature. When the laser is swept over a WGM at high power, the temperature increase in the disk gradually red-shifts the WGM resonance. As a consequence the WGM produces a triangular profile in the transmission spectrum. From p. 35 in [139].

As optical absorption occurs, when light is injected in the cavity its temperature rises. The greater the power injected in the cavity, the greater the temperature increase. As the refractive index  $n_{eff}$  rises with temperature, the effective length of the cavity  $L_{cav} = 2\pi R n_{eff}$  also increases, increasing the resonance wavelength<sup>35</sup> (Figure 44). This thermal effect gives rise to an optical bi-stability, revealed when the laser wavelength is swept upward or downward.

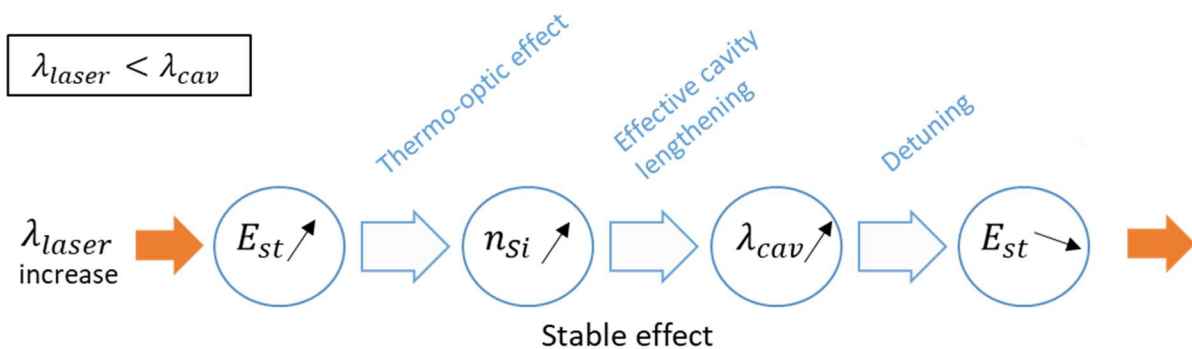


Figure 44: Scheme of the phenomena at play in the ring when laser wavelength is increased. This process applies when the laser is blue-detuned ( $\lambda_{laser} < \lambda_{cav}$ ) and swept towards larger wavelengths.  $E_{st}$  is the optical energy stored in the cavity,  $T$  its temperature,  $n_{si}$  its refractive index and  $\lambda_{cav}$  its resonance wavelength. In the end, there is an overall increase of  $\lambda_{cav}$  because  $E_{st}$  increases more than it diminishes. If the laser is red-detuned and swept towards smaller wavelengths, the process becomes unstable.

<sup>35</sup>This phenomenon could also be explained by thermal expansion or AC Kerr effect. However in silicon, they are negligible over the thermo-optic effect. Numbers are given in Appendix I:.

In practice, for a transduction application one wants to keep power injected low to avoid this effect. However, a cavity showing this thermo-optic behavior can be used as an OM probe, given that this effect is slow enough compared to the mechanical resonance or with a small enough magnitude. A majority of the results shown in this manuscript come from OM probe showing this thermo-optic behavior, as high laser power is needed for a better mechanical to optical transduction (see Sec. III.4.1).

Now that we know how to address an optical cavity and what optical behavior to expect from such a ring cavity, we will study the mechanical aspects of the cavity before introducing the OM coupling.

### II.3 Mechanical resonator

In this part, we study the mechanical aspect of the cavity and how to exploit it in an AFM probe framework. Indeed, the rings used in this thesis work are free to move. The dimensions of each ring define the mechanical resonance frequencies of the structure.

#### II.3.1 Mechanical modes, AFM considerations

Resonance modes of the ring structure can be sorted in flexural out-of-plane and in-plane modes (Figure 45). The modes used in optomechanical sensors are the most coupled to optics, *i.e.* the ones that have largest influence on cavity length (see Sec. II.4.1 and the  $g_{O\leftarrow M}$  factor). One can highlight the out-of-plane flexural and in-plane breathing modes.

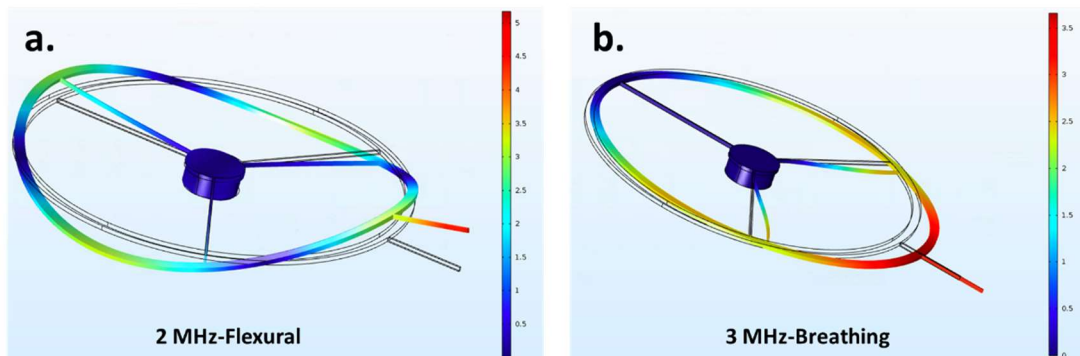


Figure 45: Numerical simulations of mechanical resonances of ring of diameter  $\varnothing = 20 \mu\text{m}$ , of cross-section  $0.5 \mu\text{m} \times 0.22 \mu\text{m}$  and with  $100 \text{ nm}$  wide spokes and tip. One can define an azimuthal order which is the number of nodes of the resonance, *i.e.* the points of the ring that does not move, in dark blue. (a.) A flexural mode of azimuthal order 4. (b.) An in-plane mode of azimuthal order one.

Among in-plane mechanical modes, radial breathing modes with azimuthal order around 9 were chosen for their high frequency, over  $100 \text{ MHz}$  (Figure 46). As a reminder, we look for high-frequency mode as they induce a larger bandwidth of the probe.

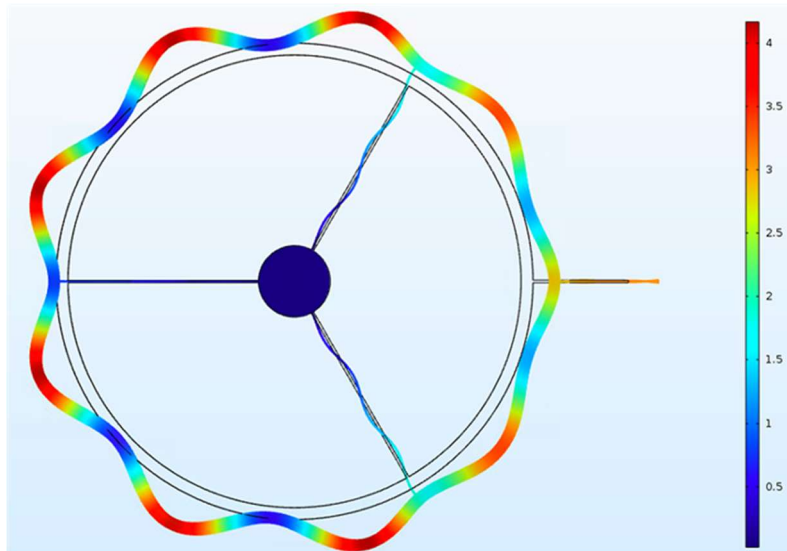


Figure 46: Numerical FEM simulation of a 132 MHz breathing mechanical resonance of a  $\varnothing = 20 \mu\text{m}$  ring of cross-section  $0.5 \mu\text{m} \times 0.22 \mu\text{m}$  and with 100 nm-wide spokes and tip. This mode has great impact on the cavity length (*i.e.* great  $g_{O \leftarrow M}$  see Sec. II.4.1). An azimuthal order can be defined for this mode:  $m = 9$ , *i.e.* there are 9 displacement maxima on the ring. This simulation is done with the COMSOL software.

The AFM application sought for these structures imposes the presence of a tip, for spatial resolution, onto the ring. Two dispositions arise instinctively in order to avoid steric cumbersoming (Figure 47). For fabrication reasons the in-plane option was preferred, as it allows etching the tip and the ring in a single step. Furthermore, they are the most coupled to optics.

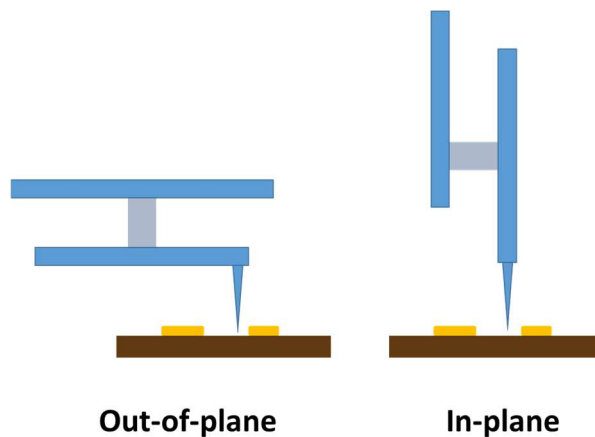


Figure 47: Scheme of two possible optomechanical AFM probe structures, using two different mechanical modes.

### II.3.2 Position of the tip relative to the spokes

To be more force-resolved, it is necessary to reduce the effective stiffness  $k_{eff}$  of the probe at the tip location. The tip must therefore be placed at the maximum displacement of the

mechanical mode being excited<sup>36</sup>, which is actually the lowest stiffness point. A variety of different design and their simulated stiffness is summarized in Table 4.

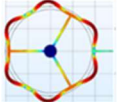
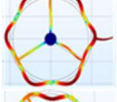
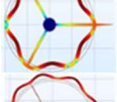
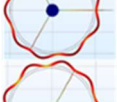
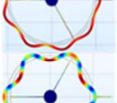
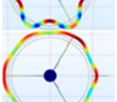
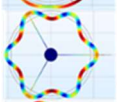
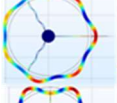
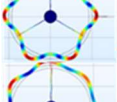
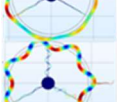

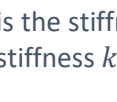
	Spokes angle (°)	$m$	$w_{ring}$ (nm)	$w_{spk}$ (nm)	$w_{tip}$ (nm)	$f_m$ (MHz)	$k_{eff}$ (N/m)	$k_{static}$ (N/m)
	0	6	750	500	500	118.6	2700	18
	90	6	750	500	500	114.1	5	32
	60	6	750	500	500	118.1	43	934
	60	9	500	100	100	133.6	40	269
	0	9	500	100	100	132.8	7	2.3
	0	6	750	100	100	108.0	13	7.9
	0	6	750	100	100	136	9,7	7.9
	60	6	750	100	100	108.1	7,1	195
	60	7	750	100	100	135.3	5,2	195
	90	6	750	100	100	107.7	6,6	1.4
	90	7	750	100	100	136.1	7,5	1.4
	90	7	750	100	100	137.9	11,8	1.4

Table 4 : OM probe designs and their associated simulated mechanical modes and stiffness. The shades of blue indicate the 3 design families in terms of ring, spokes and tip width. The static stiffness  $k_{static}$  is the stiffness considered when then probe is deformed in the quasi-static assumption. The effective stiffness  $k_{eff}$  is the stiffness considered at the associated resonance frequency  $f_m$ .

From an optical perspective, the presence of the tip in front of a spoke lowers the  $Q_{opt}$  because it hinders the "bouncing mode" (see Sec. III.2.2). From a mechanical perspective, the presence of the tip in front of a spoke increases the static stiffness<sup>37</sup>. This increase is welcome

<sup>36</sup> Assuming the tip addition has a negligible impact on the mechanical mode.

<sup>37</sup> The static is not to be confused with the effective stiffness at resonance  $k_{eff}$ . The static stiffness is the stiffness of the probes considered when the interaction forces vary slower than the first resonance of the resonator, that is to say in the quasi-static approximation.

as it limits the jump-to-contact phenomenon. In general, all configurations are mechanically acceptable with a  $k_{eff}$  in the kN range, except for the design presented in the first line of Table 4.

**Note:** One could ask why disks were not considered in this manuscript. Looking at the mechanical figure-of-merit  $\mathcal{F}_m$  given in Sec. I.3.4, one can see that the effective stiffness  $k_{eff}$  must be kept low. Thus a ring shaped cavity with  $k_{eff} \approx 10$  kN/m (Table 4), was preferred over a full disk with  $k_{eff} \approx 260$  kN/m (p. 110 in [127]).

### II.3.3 Damped harmonic oscillator mass-spring model, losses

To simplify the whole ring, we turn the 3D mechanical problem in a 1D one. The whole ring can be considered as a lumped mass-spring model via reduction in one point<sup>38</sup>. We conserve the amplitude vibration at the reduction point and the total energy of the resonator. As the mechanical interaction with a sample will occur at the apex of the tip, this point is chosen for reduction (Figure 48).

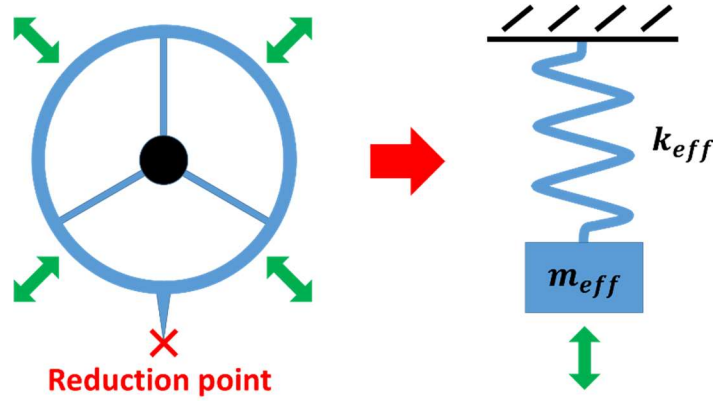


Figure 48: Scheme of the lumped model simplification of the OM probe. This lumped model allows us to work with the effective mass  $m_{eff}$  and effective stiffness  $k_{eff}$  parameters.

Neglecting the tip movement orthogonal to its direction, its displacement parameter  $z$  is therefore introduced. From a damped harmonic oscillator picture, only excited by temperature, one can write:

$$m_{eff} \left[ \ddot{z} + \frac{\omega_m}{Q_m} \dot{z} + \omega_m^2 z \right] = F_{th} \quad (32)$$

Where  $m_{eff}$  is the effective mass (dependant on the mode and the reduction point),  $Q_m$  is the quality factor of the mechanical resonance,  $\omega_m$  is the resonance pulsation with  $\omega_m = \sqrt{k_{eff}/m_{eff}}$  and  $F_{th}$  is the thermomechanical (or Langevin) force.

The motion damping (inversely proportional to  $Q_m$ ) can occur through different channels (p. 52 in [142]):

<sup>38</sup> This picture is valid, for a given mode, as long as the oscillator stays in linear regime, that is to say that vibrational amplitude must be negligible in front of the characteristic length of the structure (for a ring we take the spoke width 100 nm), so 10 nm amplitudes. The reduction point position changes the value of  $k_{eff}$ .

- Medium: viscous (friction) and acoustic (acoustic wave emission) damping in air and liquids.
- Anchoring: mechanical wave is emitted in the substrate (this issue was addressed with a mechanical shield for example in [143]).
- Material: damping due to lattice defects.
- Thermo-elastic damping: contracting parts of the structure heat up while extending one cool down, leading to thermal dissipation.

For our structures, experiments shows that medium damping is the main damping channel in air, limiting the quality factor to  $Q_m \approx 1\,000$ . Under vacuum anchoring damping takes over, limiting the quality factor to  $Q_m \approx 10\,000$ .

#### II.4 Optomechanical coupling, equations, resonance

The optical and mechanical resonator, that the ring structure consists in, are coupled through different phenomena. The optical power injected in the optical cavity has an actuating effect, through optical forces  $F_{opt}$ , on the mechanical resonator. The mechanical resonator in turn modifies the cavity length, which modifies the power injected in the cavity and the overall transmission of the device (Figure 49). This coupling allows one to retrieve mechanical information on the optical signal.

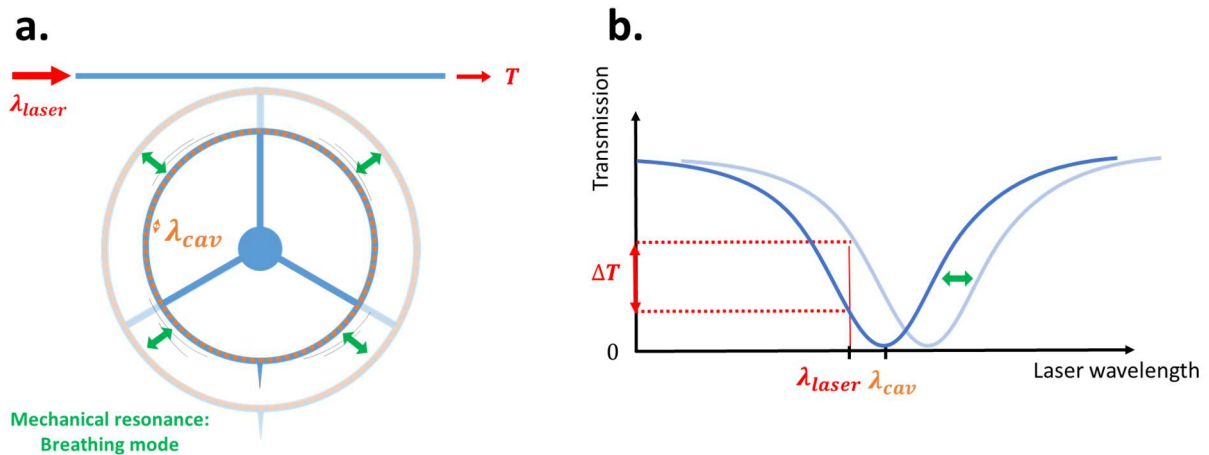


Figure 49: Illustration of the optical read-out of the mechanical motion. **(a)** Scheme of the OM probe and its associated waveguide. When the ring expands in a breathing fashion (green arrow), its optical resonance wavelength  $\lambda_{cav}$  grows and thus, for a fixed-wavelength  $\lambda_{laser}$  laser is used, its transmission is impacted. Note: the gap distance between the ring and the waveguide can be considered fixed as the ring expands (typical values are  $d_{gap} = 150\text{ nm}$  and a mechanical resonance amplitude of  $10\text{ pm}$ ). **(b)** Optical transmission spectrum associated with the scheme on the left hand side. One can note that better sensitivity (more transmission variation relative to motion) is achieved with a steeper optical resonance flank. That is to say with a higher  $Q_{opt}$  (*i.e.* less optical losses) and contrast (*i.e.* critical coupling to waveguide). One can also note that better sensitivity is achieved if the detuning according to mechanical motion (in green) is greater. That is to say higher  $g_{O \leftarrow M}$ .

We define two coupling factor  $g_{O \leftarrow M}$  and  $g_{O \rightarrow M}$  respectively the optical resonance frequency shift of  $f_0$  ( $f_0 = c/\lambda_0$ ) versus mechanical displacement  $z$ :  $g_{O \leftarrow M} = \partial f_0 / \partial z$  (also named frequency-pull parameter in literature) and the force applied on the resonator versus the



optical power stored in the ring  $g_{O \rightarrow M} = \frac{\partial F_{opt}}{\partial P_{st}}$ . They include several physical phenomena as displayed in Figure 50, let us discuss the latter.

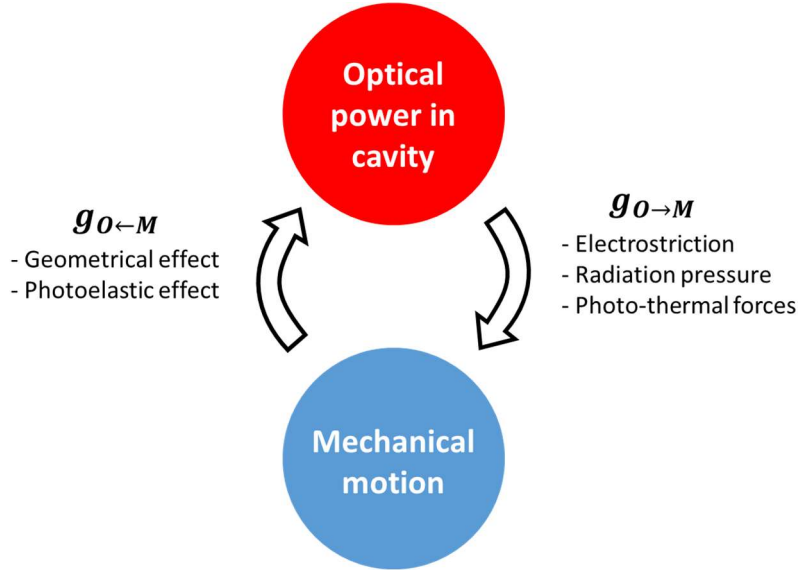


Figure 50: Scheme of the OM coupling highlighting the different phenomena at play.

#### II.4.1 Optical sensing of the mechanical motion $g_{O \leftarrow M}$

The optical cavity length change with mechanics  $g_{O \leftarrow M} = \partial f_0 / \partial z$  is done through two phenomena<sup>39</sup>:

- **Photo-elasticity**  $g_{O \leftarrow M_{pe}}$ : as the ring gets wider, it is strained and its refractive index changes and thus its optical length too.  $g_{O \leftarrow M_{pe}} = \frac{\partial f_0}{\partial n} \times \frac{\partial n}{\partial z}$ .
- **Geometrical boundaries displacement**  $g_{O \leftarrow M_{geo}}$ : as the ring gets wider (radius increase) its physical length increases and thus its optical length too (Figure 49).  $g_{O \leftarrow M_{pe}} = \frac{\partial f_0}{\partial L} \times \frac{\partial L}{\partial z}$ . Considering a simple mechanical breathing mode with azimuthal order 1 (Figure 49), it comes  $g_{O \leftarrow M} = -f_0/R$  [144] as the optical resonance frequency is inversely proportional to the radius (equation (21)). Since we use a more complicated mechanical mode (Figure 46), this value, as the photo-elastic one, is numerically calculated with the COMSOL software.

The geometrical contribution is dominant in silicon rings, when the radius is above a few micrometers ([145] and p. 100 in [146]). The FEM calculated values we found for our mechanical modes were in the order of  $g_{O \leftarrow M} = -10$  GHz/nm.<sup>40</sup> It is dependent on the chosen reduction point for the lumped model. To get rid of this dependency, the  $g_0$  is introduced in literature. It is the  $g_{O \leftarrow M}$  normalized by the zero-point fluctuation (*i.e.* the quantum motion) of the chosen reduction point  $Z_{ZPF}$ .

$$g_0 = g_{O \leftarrow M} \times Z_{ZPF} \quad (33)$$

<sup>39</sup> Their complete formulas can be found p. 58 in [146].

<sup>40</sup>  $g_{O \leftarrow M} = -10^{19}$  Hz/m is in optical frequency per displacement. Differently put, the coupling coefficient is worth  $g_{O \leftarrow M} = 80$  fm/pm in optical resonance wavelength per motion.

Where  $z_{ZPF}$  is given by  $z_{ZPF} = \sqrt{h_p f_m / k_{eff}}$ ,  $h_p$  being the Planck constant. Which gives us  $g_0 = 15$  kHz. As a note the  $g_{O \leftarrow M}$  unit chosen in this manuscript is in optical frequency in Hertz per mechanical displacement in meters, contrary to the literature where the optical angular frequency is preferred.

#### II.4.2 Optical actuation of the mechanical motion $g_{O \rightarrow M}$

As actuation can occur through different phenomena, we will differentiate the respective OM coupling factors in the next paragraph.

The optical forces at play in the resonator are (p. 30 in [123]):

- **Electrostriction  $g_{O \rightarrow M_{es}}$** : stemming from material polarization, stress is applied to the material due to the electric field of the light. It acts in a similar fashion to piezoelectric effect but is proportional to the squared electric field (so proportional to the optical power). Bandwidth of this effect is limited by the time for which the power in the cavity can change  $\frac{f_0}{Q_{opt}}$ , for  $Q_{opt} = 50\,000$ , this gives 4 GHz.
- **Radiation pressure  $g_{O \rightarrow M_{rp}}$** <sup>41</sup>: the photons communicate their momentum to the waveguide they circulate in. In a simple particle picture, one can imagine the photons bouncing and hence pushing the outer wall of the ring. This force is also proportional to the optical power. Bandwidth of this effect is the same as electrostriction.
- **Photo-thermal  $g_{O \rightarrow M_{pt}}$** : photon absorption leads to heating of the material and thus thermal expansion. In a micrometer structure ( $L = 1\ \mu\text{m}$ ), thermalisation time  $\tau_{th}$  is typically worth a hundred of nanoseconds. It can be roughly calculated using  $\tau_{th} = L^2 / \alpha$  with a thermal diffusivity of silicon of  $\alpha = 1\ \text{cm}^2/\text{s}$  [147]. It is to note that this coupling, as it is dissipative, is only from optics to mechanics so for excitation purpose and not sensing of the mechanical motion. Thermal expansion factor of silicon is  $\alpha_{th_{exp}} = 2.5 \times 10^{-6}\ \text{K}^{-1}$  at room temperature [148]. For a  $10\ \mu\text{m}$ -radius ring and a temperature rise  $\Delta T = 1\ \text{K}$ , assuming a breathing mechanical motion, deformation of the cavity is:  $z = \alpha_{th_{exp}} R \Delta T = 25\ \text{pm}$  in steady state. Its magnitude will decrease with increasing frequency modulation past a few tens of MHz, corresponding to thermalization time.

Which force is the dominant one? This question is not definitely answered yet. In similar devices in GaAs, photo-thermal forces were shown to dominate [149]. From experimental considerations that are not shown in this manuscript, I personally conclude that the thermal expansion effect (*i.e.* photo-thermal forces) is not actuating the ring. This lets two contenders for the optical actuation phenomenon: electrostriction and radiation pressure. Radiation pressure nearly always has a similar to greater impact than electrostriction in silicon waveguides, depending on its dimensions<sup>42</sup>. In a  $0.5\ \mu\text{m} \times 0.22\ \mu\text{m}$  waveguide, neglecting orientation changes, the two forces approximately have the same value at  $\beta_{rp} = 5\ \text{pN}/\mu\text{m}/\text{mW}$ , analytically computed in [150], on the vertical walls of the waveguide. We can

---

<sup>41</sup> As this force is extracted from the Maxwell Stress Tensor (MST), we consider that the optical gradient force is merged in this radiation pressure denomination.

<sup>42</sup> Interestingly, both can cancel out in certain materials [150].

write  $g_{O \rightarrow M_{rp}} = \beta_{rp} \times 2\pi R$ . This gives for our 10  $\mu\text{m}$  radius cavity  $g_{O \rightarrow M_{rp}} = 3.1 \times 10^{-7}$  N/W. Typical power modulation in our rings is about  $\Delta P_{stored} = 50$  mW<sup>43</sup>, leading to an overall  $\Delta F_{opt} \approx \Delta F_{es} \approx \Delta F_{rp} = g_{O \rightarrow M_{rp}} \times \Delta P_{stored} = 16$  nN. For a typical ring of  $k_{eff} = 40$  kN/m (reduced value at the location of the tip) and  $Q_m = 1\,000$  in air, those forces give rise to a  $\Delta z = \Delta F_{opt} \times \frac{Q_m}{k_{eff}} = 400$  pm resonance. Values given in this paragraph are rough magnitude orders as they are based on analytical values.

To resume, radiation pressure and electrostriction may be the main optical actuation phenomena at frequencies over than 100 MHz, and they are expected to induce resonance amplitudes of about 400 pm. But another integrated actuation was designed to actuate the mechanical motion: the capacitive one.

#### II.4.3 Capacitive/electrostatic actuation of the mechanical motion

Even if optical actuation should work, and it does *a fortiori*, a more classic and well known actuation was planned as a back-up: capacitive, or electrostatic actuation. As it provides an optically-independent excitation, it allows to suppress possible cross-talk between actuation and detection. In our OM probe design, it is provided via large electrodes that circle the ring (Figure 51).

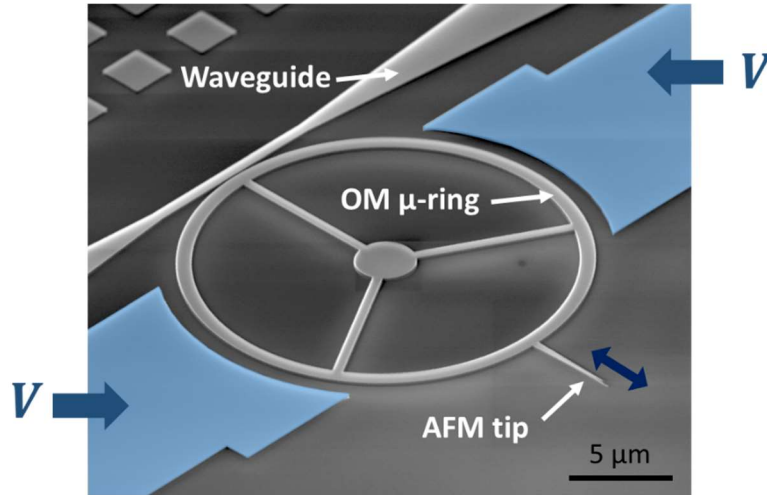


Figure 51: Colored SEM image of an OM probe. In blue are highlighted the conductive electrodes from which is applied the voltage  $V$ .

The force between two surfaces of area  $S$  separated by a gap  $d$  with a voltage difference  $V$  can be written:

$$F_{elec} = -\frac{1}{2} \frac{\epsilon_0 S}{d^2} V^2 \quad (34)$$

To drive the vibration, one can modulates the voltage. The squared voltage allows one to actuate using a modulation at either  $f_m$  or  $f_m/2$ . Indeed, taking  $V = V_{DC} + V_{AC} \cos(\omega_{mod} t)$ , we have:

<sup>43</sup> Power circulating in our rings is about 0.13 W (see Appendix I:), with an input modulation of about 30 %.

$$F_{elec} = -\frac{\epsilon_0 S}{2d^2} \left[ V_{DC}^2 + 2V_{DC}V_{AC} \cos(\omega_{mod}t) + \frac{V_{AC}^2}{2} (1 + \cos(2\omega_{mod}t)) \right] \quad (35)$$

The  $f_m/2$  modulation thus gives forces on the order of  $F_{elec} = -\frac{\epsilon_0 S V_{AC}^2}{2d^2}$ , which gives

$F_{elec} = 1.4$  nN for a  $S = 7 \times 10^{-12}$  m<sup>2</sup> electrode surface with a  $d = 1$  μm gap and a  $V_{AC} = 10$  V electric potential. This force giving rise to a resonance amplitude of the order of  $A = F_{elec} \times \frac{Q_m}{k_{eff}} = 35$  pm<sup>44</sup>.

Compared to optical actuation, it can easily be raised by decreasing the capacitive gap  $d$  and amplifying the exciting signal. To raise optical actuation magnitude, one would need a higher laser power or a higher  $Q_{opt}$ . However it induces more losses as it triggers non-linear effects (see 2PA).

#### II.4.4 Optomechanical coupling model

To better grasp how mechanical and optical resonators are interconnected, we inject the optomechanical coefficients  $g_{O \leftrightarrow M}$  in the optical resonator equation and the mechanical spring-mass model. Injecting the  $g_{O \leftarrow M}$  factor as a frequency shift in optical cavity and the  $g_{O \rightarrow M}$  factor as a force in the mechanical resonator, we find the coupled optical and mechanical equations<sup>45</sup>:

$$\dot{a} = -\left(\frac{\gamma_{tot}}{2}\right) a + i(\omega_{laser} - \omega_{cav} + 2\pi g_{O \leftarrow M} z) a + \sqrt{\gamma_e} \sqrt{P_{in}} \quad (36)$$

$$m_{eff} \left[ \ddot{z} + \frac{\omega_m}{Q_m} \dot{z} + \omega_m^2 z \right] = g_{O \rightarrow M} |a|^2 / T_0 \quad (37)$$

Where  $g_{O \leftarrow M}$  is in Hz/m and assuming  $g_{O \rightarrow M}$  is the sum of  $g_{O \rightarrow M, rp}$  and  $g_{O \rightarrow M, es}$  in N/W.  $T_0$  is the time for a photon to complete a lap in the cavity in seconds, giving us  $P_{stored} = |a|^2 / T_0$ . In equation (37), thermomechanical forces were neglected for clarity. One can note that higher order effects are neglected. To account more precisely for thermal effects, a third coupled thermal equation was used in the literature (p. 18 in [127]), we chose to account for thermal effects only in the  $g_{O \rightarrow M}$  coefficient.

**Note:** Even in the framework of a ring coupled to a straight waveguide, many set-up configurations allow exciting/retrieving mechanical motion via the optical signal. We used optical power modulation upstream of the ring to excite its movement and electrical demodulation downstream. Phase modulation can also be used for the read-out [151][152] in a Pound-Drever-Hall (PDH) fashion, *a priori* improving the optical read-out bandwidth<sup>46</sup>.

The top part of the equation means that the cavity's optical resonance wavelength varies with the cavity motion as pictured in Figure 49.

<sup>44</sup> Here, we assumed the  $\Delta z \times k_{eff}$  product is constant over the interaction surface.

<sup>45</sup> We consider the coupling factor fixed and in particular not dependent on the motion as the motion up to 10 pm observed in our device is negligible over the coupling gap (distance between cavity and waveguide) of more than 100 nm.

<sup>46</sup> Considering the optical read-out bandwidth:  $f_{opt}/Q_{opt} = c/\lambda_0 Q_{opt}$ .

### 11.4.4.1 Optical dynamical effects and feedback

As excitation and sensing are done through the same optomechanical transduction as shown in Figure 50, the system can be considered a feedback system. Effects named optical dynamical back-action [103][108], optical spring [153][154], side-band cooling [103][113] or self-oscillation ([103] and p. 20 in [127]) may thus rise. These feedback effects significantly appear when optical forces are large enough and delayed enough to be out of phase from the motion. In other words when  $f_m \approx \frac{f_{opt}}{Q_{opt}}$  or even gets superior  $f_m > \frac{f_{opt}}{Q_{opt}}$  and when optical power in cavity is high enough<sup>47</sup>. A simple explanation of the rise of these effects is given in Figure 52 but they can also be explained in the frequency domain [155].

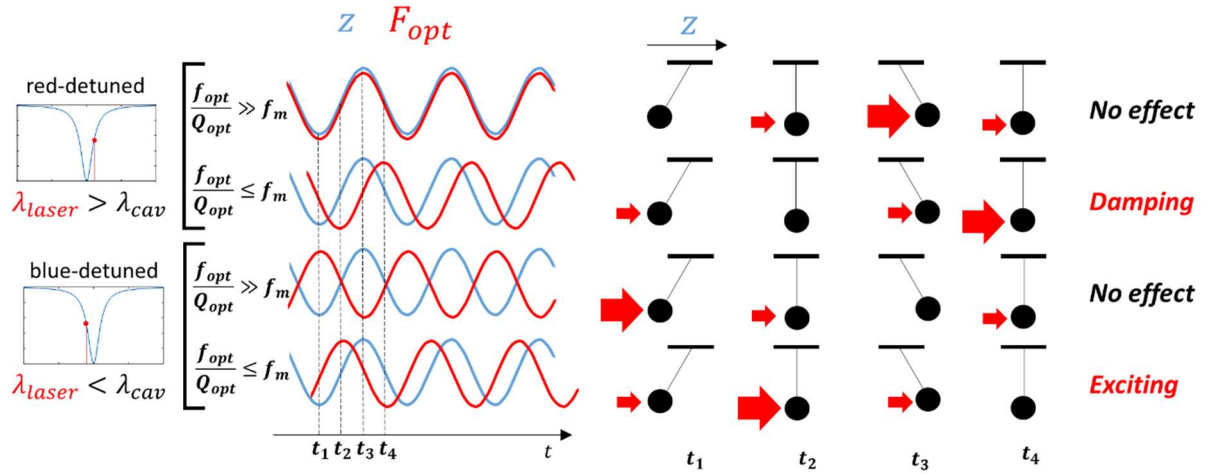


Figure 52: Scheme explaining exciting and damping effects of optical back-action for blue and red detuning using the swing picture. In the red-detuned regime, a cavity length increase induces a higher power circulating in the cavity,  $z$  and  $F_{opt}$  are thus in phase.

When  $Q_{opt}$  is so large that  $\frac{f_{opt}}{Q_{opt}} \leq f_m$ , the optical forces accumulate a phase shift and their amplitude is lowered. Thus, their work change from “no effect” to “damping” in red-detuned configuration or “exciting” in blue-detuned configuration. A quantitative calculation of the retardation and amplitude are given for GaAs structures p. 46 in [123].

Quickly put, when the laser injected in the cavity is blue-detuned (*i.e.*  $\lambda_{laser} < \lambda_{cav}$ ), the OM feedback effect increases the mechanical frequency (added optical spring) and amplifies the motion. When the laser injected in the cavity is red-detuned (*i.e.*  $\lambda_{laser} > \lambda_{cav}$ ), it decreases the mechanical frequency (negative optical spring) and damps the motion (Figure 53).

<sup>47</sup> In this case we consider that the delay (between optical forces and motion) is induced by the optical quality factor of the cavity. This effect would also rise for an actuation delay for example taking thermal expansion excitation with a time constant comparable to  $1/f_m$ .

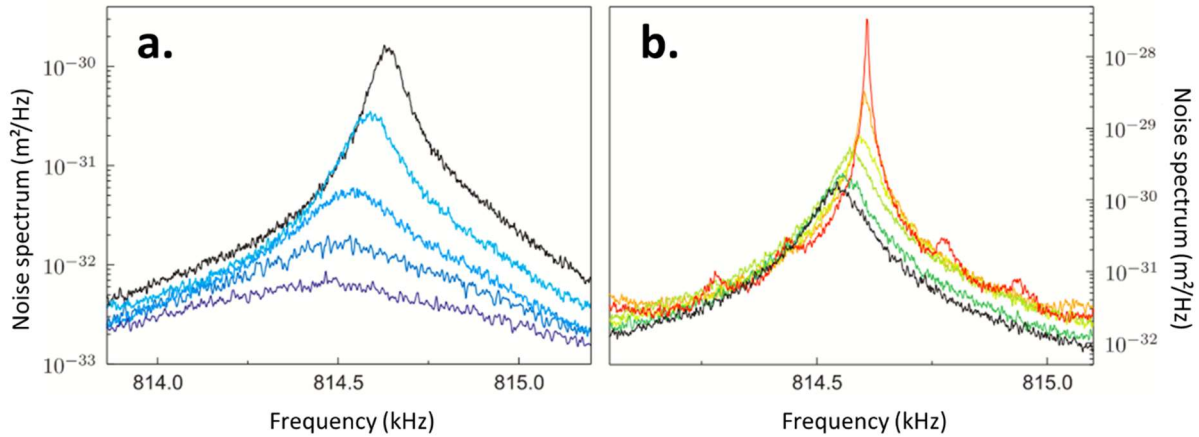


Figure 53: Mechanical noise spectra varying the laser detuning to the optical cavity. **(a)** When the laser is red-detuned\*, *i.e.* when  $\lambda_{laser} > \lambda_{cav}$ , the motion is damped and frequency is lowered, from the black curve, detuning is increased. **(b)** When the laser is blue-detuned, *i.e.* when  $\lambda_{laser} < \lambda_{cav}$ , the motion is excited and frequency increases. Black curves have the same amplitude in both graphs. \*blue and red detuning refers to the visible light spectrum. From p. 201 in [110].

From an AFM, mechanical oscillator perspective, this phenomenon allows one to tune the  $Q_m$ , and with a much lower amplitude the  $k_{eff}$ , of an OM AFM probe.

This optomechanical effect, changing the mechanical frequency, is to be distinguished from the temperature coefficient of frequency (TCF) effect. When laser light is injected and absorbed in the ring, the ring heats up. This heating changes the materials' Young modulus, which changes the resonator's overall  $k_{eff}$  and induces a mechanical frequency shift. In silicon resonators, this TCF is about: -30 ppm/K [156]. This negative value means that the frequency will diminish with increasing temperature (induced by increasing laser power injected) and acts thus opposite to the optical back-action effect seen above, as we work only in blue detuning (see Sec. II.4.4.1). From experimental characterization, we will observe that this last effect is dominant over optical spring (see Figure 69 in Sec. III.4.1).

## II.5 Force sensing/Contact operation model and considerations

Now that the OM probe behavior is clear, how will it mechanically react when brought to contact with a surface? Figure 54 displays what is expected from an OM probe. The considerations presented in this part can be applied to any AFM probe.

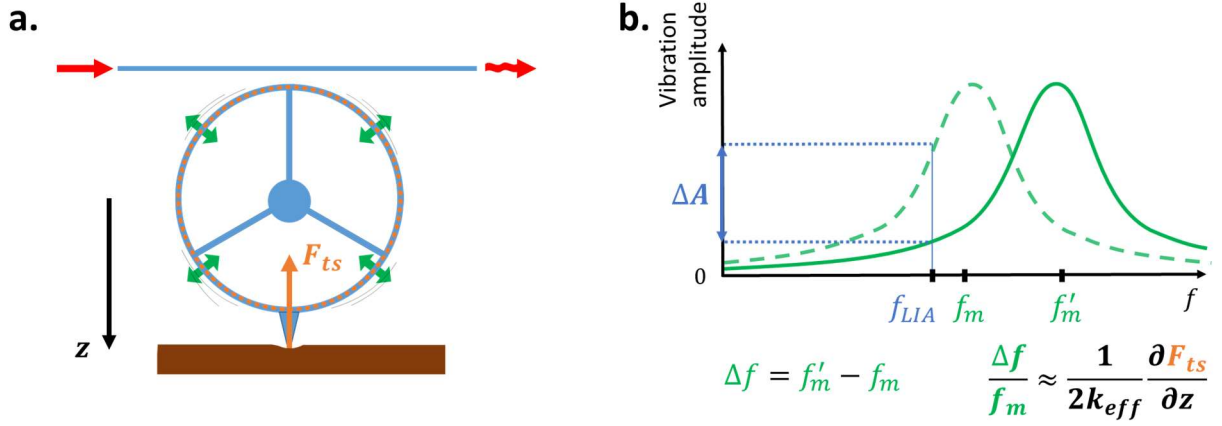


Figure 54: (a) Scheme of contact sensing by an OM probe. (b) Mechanical motion spectrum with no interaction (dashed) and when interacting with the surface (plain). This figure represents a purely elastic interaction, in reality, the resonance is damped and the peak appears flatter. The mechanical frequency shift carries the information on the force gradient felt.

To predict its behavior, applying the simplest contact model of the ones introduced in Sec. I.2.1, *i.e.* the spring plus viscous damping model (see Figure 120), to the damped harmonic oscillator formula, we find:

$$m \left[ \ddot{z} + \frac{\omega_m}{Q_m} \dot{z} + \omega_m^2 z \right] = \frac{g_{O \rightarrow M} |a|^2}{T_0} - k_{ts} z - c_{ts} \dot{z} \quad (38)$$

Where  $k_{ts}$  is the tip-sample added spring with regards to the probe and  $c_{ts}$  is the viscous damping coefficient associated with the contact. It can be re-written:

$$m \left[ \ddot{z} + \left( \frac{\omega_m}{Q_m} + \frac{c_{ts}}{m} \right) \dot{z} + \left( \omega_m^2 + \frac{k_{ts}}{m} \right) z \right] = g_{O \rightarrow M} |a|^2 / T_0 \quad (39)$$

We understand that in contact, the mechanical resonance will appear as damped and with a frequency shift: frequency increase for a repulsive force gradient and decrease for an attractive force gradient. The frequency shift can be re-written, via a limited development assuming  $k_{ts} \ll k_{eff}$  :

$$\Delta \omega_m = \omega'_m - \omega_m = \omega_m \sqrt{1 + \frac{k_{ts}}{m \omega_m^2}} - \omega_m \approx \omega_m \left( 1 + \frac{k_{ts}}{2k_{eff}} \right) - \omega_m = \frac{\omega_m k_{ts}}{2k_{eff}} \quad (40)$$

Knowing the frequency shift, one can thus retrieve the force gradient added to contact:

$$k_{ts} = \frac{2k_{eff}}{\omega_m} \Delta \omega_m = \frac{2k_{eff}}{f_m} \Delta f_m \quad (41)$$

In a similar fashion, one can retrieve the viscous damping associated with contact reading the new quality factor  $Q'_m$ :

$$c_{ts} = m_{eff} \left( \frac{\omega'_m}{Q'_m} - \frac{\omega_m}{Q_m} \right) = 2\pi m_{eff} \left( \frac{f'_m}{Q'_m} - \frac{f_m}{Q_m} \right) \quad (42)$$

Note: To avoid near-field optical perturbations of the cavity when a sample is approached, the tip needs to be longer than 3 characteristic decay lengths of the electrical field outside the ring. Numerical simulations on Comsol software showed that for a tip longer than 3  $\mu\text{m}$ , the losses induced by the tip presence do not depend anymore on its length,  $Q_{opt}$  being limited by the width of it in a scattering manner.

Now that we understand by which mechanisms the optical signal actuates and senses the mechanical motion and its perturbation by a sample, we will now see in the next section how such a probe can be fabricated.

## II.6 Fabrication

The OM probes used in this thesis work were fabricated from SOI (silicon on insulator) wafers at CEA-LETI and IEMN, I did not took part in the batch fabrication steps listed in this section but rather in single device steps in Sec. IV.6.1. Two types of device were used:

- IEMN probes that were fabricated to obtain rapid preliminary results and verify the chosen designs.
- CEA-LETI probes were fabricated on a longer timescale (about 1 year) but with fewer uncertainties on the fabrication process, more OM probe designs and more integration capability.

In the next paragraph, the CEA-LETI fabrication process is presented. As the fabrication process is quite long with many steps, only the main steps are presented in the following.

### - **Step 0: SOI wafer**

The process starts with a Silicon On Insulator (SOI) wafer of diameter 200 mm. The SOI is a stack that consists of a crystalline silicon top layer (SiTop) of thickness 220 nm<sup>48</sup> and of orientation (100). This SiTop rests on a 1  $\mu\text{m}$ -thick silica layer: the Buried Oxide layer (BOx). The BOx itself rests on the Bulk silicon substrate of thickness 700  $\mu\text{m}$ .

### - **Step 1: Grating couplers etching**

First, a deep-UV photolithography forms the grating couplers. The grating couplers are what allows one to inject and collect light in and from the wafer with optical fibers, this is detailed in Sec. IV.6.2.

### - **Step 2: OM probe etching**

Then, a variable shape beam (VSB) electronic lithography forms the rings and the spokes. For the etching of the silicon rings, it is necessary that the roughness of the etched wall remains low, in order to attain high optical quality factors (under a few nanometers to reach  $Q_{opt}$  over 100 000).

### - **Step 3: Individual chips etching**

The wafer is then covered with a SiO<sub>2</sub> encapsulation layer to protect the silicon structures. It is cut to smaller wafers with a diameter of 3 inches for fabrication compatibility. Smaller

---

<sup>48</sup> Actually, some wafer had a 400 nm top silicon layer.



wafers are then etched using a Deep Reactive Ion Etching (DRIE) Bosch process, allowing a vertical cut, to form the AFM probe chip. This step is done at the IEMN, it is detailed in Sec. IV.6.1).

- **Step 4: OM probe liberation**

Then the BOx is etched so that the OM probe is able to move. The BOx etching is actually timed so that it frees the rings but spares the thinner pedestal allowing the ring to stand on the substrate (Figure 55). Etching of SiO<sub>2</sub> is performed by vapor HF (wet HF can also be used, as it is faster, but then a critical point drying is needed to prevent the rings sticking to the substrate).

- **Step 5: Optical fibers gluing**

Last, to optically address the OM probe, optical fibers are glued on top of the chip. This is detailed in Sec. IV.6.2.

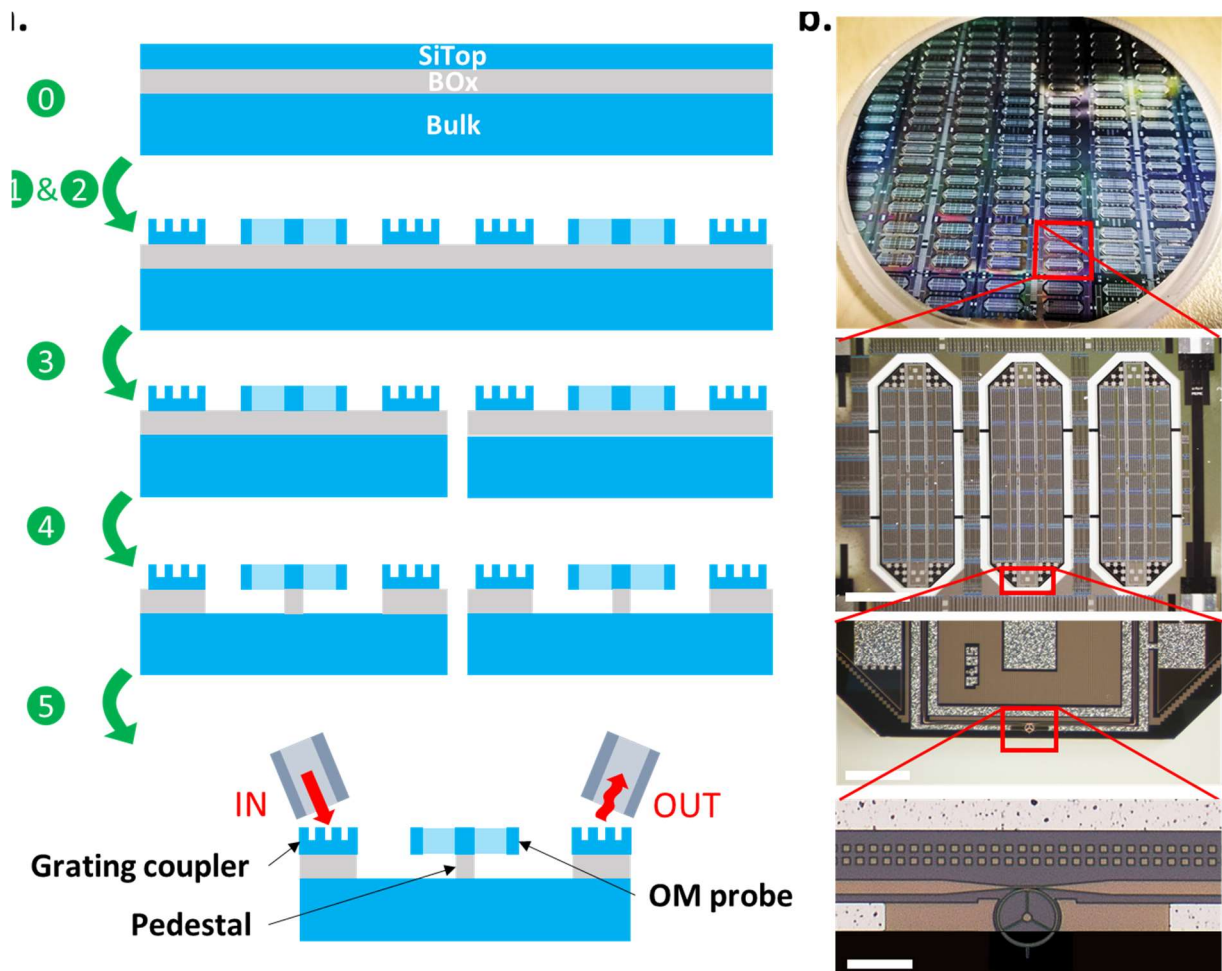


Figure 55: (a.) Scheme of the simplified fabrication process of an OM probe in a profile view. The fabrication steps are highlighted in green. (b.) Pictures of a wafer after step 4. The wafer has a diameter of 3" (or 7.62 cm). From top to bottom, the next picture features 3 OM probe chips. They still need to be detached from the "lace" wafer. The next two pictures are zoomed on the end of a chip in order to see the OM probe. The bottom picture is actually a photomontage as obtaining a protruding tip is still under developments (see Sec. IV.6.1). From top to bottom, the scale bars are respectively 1.6 mm, 130  $\mu$ m and 20  $\mu$ m long.

## II.7 Optomechanical figure-of-merit: towards the ideal OM probe

As in Sec. I.3.4, where a mechanical figure of merit was introduced (as a reminder it was  $BW/k_{ts\_lod}$ ), we define this time an optical and an OM figure-of-merit. As the motion is detected by the mechanically moving flank of the optical resonance, we want the more optical resonance displacement for a given displacement. That is to say the highest  $g_{O\leftarrow M}$ . To have the highest transmission change, one needs the highest optical resonance slope. That is to say the highest quality cavity  $Q_{opt}$  and the highest coupling contrast  $C$  (see Appendix H:). Lastly, we want the highest signal to be detected by the photodiode so the lowest injection loss<sup>49</sup>  $L_{oss}$  in the OM device. This gives us the optical figure-of-merit:

$$\mathcal{F}_{opt} = \frac{g_{O\leftarrow M} Q_{opt} C}{L_{oss}} \quad (43)$$

Multiplying this last optical figure-of-merit with the mechanical one in Sec. I.3.4, we find a figure-of-merit for dynamic AFM application of OM probes  $\mathcal{F}_{OM}$ :

$$\mathcal{F}_{OM} = \frac{g_{O\leftarrow M} Q_{opt} C}{L_{oss}} \times \frac{A f_m^{3/2}}{\sqrt{Q_m k_{eff}}} \quad (44)$$

In this chapter we defined the theoretical frame of the OM coupling. We introduced important parameters as the effective index  $n_{eff}$ , the optomechanical detection factor  $g_{O\leftarrow M}$ , the probe optical quality factor  $Q_{opt}$ , its contrast  $C$  and finally the frequency shift when in contact  $\Delta f_m$ . We seek to maximize the last four parameters to obtain the best OM probe performances. In the next chapter, and before AFM application, different designs of OM probes and set-ups are characterized to find optimal ones that maximize those parameters.

---

<sup>49</sup> Injection loss is the overall loss of optical power in the device. It includes coupling losses to the silicon chip and waveguide losses within it.



### III. Characterization of the optomechanical probe: set-up and performances

The expected behavior of optomechanical (OM) probes, from optics to mechanics, their coupling and lastly to contact sensing was described in the last chapter. In this one, we verify the expected behavior, comparing experimental characterizations to theoretical expectations. The OM probe optical and mechanical performances dependency on design and set-up is discussed according to characterization results.

#### **Optical characterizations:**

- The Coupled Mode Theory (CMT) is verified and its limits are discussed;
- The optical losses of the OM probe are quantified according to its design and the limiting loss mechanism is identified;
- Studying in details the doublet mode (CW and CCW), a new phenomenon is described: the super-mode.

#### **Mechanical characterizations:**

- Calibration of the motion is discussed and verified;
- Noise sources are investigated;
- 5 driving and sensing techniques are studied to get rid of background signal;
- Mechanical bandwidth of the probe is experimentally verified.

This chapter starts with the description of the set-up used for the characterization and then presents the characterization results obtained on different OM probes.

#### III.1 Optical characterization set-up

To assess optical performance of an OM probe, one needs a laser to inject light in the cavity and a photodiode to detect light exiting, carrying the mechanical information. A scheme of the typical set-up is shown in Figure 56. A polarization controller is present upstream of the probe to ensure the injected light has the polarization needed to be coupled in the ring. As the probe is on a silicon chip, light is injected from the laser via fibers either from the edge of the chip or the top. The end-user device have glued fibers on the top of the chip (device fabricated by the CEA-LETI) but for earlier device with cleaved facets, edge injection was used as no grating coupler was present (device fabricated by the IEMN) as can be seen in Figure 56.

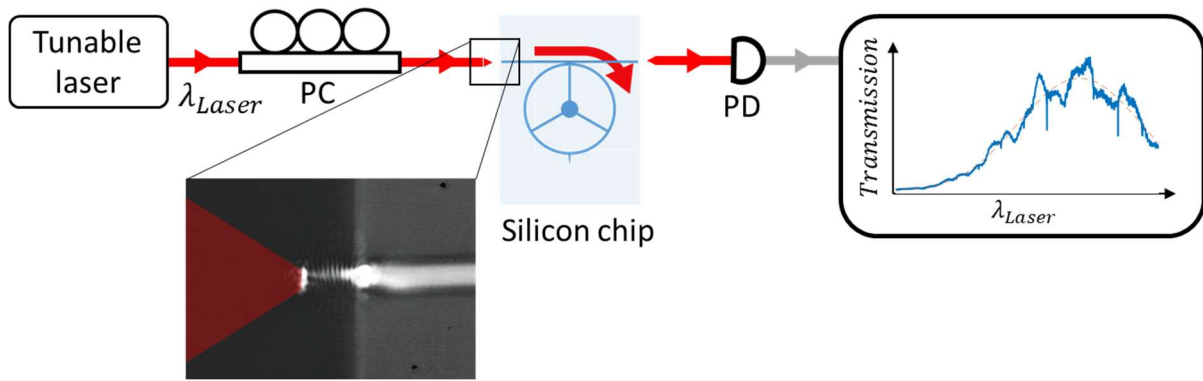


Figure 56: Simple experimental set-up to assess an optomechanical (OM) probe's optical performances. In red is the optical signal. PC: Polarization Controller, PD: Photodiode.

**Protocol:** First, one aligns the fibers in front of the waveguides<sup>50</sup> (edge injection) or grating coupler (top injection) in order to maximize the optical transmission. Then the polarization is varied to match the one of the waveguide, thus maximizing transmission. Looking at the transmission spectrum (Figure 57), one then chooses the best optical mode, that is to say the one with the highest slope (highest contrast times highest  $Q_{opt}$ ) and the highest transmitted power. To assess the mechanical behavior of the resonator, one then needs to place the laser close to the optical cavity resonance (in terms of wavelength), preferably in the blue-detuned regime if thermo-optic shift is present<sup>51</sup>.

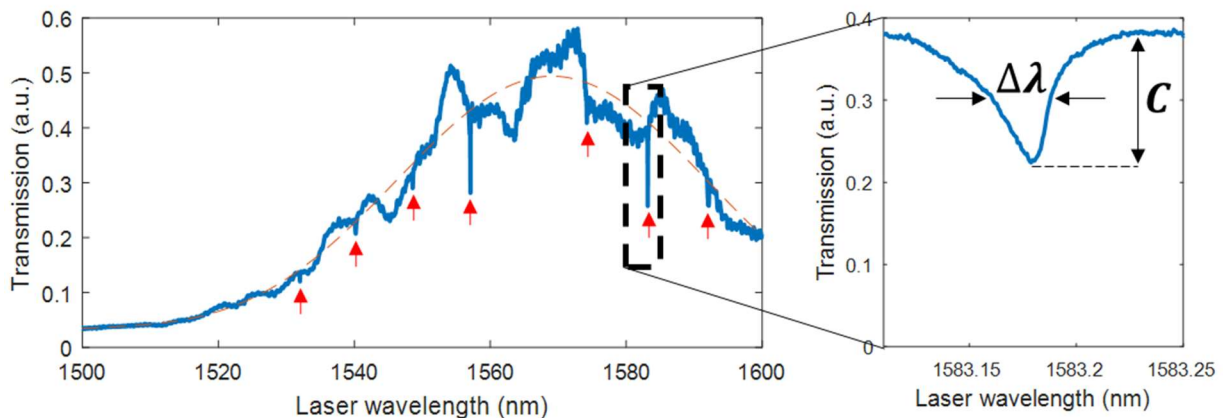


Figure 57: Optical transmission spectrum of an OM probe. (Left) The dashed red line is a Gaussian fit of the transmission, this Gaussian shape is characteristic of grating couplers. The optical resonances are marked with red arrows. (Right) Close-up of one optical resonance. One can extract the full width at half minimum (FWHM)  $\Delta\lambda = 22$  pm and the contrast  $C = 42$  %.

In Figure 57, the transmission appears noisy but when zooming one can observe oscillations. Those are due to the coupling to the optical fiber: a cavity appears between the fiber and chip causing this Fabry-Pérot effect (see Appendix G:). Comparing the optical resonance of this OM probe, namely its contrast  $C = 42$  % and width  $\Delta\lambda = 22$  pm, with other device having different waveguide-ring distance, we conclude that this OM probe was evanescently under-

<sup>50</sup> As a note, the first alignment can be rather long but as a result, it is rewarding.

<sup>51</sup> In this thesis work, the laser was always blue-detuned as thermo-optic effect was always there for mW laser powers.

coupled (see Figure 40). This transmission spectrum also verifies our assumption that the cavity is monomode as only azimuthal orders modes are seen (modes are evenly spaced). As a note, OM probe designs with a high enough optical quality factor unlike the one characterized here, the two degenerated CW and CCW modes can be resolved.

### III.2 Optical performances study

A systematic study of hundreds of OM device was performed<sup>52</sup> [157], enabling us to quantify the coupled-mode theory (CMT) and to evaluate the main optical loss source according to design dimensions.

#### III.2.1 Gap length influence on coupling

First we compared same-design device with varying gap distance  $d_{gap}$  (Figure 58a). From the transmission spectra, intrinsic and extrinsic quality factors (stemming from the FWHM  $\Delta\lambda$  and the contrast  $C$ , see Appendix H:) were extracted from each mode by fitting the transmission equation (29). Each optical mode dependency over gap distance was then analyzed separately by categorizing them by azimuthal order, *i.e.* wavelength.

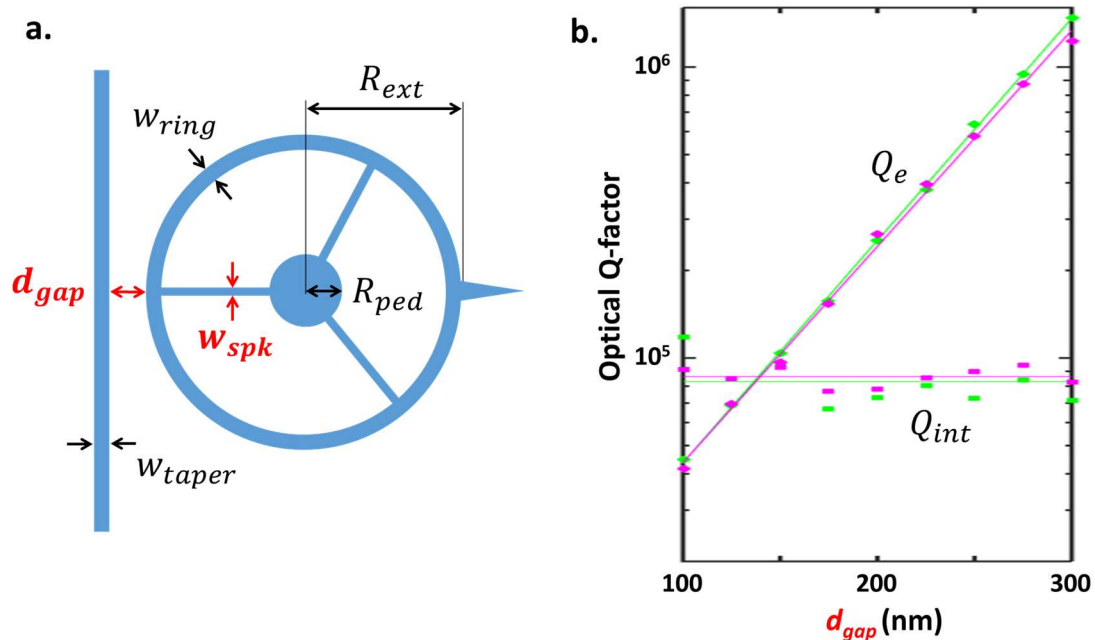


Figure 58: (a) Scheme of an OM probe highlighting important design dimensions. (b) Plot of the intrinsic  $Q_{int}$  and extrinsic  $Q_e$  quality factors for 2 different OM probes sets (green and pink) with varying gap distance  $d_{gap}$  (defined in (a)). As expected, the extrinsic quality factors decreases with decreasing gap distance, as the ring is more coupled to the waveguide. Where the line cross ( $Q_e = Q_{int}$ ) is the critical coupling, for our structure about 140 nm. One can observe that the extrinsic quality factor varies exponentially with gap distance. Actually, an incertitude on whether it is  $Q_e$  or  $Q_{int}$  remains, depending on the coupling regime chosen (see Appendix H:).

<sup>52</sup> The optical characterisations presented in this part are extracted from experiments conducted in CEA-LETI under automatic prober by Olivier Lemmonier and Philippe Grosse, then treated by Alexandre Fafin and Pierre Allain. It is important to note that these OM probes still have their Buried Oxide (BOx) layer, therefore changing the coupling and optical propagation in comparison with OM probes released in air.

We find an exponential dependency of the extrinsic quality factor over the gap distance (Figure 58b), understood as the evanescent optical field outside the waveguide and the cavity. The critical coupling  $Q_e = Q_{int}$  is reached for  $d_{gap} = 140$  nm. As a reminder, the critical coupling allows one to obtain the highest slope and thus the best optomechanical transduction.

However, in a more precise discussion on the limits of our CMT, our picture of a constant intrinsic quality factor cannot fully account for experiments. Indeed for small gaps (under 150 nm), we experimentally observed that some expected over-coupled modes displayed a full contrast, and thus were in the critical coupling regime. This behavior can be explained by a lowering of the intrinsic quality factors when the optical cavity is brought too close of the waveguide. We attribute this intrinsic quality factor decrease to two effects:

- Etch proximity effects: when small designs, in the 100 nm range, are patterned in the silicon layer via VSB lithography, distortions can appear in the geometries.
- Coupling proximity effects: the proximity of the waveguide disturbs (losses/coupling to other modes) optical cavity modes.

To overcome those proximity effects, one can decrease the waveguide and/or ring width to allow further coupling gap distances. Indeed, as seen in Figure 31 in Sec. II.2.1.3, the evanescent field extends further away when the width decreases. The former waveguide reduction might be more appropriate as decreasing the ring width tends to decrease the intrinsic quality factor which induces closer coupling distances.

As a consequence the effective highest slope, *i.e.* the maximum  $Q_{opt} \times C$ , is obtained in under-coupled regime. Experimentally, the maximum  $Q_{opt} \times C$  is approximately reached for a contrast of about 50 % (and not 89 % as predicted by CMT). For typical designs used in this thesis work ( $w_{ring} = 500$  nm,  $w_{spokes} = 100$  nm,  $w_{tip} = 100$  nm displaying  $Q_{int} = 80\,000$ ) we obtained maximum  $Q_{opt} \times C$  products for gaps between 100 nm and 200 nm but for contrasts about 50 % (see Appendix A:).

### III.2.2 Spokes and tip width scattering effect

To quantify the scattering losses according to the width of the spokes, intrinsic and extrinsic quality factors of optical modes of OM probes with different spokes widths were compared.

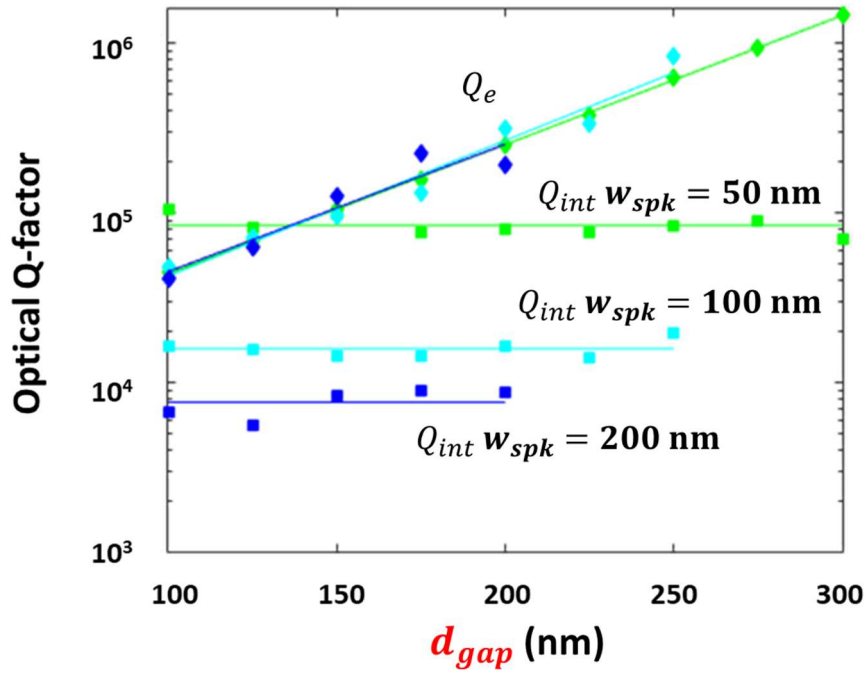


Figure 59: Optical intrinsic and extrinsic quality factors of different designs OM probes as a function of the gap distance. Each square represents an OM probe. The thinner the spokes, the higher the intrinsic quality factors.

The larger the tip and spokes, the more disruptive they are to the whispering gallery mode (WGM) through scattering losses. For  $w_{ring} = 500$  nm, the spokes width limit the  $Q_{int}$  from 50 nm onwards (Figure 59). But the scattering losses also depend on another design parameter: the ring width. For another dataset not shown here with  $w_{ring} = 750$  nm, the spokes limit the  $Q_{int}$  for widths of 100 nm and above. For a given spoke width, the spokes induce less losses for wide rings than for thinner rings. This discrepancy highlights the bouncing mode behavior (Figure 60).

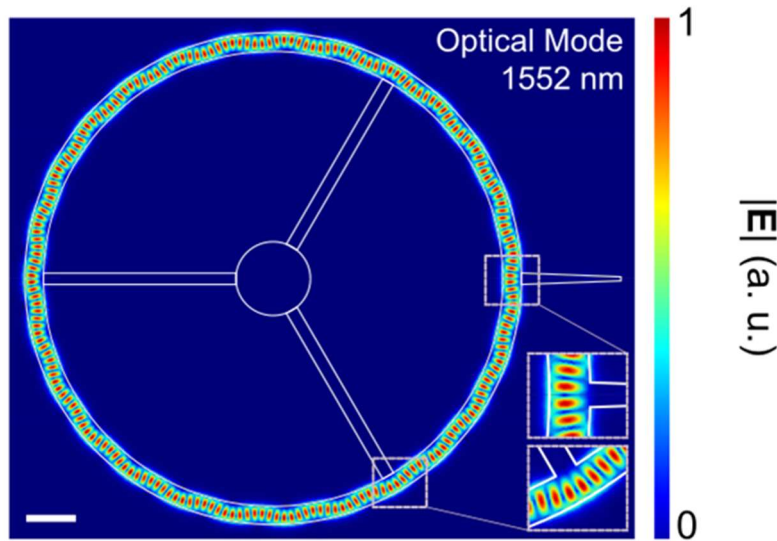


Figure 60: Optical simulation of a 10  $\mu\text{m}$ -radius OM probe. The cross-section of the waveguide is  $0.22 \mu\text{m} \times 0.75 \mu\text{m}$  and the spokes width is 500 nm. As the waveguide width is far over the single-mode width (233 nm), it displays a snake-like bouncing behavior, which allows the optical mode to avoid the spokes perturbation. Scale bar: 2  $\mu\text{m}$ .



Indeed, as  $w_{ring} = 750$  nm is far superior to the monomode condition ( $h_{monomode} = 233$  nm), the mode can distort in a bouncing fashion. It thus avoids the spokes, leading to less scattering and higher  $Q_{int}$ . Actually the monomode condition  $h_{monomode} = 233$  nm applies to a slab. For a 220 nm thick waveguide, the monomode condition on the width is about  $w_{ring} \approx 400$  nm.

### III.2.3 Losses beyond scattering, roughness or absorption?

From Figure 59, one can also extract the geometric scattering losses due to the spokes  $\alpha_{geom} = \frac{2\pi n_{eff}}{\lambda_0 Q_{int}}$ . For  $w_{spk} = 100$  nm, the intrinsic quality factor is  $Q_{int} = 15\,000$ , leading to  $\alpha_{geom} = 629$  m<sup>-1</sup>. For  $w_{spk} = 50$  nm, the intrinsic quality factor is  $Q_{int} = 85\,000$ , leading to  $\alpha_{geom} = 111$  m<sup>-1</sup>. This last value is similar to the upper bound of roughness losses value  $\alpha_{rough} \leq 207$  m<sup>-1</sup>, for a roughness  $\sigma_{rms} = 1$  nm (see Sec. II.2.3). This last comparison indicates that for small enough spokes, we could reach the roughness limitation. As a note, the 2PA limit is worth  $\alpha_{2PA} = 33$  m<sup>-1</sup> for 1 mW injected powers (see Sec. II.2.3), still negligible over scattering.

For a micro-disk cavity fabricated by the same laboratory (CEA-LETI), the intrinsic quality factor goes up to  $Q_{int} = 10^6$  [158]. This limitation was attributed to the roughness of the flanks. Hypothetically, for a ring without spokes, we thus expect a roughness limit  $Q_{int} = 500\,000$  (doubling of the rough surface with the inner face, assuming roughness limitation). This gives a loss constant  $\alpha_{rough} = 19$  m<sup>-1</sup>. The losses observed experimentally on our silicon rings do not go below 111 m<sup>-1</sup>, a value that we thus still attribute to geometrical scattering occurring at anchoring spokes.

### III.2.4 Study of doublet mode quality factor discrepancy due to symmetry

When  $Q_{int}$  is high enough (in the order of  $10^4$  for our structures), one can discriminate the co-existing clockwise (CW) and counter-clockwise (CCW) modes [159] in the structure (Figure 61). Those two propagating modes constructively interfere with themselves into 2 stationary modes. They are characterized by their own intrinsic  $Q$ -factor  $Q_{i1}$  and  $Q_{i2}$  and form a doublet in the transmission spectrum.

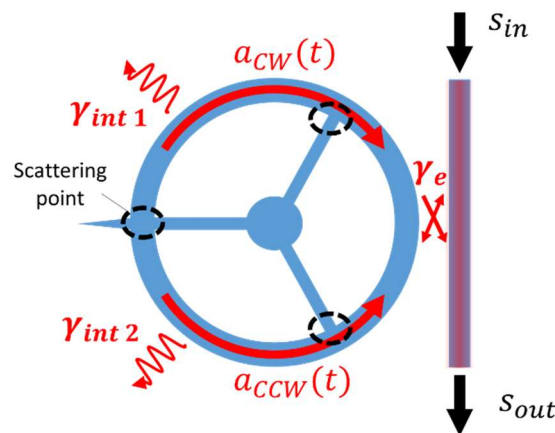


Figure 61: Scheme of the evanescent coupling of an OM probe when back scattering is taken into account, inducing a counter clockwise (CCW) mode to appear. This is the same scheme as in Figure 42.

We found that each 3 optical modes, one mode of the doublet as a higher quality factor than the other (Figure 62a).

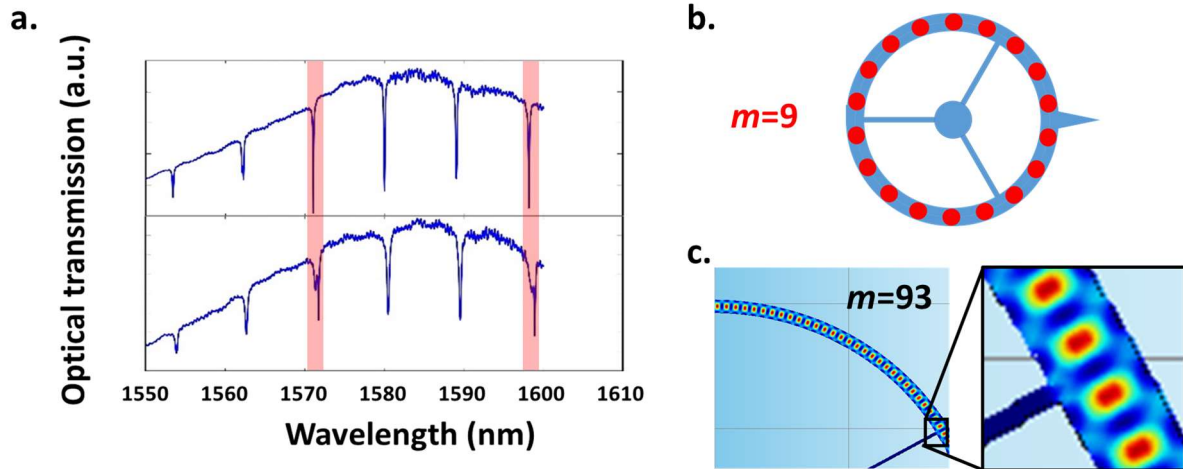


Figure 62 : (a) Optical spectrum of 2 different probes with 100 nm (top) and 200 nm (bottom) wide spokes. One can observe the doublet for each optical resonance and a discrepancy each 3 resonance. Those discrepancies are attributed to optical modes with azimuthal order multiples of 3. As can be seen on scheme (b), when the azimuthal order is a multiple of 3, one mode can exist with fields maxima out of the scattering regions. (c) FEM optical simulation of an OM probe featuring an optical mode of azimuthal order  $m = 93$ . For a zoom on the doublet, one can reach Figure 41 in page 61.

We actually reach a discrepancy as high as 2.3 between the two  $Q_{i1}$  and  $Q_{i2}$  (Figure 63a). We attribute this phenomenon to the configuration of the 3 anchoring spokes: an unbalance appears for the two modes of the doublet, assuming their mode profile is not the same. Indeed, when the azimuthal order  $m$  is a multiple of 3, for one mode of the doublet, the optical energy density is minimal at the intersection of the spoke and the ring. It thus is less scattered by the spokes (Figure 62b). For the other mode of the doublet, assuming a quarter-wavelength shifted mode profile, the energy density is maximal at the spokes inducing ample scattering. Those “super-modes” with  $m$  multiple of 3 are preferred to operate the mechanical resonators since their  $Q_{int}$  are the highest in this study (more than twice the average value) and thus offer a better transduction.

As a note, this phenomenon is only observable for spokes thin enough, under half of the effective wavelength  $w_{spk} \leq \frac{\lambda_0}{2n_{eff}} = 323 \text{ nm}$ .

This super-mode allows one to know each optical mode’s azimuthal order (Figure 63).

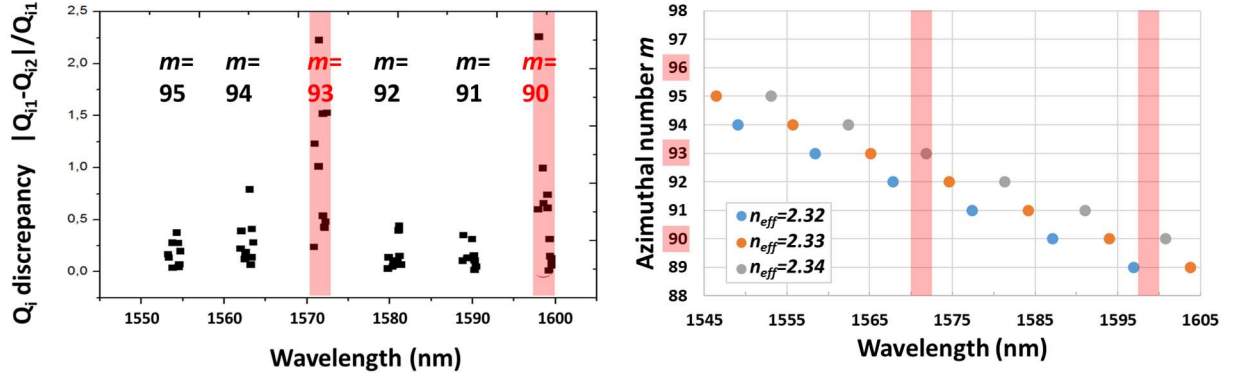


Figure 63: (a) Intrinsic quality factors discrepancy for 9 OM probes. On each probe, 6 optical modes are monitored. (b) Wavelength of optical modes given their azimuthal order and using equation (21). Each point is an optical mode. The effective index is varied, grey points are calculated with  $n_{eff} = 2.34$ , orange ones with  $n_{eff} = 2.33$ , and blue ones with  $n_{eff} = 2.32$ , those values being evaluated for a wavelength of  $1.6 \mu\text{m}$ . One can retrieve the azimuthal order of those modes with their wavelength as they are multiples of 3. The radius could also be varied to match the wavelength. However, it is well known with a 10 nm precision, insufficient to fit the modes. The effective index was thus varied to find the exact index of the OM probes. We find a 2.34 experimental effective index.

Thus one can estimate the exact value of the experimental effective index, here evaluated at  $n_{eff}(1.6 \mu\text{m}) = 2.34$ . This value is similar to the one calculated in Figure 30b:  $n_{eff}(1.6 \mu\text{m}) = 2.33$ , verifying the effective index estimation via Marcatili's method.

Now that optical characterization have been thoroughly discussed, the mechanical characterization is discussed.

### III.3 Mechanical motion calibration with Brownian motion

To quantify the amplitude of the mechanical motion of the OM probe, we relied on two techniques: calibration using the acquisition chain gains and calibration with the Brownian (or thermomechanical) motion. The former is detailed in Appendix E:. The latter is discussed here.

Even when no coherent drive is applied to the probe, it experiences thermal bath excitation or Langevin forces. The induced thermomechanical motion is amplified by the mechanical resonance.

On the one hand, as this phenomenon is non-coherent, it is a noise and limits the lowest motion detectable at room temperature. On the other hand, it provides a handy method to calibrate the motion detection. The equipartition theorem (equation 2 in p. 64 in [160]) applied to the potential energy of a mass-spring system gives us:

$$\frac{1}{2} k \langle z_{th}^2 \rangle = \frac{1}{2} k_B T \quad (45)$$

Where  $k$  is the spring's stiffness,  $z_{th}$  the thermally-excited motion of the mass,  $\langle \rangle$  the temporal average,  $k_B$  Boltzmann's constant and  $T$  the temperature.

One can therefore find the root mean square amplitude  $A_{th}$  of thermomechanical motion ( $A_{th} = \sqrt{\langle z_{th}^2 \rangle}$ ):

$$A_{th} = \sqrt{\frac{k_B T}{k_{eff}}} \quad (46)$$

This is the broadband value of the motion in meters, one can show (details in Appendix D:) that the motion's resonance spectrum looks like (neglecting other resonances):

$$NA_{th}(\omega) = \sqrt{\frac{4k_B T \omega_m}{m_{eff} Q_m \left[ (\omega_m^2 - \omega^2)^2 + \left( \omega \frac{\omega_m}{Q_m} \right)^2 \right]}} \quad (47)$$

$NA_{th}(\omega)$  being in  $m/\sqrt{\text{Hz}}$ .

Evaluated at the mechanical resonance  $\omega_m$ , we have:

$$NA_{th}(\omega_m) = \sqrt{\frac{2k_B T Q_m}{\pi k_{eff} f_m}} \quad (48)$$

This last formula is used to fit the mechanical noise signal, adding a noise floor to account for the most important flat noise source (either photodiode, laser, shot noise, see in next part).

As a note, this calibration method uses the FEM calculated stiffness of the probe  $k_{eff}$ , inducing uncertainty. This is unusual in AFM as sensitivity is often estimated first and then stiffness is estimated from thermal noise. Our method is closer to another AFM calibration where the stiffness is first estimated from the Sader method [161] and then the sensitivity is estimated from thermal noise.

Figure 64 presents a typical thermomechanical noise measurement set-up and its associated data in Figure 65.

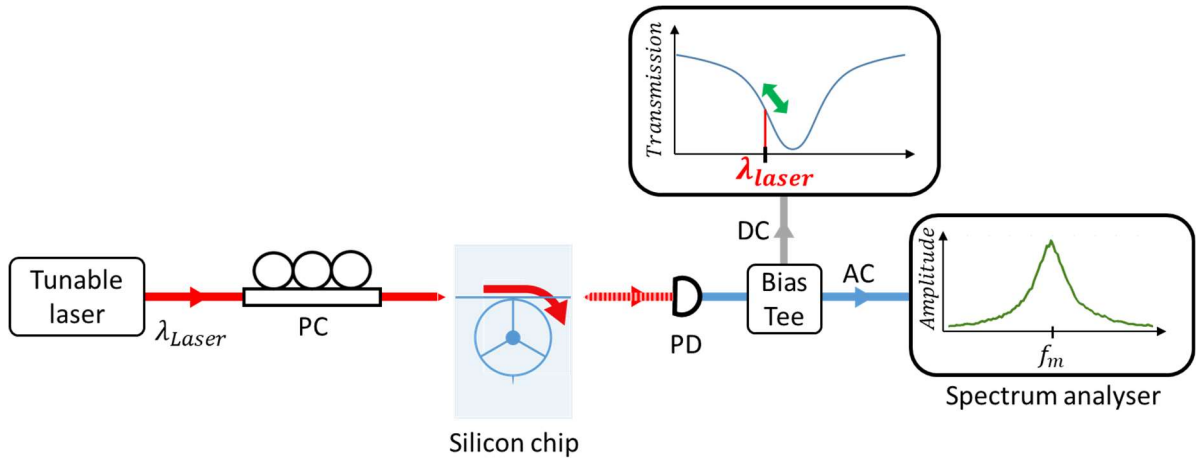


Figure 64: Experimental set-up to assess the thermomechanical motion of an OM probe. The green arrow represents the small thermally excited motion of the probe.

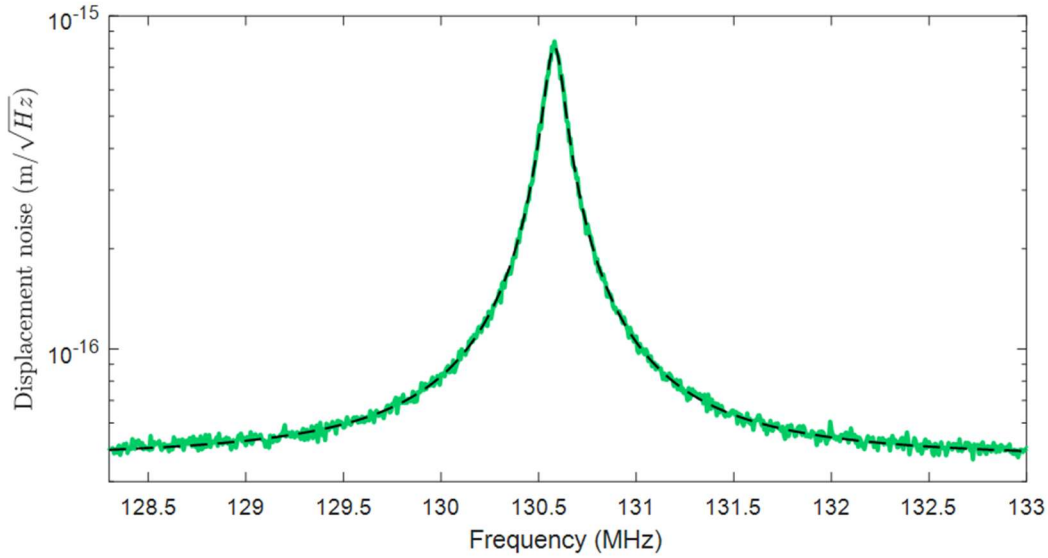


Figure 65: Thermomechanical motion of an OM probe in air. The value of the maximum is calibrated at  $8 \times 10^{-16} \text{ m}/\sqrt{\text{Hz}}$  given by equation (48), using a  $k_{eff} = 40 \text{ kN/m}$  given by FEM simulation. In dashed black is the fitted equation (47) with a noise floor of  $4.5 \times 10^{-17} \text{ m}/\sqrt{\text{Hz}}$  and a  $Q_m = 1330$ . More than that, the transmission signal, when transduced back to meters through the acquisition chain is in agreement with the theory via a 1.7 multiplication factor (see details in Appendix E:). This last agreement verifies the FEM  $g_{O \leftarrow M}$  calculation. The OM probe used for this measure is a S09B OM probe with a  $10 \mu\text{m}$  radius, a  $0.5 \mu\text{m} \times 0.22 \mu\text{m}$  cross-section,  $100 \text{ nm}$  wide spokes and tip and a  $2.5 \mu\text{m}$  pedestal diameter.

The thermomechanical motion is detected with a noise floor of  $4.5 \times 10^{-17} \text{ m}/\sqrt{\text{Hz}}$ . This value is comparative to state of the art GaAs disk [162], 2 orders of magnitude better than silicon disk in [163] and 3 orders of magnitude better than silicon disk in p. 126 in [164]<sup>53</sup>. It is limited by electrical thermal noise but highly dependent on the chosen laser power as detailed in next part.

All the graphs of this manuscript, in meter amplitude, are calibrated with this method.

### III.4 Noise/Stability

In this part we characterize the stability and noise of the instruments and of the OM probe itself, ignoring contact stability considerations (tip to surface) that we let for later. Having the OM-AFM goal in mind, the best force sensitivity and stability are required to image without damaging the sample and without distortions. We will identify the limiting device of our detection chain in noise operation and driven operation and the best operation point in laser power.

#### III.4.1 Detection noise

We compare how each instrument (Figure 66) contributes to the overall noise (shot noise, thermal noise, relative intensity noise, etc.) and compare it to experimental detection noise

<sup>53</sup> If the experimental detection noise is below the detected noise (which therefore is the thermomechanical noise), this value is highly dependent on the effective stiffness and thus the lumped model point. It is thus also highly dependent on the mechanical mode chosen.

values. A calculated graph then resumes each noise contribution. The experimental set-up is presented in Figure 66.

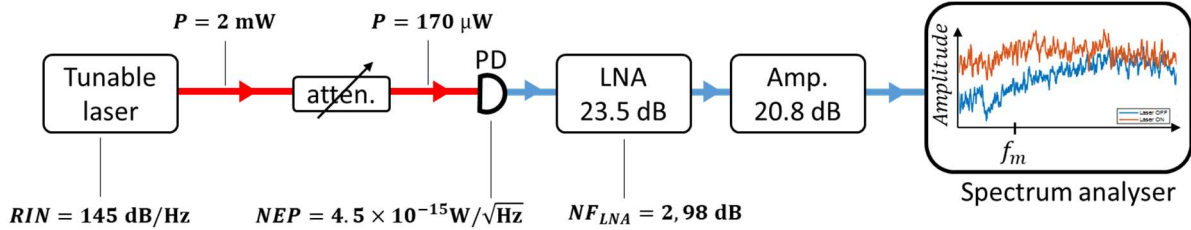


Figure 66: Scheme of the experimental set-up used for noise verifications. The variable attenuator is set to match the transmission of an OM probe, that is -11 dB (-4 dB per grating coupler plus the injection in the optical mode -3dB). LNA: Low noise amplifier.

In a similar fashion to what is described p. 94 in [164], each instrument is put ON from the last one to the first one (Figure 66). Figure 67 presents the last step of this procedure.

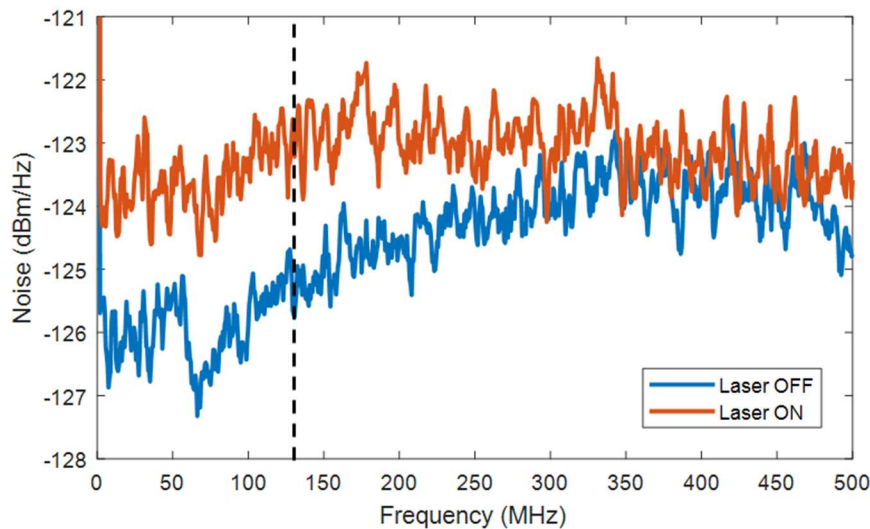


Figure 67: Power spectrum analysis of the detection chain. When the laser is ON, the initial noise floor (in blue) goes up (in orange). The dashed line is placed at 130 MHz, there the laser noise is 2 dB over the post-photodiode amplifier’s noise. The laser is thus not the main noise source but 1 dB under the noise coming from the amplifiers. This data was acquired with a 10 kHz bandwidth, point-averaged 16 times and was smoothed for better readability with a 5 points moving average. The experimental value at 130 MHz (around the mechanical frequency) are  $-125.2$  without and  $-123$  dBm/Hz with the laser ON.

The first noise to surpass the spectrum analyzer’s one is the amplified electrical thermal noise (blue curve in Figure 67). Then the photodiode adds no noise. Finally, we observe that the detected noise when laser is ON is higher of 2.2 dB (orange curve in Figure 67) over the amplified electrical thermal noise. From now we quantify each noise source. In this section and only in this section, we will consider the transmitted laser power  $P_{laser}$ .

We studied 5 noise sources<sup>54</sup>:

- Electrical thermal noise before the LNA (Johnson)
- Laser relative intensity noise (RIN)
- Laser shot noise
- PD noise-equivalent power (NEP)
- PD current shot noise (Schottky)

#### III.4.1.1 Thermal noise (Johnson)

When the laser is OFF, the detection noise at 130 MHz is limited by the thermal noise of the PD current in our setup. The thermal agitation of the electrons provides a noise floor that is amplified by the LNA. Its value is given by  $S_{thermal} = k_B T$ . For a 20°C temperature, it yields  $S_{thermal} = 4.0 \times 10^{-21}$  W/Hz (or -174 dBm integrated on a 1 Hz BW). Here we talk of electrical Watts.

The power spectrum read by the spectrum analyzer  $S_{thermal\_amp}$  takes the amplification into account:

$$S_{thermal\_amp} = S_{LNA_{out\_dB}} + G_{amp.} = S_{thermal} + G_{LNA} + NF_{LNA} + G_{amp.} \quad (49)$$

Where  $S_{LNA_{out}}$  is the output of the LNA,  $S_{thermal}$  is in dB,  $G_{LNA}$  and  $G_{amp.}$  respectively are the LNA and the second amplifier gains in decibels and NF is the noise factor of the LNA. Here the noise factor of the 2<sup>nd</sup> amplifier is not considered as the amplified noise of the first is well above the thermal noise at the 2<sup>nd</sup> amplifier input. Using values of Figure 66, it comes  $S_{thermal\_amp} = -126.7$  dBm/Hz.

#### III.4.1.2 Laser relative intensity noise (RIN)

The Laser power-spectral-density noise  $S_{laser}$  [W<sup>2</sup>/Hz], here talking of optical watts, is given by the RIN:

$$S_{laser}(P_{laser}) = P_{laser}^2 \times 10^{\frac{-RIN}{10}} \quad (50)$$

From our laser (see C.1.1 in Appendix C:), the RIN at 100 MHz is 145 dB/Hz.

The laser power spectral density of the laser is transduced to electrical power spectral density  $S_{laser\_PD}$  [W/Hz] by the PD through its responsivity  $R_{esp}$  [A/W]:

$$S_{laser\_PD}(P_{laser}) = S_{laser}(P_{laser}) \times R_{esp}^2 \times r \quad (51)$$

With  $r = 50 \Omega$  being the photodiode output impedance.

The power readout by the spectrum analyzer  $S_{laser\_after\_PD\_amp}$  [dBm/Hz] is amplified by an exact 44.3 dB amplification (see Figure 66), giving at last:

$$S_{laser\_PD\_amp}(P_{laser}) = 10 \log \left( S_{laser\_PD}(P_{laser}) \right) + 30 + G_{LNA} + G_{amp.} \quad (52)$$

---

<sup>54</sup> And neglected laser wavelength fluctuations, light polarization fluctuations and EOM fluctuations.

#### III.4.1.3 Laser shot noise

The laser optical shot noise  $S_{shot}$  [ $W^2/Hz$ ], due to particle behavior of light, is given by:

$$S_{shot}(P_{laser}) = 2h_p f_{laser} P_{laser} = \frac{2h_p c P_{laser}}{\lambda_{laser}} \quad (53)$$

Where  $h_p$  is the Planck constant and  $\lambda_{laser}$  the laser wavelength.

The amplified noise on the spectrum analyzer is similarly in [dBm/Hz]:

$$S_{shot\_PD\_amp}(P_{laser}) = 10\log(S_{shot}(P_{laser})R_{esp}^2 r) + 30 + G_{LNA} + G_{amp}. \quad (54)$$

#### III.4.1.4 PD NEP noise

The noise equivalent power our PD, given by the manufacturer is  $NEP = 4.5 \times 10^{-15} W/\sqrt{Hz}$  in optical Watts, this gives a flat output noise  $S_{PD\_NEP}$  of, in W/Hz:

$$S_{NEP} = NEP^2 \times R_{esp}^2 \times r \quad (55)$$

The calculated value  $S_{NEP} = 1.0 \times 10^{-27} W/Hz$  (or -193 dBm integrated on a 1 Hz BW) is negligible over the other contributions and in particular over Johnson noise at -174 dBm.

#### III.4.1.5 PD shot noise (Schottky)

The electrical shot noise  $S_{Schottky}$  [W/Hz], due to electrons, is given by:

$$S_{Schottky}(I) = r \times 2 \times e \times I \quad (56)$$

Where  $r$  is the PD output impedance  $r = 50 \Omega$ ,  $e$  is the electron charge and  $I$  is the PD output current, proportional to laser power  $I = R_{esp} P_{laser}$ .

The amplified noise on the spectrum analyzer is similarly in [dBm/Hz]:

$$S_{Schottky\_amp}(P_{laser}) = 10\log(2reR_{esp}P_{laser}) + 30 + G_{LNA} + G_{amp}. \quad (57)$$

If we plot all those noises versus laser power coming onto the photodiode we find:



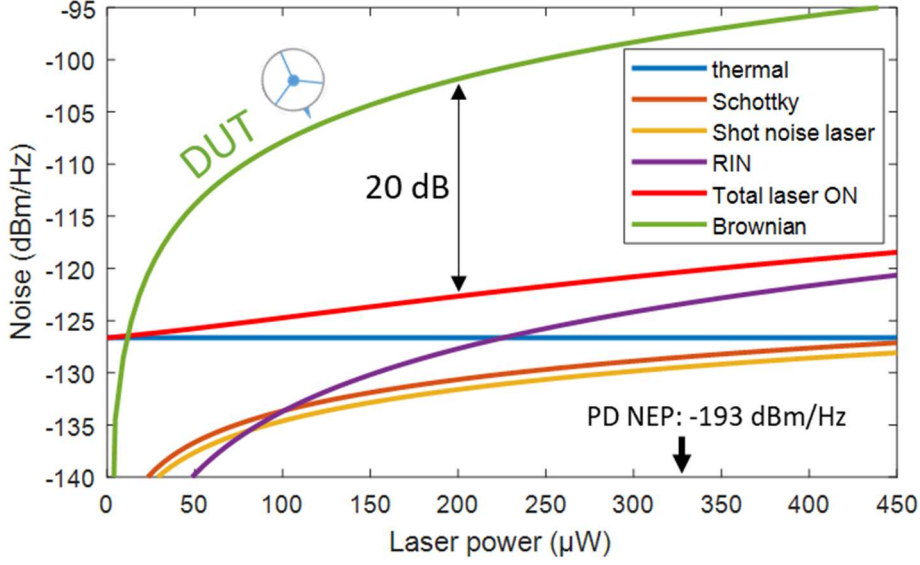


Figure 68: Graph of the calculated noise sources of the detection set-up according to laser transmitted power (power read on the photodiode, not the injected laser power). The noise is calculated at the spectrum analyzer input. For low laser powers, thermal noise after the photodiode is the limiting noise. However for higher laser powers ( $>150 \mu\text{W}$ ), the relative intensity noise of the laser takes over. For the Brownian signal calculation, a  $k_{eff} = 40 \text{ kN/m}$  probe was chosen with  $f_m = 130 \text{ MHz}$ ,  $Q_m = 1000$ ,  $g_{O \leftarrow M} = 7.7 \text{ GHz/nm}$ ,  $\lambda_{opt} = 1.55 \mu\text{m}$ ,  $C = 50 \%$ ,  $Q_{pt} = 38750$ . Its formula can be found in equation (59).

From Figure 68, we find that the electrical thermal noise (blue curve) dominates for low laser power and then the RIN (purple curve) takes over around  $225 \mu\text{W}$ . Assuming the device's transmission is  $-11 \text{ dB}$  and the injected laser power  $2 \text{ mW}$ , typical values used in experiments, our operating point is  $170 \mu\text{W}$  where thermal noise dominates. At  $150 \mu\text{W}$  (the value chosen in Figure 67), the total laser OFF and total laser ON signals are worth respectively  $-125.4 \text{ dBm}$  and  $-123 \text{ dBm}$ , in agreement with the experiment at  $-125.2 \text{ dBm}$  and  $-123 \text{ dBm}$ . The small discrepancy ( $0.2 \text{ dB}$ ) can be caused by temperature rise, higher amplifier gains, a LNA higher noise factor and spectrum analyzer noise around  $-145 \text{ dBm}$ .

This detection noise is to be compared with what we want to detect: motion of the probe limited by its thermomechanical noise (green curve in Figure 68).

The motion of the probe is given by transducing the thermomechanical motion noise maximum  $NA_{th}(\omega_m)$ , given by equation (48), using the  $g_{O \leftarrow M}$  [Hz/m] and the optical resonance slope [W/Hz]:

$$S_{th-m}(P_{laser}) = NA_{th}(\omega_m) \times g_{O \leftarrow M} \times \frac{\lambda^2 P_{laser}}{c \Delta \lambda} \quad (58)$$

Where  $S_{th-m}$  is in  $\text{W}/\sqrt{\text{Hz}}$ ,  $g_{O \leftarrow M} = 7.7 \text{ GHz/nm}$ ,  $\lambda_{opt} = 1.55 \mu\text{m}$ ,  $C = 50 \%$  and  $\Delta \lambda = 40 \text{ pm}$  i.e.  $Q_{opt} = 38750$ .

Taking the photodiode and amplifiers in account, we have on the spectrum analyzer, in dBm:

$$S_{th-m\_amp}(P_{laser}) = 20\log\left(S_{th-m}(P_{laser}) \times \frac{1}{R_{esp}} \times \frac{1}{\sqrt{r}}\right) + 30 + G_{LNA} + G_{amp}. \quad (59)$$

To verify this last formula, giving the thermomechanical motion maximum, we plot the spectrum of the thermomechanical noise for increasing laser powers  $P_{laser}$  (Figure 69a).

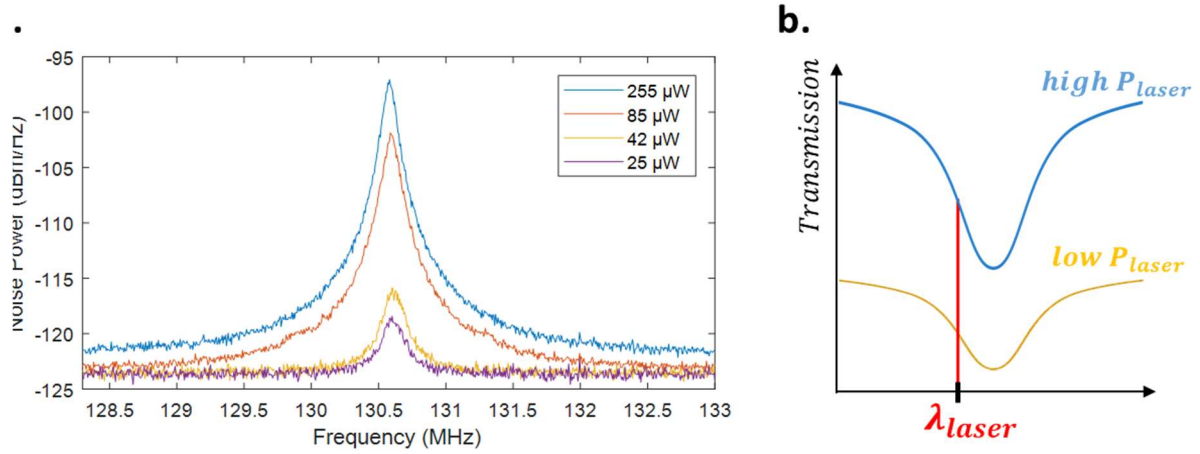


Figure 69: (a) Thermomechanical motion of the OM probe with different transmitted laser power. (b) Scheme of optical transmission for high laser power in blue and low laser power in yellow. For low laser powers, electrical thermal noise limits the observation of the Brownian motion. For higher laser powers ( $\geq 85 \mu\text{W}$ ), looking at the noise floor, the laser noise becomes predominant over the electrical thermal one. For higher laser powers, the Brownian motion is also better transduced as the optical slope is steeper (scheme b). For the detailed explanation and transduction formula, see Appendix E. However, one can observe that this better transduction is not exactly following the Brownian tendency as in Figure 68. This can be explained by not the same detuning for each curve, as detuning was not carefully checked in this experiment. Another observation can be made out of this curve: the mechanical resonance frequency is slightly lowered as more power is injected in the ring. This indicates that the TCF has greater impact on frequency than optical back-action (that only has a frequency increase effect when blue-detuned). From the frequency shift, we estimate the temperature increase at 10 K for the 255  $\mu\text{W}$  transmitted laser power.

We verify that the more laser power is injected in the device, the more transduced is the mechanical motion, as is intuitively deduced from Figure 69b.

To conclude this part, the highest laser power is preferred to surpass the electrical thermal noise and to improve optomechanical transduction. Our detection noise is limited by either the thermal noise or the laser relative intensity noise depending on the laser power. Typically, our detection noise  $N_{Z_{det}}$  is more than 20 dB under the thermomechanical noise  $N_{Z_{th}}$ . Typical values are  $N_{Z_{th}} = 7 \times 10^{-16} \text{ m}/\sqrt{\text{Hz}}$  and  $N_{Z_{det}} = 4.5 \times 10^{-1} \text{ m}/\sqrt{\text{Hz}}$ . This detection noise is two decades under any AFM probe detection noise (see Table 2).

To perform dynamic AFM, one needs to operate in the driven regime of the mechanical resonator so to actuate it. In the next part we study its drifts while actuated.

### III.4.2 Stability and drifts

As a force-gradient sensor in dynamic AFM, the OM probe recorded output is its frequency, as shown in Sec. II.5. Its frequency stability thus determines the force-gradient resolution of the OM probe. This resolution, associated with the frequency stability, can be assessed for different integration times depending on measurement speed requirements. To assess the OM probe's frequency stability, we used the Allan deviation. Noting  $y = \Delta f/f$  the normalized relative frequency shift and  $N = T/\tau$  the number of sub-groups (green squares in Figure 70) with  $T$  the time trace duration, the Allan deviation can be written [165]:

$$\sigma_y(\tau) = \sqrt{\frac{1}{2(N-1)} \sum_{i=1}^{N-1} (\bar{y}_{i+1} - \bar{y}_i)^2} \quad (60)$$

It briefly consists in a squared relative deviation of a size-changed (according to  $\tau$ ) moving average without overlapping (Figure 70).

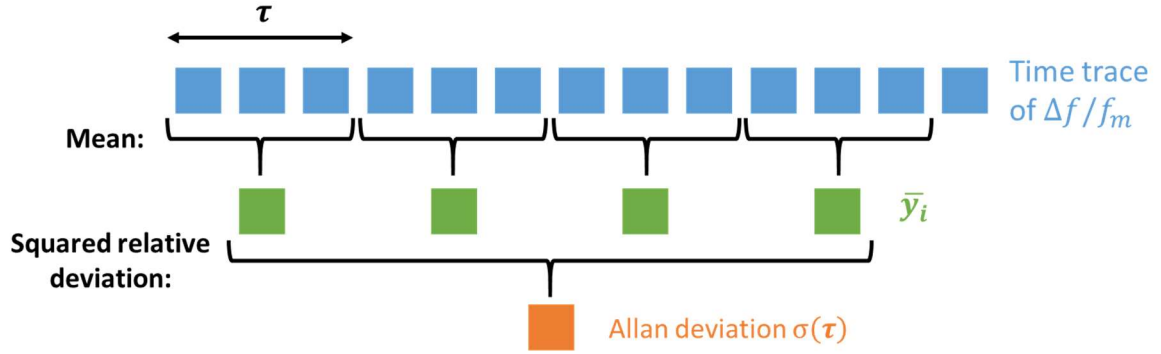


Figure 70: Scheme of the Allan deviation operation. Each blue square represents a sample of  $\Delta f/f_m$ .

Put differently, the Allan deviation gives the deviation of the signal as if it was seen through a LPF of frequency  $1/2\tau$ . It allows one to consider deviation for different integration times.

We performed it on the OM-probe mechanical phase LIA-readout time trace, retrieving the normalized frequency shifts given the phase slope. To operate the OM probe as in dynamic modes of AFM, it is driven at a fixed frequency  $f_{LIA}$ . To drive it, we used an Electro-Optical Modulator (EOM) to modulate the input laser. We then recorded the OM probe phase in opened loop configuration, *i.e.* at a fixed excitation frequency  $f_{LIA}$  close to  $f_m$  (Figure 71).

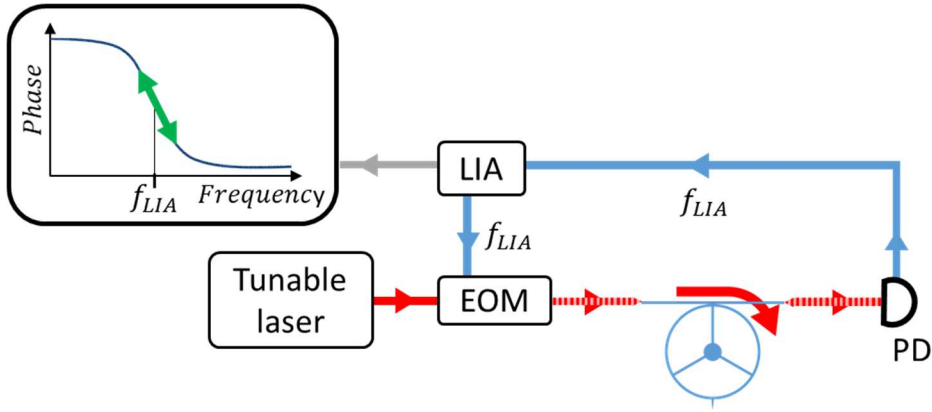


Figure 71: Scheme of the Allan variance set-up. The LIA exciting frequency is fixed. The phase difference  $\Delta\phi$  between the readout signal and the excitation one is given by the LIA. The frequency shift  $\Delta f = f_m - f_{LIA}$  is then retrieved knowing the phase slope  $p_\phi$ :  $\Delta f = \Delta\phi/p_\phi$ . The amplitude of the exciting signal coming to the EOM is noted  $V_{OM}$

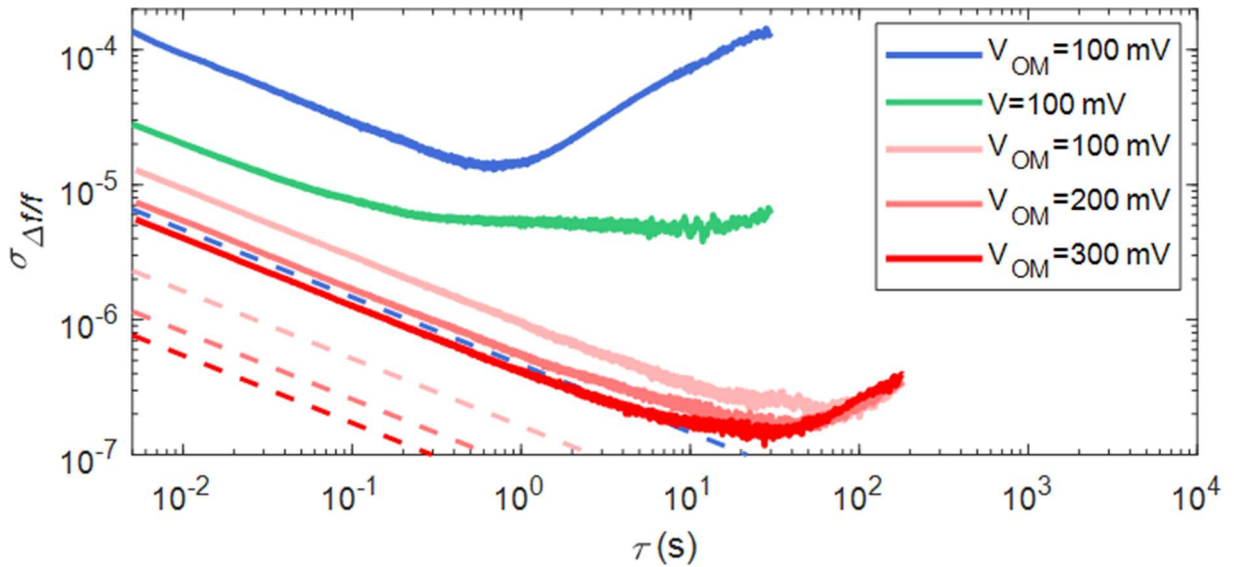


Figure 72: Graph of Allan deviations of a Vmicro ring probe (green) and two OM probes (blue and red) normalized frequency shifts for different drives, respectively  $V$  and  $V_{OM}$ . The Vmicro ring probe is a capacitive AFM probe with high-resolution, it was tested with the detection circuit described in [55]. The top two curves are taken with the same apparatus in air, unlike the red traces that are acquired in a different set-up under vacuum. In dashed are the DR formula traces (see equation (61)). For the Vmicro DR curves, DR curves could not be traced as the thermomechanical noise was not measured and thus did not provide a calibration for the vibration amplitude. The vibration amplitudes corresponding to the different drives are (blue trace)  $V_{OM} = 100$  mV:  $A = 400$  fm, (red trace)  $V_{OM} = 100$  mV:  $A = 100$  fm<sup>55</sup>. For the Vmicro probe, one can only estimate the vibration from similar device at tens to hundreds of picometers [55]. All these curves are taken with a LIA LPF at 100 kHz. Probes parameters: OM red (under vacuum)  $f_m = 117$  MHz,  $Q_m = 10500$ ; OM blue (in air)  $f_m = 130$  MHz,  $Q_m = 1000$ ; Vmicro (in air)  $f_m = 13$  MHz,  $Q_m = 100$ .

<sup>55</sup> Those values are dependent on the chosen lumped model, here on the tip's apex yielding for two different OM probes:  $k_{eff} = 2.6$  MN/m for the probe used in vacuum and  $k_{eff} = 40$  kN/m for the one used in air.

For a resonator, the Allan deviation displays a down slope for low retardation, which means that with increasing integration time, the frequency can be averaged to a single value. However a limit appears in the integration time where it will no more decrease noise and possibly increase it: the flat or up tendency on the right hand side (Figure 72).

Left-hand side: The left hand side slope position is defined by the resonator's quality factor and the signal to noise ratio by the Robin's formula (or DR formula) considering an additive white phase noise (here the thermomechanical noise) [164][166][167]:

$$D_{Allan} \left( \frac{\Delta f}{f} \right) = \frac{1}{2Q_m} \frac{1}{SNR} = \frac{1}{2Q_m} \frac{N_{Zth}}{A} \sqrt{\frac{1}{2\tau}} \quad (61)$$

Where  $SNR$  is the amplitude signal to noise ratio and  $N_{Zth}$  is the thermomechanical noise in  $m/\sqrt{\text{Hz}}$ . Under the square root on the right hand side of the equation is the bandwidth over which the noise is integrated. This equation is valid as long as we consider high  $Q_m \gg 1$  [168]. In a log-log graph of the Allan deviation, this formula gives a slope of -1/2.

The DR dashed curves are about a factor 10 under the real curves (Figure 72), indicating that another additive white noise than thermomechanical one was limiting the  $SNR$ <sup>56</sup>. This noise was not present during thermomechanical measurement, we therefore attribute this discrepancy to the background noise. Indeed, when the EOM modulates the optical signal to excite the OM probe, not all the modulated signal is coupled in the OM probe and depending on the contrast of the optical mode, part of the modulated signal goes directly to the PD. This signal can potentially carry more noise than the thermomechanical one. This through signal is detailed in next part III.5.

This Allan deviation analysis was also performed on commercial AFM probes: capacitive Vmicro ring probes (see Sec. I.4). Roughly similar values to OM probes ones are reached by the Vmicro probes as they display a better  $SNR$ , being more actuated, but with a higher detection noise (see Table 2) and a lower quality factor  $Q_m$ .

Right-hand side: To explain the up tendency in the Allan deviation, one can advance thermal drift of the mechanical resonance. Experimentally, the mechanical frequency was observed to move slightly to the higher frequency in vacuum. This phenomenon was observed just after the laser was injected in the ring with a high initial rate, decreasing with time with a time constant of about 10 minutes, stabilizing after 30 minutes. We attribute it to the thermalization of the whole sample even if it has an opposite effect as the TCF.

One can observe that the frequency is more stable in vacuum (red traces) down to  $1.5 \times 10^{-7}$  demonstrating that our setup can detect down to 20 Hz frequency shifts with 30 s integration times. As expected in a less controlled environment, the drifts (the up tendency on the right of the curves) are almost 3 decades stronger in air. One can observe that the OM probe is

---

<sup>56</sup> Other work have shown that this discrepancy between the DR formula and the experiment might be of another unknown nature, due to frequency fluctuations [166]. This is not the limiting effect in this experiment as it is primarily white noise.

more prone to drifts than the capacitive Vmicro probe. Having the OM-AFM application in mind with a 10 fr/s, the drifts that appears after 1 s can be digitally compensated.

The absolute lowest force gradient detectable with such an OM probe can be extracted from the Allan deviation of the frequency fluctuations and then using equation (41). The lowest normalized frequency shift detectable is attained for a 0.05 Hz bandwidth under vacuum and is worth  $\Delta f/f = 1.5 \times 10^{-7}$ , giving us a  $k_{ts\_LOD} = 1.2 \times 10^{-2}$  N/m (using equation (41)). For comparison, for a 100 kHz bandwidth, this value is worth  $k_{ts\_LOD} = 8$  N/m. In air this value is worth, for a 100 kHz bandwidth,  $k_{ts\_LOD} = 80$  N/m.

As a more general note on experimental stability considerations, let us discuss the stability of the optical resonance. When coupling light to the sample with micro-positioned micro-lensed fibers, the laser would often decouple from the cavity as someone closes a door, as the mechanical vibrations propagated to the coupling fibers. With glued fibers on the chip, this phenomenon completely disappeared. This decoupling is only present when the OM device exhibits thermo-optic behavior.

Now that the detection limits in terms of signal are clear, we test the actuation of the OM probe.

### III.5 Actuation and background

To excite its mechanical motion, two transductions were chosen in this project. One can either use optical or electrostatic (*i.e.* capacitive) actuation, we will present the former and end with the latter.

In optical actuation, power is modulated by the EOM upstream of the probe so that the power injected in the cavity is also modulated. The optical radiation pressure and electrostriction forces then push the flanks of the ring and excite its resonance. When the sensor is oscillating, a lock-in amplifier (LIA) is used to retrieve the amplitude and phase of the motion (optically read-out) signal, at the same frequency than the excitation. To modulate the optical power upstream of the probe we used an Electro-Optical Modulator (EOM).

Laser wavelength sweet spot assuming a given laser power: For detection purposes, the laser is placed (in wavelength) on the flank of the optical resonance, at the maximal slope. However for actuation purposes, one wants to inject the maximal power in cavity to apply greater forces, *i.e.* to put the laser exactly at the optical resonance. Taking into account the background (discussed in next paragraph), the best spot was close to the optical resonance, in the low part of the optical mode.

To test optical actuation we used the set-up presented in Figure 73. In order to test the actuation linearity, this was done for different amplitudes of modulation of the EOM.

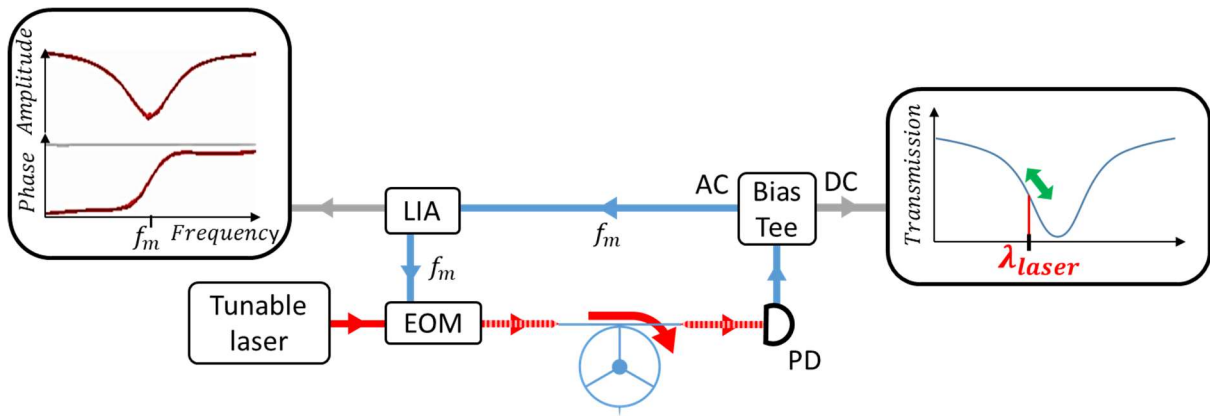


Figure 73: Scheme of the experimental set-up used to optically actuate and detect the mechanical motion of the OM probe. Polarization controllers before the device and the EOM, as well as RF amplifiers have been removed for clarity. One can note that the inset out of LIA looks like an inverted resonance. This is because the motion-modulated signal of light is superimposed to the actuation-modulated signal.

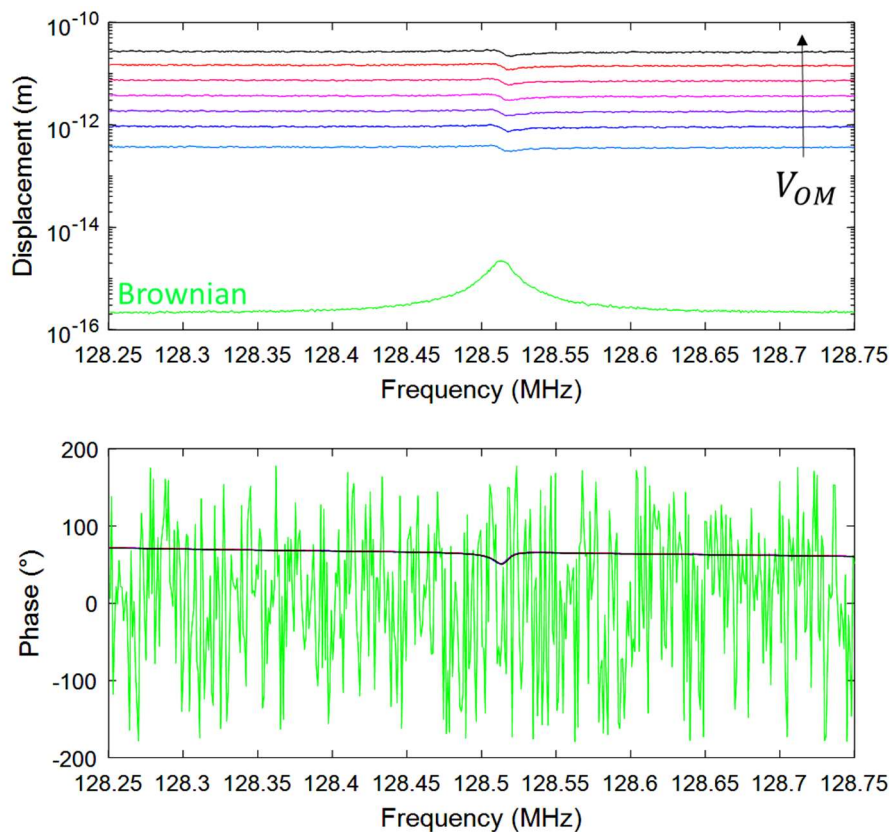


Figure 74: Plot of the amplitude and phase of the mechanical motion, using experimental set-up described in Figure 73. One can observe the random phase associated with the non-coherent thermal bath-excited Brownian motion.  $V_{OM}$  is the electrical amplitude of the excitation signal applied to the EOM. One can further observe that the traces does not look like a typical resonance. This is because the motion-modulated signal is superimposed on the actuation-modulated signal.

The Brownian motion is traced in green. One can see that modulated curves are over it but do not display the classical shape of a resonator: lorentzian peak and a  $180^\circ$  degrees rotation. Instead, the phase rotation is about 10 degrees and the peak has a small Fano-like shape (Figure 74). This means that there is a background signal, at the actuation frequency, that

superimposes on the useful mechanical motion signal. This background is proportional to  $V_{OM}$ . More problematic, it prevents thermomechanical calibration.

Now that we modulate the laser upstream of the probe (Figure 75), in transmission will appear two signals at the same frequency (driven frequency):

- background signal, carrying the actuation modulation
- motional signal, carrying the motion modulation:

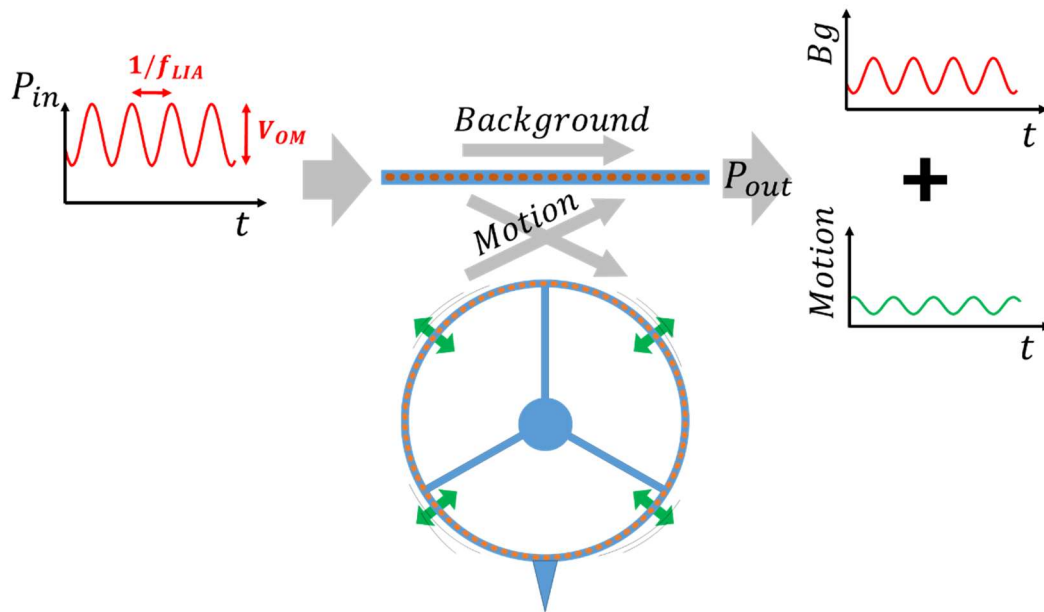


Figure 75: Scheme of the different signals considering evanescent coupling. The input laser is modulated so that when injected in the OM probe, it actuates the mechanical motion. The part of this modulation which is not injected goes directly to the output: this is the background signal. The motional signal that couples back to the waveguide is phase shifted and adds up to the background signal in output.

We can differentiate them by sweeping the modulation frequency with the lock-in amplifier: the actuation-modulated signal will have a constant amplitude and phase, *i.e.* flat response<sup>57</sup>, and the motion-modulated signal will feature the mechanical resonance in amplitude and the  $\pi$ -rotation of the phase. They are however added (in the complex domain) in the transmission signal, leading to a distorted resonance in a Fano fashion (Figure 74). It is important to note at this point that the higher the contrast of the optical mode and the more the laser wavelength is close to that optical resonance, the less actuation-modulated background signal will be transmitted<sup>58</sup>.

We presented the optical background as a through optical signal, it however could be a thermo-optic effect happening in the ring. Using experimental considerations on this

<sup>57</sup> Provided that the LIA can compensate for the delay acquired in the actuation-acquisition loop, see details in Appendix F:.

<sup>58</sup> Assuming that the background signal does not come from the OM ring probe. Which is the case for our structures.



background, we will show in the next paragraph that this effect can be neglected. Neglecting it further gives us information on the optical phenomena at play in the actuation of the probe.

#### *III.5.1.1 Thermo-optic effect could imply a fake motion signal*

The thermo-optic effect (*i.e.* refractive index change with temperature, see Sec. II.2.7) is shortcutting the mechanical motion excitation. Indeed, when optical power in the cavity is modulated, its temperature is also via absorption. When heating the optical cavity, its refractive index changes, changing in turn the transmission of the probe. Hence, the sensing signal might be associated with the refractive index's oscillations and not the real mechanical motion. This could explain the actuation-modulated background signal. However, the background signal diminishes when laser is put closer (in wavelength) to the optical resonance, so when injecting more light in the ring. It is thus not associated with thermo-optic effect but rather a "through" signal. Indeed, if it was associated with thermo-optic effect, the background would increase. To resume, thermo-optic effect is unseen at the actuation frequency (over 100 MHz). Stays the question why we can see the thermo-optic shift when optically sweeping but not when looking at the mechanical motion at over than 100 MHz frequencies. We attribute this to the cut-off of thermal effects over a few MHz (because of heating time constant of about hundreds of nanoseconds).

From AFM use considerations and more precisely phase locked loop (PLL), this background can be ignored if it is stable. Its only problem is the saturated transmitted signal, where the motion signal can only constitute a small fraction in the total signal. Put differently, the LIA input has a resolution that depends on the signal amplitude, *i.e.* a fixed dynamic range. If the input signal is made of a background signal higher than the motional one, one needs a higher maximal input and thus a lower resolution than what needed for the motional signal only. However, the initial assumption that it is stable is not true, EOM fluctuations and thus the amplitude of both background and motional signal vary.

Another phenomenon that can be problematic for PLL operation is the delay line effect, the slope appearing on the phase when sweeping. At high frequencies (over 100 MHz), the propagation delay in the cables and device is not negligible and induces a variable phase shift with frequency (for a detailed explanation, see Appendix F:). This artificial phase-shift must be lower than the motional one or compensated.

To retrieve the pure motional signal and get rid of the actuation-modulated background, we tested 5 options:

- Digital data post-processing
- Saving reference traces and subtraction (with the instruments)
- RF interferometry in the electrical domain
- Using 2 lasers: for actuation and detection
- Using a non-optical actuation transduction (capacitive)

#### *III.5.2 Data post processing*

As the motion-modulated signal is added to the actuation-modulated one in the complex domain, one can fit the distorted signal at resonance with a model to then extract the motion-modulated signal. One can argue that it could be implemented for live operation but the fitting

delay induced would be detrimental to the BW for fast-AFM operation. The first model of the transmitted signal we used to fit the data is as follows, placing ourselves in the LIA modulation  $\omega_{LIA}$  rotating picture:

$$X_{fit}(\omega) = R_m e^{i\phi_m} \times \frac{1}{m_{eff} \left[ \omega_m^2 - \omega^2 + j\omega \frac{\omega_m}{Q_m} \right]} + R_{bg} e^{i\phi_{bg}} \quad (62)$$

The fitted amplitude being  $|X_{fit}(\omega)|$  and phase being  $\arg(X_{fit}(\omega))$ . Where  $R_m e^{i\phi_m}$  is the optical actuation forces exciting the mechanical resonator and  $R_{bg} e^{i\phi_{bg}}$  is the optical actuated-modulation background signal. In details,  $R_m$  represents the force amplitude of the optical forces and  $\phi_m$ , which could be noted as  $\phi_{bg} + \Delta\phi$ .  $\Delta\phi$  represents the phase-difference due to the delay of optical forces actuation (for example thermalization time for photo-thermal forces) and the delay due to the optical cavity<sup>59</sup>. Fitting those parameters, we can then subtract the background from the measured signal and retrieve a typical resonance form.

$$X_{treated}(\omega) = R_{LIA} e^{i\phi_{LIA}} - R_{bg} e^{i\phi_{bg}} \quad (63)$$

The treated data is shown in Figure 76.

---

<sup>59</sup> In this model, the thermomechanical force is not taken into account. It could be adding a  $R_{th} e^{i\phi_{th}}$  actuation force with random phase  $\phi_{th}$ .

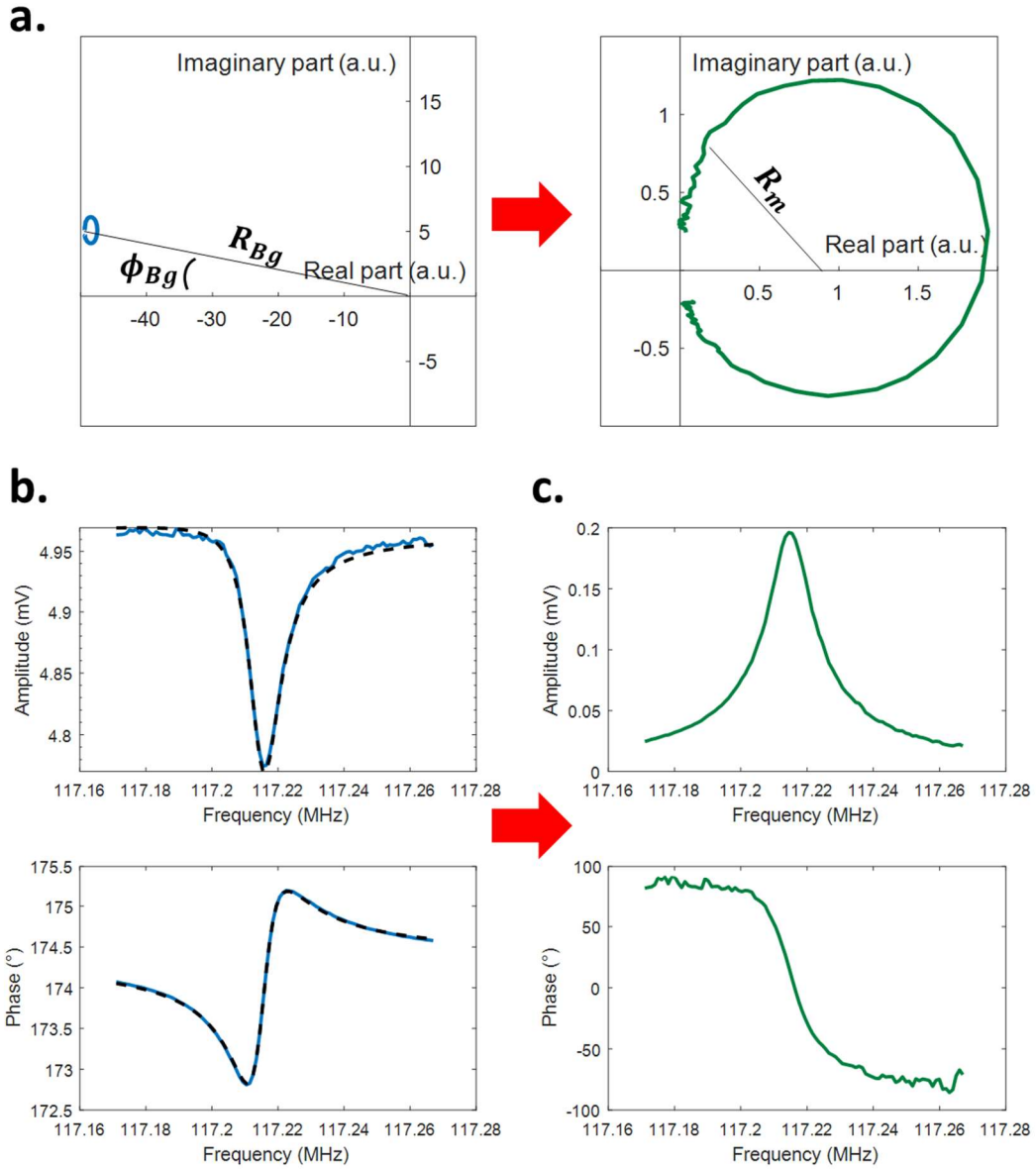


Figure 76: Pre- and post-processed data in polar (a) and Bode frames (b) and (c). Lock-in signal raw (b) and post treatment (c). (b) The raw signal in blue is fitted with the dashed black model of equation (62), then the fitted background is subtracted (in the complex domain) to retrieve the motional signal (c) that can then be calibrated with Brownian motion. For this fit, parameters were:  $R_m = 0.81$  mV,  $\phi_m = 1.777$  rad,  $R_{bg} = 4.965$  mV,  $\phi_{bg} = 3.0431$  rad and  $Q_m = 9900$ .

One can observe that this treatment effectively allows the recovering of a lorentzian-shaped resonance and a  $180^\circ$  phase rotation as expected from a resonator.

With the fitting parameters, one can estimate the optical force delay  $\tau$  with  $\tau = \Delta\phi/\omega_m$ . With the fitted phase-shifts in Figure 76, we find  $\tau = \frac{\phi_{bg} - \phi_m}{\omega_m} = 1.7$  ns. This value is to compare with the cavity's optical delay, *i.e.* the time a photon takes to get coupled out of the cavity. It is given by<sup>60</sup>  $\frac{Q_e}{f_{opt}} = \frac{440\,000}{193 \times 10^{12}} = 2.3$  ns, with the same magnitude order.

<sup>60</sup> The  $Q_e$  chosen here is extrapolated from the contrast  $C = 20\%$  and FWHm  $\Delta\lambda = 35$  pm (so  $Q_{tot} = 44\,000$ ) of the optical mode (see Appendix A:). As the coupling gap is 300 nm for this OM

### III.5.3 Saving reference traces and subtraction

One can record a LIA sweep when the laser is out of an optical resonance. Thus the actuation-modulated background is saved as a reference signal for the further measurements. When the laser is injected in the optical cavity, the measurement will only display the motion-modulated signal as the background is subtracted. The instruments that we used for the sweep (Network Analyzer or lock-in amplifier, see Appendix C: for instrument details) had this feature integrated. The result is the same as in the post-processing one.

### III.5.4 RF Interferometry in the electrical domain

One can separate the actuation signal to subtract it to the signal exiting the PD. For this technique to function, the added modulation amplitude must match that of the exiting signal and its phase must match the one of the exiting signal ( $+\pi$  for a perfect destructive interference). In addition its propagation delay must be the same as the signal passing through the OM probe to avoid phase shifting effect when sweeping. From an electrical implementation of this technique as shown in Figure 77, we conclude that it is not stable enough to be performed in an experiment.

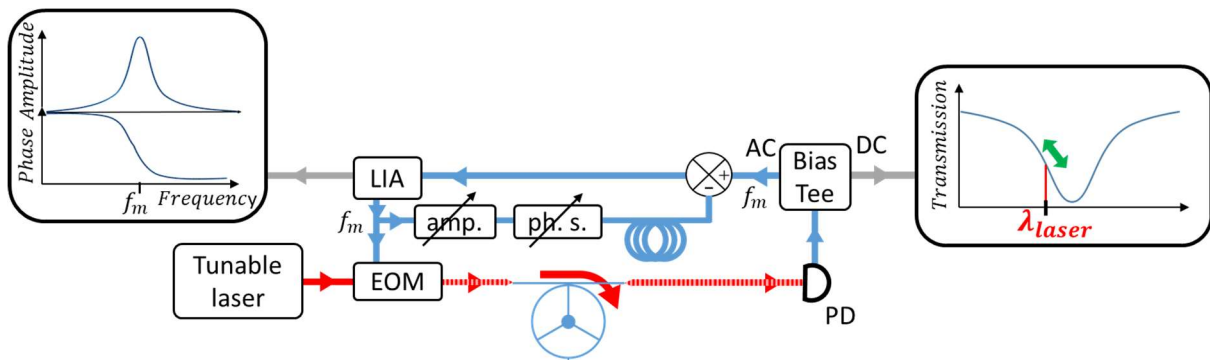


Figure 77: Scheme of the experimental set-up allowing one to get rid of the actuation background. The "amp." and "ph. s." blocks are respectively a variable amplifier and a variable phase shifter to obtain a destructive interference; they were integrated in our LIA instrument. The coil represents a long cable acting as a delay line, whose purpose is to balance the electrical length of the two arms of the electrical interferometer. It is necessary to get rid of a phase slope when sweeping frequency around the  $f_m$  one (This is only necessary as our probe has a high frequency  $f_m$ , see Appendix F:).

The result, not shown here, is the same as in the post-processing one.

### III.5.5 Using 2 lasers for actuation and detection

This technique offers an expensive alternative due to the cost of a 2<sup>nd</sup> tunable laser to get rid of the actuation background, it is however effective. The idea is to inject one laser dedicated to detection (*i.e.* probe laser) and another one at a different wavelength dedicated to actuation (*i.e.* pump laser) and then to filter out the actuation laser to retrieve only the detection signal. The set-up is presented in Figure 78, and the associated results in Figure 79.

---

probe, we consider the optical cavity to be under-coupled, thus assuming  $Q_{int} \approx Q_{tot}$ . Using Figure 40, we find the ratio between  $Q_e$  and  $Q_{int}$  to be about 10.

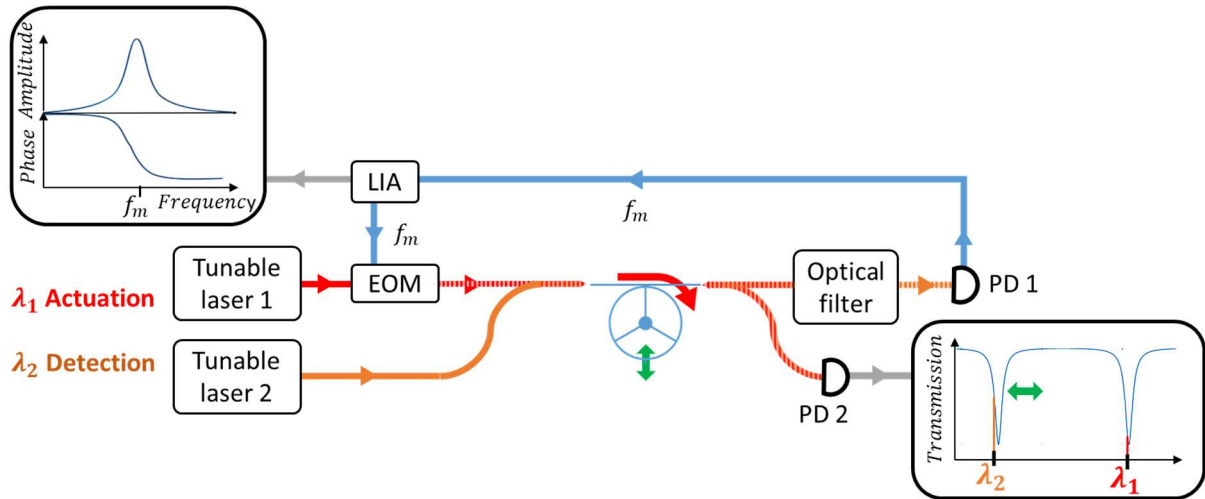


Figure 78: Scheme of the experimental set-up to optically actuate and detect the OM probe motion with 2 lasers.

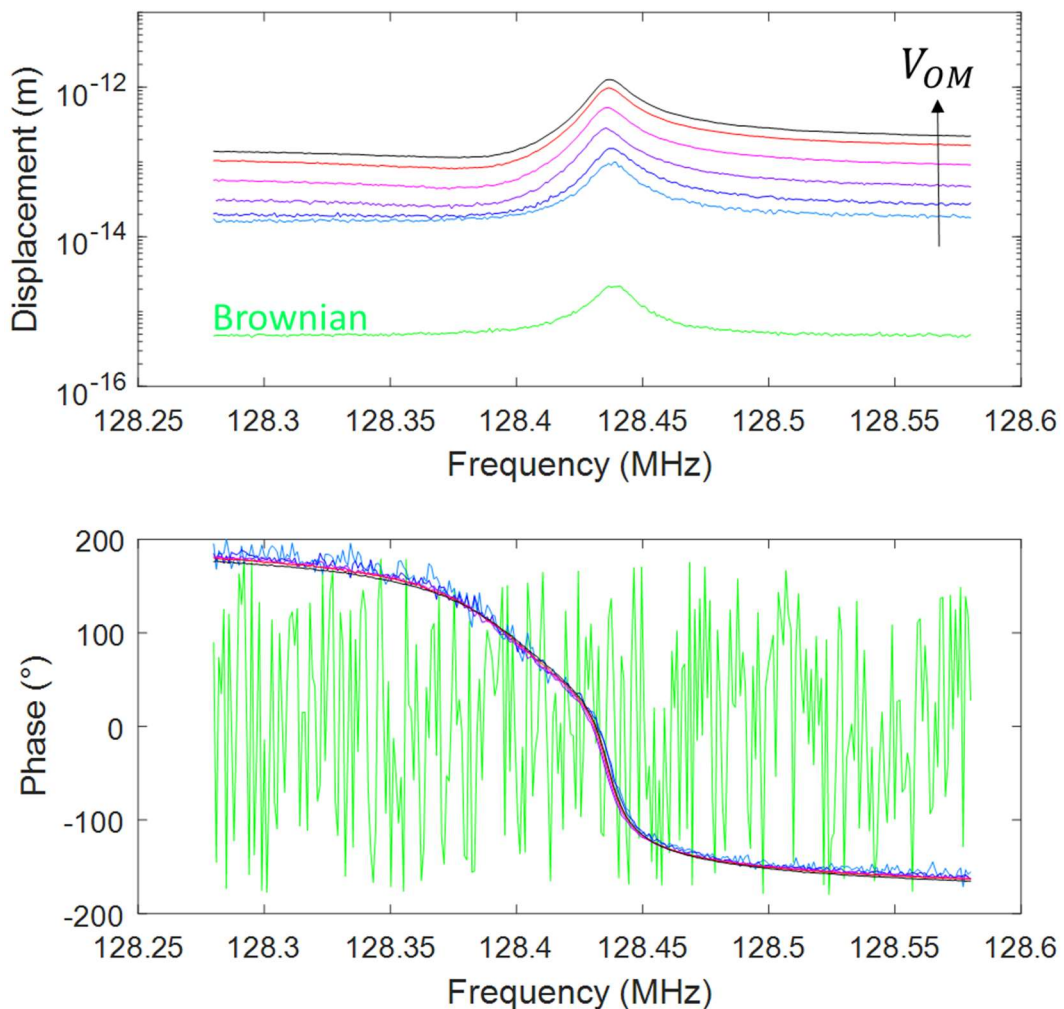


Figure 79: Graphs of the two-lasers set-up results. The modulation amplitude on the EOM  $V_{OM}$  was gradually increased from 0 V to 8 V. One can observe a  $2\pi$  phase rotation instead of a  $\pi$ , we have no explanation of this effect.

So that one can filter out the actuation laser, the two lasers must be injected in two different optical modes of the cavity, at two different wavelengths. Usually, the actuation laser is

chosen more powerful than the detection one in order to actuate more the cavity. Additionally, for experimental ease, one might prefer to have only one laser powerful enough to induce thermo-optic shift<sup>61</sup>. The amplitude reached with this two-laser actuation is comparable to the one-laser one, about 1 pm. This value is two-orders of magnitude lower than expectations from analytical computations giving amplitudes of 400 pm (see Sec. II.4.2). Indeed, to obtain the 400 pm value, we made the brutal assumption that the radiation pressure force, pushing out the walls of the cavity, could directly be applied to the lumped spring-mass model of the OM probe. This discrepancy could then be explained by considering the real mechanical mode profile. This was not investigated.

### III.5.6 Using an alternative actuation (capacitive):

Using another transduction than the optical one for actuation allows to get rid of the optical modulation background. As explained earlier (see Sec. II.4.3), we realized electrostatic actuation with large electrodes close to the OM probe (Figure 80).

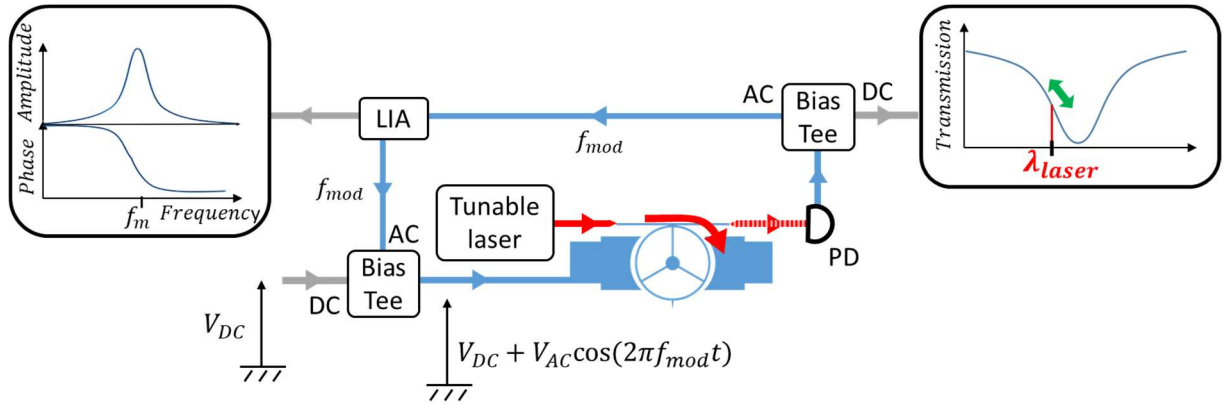


Figure 80: Scheme of the experimental set-up used to capacitively actuate and optically detect the OM probe motion. Not shown in the scheme is that the two capacitive blue electrodes are electrically connected.

As shown previously in equation (35) (noted here (64)), to excite the mechanical resonance at frequency  $f_m$  one can use either an electrical modulation at  $f_{mod} = f_m$  or  $f_{mod} = f_m/2$ .

$$F_{elec} = -\frac{\epsilon_0 S}{2d^2} \left[ V_{DC}^2 + 2V_{DC}V_{AC} \cos(2\pi f_{mod}t) + \frac{V_{AC}^2}{2} (1 + \cos(2\pi 2f_{mod}t)) \right] \quad (64)$$

The electrical actuation force at  $f_{mod} = f_m$  will be proportional to the product  $V_{DC} \times V_{AC}$  and the one at  $f_{mod} = f_m/2$  to  $V_{AC}^2$ . However comparing equation (64) and Figure 80, one can see that we assumed the ring was electrically conducting and grounded which is not true. The ring is in silicon and at a floating potential so that the  $V_{DC}$  applied on the electric pad is not exactly the real  $V_{DC}$  in equation (64). The  $f_m/2$  modulation with a  $V_{AC}^2$  amplitude is thus preferred because it is more stable and has a higher DR as can be seen in Figure 81.

<sup>61</sup> As a note, the experimental procedure is not straightforward.

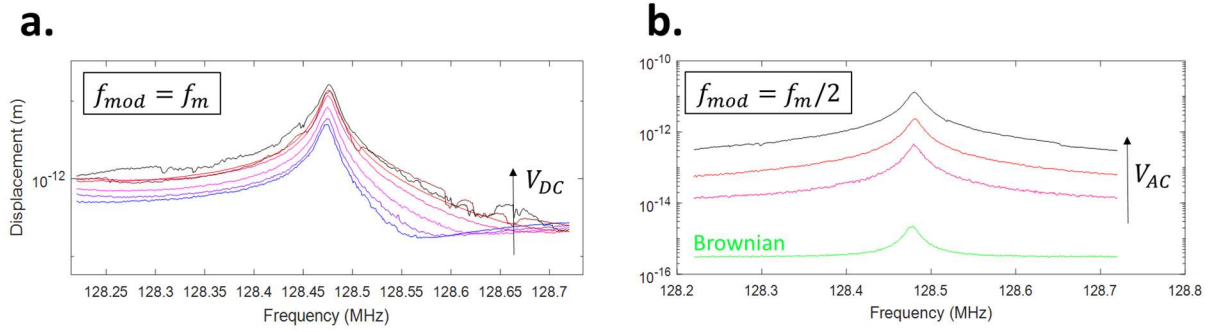


Figure 81: Comparison of capacitive actuation at  $f_m$  (a) and  $f_m/2$  (b). (a)  $V_{DC}$  is varied from -10 to 8 V. (b)  $V_{AC}$  is varied from 0 to 10 V. The two experiments are carried out in a secondary-vacuum chamber. One can note that the maximal resonance amplitude is about 10 pm for  $V_{AC} = 10$  V, limited by the instruments used. The 10 pm amplitude reached in  $f_m/2$  actuation is of the same order of magnitude of the calculated value of 35 pm (see Sec. II.4.3).

In comparison with the 2-laser set-up, it is simpler and reaches higher actuation amplitudes. For two  $14.4 \mu\text{m} \times 0.22 \mu\text{m}$  actuation electrodes so that  $S = 7 \times 10^{-12} \text{m}^2$ , at a  $d = 1 \mu\text{m}$  distance from the ring and with a 24 dBm excitation, we were able to actuate a 10 pm displacement in vacuum, close to the predicted magnitude order of 35 pm (see Sec. II.4.3). The only drawback to this technique is the addition of an electrical connection.

The 10 pm capacitive actuation is to compare with the 2 pm optical actuation with a 10 mW pump laser command and a 30 % modulation. To improve optical actuation, one improves the laser power circulating in the ring. But the optical cavity is close to non-linear effects that arise with over 10 W circulating in the cavity (p. 130 in [146]). With capacitive actuation, one can *a priori* improve the RF power applied to the actuation electrodes without non-linear effect.

The limiting effects encountered for a higher actuation would then be of mechanical nature: Duffing non-linear behavior or sticking. The former (Duffing) is expected for vibration amplitude in the order of the smallest characteristic length of a structure: 100 nm wide spokes. The latter (sticking) is expected for oscillations in the order of the gap between actuation electrodes and the ring, which is  $1 \mu\text{m}$  for our designs.

#### Set-ups overview:

One has to keep in mind that this background problem appears when the contrast of the optical mode is not 100 % (*i.e.* the optical mode transmission does not reach zero). With perfectly coupled OM probes, this background nearly vanishes (not completely as the laser would be just before the optical resonance (in wavelength)). That being said, to fabricate an ideally (*i.e.* critically) coupled OM probe is not trivial and we have seen that the actual best optical slope is reached for contrasts of 50 % (see Sec. III.2.1). Background removing techniques are thus still of interest. They are only effective if the background is suppressed by the set-up (2 lasers or capacitive), for the best use of the dynamical inputs of instruments. The digital background subtraction is only interesting to calibrate signal with Brownian motion.

In the AFM perspective, one can note that maximum vibration amplitudes reached with optical actuation are in the 1 pm order in air, more than two decades lower than the atomic

lattice constant about a few angstroms. This 1 pm actuation was obtained with maximal optical modulation and to increase further vibration amplitudes, one would need higher laser power, that would *a priori* trigger non-linear effects. To reach higher vibration amplitudes, one can potentially reach it with capacitive actuation with an amplified driving modulation.

In this part, we quantified the actuation amplitudes and methods to retrieve it. Next, we present an experiment to verify the theoretical mechanical bandwidth of the probe.

### III.6 Determination of the OM probe's mechanical bandwidth

The mechanical bandwidth of the resonator is defined as  $BW = f_m/Q_m$ . To verify the high mechanical bandwidth of our probe, we added an electrostatic modulation close to the OM probe's apex in an atomic force acoustic microscopy-like set-up. To simulate a mechanical perturbation by a surface, an electrostatic force was applied on the apex of the OM probe. To this end, a conductive tip was approached of the apex of the OM probe. Its electrical potential  $V_{elec}$  was modulated at  $f_{elec}$ . To retrieve this force modulation effect on the motion of the probe, a second LIA was used (Figure 82).

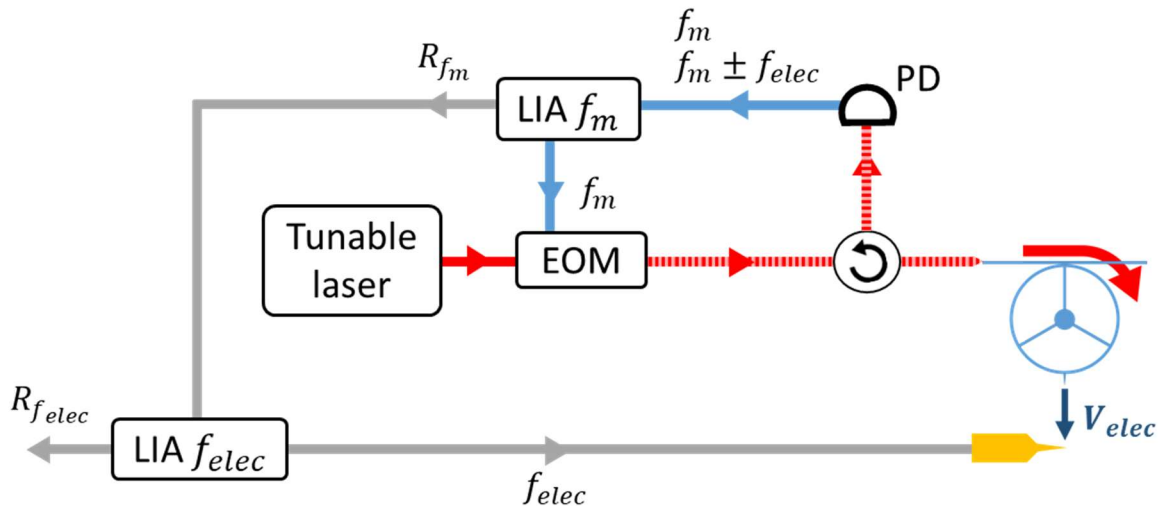


Figure 82: Scheme of the experimental set-up used to add electrostatic force modulation.  $f_m$  is about 130 MHz and  $f_{elec}$  is varied up to 1 MHz. In yellow is a conductive gold-sputtered tip. It is placed at about 10 nm from the apex of the OM probe. Contrary to previous experiments, this one is done in reflection of the laser by the device and a circulator. The reflection configuration was only possible because we used cleaved facet side injection (see Appendix I:). For this measure the  $f_m$  LIA LPF had a frequency of 500 kHz and the  $f_{elec}$  LIA LPF had a frequency of 0.5 Hz.

As expected, when sweeping the electrostatic modulation frequency, the amplitude of motion detected with the OM probe decays according to its mechanical bandwidth (Figure 83).



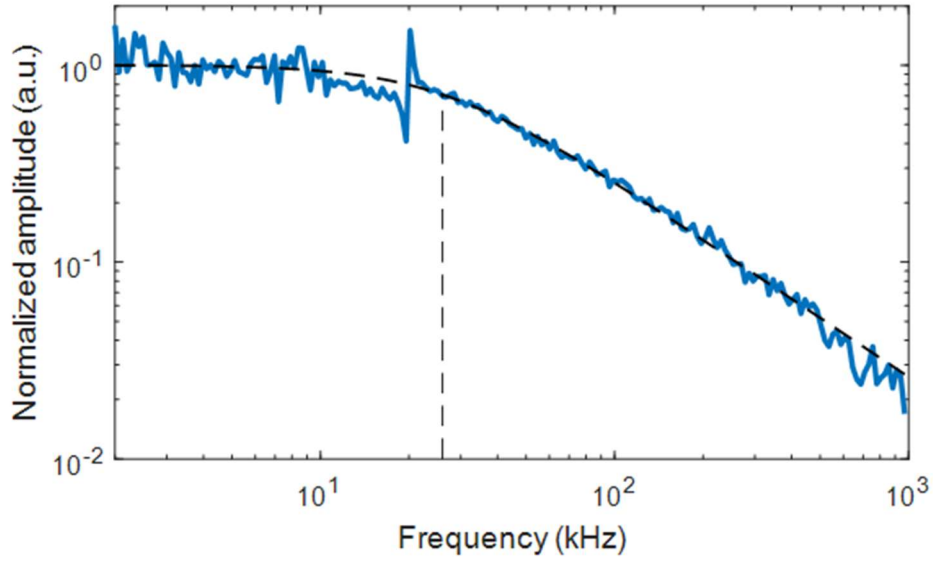


Figure 83: Normalized amplitude (in blue) versus electrostatic modulation frequency. It is fitted with a low-pass filter of cut-off frequency 26 kHz. The narrow peak around 20 kHz is attributed to the mechanical resonance of the golden tip used to poke the OM probe. Indeed, we used an AFM cantilever of frequency 15 kHz with a 7 kHz to 25 kHz fork [169]. This trace was extracted from the raw data by subtracting non-mechanical modulations and then by de-embedding instruments cut-off responses. The cable bandwidth (the one connecting the golden probe to LIA) and the LIA LPF (at 500 kHz), both had their spectral response recorded beforehand and were de-embedded from the raw data. The raw data was subtracted another trace taken out of mechanical resonance (with a 3 MHz shift on the frequency of the first LIA) to filter out any modulation which would not be mechanical<sup>62</sup>.

This OM probe had a mechanical quality factor in vacuum of  $f_m = 2813$  and a frequency of  $f_m = 118$  MHz. The experimental cut-off at 26 kHz is in agreement with the theoretical mechanical bandwidth of the probe:  $BW = f_m/Q_m = 42$  kHz.

---

<sup>62</sup> To have further information on this experiment, those results were published in [202].

In this chapter, we thoroughly characterized the OM probe, from optical performances according to dimensions, to detection noise and stability. We identified the main optical loss source as the geometrical scattering occurring at the spokes anchoring. For our structures, the spokes thus need to be thinner than 100 nm. We also quantified the optimal gap distance, between 100 nm and 200 nm. Mechanically, the limit of detection of our OM probe was identified at  $4.5 \times 10^{-17} \text{ m}/\sqrt{\text{Hz}}$ , two decades lower than any AFM probe. Among the different set-ups compared to remove the background and actuate the probe, the capacitive actuation is the more promising. Indeed, it can *a priori* be amplified arbitrarily. The probe's mechanical bandwidth was experimentally verified. But before testing the OM probe in AFM operation, one needs to integrate the OM probe in a positioning system as well as a feedback loop to control the probe-sample distance. Achieving high speed with such an instrument needs developments as is detailed in next part.



## IV. A fast AFM environment to operate the optomechanical sensor

To exploit the performances of the high frequency OM probe, a fast AFM instrument was developed<sup>63</sup> from scratch. As demonstrated in the last chapter, the OM probe has a mechanical bandwidth in air of  $f_m/Q_m \approx 100$  kHz. This means that it can acquire the mechanical information of the surface in  $10 \mu\text{s}$ . Taking a  $100 \text{ px} \times 100 \text{ px}$  AFM image and a  $10 \mu\text{s}$  time per pixel, we could obtain a frame rate of 10 fr/s. We thus aim for an AFM instrument able to position a sample, acquire data, process data and give a positioning feedback in about  $10 \mu\text{s}$  or less. For example, the feedback loop's function is to prevent the tip from crashing onto/damaging the sample. For this function to be effective, the whole feedback loop that links the probe's signal to the Z-actuator must be fast enough. The limit being the acquisition speed of the probe which is  $10 \mu\text{s}$ . This positioning, data acquisition and feedback speed is state of the art as it is reached by only two fast AFM instruments, using ultrashort cantilevers with mechanical frequencies in the few MHz range: RIBM Ando-type and Cypher VRS AFMs. Each block's bandwidth can be lightly improved by mechanical design and/or signal processing. This part resumes the choices made to reach this  $10 \mu\text{s}$  (*i.e.* 100 kHz BW) feedback loop goal along with OM probe experimental integration. An outline of this part is presented in Figure 84.

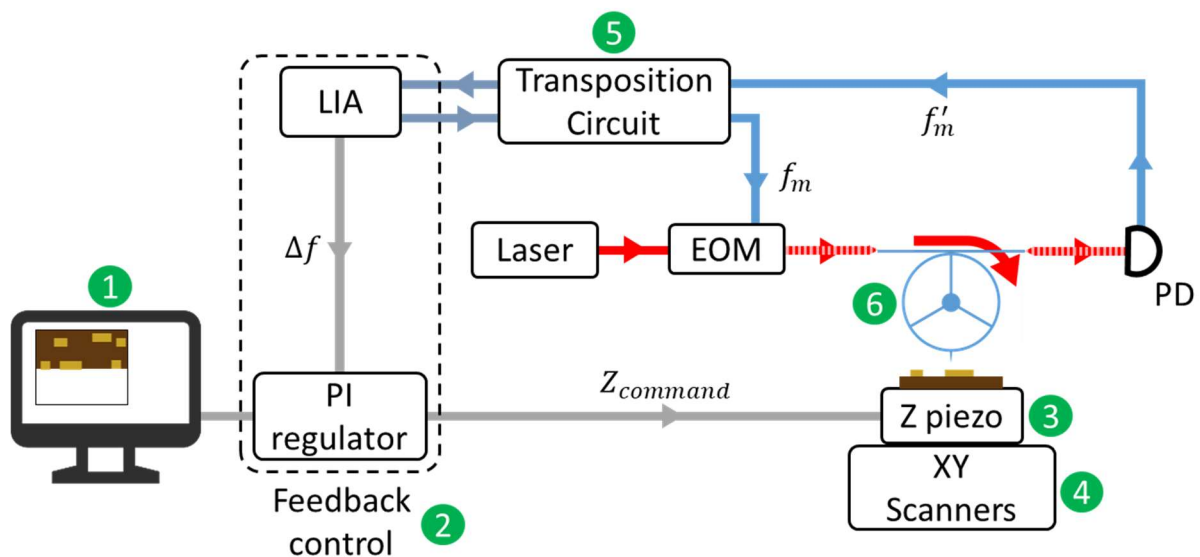


Figure 84: Scheme of an OM AFM featuring main instruments. This chapter outline is highlighted by green marks. (1) Computer interface. (2) High-BW feedback control. (3) High-BW Z-actuator. (4) High-speed scanning. (5) Transposition circuit, whose only purpose is to match the frequency of a certain LIA (<50 MHz) with the mechanical one (130 MHz). (6) OM probe integration.  $\Delta f = f_m - f_{set}$ .

### IV.1 Computer interface

How the probe signals are acquired, generated and displayed on the user interface? This work was directed by B. Legrand and realized by N. Mauran with custom electronics by D. Lagrange. It is presented as a simplified scheme in Appendix J:.

<sup>63</sup> This chapter mainly consists in developments, made by Laurent Mazenq, Nicolas Mauran, Denis Lagrange and Bernard Legrand, in which I took part occasionally.

## IV.2 High-BW feedback control

The speed limiting aspect of the servo loop is the overall delay between signal detection and new position command emitting. Indeed, if the phase shift of the loop is  $\pi$ , with a feedback magnitude without amplification, the system is unstable. To better grasp why, some control theory is presented for a simple system (Figure 85).

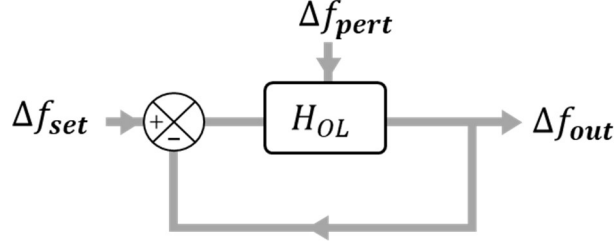


Figure 85: Scheme of a simple feedback system.  $H_{OL}$  stands for the transfer function of the open loop. Applied to our system in a FM-AFM configuration,  $\Delta f_{out}$  would be the OM mechanical frequency shift. As a reminder it is proportional to the force gradient felt by the tip.  $\Delta f_{set}$  would be its desired value to keep a constant force gradient. Finally,  $\Delta f_{pert}$  would be the frequency shifts associated with the force profile of the sample, changing while scanning the surface.

The total closed loop transfer function  $H_{CL}$  of such a feedback system (Figure 85) is given by:

$$H_{CL}(j\omega) = \frac{H_{OL}(j\omega)}{1 + H_{OL}(j\omega)} \quad (65)$$

One can straightforwardly derive that the system is unstable for  $H_{OL} = -1$ , *i.e.* when its magnitude is 1 and its phase  $-\pi$ . This case is often not perfectly matched and one can hence define gain and phase margins: respectively the gain of the transfer function when it has a  $-\pi$  phase and its phase above  $-\pi$  when it has a 1 magnitude, defining how close the system is of this unstable point.

One could write this open loop transfer function in the case of the AFM set-up we developed (Figure 86):

$$H_{OL}(j\omega) = H_{PID}H_{DAC}H_{amp}H_{piezo}H_{sample}H_{probe}H_{LIA}H_{ADC} \quad (66)$$

$H_{DAC}$  and  $H_{ADC}$  are just phase delays  $e^{j\varphi}$ .  $H_{piezo}$  is experimentally known (Figure 92), as  $H_{amp}$ .  $H_{PID}$  is known as set by the user. Stays  $H_{sample} \times H_{probe+LIA}$  which gives a mechanical-resonance-frequency shift output for a Z-piezo motion input.  $H_{sample}$  is a transduction gain, from piezo motion to force gradient modulation.  $H_{probe+LIA}$ 's output is a frequency shift, for a force gradient input. Its magnitude is  $\Delta f = \frac{f_m}{2k_{eff}} k_{ts}$  (see equation (41)) with  $k_{ts}$  the force gradient and a phase shift up to the mechanical resonance frequency [56].

This overall function's magnitude is not fixed as the  $H_{sample}$  depends on the imaged sample. To decrease the instability likelihood and aim for the fastest feedback, the phase shifts (*i.e.* delays) must then be reduced so that the  $-\pi$  condition is only met for higher frequencies (it will unfortunately always be met at some point).

### Feedback loop delays and latency

The delays or latencies were experimentally measured for each instrument of the feedback loop to pinpoint the limiting one (Figure 86).

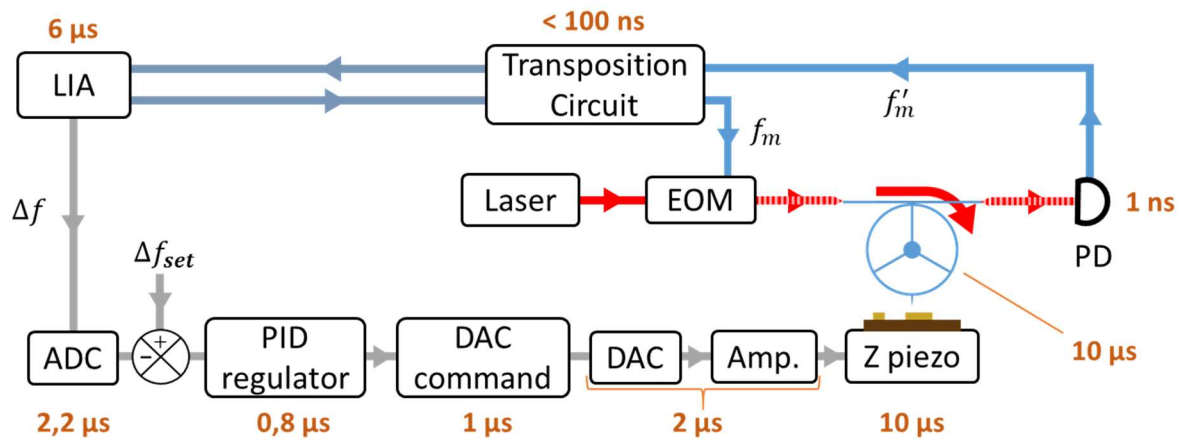


Figure 86: Scheme of the feedback loop. Delay of each instrument is highlighted in orange.

The main delays in our feedback loop are the probe's mechanical response, the Z-piezo response and the LIA detection of the amplitude and phase. We study first the two last.

#### IV.2.1 High-BW detection

The LIA 6 μs latency depends on the chosen LPF which was limited to 100 kHz for our LIA. To have a faster detection one can use a faster LIA or another detection scheme as synchronous triggered phase detection, which is theoretically faster but comes with more noise [170]. It was tested in our apparatus, displaying a few hundreds of nanoseconds of delay: way faster than the previous LIA. Those results are under publication [171].

#### IV.2.2 Better surface tracking: dynamic PID

When improving the scanning speed of the tip over the sample, at a brutal downhill, the parachute effect can appear. There is thus temporary saturation of the deflection signal. Whereas at a brutal uphill the error signal can increase a lot, at a downhill, the tip can detach (*i.e.* lose the tip-sample interaction force) from the sample and feel nothing for the time needed by the PID to move the sample close to the tip again (Figure 87). This phenomenon lowers the information close to abrupt motifs and decreases the imaging speed necessary to feel/image those cliffs.

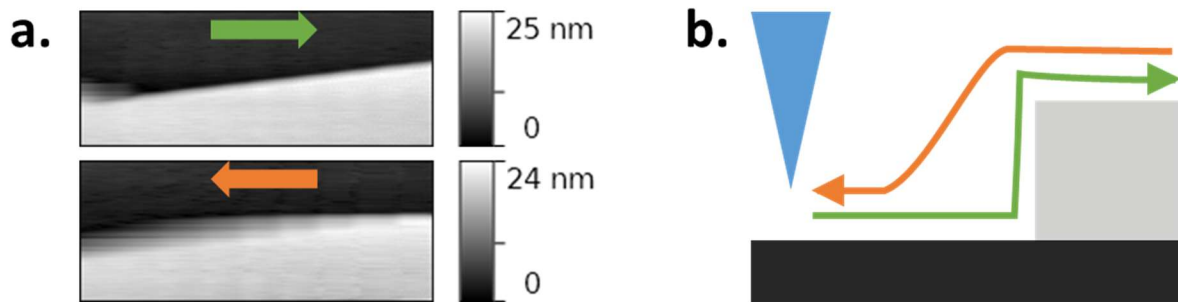


Figure 87: (a) 185 nm x 70 nm forward and backward AFM images of a HOPG sample taken with a Vmicro probe. In the bottom image, the tip is going downhill (orange trace), detaching from the surface: the parachute effect. (b) Scheme of the parachute effect.

To overcome this limitation, the classical PID can be changed into a dynamical one [172], the idea being that the gains become stronger with increasing error. In particular, its gains are stronger when the error signal saturates. Thus the tip recovers faster the set-point it was before falling off the cliff. This dynamic PID was implemented in our AFM instrument as a second faster PID taking the control when error is too large.

The most limiting component in the feedback loop is the Z-piezo, its developments are discussed in next part.

### IV.3 High-bandwidth Z piezo actuator

So that the tip does not crash onto/damage the sample, the Z-piezo response must be fast enough when its  $Z_{command}$  is updated. Put differently, its bandwidth must be high enough, our goal being 100 kHz. To reach this bandwidth, an actuator can be improved by two ways: mechanical design and signal processing pre-positioner. For now only mechanical design was implemented in our instrument, but we also present signal processing improvements thought for our apparatus.

#### IV.3.1.1 Experimental set-up: frequency response characterization

To test the different Z-module designs, the protocol is to excite the piezoelectric component with a sweeping frequency and to record the overall block vibration amplitude. Ideally, the frequency response is flat from 0 Hz to 100 kHz, our bandwidth aim. Different vibration amplitude measuring methods were tried:

- STM: an STM probe is put on top of the block and records its motion;
- XY Scanner Z-sensor: a capacitive sensor tracks the Z movement of the XY scanner;
- Self mixing laser diode: a laser is shot at the surface of the block and the reflected laser mixes back with the laser diode, modulating its current consumption;
- Optical profilometer: a laser is shot at the surface of the block and the reflected laser mixes back with the initial laser;
- Impedance measurement: current flowing through the piezoelectric component is measured when excitation frequency is swept;
- Doppler Laser vibrometer: a laser is modulated and shot at the surface of the block and the reflected laser mixes back with the initial laser.

Only XY Scanner Z-sensor and laser vibrometer measurements are presented in this manuscript as there were the most reliable ones.

### IV.3.2 Mechanical design

As a general rule, the maximal displacement intended roughly sets the maximal bandwidth of the piezoelectrical actuator (see Sec. I.2.2). For our intended  $2\ \mu\text{m}$  displacement, piezoelectrical actuators have an approximate 500 kHz bandwidth (or first resonance) (we used PICMA actuators [173]). But if used as it is (Figure 88a), the actuator can display lateral bending or break. To prevent this component from being damaged and to guide it, flexures are widely used in different configurations (Figure 88b) [174]. They offer better positioning at the cost of a reduced bandwidth due to added moving parts with lower resonance frequencies. When using flexures, the bandwidth can be lightly improved (under the piezoelectrical component itself limit) by mechanical design.

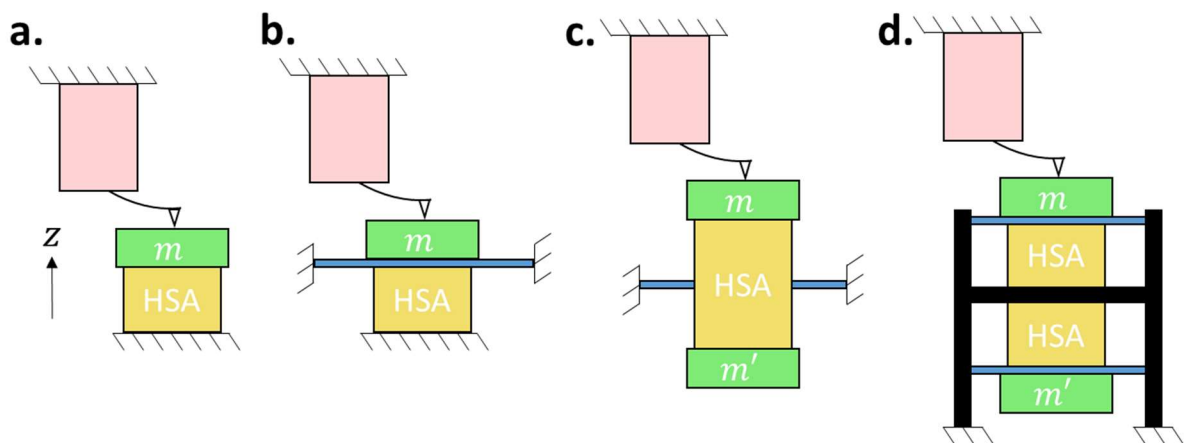


Figure 88: Mounting configurations for a high-speed piezoelectric stack actuator (HSA) with sample mass  $m$ : (a) fixed-free configuration, (b) fixed-free with flexure guidance, and (c) inertial cancellation with a dummy mass  $m'$ . The actuation direction is denoted by  $z$ . From [61]. In the first mounting (a), two problems can arise: bending of the structure if the height is bigger than the width of the HSA, and detachment when inertial forces cause the bonding/gluing to break. To prevent both phenomena, one can mechanically block the HSA with a pre-loading (chosen stronger than inertial forces can get) (b). The pre-loading also increases the stiffness in the Z-axis, raising the resonance frequency of the first resonating mode. In the third mounting scheme (c), inertial forces in actuation are compensated by design. In this configuration, the HSA is chosen 2 times higher in order to provide the same maximal displacement than previous designs. (d) Our actual mounting, in black is a rigid host body, it is detailed in next paragraph.

Mechanical design improvement can be provided by inertia balance (Figure 88c) with a dummy mass [175][61], providing a 2 times improvement factor on the positioner bandwidth [58]. To damp remaining vibrations, a filling polymer with a high loss factor can be used [175]. We followed those two ideas with our Z-positioner while characterizing results recording the resonance frequency response.

#### IV.3.2.1 Inertia-balance

It consists in 2 piezoelectrical actuators, each mounted in front of the other so that the inertial forces applied by the first piezoelectrical actuator are compensated, and thus not exciting other



mechanical parts. We used a rigid body host to implement inertia-balance (Figure 89), following work in [61].

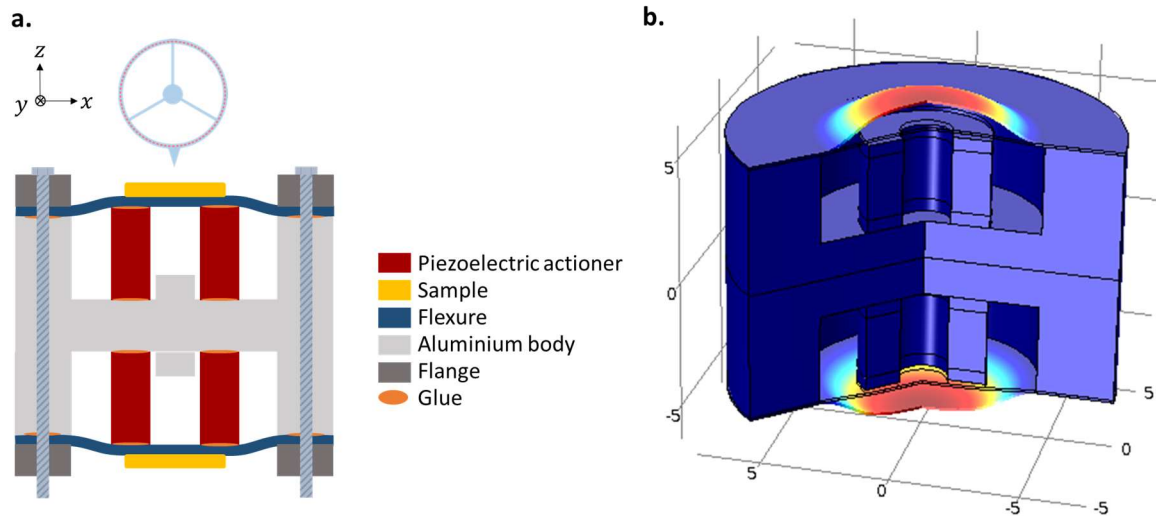


Figure 89: (a) Scheme of a vertical cut of the high speed Z-scanner structure. The OM probe is represented as a reference. The piezoelectric component (red) is a cylinder with a total diameter of 5 mm and a height of 3.5 mm, PICMA multilayer piezoelectric actuator from Physik Instrumente (PI) with insulating endcaps and with a resonance frequency of 500 kHz (ref: PD050.3x). A flexure (dark blue) preloads the piezoelectric component to gain in stiffness and thus in mechanical bandwidth as  $f = \sqrt{k_{eff}/m_{eff}}$ . This is an inertia balance scheme, with a “dummy” piezoelectric component to compensate for inertial forces applied by the first one when in operation. The glue between the flexure and the piezo and the body is necessary to prevent spurious resonances of the flexure itself. The height difference between the top of the aluminum body and the top of the piezoelectric component is 20  $\mu\text{m}$ . This value is critical as it changes the pre-load applied to the piezoelectric component. The pre-load value advised by the constructor is 15 MPa. As a guideline, to prevent blocking, it has to be lower than half of the maximal load that the piezoelectric component can develop. For a better-controlled height difference, the glue bonding of the flexure was done under pressure. The screw in the bottom are here to allow screwing to the XY scanner. The overall block dimensions are 2 cm x 2 cm x 1 cm. (b) FEM simulation with the Comsol software of such a structure, showing the flexure deformation. As a note, the final design used was a square one and not cylindrical as shown in this simulation.

The mounting and assembly of such a structure was conducted by L. Mazenq and S. Charlot and is depicted in Figure 90.

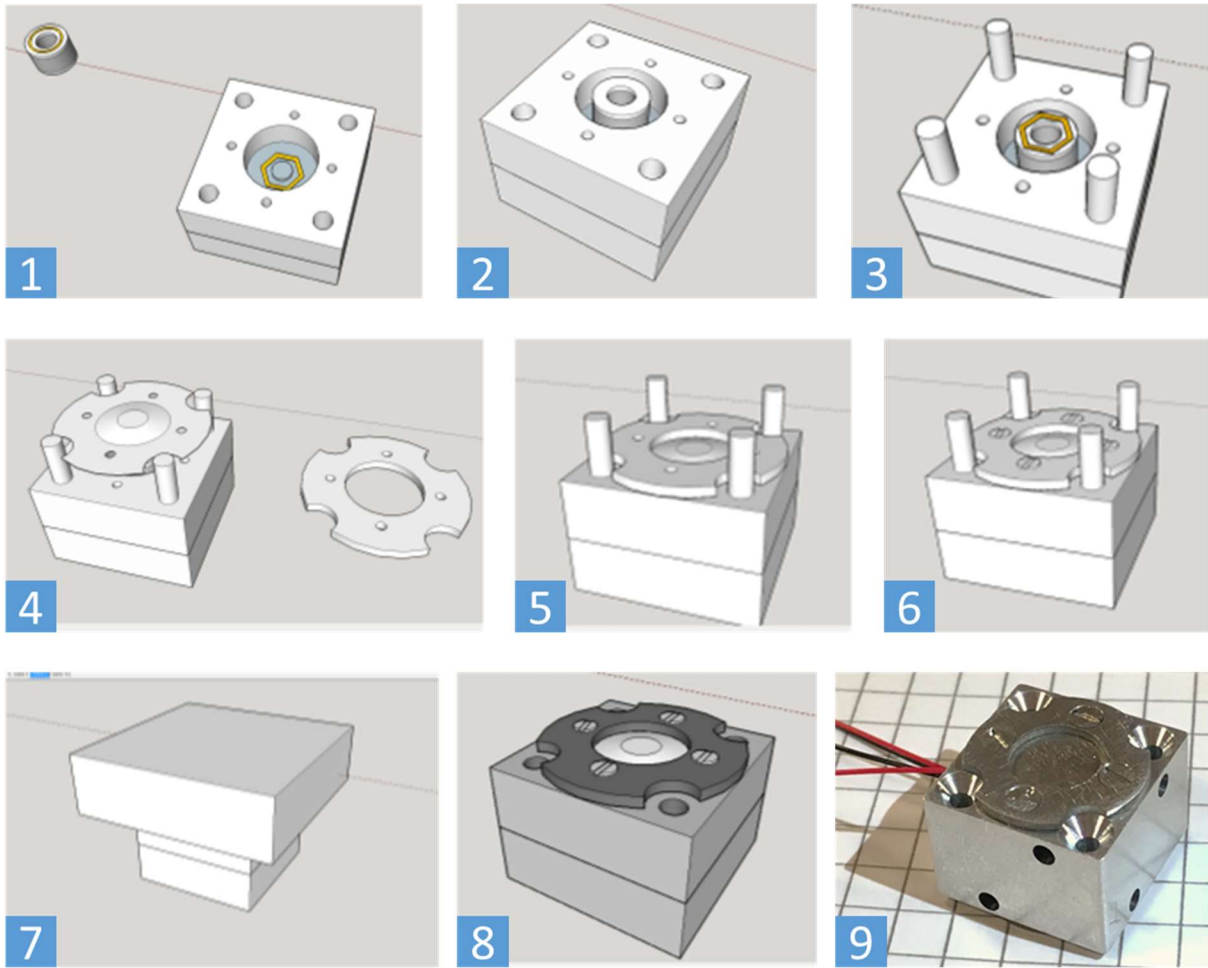


Figure 90: 3D models of the different steps of the assembly of the high bandwidth Z-actuator. 1) Glue is deposited on the cylindrical piezoelectric piece (left) and at the bottom of the aluminum body (right). 2) Both are assembled. 3) Glue is deposited on top of the piezoelectric actuator, poles are screwed on the side for future flexure guidance. 4) Flexure is assembled. 5) Flange is assembled. 6) Flange is screwed. 7) Glue reticulation is done with an applied pressure. 8) Final Z-actuator. 9) Real Z-actuator with the electrical connections to piezoelectric piece. The final block dimensions are 2 cm x 2 cm x 1 cm.

In practice, for our structure, the inertia-balance mounting scheme cancels one resonance out as expected, but leaves all the higher frequency ones (Figure 91).

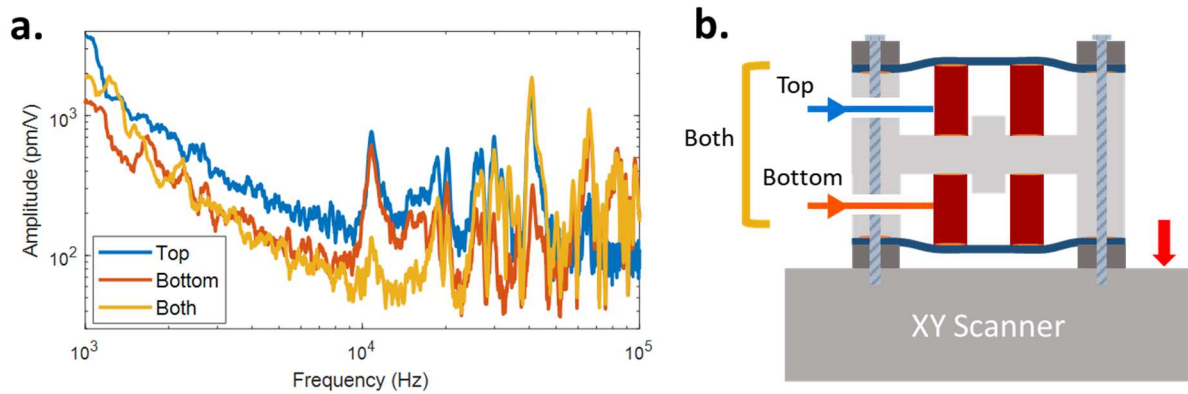


Figure 91: (a) Laser vibrometer measures of the frequency response of the XYZ scanner when fast piezo was excited. (b) Scheme of the different excitation configurations used for the graph. The red arrow represents the laser position, where the amplitude measurement is made with the laser vibrometer.

Looking at the first resonance at 10 kHz, that we attribute to a Z-resonance of the whole module, when both actuators are excited it damps the resonance effectively (yellow trace). However, for peaks of higher frequency, this is not the case. It follows approximately the absolute difference of the 2 curves indicating that the phase-shift between the two is negligible. But one can observe that initially both actuators individually do not have the same impact on the XYZ scanner and their difference is not constant over the full frequency spectrum. This is why the compensation is not fully effective and we attribute this discrepancy to slight mechanical displacement between the two actuators, breaking the symmetry of the structure. The slope on the left hand side is attributed to better transmission of the low frequencies from the Z-actuator module to the XY scanner.

To reach perfect compensation is non-trivial. Indeed, the two actuators do not have the same impact on motion, due to non-perfectly similar actuators, slight displacement between the two piezoelectric actuators or different glue repartition. For this reason, another technique was tested to get rid of the resonances.

#### IV.3.2.2 Damping polymer

Instead of compensating the inertial forces, one can damp them using a high loss material to cover moving parts. We tested the frequency response of this Z-actuator with and without a filling polymer with a high loss factor (Polyisobutylene). The damping provided a doubled bandwidth, from 32 kHz to 70 kHz (Figure 92), smoothing resonances out.

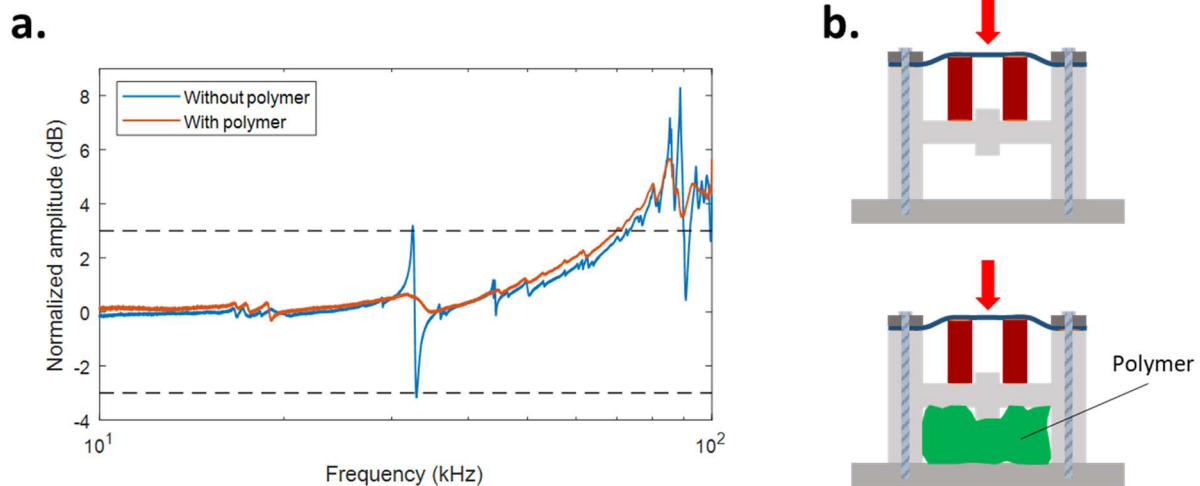


Figure 92: (a) Graph of the normalized amplitude of the Z-actuator versus its excitation frequency. One can observe that the polymer absorbs the first resonance energy, thus increasing the bandwidth from 32 kHz to 70 kHz. (b) Schemes of the different configurations used for the graph, the red arrow represents the laser position of the amplitude measurement with the laser vibrometer. The polymer used was mainly Polyisobutylene (patafix).

This damping was possible only because the 32 kHz resonance peak was associated with a resonance of the whole body of the Z-actuator (in light grey). It is important to note that those measures were conducted outside of the whole AFM instrument to be able to use the vibrometer. The Z-actuator module was screwed to a 67 g support. In the AFM instrument, the module is screwed to a XY piezo-controlled platform, the response of the whole should thus be slightly different. Compared to Figure 91, one can observe that there is considerably less resonances visible. This is because on this high-BW Z-module, the flexure was glued to the piezo component and the module's body, thus suppressing moving parts resonances.

To date, our Z-module, reaching  $BW = 70$  kHz nearly rivals the highest bandwidth Z-actuators in the literature, that reach  $BW = 100$  kHz [58][61] thanks to a  $3 \times 3 \times 3$  mm<sup>3</sup> piezoelectric ceramic stack of initial bandwidth 420 kHz<sup>64</sup>. The following results of this manuscript were obtained with this second damping technique configuration.

Apart from mechanical design, signal processing upstream of the actuator can provide a higher bandwidth.

#### IV.3.3 Signal processing

In signal processing upstream of the actuator, one can distinguish 2 techniques. The first is signal processing according to scanner, *i.e.* filtering out of the input signal the frequencies that excite the actuator resonances. The second is signal processing according to sample, *i.e.* adjusting the command with what the sample is expected to be, the expectation being built from earlier AFM images of the same sample.

<sup>64</sup> The overall system has an open-loop bandwidth of 150 kHz, using piezo components having up to 420 kHz bandwidth.

#### IV.3.3.1 Signal processing pre-scanners, according to scanners

For a given actuator with its resonances, one can modify the command signals upstream to damp or avoid them, thus improving their maximal operation frequency. To avoid those harmonics, one can filter them out of the command. Filtering the command can be done with a low-pass filter or a notch filter, or more specifically using an inverse function to compensate for the positioner's resonances [58]. The latter is presented in Figure 93.

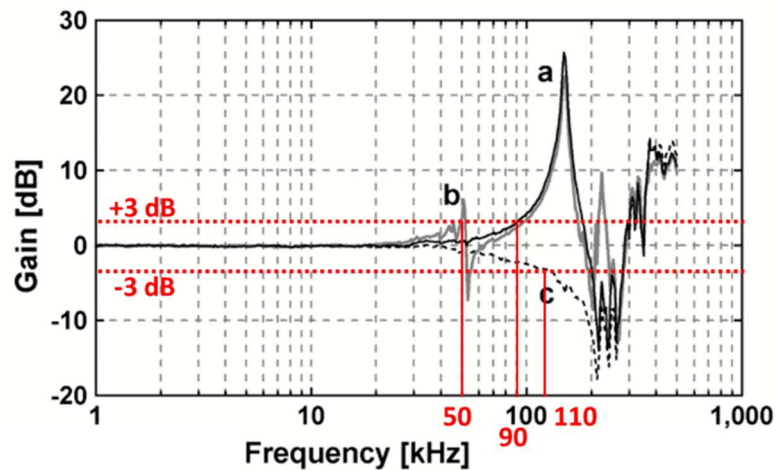


Figure 93: "Open loop transfer functions of the Z-scanner. (a) Without active damping and with counter balancing, (b) without active damping and counter balancing, and (c) with active damping and counter balancing." from [58]. Red lines were added to better read the BW of the different configurations.

It allows one to gain a few tens of kHz on the actuator BW.

#### IV.3.3.2 Signal processing pre-scanners, according to sample

As the tip goes raster scanning the surface, it does not know where it is going and whether the obstacles will need some large tip-surface distance adjustments or not. Another way of speeding the scanning is to adjust the positioner's controls according to previous lines. It can take the form of dynamic scanning speed [176]. Another example is a feed-forward technique implemented by Ando's team (p. 379 in [5]) which idea is to feed the Z-positioner with the PIDed error and to add the error from the last line. The result is a compensation for feedback delay.

### IV.4 High-speed scanning

Scanning operation is not in the feedback loop. It however can distort the image if used too fast and thus adds more performance constraints on the feedback loop. Indeed, as the high-BW Z-actuator seen above, the XY scanner also has resonances. For high-speed XY-axis scanning, a commercial E-363 PicoCube scanner was used with a  $\pm 2.5 \mu\text{m}$  XYZ travel range with XY resonance frequencies of 3 kHz (or 1.5 kHz when loaded with 20 g) and a Z resonance frequency of 10 kHz. Its upper stage was replaced by our custom High-BW Z-actuator (Figure 94).



Figure 94: Picture of our scanning apparatus. One can recognize the high-BW Z-actuator block at the top with its electrical connections. On the bottom is the commercial scanner E-363 PicoCube.

A limiting scanning effect for our structure was the scanner's X resonance, inducing a ringing distortion of the AFM image (Figure 95).

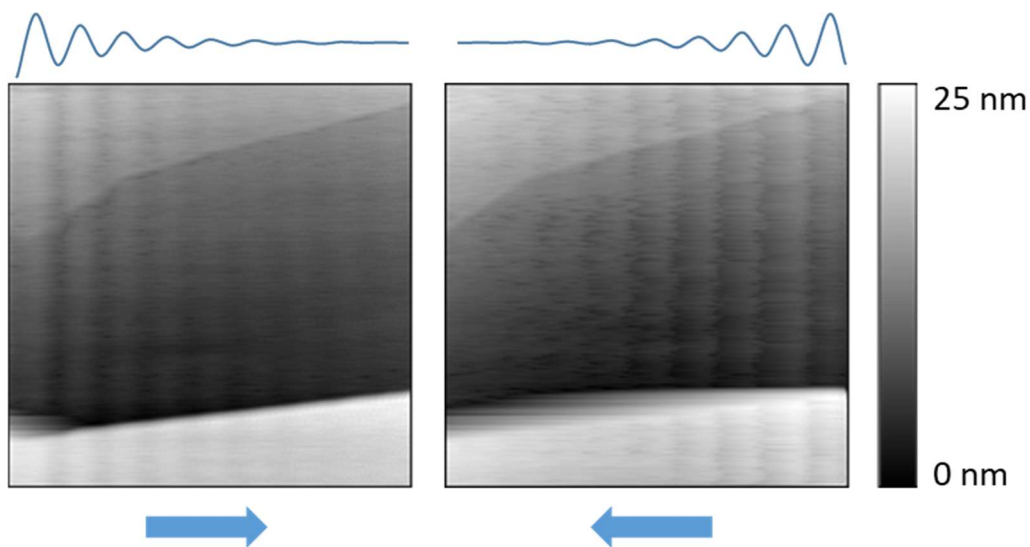


Figure 95: 185 nm x 185 nm forward and backward AFM images of an HOPG sample, taken with a Vmicro probe in our apparatus in 16 s. One can observe fringes respectively on the left and right-hand side of the images, highlighted by blue traces over the images.

This wave pattern in Figure 95 is perfectly synchronized with the raster scan, it therefore is associated to the ringing of the XYZ scanner in the X direction, either an X-axis resonance or a Z-axis one by cross-talk. Indeed, when the scanner of the fast axis reaches the border of the image, it brutally stops and goes back in the other direction. This brutal inertial energy change of the moved part (sample + Z-module) is important at the border and some of it excites resonances of the structure. Here, either a Z-resonance is excited and creates this pattern or an X-resonance is excited and appears on the Z measure because of the slope of the sample. This image was taken with an earlier High-BW Z-actuator design, the ringing associated is estimated at 250 Hz.

This image was taken with an earlier High-BW Z-actuator design. For newer, polymer-damped, design this ringing was not observable on AFM images. We however characterized the different resonances of it to know their relative magnitudes (Figure 96).

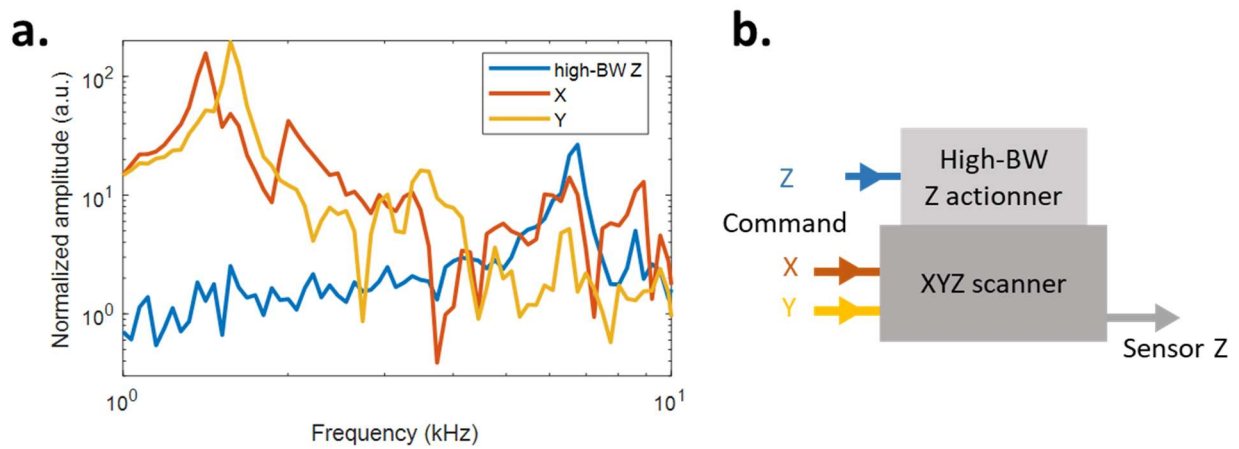


Figure 96: (a) Frequency responses of the XYZ scanner (PicoCube) loaded with the screwed high-BW Z-actuator. (b) Scheme of the set-up associated with the measures. The arrows represent the LIA inputs and outputs. The integrated capacitive sensor used for those measures has a bandwidth of a few kHz, its response was subtracted from those curves as a fitted 2<sup>nd</sup> order LPF of frequency 4 kHz. The high-BW Z-positioner was excited with a 400 nm peak-to-peak amplitude, the X and Y channel were excited with a 60 nm amplitude.

One can observe the X and Y resonances of the XYZ scanner (orange and yellow curves) around 1.5 kHz, as expected from the datasheet, highlighting the cross-talk between X, Y and Z axis. The XYZ scanner Z-resonance is at 6.5 kHz (blue curve), as expected from the datasheet. Looking at the amplitude of the curves, this explains the nature of the ringing effect when raster scanning: the harmonics of the scanning signal, fed to the fast scanning-axis signal, cross-talkingly excite the Z-motion of the high-BW Z-actuator and thus of the sample. The main resonances remain the X and Y-axis resonances of the XYZ scanner.

To prevent this ringing phenomenon and damp those resonances, one can use the same signal processing according to the actuator, shown in the previous part on the High-BW Z-actuator. For a typical raster scan, the X and Y positioners' signals are triangles. Considering a 100 x 100 pixels raster scan with a 100 kHz Z-bandwidth, the triangle signals frequencies are 1 kHz for the X-positioner and 10 Hz for the Y-positioner. But in the frequency domain, those triangles carry higher harmonics that can excite mechanical resonances higher than the kHz. To avoid those harmonics, one can filter them out of the command (Figure 97a) or change the scan pattern. Spiral scanning pattern (Figure 97b) provides a 4 times improvement factor on the scanning speed [177] compared to raster scan. This last two techniques are on-going developments on our apparatus, using a digital implementation of the scanning map.

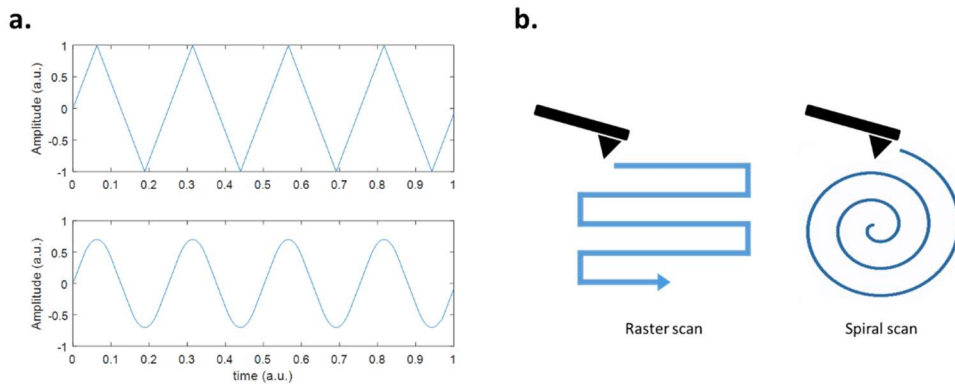


Figure 97: (a) Temporal traces of raster scan positioner command before (up) and after low-pass filtering (down). (b) Spiral scan pattern scheme

**Note:** One could also use piezoelectric positioners working at resonance to scan the sample, however speed would not be controllable.

#### IV.5 Transposition

As we use a 50 MHz-limited LIA to demodulate the 130 MHz mechanical resonance signal, we need a frequency transposition to be able to excite and detect mechanical motion (a higher bandwidth LIA is also a simpler option but a more expensive one, around 20 k€ more expensive<sup>65</sup>). A simplified transposition circuit is presented in Figure 98.

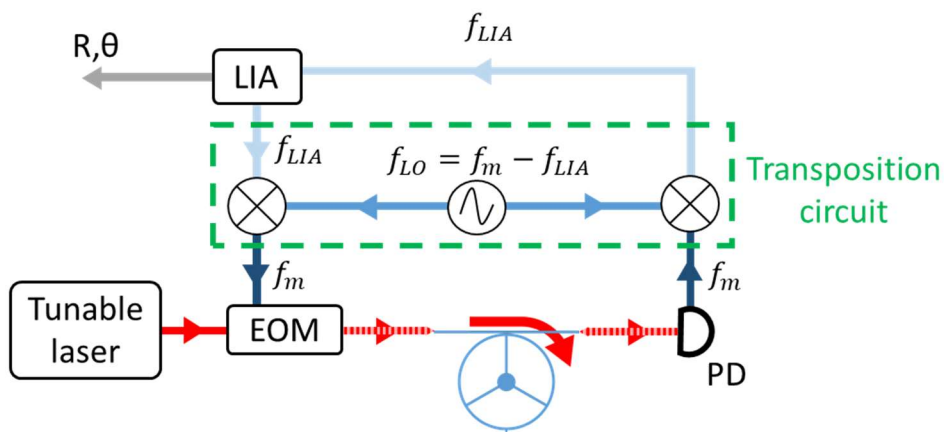


Figure 98: Scheme of the transposition circuit used in the case of the OM probe. It consists in a local oscillator (LO) modulating the excitation signal and demodulating the output signal with frequency mixers.

To choose the components of the transposition circuit, the constraints are given by the initial instruments (Local Oscillator LO, LIA, EOM, OM probe and PD) in/output powers and frequencies. We followed the advice given in the Minicircuits website [178]. Frequency mixers are designed for certain LO power. The output of a mixer is in general 7 dB lower than its input and the LO power should in general be 10 dB greater than the input power. Our LO can only deliver a maximum of 6 dBm, our LIA a maximum 14 dBm and to operate in linear regime the

<sup>65</sup> 20 k€ is approximately worth 6 months of a Ph.D. student. Given the good Ph.D. student can do the transposition circuit in much less time, transposition is a good deal.



EOM input needs to be lower than 10 dBm. Every component of the transposition circuit is detailed in Appendix C:.

This montage unavoidably adds noise to the signals. To quantify it, the transposition circuit was compared to a higher frequency LIA (Figure 99).

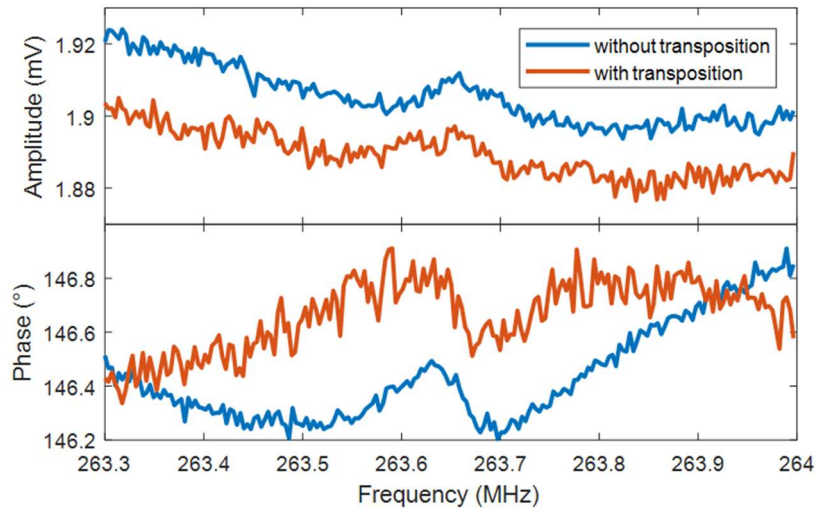


Figure 99: Amplitude and phase of a mechanical resonance at 263.65 MHz with and without transposition, all other things being equal. The local oscillator was at a 220 MHz frequency and the sweep was around 43 MHz. The orange amplitude trace was multiplied by a factor 3.27 and the orange phase trace was added a  $314.5^\circ$  offset so that both curves can be compared more easily. The transposition thus lowers the SNR from a 3.27 factor.

The transposition montage lowers the signal by about 10 dB, as expected from the mixers, but does not seem to add any noise to our experiment.

#### IV.6 Integration of the probe into the AFM

From silicon wafer to an usable AFM probe, one needs to etch a chip with the OM probe's tip protruding in order to image samples (Step 3 in Sec. II.6). This fabrication step follows the OM probe silicon etching at CEA-LETI. It was initially planned with a back-side deep reactive ion etching (DRIE) by IEMN/Vmicro as they already performed similar etching on larger scale device [89]. On the one hand, this back-side etch defines the overall “boat” shape (Figure 100, left-hand side) of each individual chip, with a back-side DRIE going all the way to the front side<sup>66</sup>. On the other hand, it makes the tip protrude over the substrate, with a back side DRIE stopping on the buried oxide (BOx) layer (Figure 100, right-hand side). This back-side DRIE is a state-of-the-art fabrication step and is still under developments. We discuss why in the next part and alternatives are discussed in the following.

---

<sup>66</sup> To define chips (*i.e.* dicing), other techniques exist as cleaving with KOH V-grooves [14] or laser cleaving.

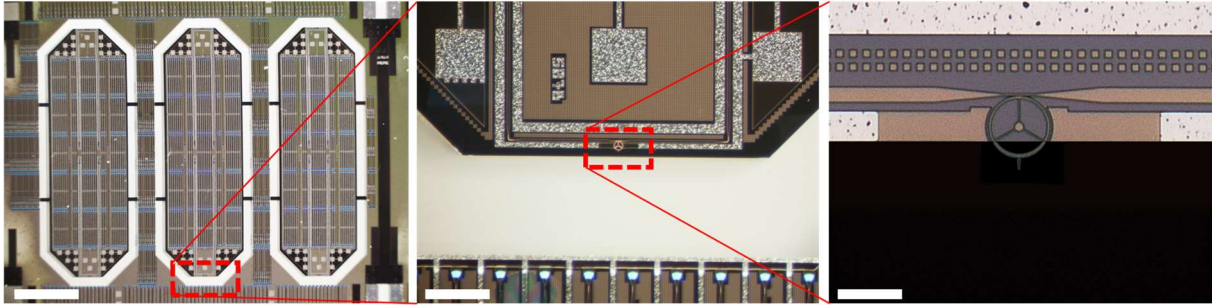


Figure 100: Pictures of an OM probe on its chip. On the left hand side image one can see 3 chips, still attached to the wafer. On the middle and right hand side images one can see the end of the “boat”, to etch before using the OM probe. The right hand side is an ideal case photomontage highlighting the protruding tip of the OM probe, one can imagine a surface coming from the bottom of the image. Scale bars from left to right respectively are: 1.6 mm, 130  $\mu\text{m}$  and 20  $\mu\text{m}$ .

#### IV.6.1 Protruding tip: getting rid of the substrate under the tip

We will first describe why the initial back-side DRIE was not successful. Then we discuss investigated and future alternatives, namely front side DRIE, Focused Ion Beam (FIB) etching, isotropic plasma etching and anisotropic wet etching.

##### IV.6.1.1 Initial back-side Deep Reactive Ion Etching (DRIE)

To make the tip protrude out of the chip, a DRIE back-side etch was planned. As it features a selective chemical etching, it etches the silica buried oxide layer at a rate negligible over the silicon etching.

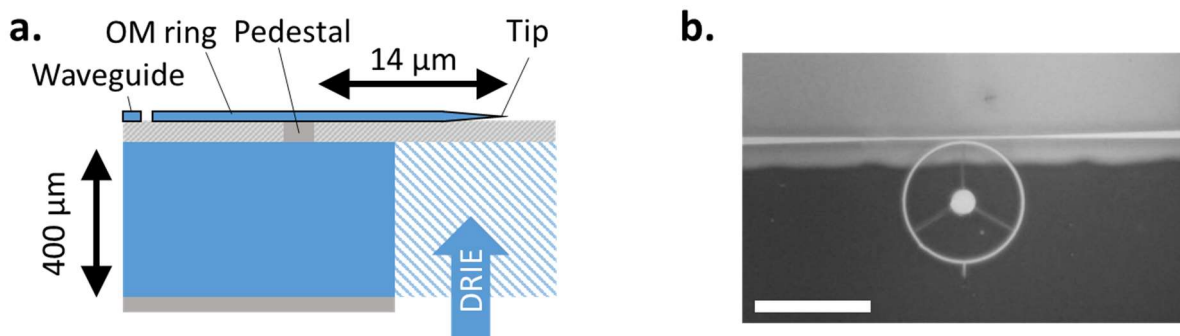


Figure 101: (a.) Cross-section scheme and (b.) picture of an OM probe silicon chip which has been etched with back side DRIE. (a.) One can observe the SOI stack of the wafer with its BOx layer in light grey and the future pedestal in grey. The back-side DRIE (blue stripes) is realized before the releasing, so that it stops on the buried oxide layer in light grey. The back-side DRIE is represented in blue stripes. (b.) One can see that the substrate (the blurred light-grey background) is over-etched, as its edge is not between the pedestal and the end of the tip. Scale bar: 20  $\mu\text{m}$ .

Looking at Figure 101a, if the back-side etch arrives before the end of the tip, the OM probe cannot image anything as its tip does not protrude, and if the etch arrives after the pedestal, the OM probe will fall after oxide etching. One thus understands that the back-side etch has to arrive in a  $\pm 7 \mu\text{m}$  window on the front side, between the end of the tip and the pedestal. This means that the etch edge on the back must be localized in a  $\pm 3.5 \mu\text{m}$  window and the DRIE must be vertical with an angle precision of  $\pm 0.5^\circ$  ( $\arctan(3.5/400) = 0.5^\circ$ ). On the right hand side, the picture displays an already etched device that is still standing on the BOx layer. Indeed the silica BOx layer is transparent to observable light. One can see that the substrate

below has been etched but after the pedestal. Therefore, the etching alignment constraint is lower than the fabrication process precision.

To relax the technological manufacturing alignment constraint, one could imagine reducing the thickness of the substrate, lengthening the tip or using larger radii OM probes.

- In practice, the initial 750  $\mu\text{m}$ -thick SOI wafer was already mechanically thinned down to 400  $\mu\text{m}$ . Reducing the thickness past this 400  $\mu\text{m}$  limit weakens the whole wafer, and 400  $\mu\text{m}$ -thick ones are already easily breakable (the ones we used often broke).
- As the tip is thin to limit optical scattering, lengthening the tip quickly exacerbates the mechanical movements of it as shown from mechanical simulation, to the point where it has the same resonance amplitude in the Z-axis (normal to sample) and X or Y axis (in the sample plane). Its maximum length was hence fixed to 5  $\mu\text{m}$  as a trade-off.
- Larger radii OM probes could be used. However as a guide-line, the optomechanical factor  $g_{O \leftarrow M} = -f_0/R$  is inversely proportional to the radius  $R$  (see Sec. II.4.1). Therefore, increasing the radius decreases the detection transduction factor.

Adding to this back-side DRIE complexity, its prerequisite mechanical thinning process disabled a lot of our devices by creating cracks in the top silicon layer (Figure 102a), in practice totally suppressing the optical transmission if the waveguides were damaged.

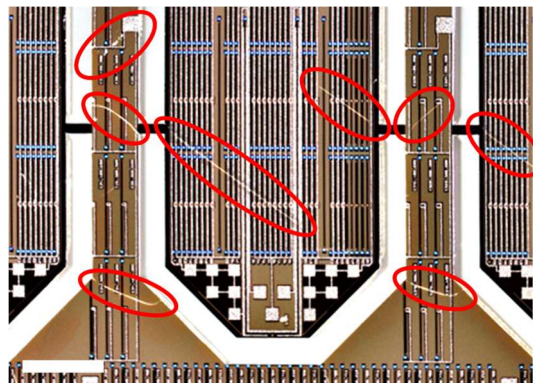


Figure 102: Picture of an OM probe chip still attached to its wafer. In red are circled cracks on the chip. Scale bar: 700  $\mu\text{m}$ .

To form new probes with new designs (e.g. with larger radii), one needs to start over the whole fabrication process which is long and demands adjustments. To replace this DRIE back-side etch, one can think of using a back-side anisotropic wet etch.

#### IV.6.1.2 Back-side anisotropic wet etching

Alike the initial back-side DRIE, one can use a backside anisotropic wet etching using TMAH or KOH as in [179]<sup>67</sup>. Anisotropic wet etching of silicon usually leaves the {111} planes visible. For our boat-shaped silicon chip with the long length in the [110] direction on a (100) wafer<sup>68</sup>, the etching walls are represented in Figure 103b. As a note, to protect the sensitive parts an

<sup>67</sup> To have precise details on and parameters of fabrication processes of similar device, the reader is referred to reference [179].

<sup>68</sup> As a reminder, [100] is a direction, <100> is a family of direction, (100) is a plane and {100} is a plane family.

anisotropic wet etch needs a top oxide resistant enough to withstand TMAH etching and protect the optomechanical structures, *i.e.* without voids, like thermal oxide. The deposited covering oxide we used had voids, creating fabrication difficulties in practice.

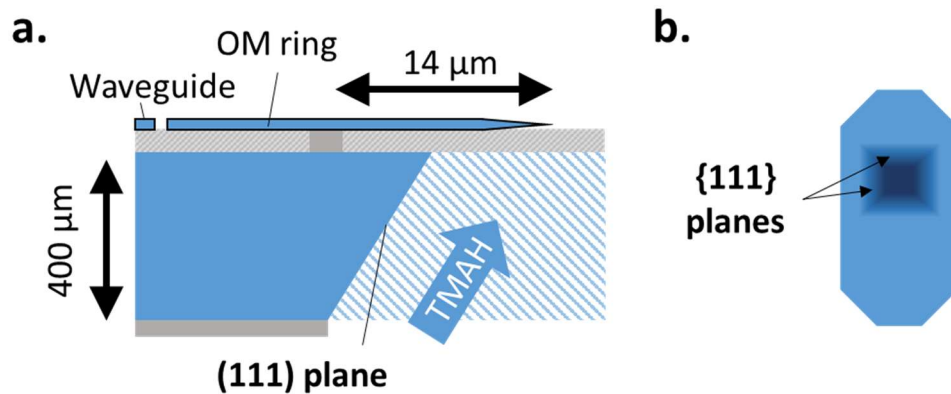


Figure 103: Schemes and picture of an optomechanical (OM) probe boat-shaped silicon chip. (a.) One can observe the SOI stack of the wafer with its BOx layer in light grey and the future pedestal in grey. The back-side anisotropic etch (blue stripes) is realized before the releasing, so that it stops on the buried oxide layer in light grey. The back-side anisotropic etch with TMAH is represented in blue stripes. The planes left by the wet anisotropic etch of silicon are the {111} planes. (b.) One can observe an anisotropic etch from the top as an example, on an OM probe chip.

But this back-side anisotropic wet etch would be hours long and it has the same alignment constraint than the DRIE back-side etch.

To bypass this back-side etch step and work with already fabricated device, a DRIE was performed on the front side of the wafer to form the “boat”-shaped chips (Figure 104).

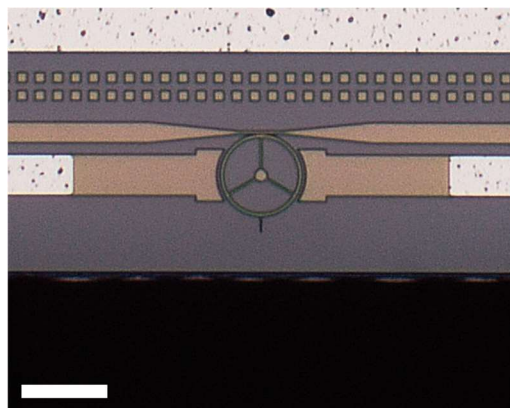


Figure 104: Picture of an OM probe. On this chip, a front side DRIE was performed, defining the boat-shape of the chip but not making the tip protrude. Scale bar: 20 μm.

From now on, we present investigated techniques and future techniques that can be used to obtain the protruding tip from a front DRIE defined chip. We list:

- Micro-milling and Focused Ion Beam (FIB) etching
- Local, side anisotropic wet etching
- Side anisotropic wet etching
- Side isotropic plasma etching
- Modified DRIE: front side isotropic plasma etching

#### IV.6.1.3 Micro-milling + Focused Ion-beam Etching (FIB) etching

Similar devices were realized with **micro-milling** machine at a 45° angle and Focused Ion Beam (**FIB**) etching [9][14]. The micro-milling gets rid of most of the substrate in a coarse etch. Then FIB allows fine etching of the substrate in the tip area. We tried those techniques in our lab.

**Micro-milling:** Back-side micro-milling was tested to get rid of most of the substrate and allow cleave. Using equipment in our LAAS laboratory, it is coarse with a 50 µm thick circular saw, the depth is only controlled in a 10 µm margin, significantly more than the oxide thickness of 1 µm and only vertical milling was available. Most of the substrate could be removed using this technique but not too close from the tip.

**FIB:** To locally etch the substrate under the tip, Focused Ion Beam (FIB) etching was tested before and after releasing the buried oxide layer (BOx). When etching before, the device was still covered with a thick protective oxide (or back-end oxide). This oxide prevents the observation of the OM probes and thus precise positioning of the etching. When etching after, the sputtered particles deposited on the tip, bonding it to the non-etched part (Figure 105).

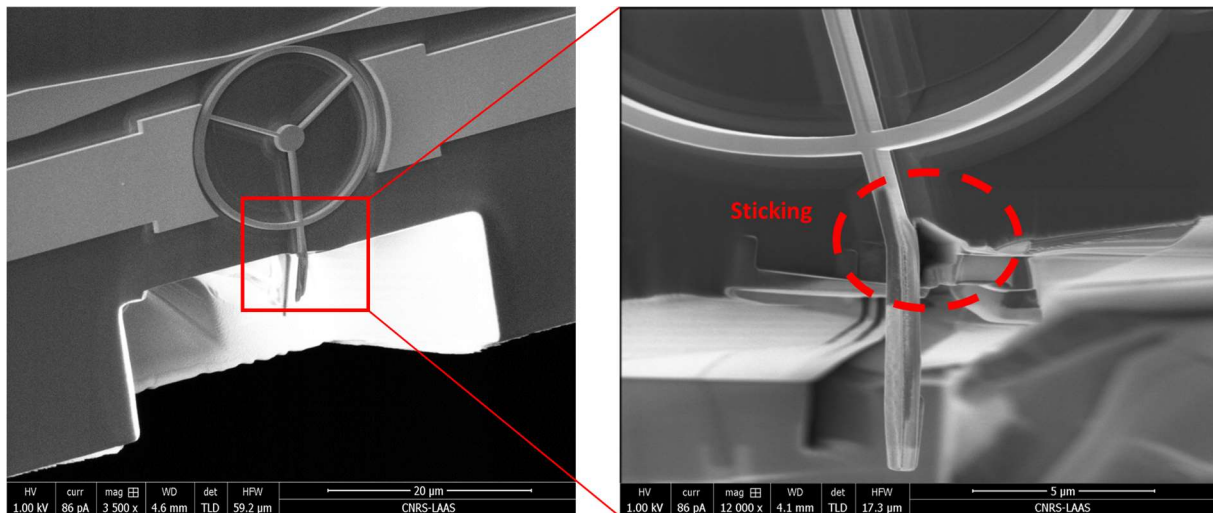


Figure 105: Scanning Electron Microscope (SEM) image of a FIB-etched window under the tip of an optomechanical probe. On the left-hand side, one can observe a slight tilt of the whole OM probe because its tip is sticking to the substrate. The zoomed image is taken from the other side; one can observe that the tip is thicker at the end, due to etched particles deposition when etching. The tip, which was hanging beforehand, could also have experienced a sticking force due to electrical charges created when etching with the FIB. This etch was done in a few hours.

Therefore, for this FIB etching technique to be effective, it must be realized before releasing the BOx to prevent particle re-deposition. The main drawbacks of this FIB etching are its slow etching rate and its non-negligible drifts for such dimensions. Consequently, a new DRIE cut of the boat-shaped chip was proposed, letting less substrate to be etched by FIB (yellow line in Figure 106).

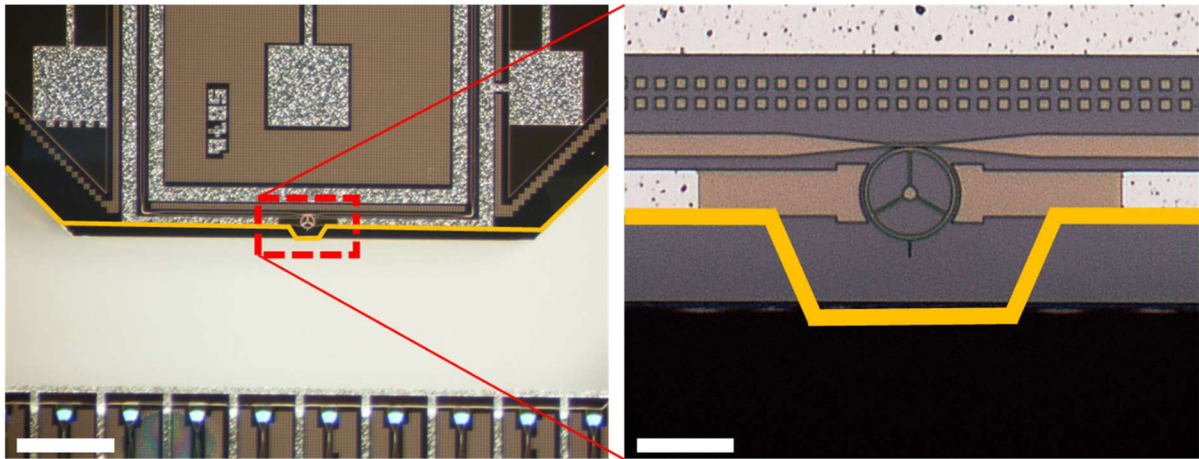


Figure 106: Drawing of the new front-side DRIE etch mask. It removes more substrate at the edge of the chip.

To date, no chip was fabricated with this new DRIE mask.

#### IV.6.1.4 Local front-side anisotropic wet etching (TMAH)

To use a front-side wet etch, one can use a modified boat-shape of the chip. The modification being a triangle shape in front of the ring to be etched by TMAH (Figure 107). This allows anisotropic etch from the side.

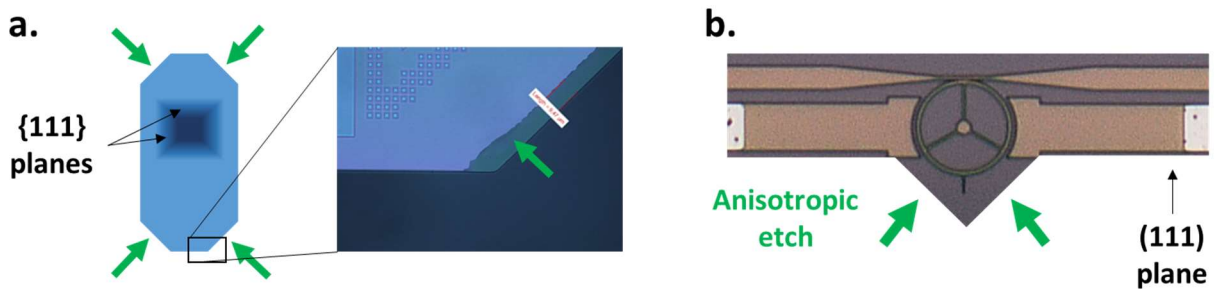


Figure 107: Schemes of an OM silicon chip. In green arrows is represented anisotropic etch. Its etching speed is ten times quicker on angled planes.

As the precedent technique, to date, no chip was fabricated with this new DRIE mask.

As a note, one could also consider a front-side anisotropic wet etching if the chips were fabricated with a new mask rotated with a 45° angle (Figure 108). This front side anisotropic etching would need the overall boat-shape to be defined beforehand. But this would imply to start over the whole fabrication process which is long and demands adjustments.

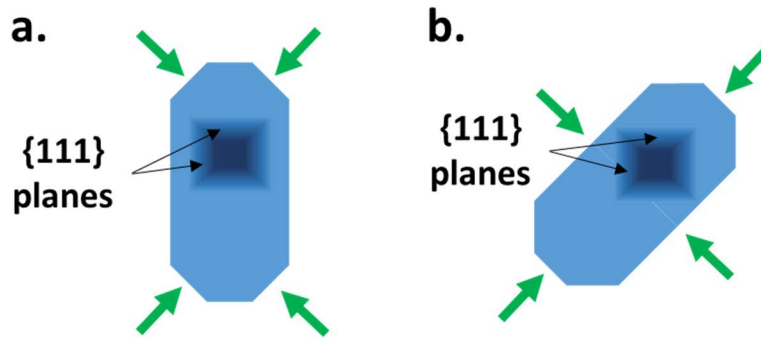


Figure 108: Schemes of (a.) the initial OM chip and (b.) the new OM chip with a fabrication mask rotated of 45°. Green arrows indicate the planes etched by anisotropic wet etching. (b.) This rotation allows the substrate under the tip to be etched by anisotropic wet etching.

#### IV.6.1.5 Anisotropic wet etching

TMAH does actually etch the {111} planes, however at a really slow pace. TMAH has an anisotropic selectivity  $\langle 111 \rangle / \langle 100 \rangle$  of 1/10, so that it can etch the substrate under the tip albeit ten times slower than the  $\langle 100 \rangle$  etching (Figure 109). This etch would require an even better or thicker oxide as it is slower and thus more likely to etch the top silicon layer.

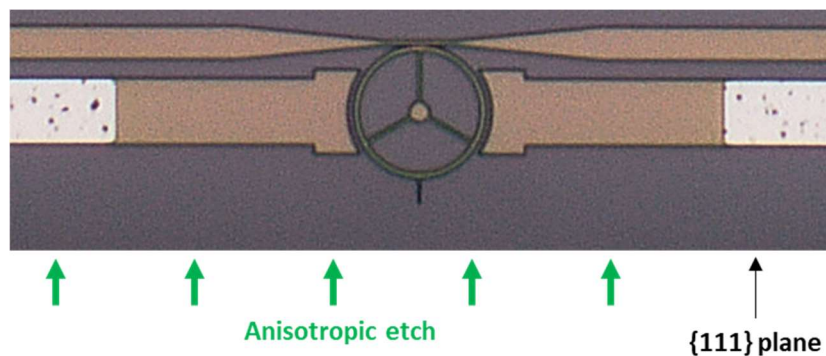


Figure 109: Scheme of the end of an OM chip. In green arrows is represented anisotropic etch.

#### IV.6.1.6 Side isotropic plasma etching ( $SF_6$ ).

As the front-side DRIE leaves about only 10  $\mu\text{m}$  of substrate in front of the tip (Figure 104), isotropic plasma etching could be used to etch the remaining micrometers from the side of the chip (Figure 110). Isotropic plasma etching has a Si/SiO<sub>2</sub> chemical selectivity of 40/1 [180]. Therefore, a 250 nm SiO<sub>2</sub> protective layer is needed on the front side in order to etch the 10  $\mu\text{m}$  substrate. As a reminder, this step could be performed only after a front-side DRIE etch of the chips

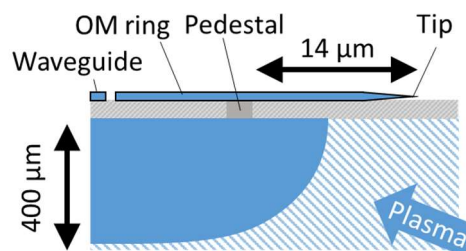


Figure 110: Scheme an isotropic plasma etch of the OM silicon chip. In blue is the etched chip and in striped blue the initial chip. The thickness of the chip is magnitude orders over the few micrometers to etch from the side of the chip.

#### IV.6.1.7 Modified DRIE: front side isotropic plasma etching ( $SF_6$ ).

The DRIE consists in a Bosch process alternation between isotropic etch and wall passivation, resulting in overall vertical etching walls. By slightly increasing the isotropic etching time of the first step, one could etch the substrate under the tip (Figure 111).

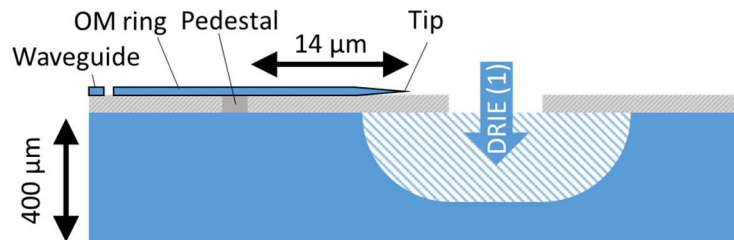


Figure 111: Scheme of the first step of a front-side DRIE. In blue is the etched chip and in striped blue the initial chip.

This last technique was tested in the IEMN laboratory by Marc Faucher with promising results, but is still under developments.

To resume, we presented on-going fabrication developments and future techniques to make the tip protrudes but no functioning OM probe was fabricated with those techniques. This prevented our fabricated OM probe to approach any surface. We will see that to bypass this substrate problem and perform mechanical perturbation experiments, another AFM tip was used, as described in Sec. V.

#### IV.6.2 Sensor integration: optical and electrical interconnects

As the OM probe presented needs a tunable laser and a photodiode to transduce the optical signal to an easier processed electrical signal, it needs integrated optical interconnects to the aforementioned laser and photodiode. Optical fibers are generally used to convey the optical signals but how are they coupled to the OM probe silicon chip and more precisely the waveguides? Two techniques are actually available:

- V-grooves (edge coupling): substrate in front the waveguide is etched in a V-shape, allowing one to place a fiber end in the slot and precisely align the fiber core with the chip waveguide (Figure 112a). To have optimal coupling, the silicon waveguide can feature an inverted taper and a lensed fiber can be used to focus laser light yielding typical losses below 1 dB [181].
- Gratings + Ferule (top coupling): a periodical pattern is etched in the silicon waveguide, it deviates the light with an angle out of the chip by diffraction. Light is then collected by a fiber on the top on the chip (Figure 112b). To ensure mechanical stability, the top fiber is usually maintained by a ferule glued on the chip (Figure 113). As it is a diffraction phenomenon, different wavelengths are diffracted at different angles and a stable fiber only provides a typical 50 nm bandwidth [182]. Typical losses are below 3 dB [182].



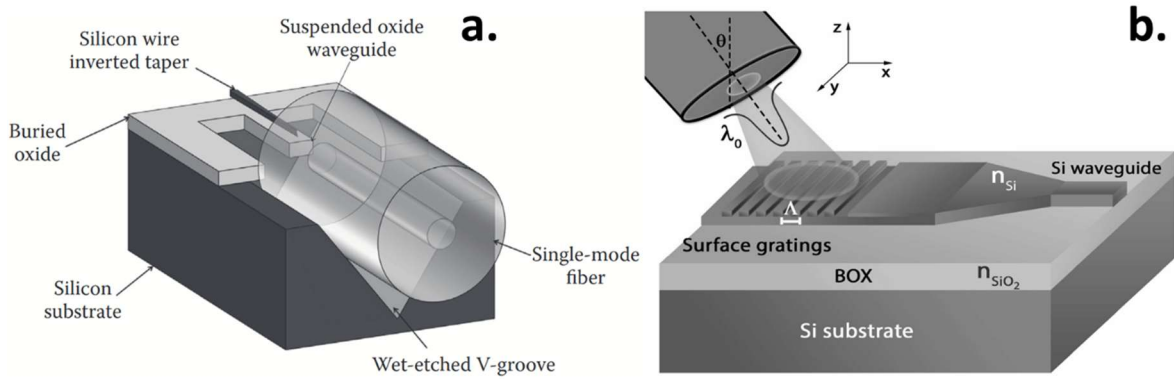


Figure 112: Schemes of (a) a V-groove coupled fiber (from p. 108 in [183]) and (b) a grating coupled fiber to a SOI (silicon on insulator) chip [182].

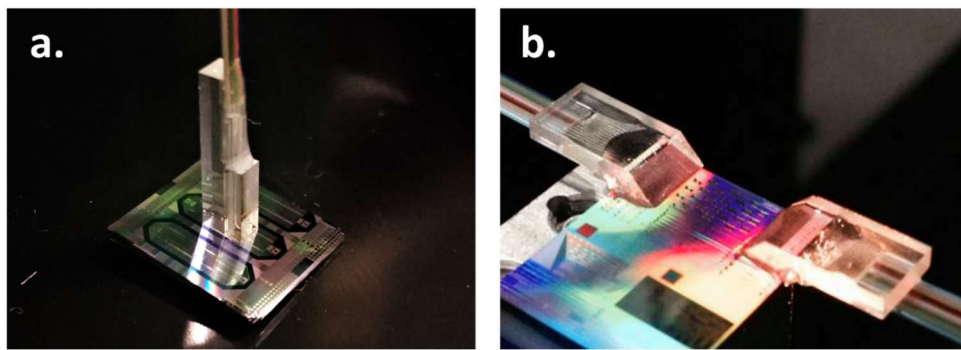


Figure 113: Picture of fibers grating coupled to photonic chips. (a) Straight ferule featuring 5 fibers connected to an OM probe. (b) Quasi-planar ferule featuring 12 fibers [184].

The device presented in this manuscript were grating coupled with a glued straight ferule (Figure 113a), displaying an overall transmission (or injection) loss of 7 dB, that is to say 3.5 dB per grating coupler<sup>69</sup>. We will now briefly describe the theory behind a grating coupler.

#### IV.6.2.1 Grating coupler focus: patterns and dimensions

The angle of the light path out of the chip depends on the pattern used and their dimensions (etch depth, pattern length  $a$  as shown in Figure 114b and filling factor). We used curved grooves which dimensions are displayed in Figure 114a<sup>70</sup>.

<sup>69</sup> This value is the packaged one, where the optical fiber is glued on the chip. It is state of the art.

<sup>70</sup> Sub-wavelength gratings can also diffract light [182].

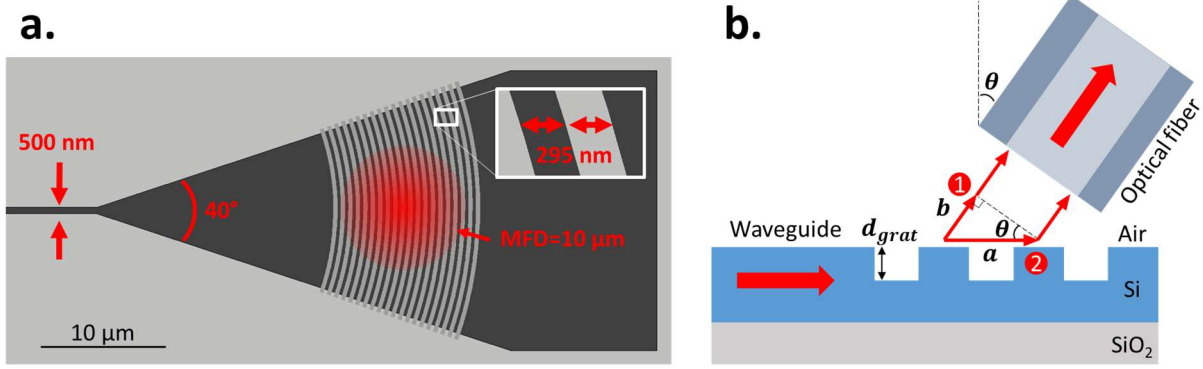


Figure 114: (a.) Top-view scheme at scale of the grating coupler used in the device tested in this manuscript. A typical fiber mode field diameter (MFD) is drawn over the grating; its value is taken from [185]. In dark grey is the 220 nm thick silicon layer and in light grey is the SiO<sub>2</sub>. The curved grooves have an etch depth of about 100 nm. (b.) Profile-view scheme of the grating coupler.

The formula giving the diffraction angle is the constructive interference condition, looking at Figure 114b, the phase of two diffracted rays are in phase if  $\phi_2 = \phi_1 + m2\pi$ :

$$k_{grating}a = k_{air}b + m2\pi \quad (67)$$

$$n_{eff}a = n_{air}b + m\lambda \quad \text{with} \quad b = a \sin \theta \quad (68)$$

Where  $m$  is the diffraction order and the effective index in the grating area  $n_{eff}$  depends on the etching depth  $d_{grat}$  and the filling factor  $f$ <sup>71</sup>.  $a$ ,  $b$  and  $\theta$  are defined in Figure 114b.

Our grating etching depth is  $d_{grat} = 70$  nm for 220 nm silicon thickness (and  $d_{grat} = 200$  nm for 400 nm silicon thickness) and the grating period is  $a = 590$  nm with  $f = 1/2$ . It induces an approximate  $n_{eff} = 2.7$  leading to a fiber angle for the first order diffraction ( $m = 1$ , actually no other mode is supported)  $\theta = 5^\circ$  (nearly normal to the chip as seen in Figure 113a). As a note, the coupling angle is highly dependent on the etch depth, a 10 nm over-etch can for example lead to a  $2^\circ$  mismatch.

Now that we saw how the OM probe is optically connected to the instrument by fibers, we will see how it is mechanically mounted in it.

### IV.6.3 Mounting

A few mounting tips prevent the OM probe chip to accidentally touch the sample. The edges of the boat-shaped chip can touch the sample if the chip is not mounted perfectly vertical. With a theoretical protruding tip length of  $L_{protruding} = 7$   $\mu\text{m}$  and a half boat width of  $w_{boat} = 250$   $\mu\text{m}$  (Figure 115a), the operating window angle is  $2\alpha = 2 \times \text{atan}\left(\frac{L_{protruding}}{w_{boat}}\right) = 3.2^\circ$ . To prevent any misalignment, the aluminum piece on which the silicon chip is glued has an etched guide for the chip to be along to (Figure 115b). The mounting piece is also angled so that the back-side of the chip does not touch the sample (Figure 115c).

<sup>71</sup> The effective index of the grating is given by  $n_{eff} \approx fn_{no\_etch} + (1 - f)n_{etch}$ .  $n_{no\_etch}$  and  $n_{etch}$  being respectively the effective index of a slab of thickness  $h$  and  $(h - d_{grat})$ . The intermediate  $n_{no\_etch}$  and  $n_{etch}$  can be handily found via the online calculator of  $n_{eff}$  for a slab in [192].

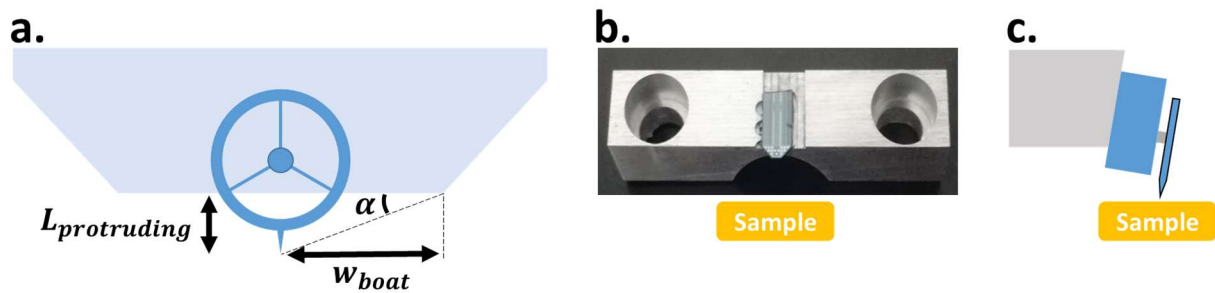


Figure 115: (a.) Scheme of the OM probe at the end of its silicon chip. (b.) Aluminum piece with a half OM “boat” chip mounted on. A hole is etched in the back of the piece to allow backside visualization. (c.) Cross-sectional scheme of the (b.) mounting. The piece is angled so that only the tip, and not the blue substrate under it, touches the sample’s surface.

With an optically connected and mounted OM probe in the AFM instrument, we were able to perform mechanical contact experiments.

In this chapter, we presented developments on the fast AFM instrument components: LIA, feedback control and in the fast Z-actuator that demonstrated a bandwidth of 70 kHz. We also presented the integration of the high-frequency OM probe in this instrument, from transposition RF circuit to optical interconnects with gratings and to fabrication steps leading to the protruding tip. The latter are still under developments and we consequently had to find an alternative solution to test the mechanical behavior of the OM probe.

## V. Towards OM AFM

As the substrate under the probe was not successfully etched up to the writing of this manuscript, no image of a sample surface was yet acquired with our AFM. However, we were able to work around it and study the mechanical behavior of the OM probe by using a classical AFM cantilever (Figure 116). It allowed to poke the OM probe without the need for it to protrude. In this part, contact detection is demonstrated through approach-retract curves and quantified to drive physical insights on the contact behavior in vacuum and in air (water meniscus, regime of forces, etc.). Then feedback operation is demonstrated in air to find the maximal feedback loop bandwidth in practice. Finally, to prove that our instrument can already provide images, a pseudo OM-AFM image of the classical cantilever tip is demonstrated.

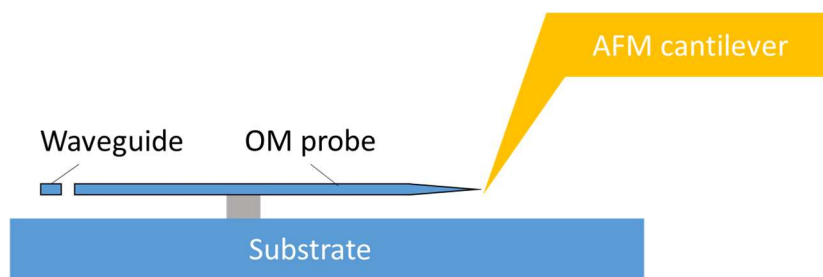


Figure 116: Scheme of the AFM cantilever poke experiments configuration, in a profile view. As the substrate under the OM probe was not etched, a gold-coated AFM cantilever was used to mechanically interact with it.

### V.1 Mechanical interaction detection in point mode

To prove that this OM probe can detect a mechanical interaction, we poked it with another AFM cantilever tip and monitored its mechanical resonance. First, we present the experimental set-up and the results obtained as approach-retract curves, where the mechanical resonance frequency of the OM probe is monitored while the cantilever tip is brought in and out of contact (Figure 117). This experiment was done twice, the first time manually in vacuum with the cantilever tip perpendicular to the OM tip and the second time in the AFM instrument in air with the cantilever tip facing the OM tip. In the second part, the frequency shift associated with contact is fed back to the Z-actuator to control the tip-sample distance, stable feedback is demonstrated.

#### V.1.1 Approach-retract curves

##### V.1.1.1 In vacuum

To better grasp what is the expected behavior of the mechanical resonance in contact, the reader is referred to Sec. II.5.

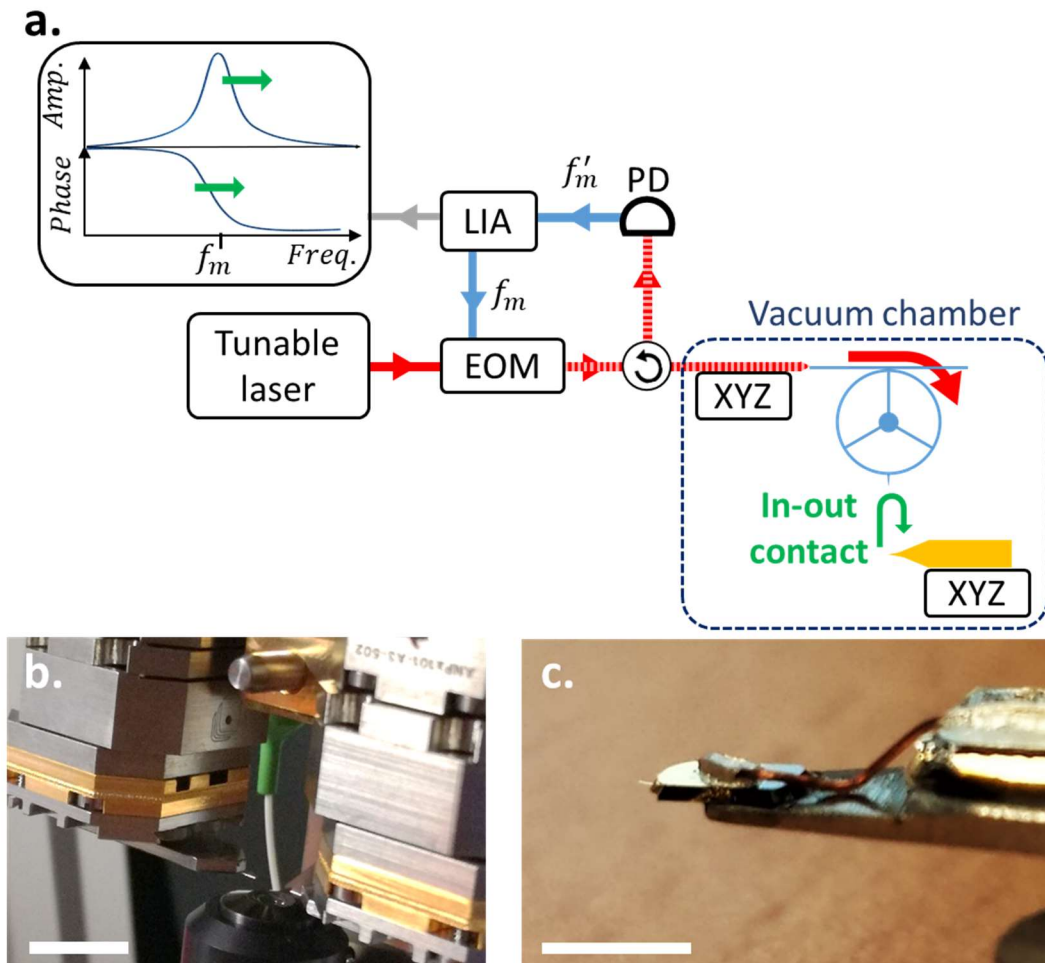


Figure 117: (a) Experimental set-up to assess mechanical interaction detection with an OM probe. The XYZ blocks represent piezoelectric stacks, allowing to place the fibers in front of the silicon chip. When in contact, the mechanical resonance frequency is expected to go up. (b) Picture of the inside of the vacuum chamber. One can see the black microscope objective at the bottom and just over the fibers injecting and collecting laser light. Actually for this experiment, one of the fiber was replaced by the AFM cantilever seen in (c). Both of the fibers are mounted on XYZ piezo stacks (right and left hand sides of the picture). The sample is positioned in between the fibers with a holding piece mounted on the golden pimple at the top of the picture. Scale bar: 2 cm. (c) Cantilever tip mounted on the fiber holder, with an electrical connection. Scale bar: 5 mm.

As a note, for this experiment, cleaved facets OM chips were used (see Appendix G: for more details). One can think that this experiment was only possible in reflection because of the reflection of cleaved facet. Nevertheless, it could potentially have been made in reflection with a fibered chip through grating couplers, with less reflection. Indeed, thanks to the CCW optical mode some optical power is reflected back to the injection fiber. The result associated with this experiment is displayed in Figure 118.

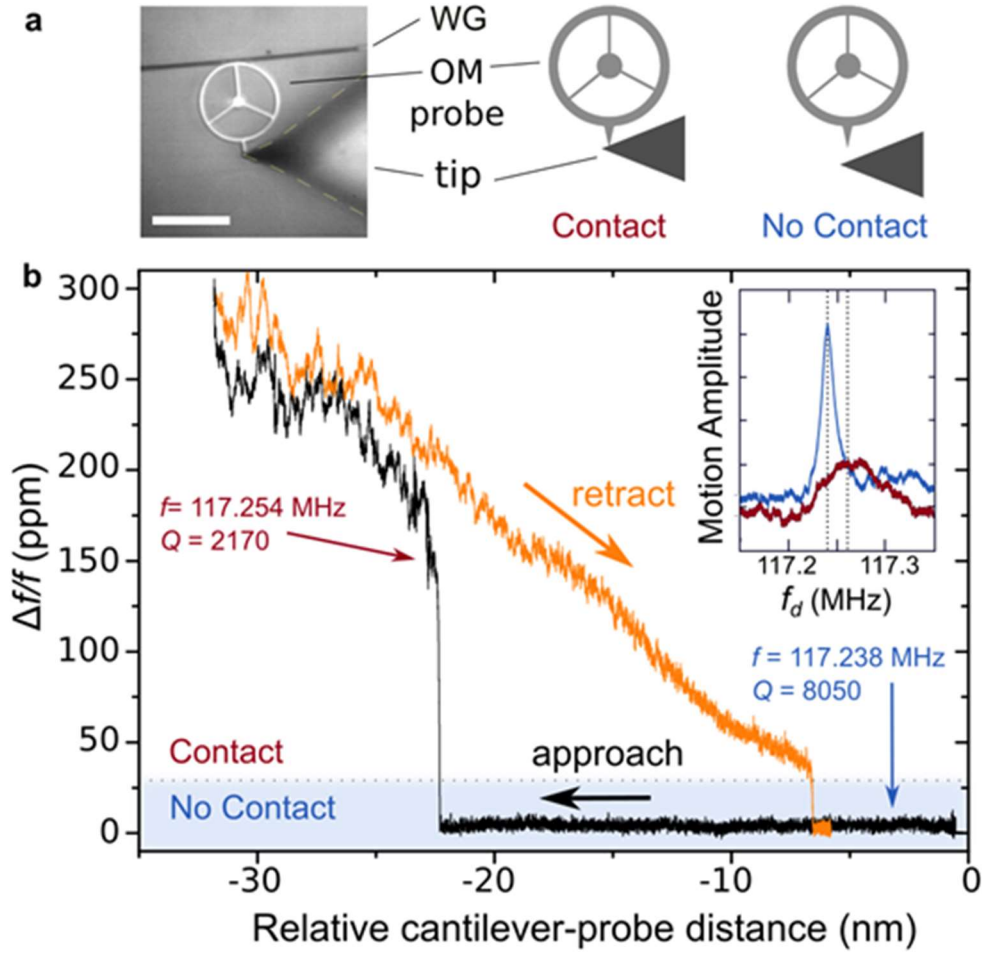


Figure 118: (a) Picture and schemes of the mechanical configuration. Scale bar 20 μm. (b) Normalized mechanical frequency shift according to the tip-OM probe distance.<sup>72</sup>

The golden tip is first approached (in black) until the contact, indicated by abrupt frequency shift. It is then retracted (in orange) until contact is broken and the frequency shift goes back to its rest value. Inset shows the mechanical resonance behavior in (blue) and out (red) of contact. The red curve is frequency shifted to the right, as expected for a repulsive force gradient, and is damped as expected from contact. This experiment was performed under secondary vacuum with a LIA LPF bandwidth of 100 kHz.

The first value hit by the frequency shift in contact (150 ppm) gives insight on the tip sample interaction. Following equation (41), the corresponding force gradient, or stiffness, is  $k_{ts} = \frac{2k_{eff}}{f_m} \Delta f_m = 810$  N/m. The  $k_{eff}$  stiffness of this probe was simulated to be 2 700 kN/m and its one  $k_{static} = 18$  N/m. In the next paragraphs, we first find which structure is bending in contact and when the jump-to-contact condition is met by static consideration. Then, we

<sup>72</sup> To evaluate measurements coherence, one can observe that the deviation of the normalized frequency shift is about  $10^{-5}$  out of the resonance, lower than the expected value  $10^{-4}$  extracted from the Allan deviation in Figure 72 in Sec. III.4.2, for  $\tau = 10^{-5}$  s associated to the LPF bandwidth of 100 kHz. This little discrepancy is partly explained by the higher driving modulation used in this contact experiment (750 mV applied on the EOM and 200 mV in the Allan variance). We also attribute this difference to a higher laser power used in this experiment, yielding a better SNR.

compare the recorded force gradient to the expected one extracted from the force profile in a dynamic consideration.

- Static considerations: static stiffness ( $k_{static}$ ), attractive force and jump-to-contact

The jump-to-contact (*i.e.* when both surfaces slip into contact due to attractive forces) appears when the attractive force gradient is stronger than the lowest static stiffness involved. We will first find the lowest static stiffness and then evaluate attractive forces to find when this jump happens.

When the probe is brought to contact, the lowest static stiffness of the structure will bend, it can either be the pedestal, the spokes and ring or the sample (Figure 119). Those bendings limit the maximal force applied to the probe.

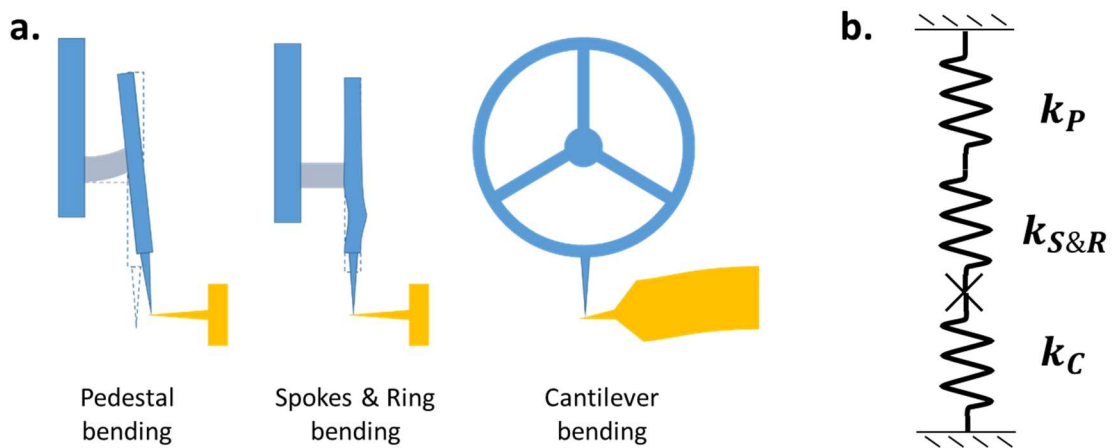


Figure 119: (a) Schemes of the possible bendings of the OM probe structure when brought in contact. In practice, one is negligible over the others and this lowest stiffness is the one in motion. Typical deformations amplitude is a few nanometers or less. (b) Equivalent scheme of the static contact represented by the black cross, each stiffness is associated with the schemes in (a).

Following the notation of Figure 119, we define the overall contact static stiffness as  $\frac{1}{k_{contact}} = \frac{1}{k_P} + \frac{1}{k_{S\&R}} + \frac{1}{k_C}$ .

For complex structures, FEM simulations are preferred to find the stiffness. However for simple ones, analytical formula can be used. We used the formula of the stiffness of a simply-clamped beam of rectangular section, at the free end, perpendicular to the beam in the thickness plane [186]:

$$k_{beam} = \frac{E \times w \times t^3}{4L^3} (1 - \nu^2) \quad (69)$$

$E$  being the Young modulus of the material,  $w$ ,  $t$  and  $L$  respectively being the width, thickness and length of the beam. The Poisson coefficient  $\nu$  can be neglected in first approximation.

The stiffness of the cantilever given by equation (69) is  $k_{golden\_tip} = 123 \text{ N/m}$  (Figure 119a). The pedestal bending is similarly calculated:  $k_{pedestal} = 700 \text{ kN/m}$ . For the spokes and ring

bending, we find a simulated  $k_{S\&R} = 18 \text{ N/m}$ . Therefore, it is most likely the spokes and ring that bend when the golden tip is put closer<sup>73</sup>. From now on, we will consider the total static stiffness of the contact to be  $k_{contact} = 18 \text{ N/m}$ .

### Attractive force

The jump-to-contact is most likely caused by attractive Van der Waals forces in vacuum. One can approximate them with equation (2):  $F_{VdW/sphere-plane}(z) = -\frac{HR_{tip}}{6z^2}$ . Here, we make the assumption that the OM probe tip is a sphere and the cantilever tip a plane as the first radius of curvature is about 50 nm and the second is 200 nm, thus slightly over-estimating the attractive force. This leads to a force gradient profile:

$$\frac{d}{dz}F_{VdW/sphere-plane}(z) = \frac{HR_{tip}}{3z^3} \quad (70)$$

The contact forms when the attractive force gradient is stronger than the lower static stiffness involved, in that case the one of the probe  $k_{static} = 18 \text{ N/m}$ . For a 50 nm tip radius and for  $H = 3.5 \times 10^{-1} \text{ J}$ <sup>74</sup>, this gives a tipping distance of 0.7 nm<sup>75</sup>.

To further validate this statement, we will follow the same reasoning but for the effective stiffness. That is, find a model which gives a stiffness profile that match the experiment and thus extract the equilibrium distance.

- Dynamic considerations: effective stiffness  $k_{eff}$ , repulsive force and equilibrium

From Figure 118, we obtain the value of the equilibrium repulsive force gradient: 810 N/m. That is to say the force gradient felt by the tip when in contact, it is repulsive as the frequency shift is positive (see Sec. II.5). This value is the force gradient felt by the OM tip at its resonance frequency at 117 MHz, it thus cannot compare to the static stiffness of the different component at play, too massy to follow the oscillation at this frequency. It rather compares with the local material stiffness, able to follow. To evaluate added stiffness to the tip, we use a Hertzian model as in Figure 120b, considering a sphere-plane interaction between a silica OM tip and a golden plane.

---

<sup>73</sup> This conclusion is highly dependent on the mechanical design of the device. Here we took a  $w_{ring} = 750 \text{ nm}$  and  $w_{spokes\&tip} = 500 \text{ nm}$  design with a pedestal diameter of 2.5  $\mu\text{m}$ . For others designs explored,  $k_{spokes}$  varied in a 1 to 1000 N/m range (see Sec. II.3.2).

<sup>74</sup> We chose a Hamaker constant in between  $H_{gold} = 4.5 \times 10^{-19} \text{ J}$  and  $H_{silicon} = 2.5 \times 10^{-19} \text{ J}$  [203], as shown by calculations over two different material interacting [204].

<sup>75</sup> For comparison, the lattice constant of gold is 0.4 nm and the one of silicon is 0.5 nm.



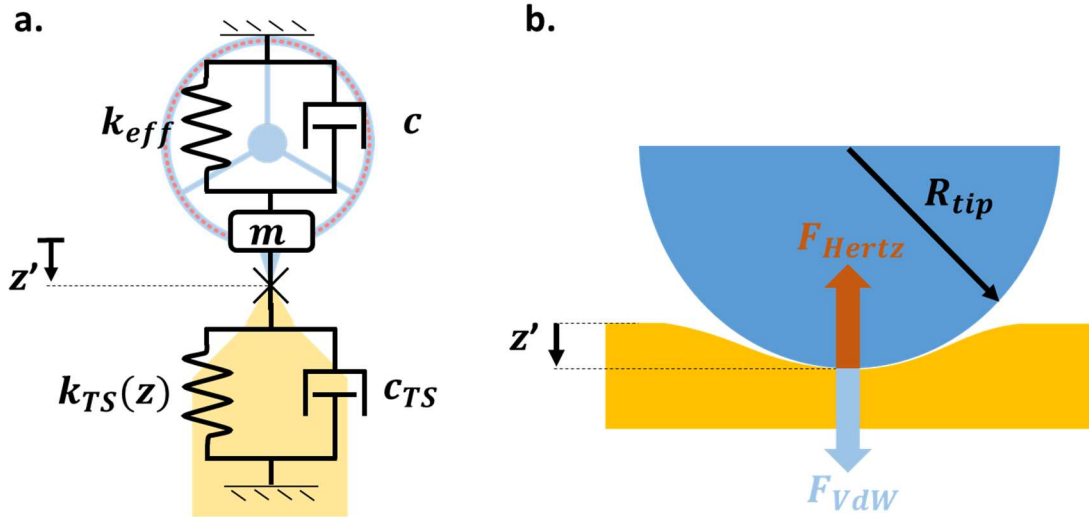


Figure 120: (a) Scheme of the general contact model. The OM probe is considered a spring-mass damped system and the surface a spring ( $k_{ts}$ ) - damping ( $c_{ts}$ ) system as defined in Sec. II.5. Contact is represented by a black cross. The  $z'$  position is the difference between the surface spring previous free position and its position in contact. (b) Scheme of the Hertzian contact featuring the OM tip in blue and the golden tip in yellow. The VdW force acts as a local attractive force, indenting the OM tip in the golden one. The  $k_{eff}$  variation with indentation is neglected. This scheme of contact is highly hypothetical, contact could also happen locally on a surface defect on the outermost part of the OM tip.

From the Hertzian contact one can find the expected force profile and stiffness when indenting [32]:

$$F_{Hertz}(z') = \frac{4E^*\sqrt{R^*}z'^{3/2}}{3} \quad (71)$$

$$\frac{d}{dz}F_{Hertz}(z') = 2E^*\sqrt{R^*}z' \quad (72)$$

With  $R$  and  $z$  the sphere radius and the indentation depth as defined in Figure 120 and with  $E^*$  the effective Young modulus (neglecting Poisson coefficient):  $1/E^* = 1/E_1 + 1/E_2$ , with  $E_1$  and  $E_2$  the Young moduli of both materials at play. Similarly,  $R^*$  is the effective tip radius when considering to spheres interacting:  $1/R^* = 1/R_{tip} + 1/R_{sample}$ .

One can observe that the Hertzian model gives the repulsive force for the indentation depth  $z'$  and the VdW model gives the attractive force for the distance between the two surfaces  $z$ . To match both, we consider that the VdW forces are fixed in contact (Figure 121), with a force dictated by the maximum lattice constant of both surfaces' materials<sup>76</sup>. Thus getting rid of the VdW divergence in contact. Choosing a minimal distance of 0.5 nm, we find with equation (2) the VdW sticking force in contact to be 11 nN.

<sup>76</sup> One could also choose the roughness.

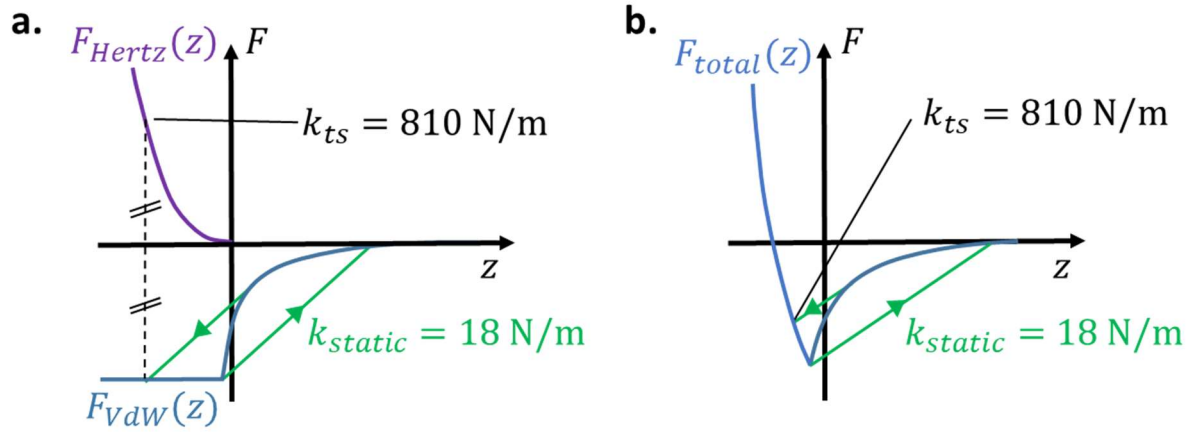


Figure 121: (a) Scheme of the force profile model, figuring Hertz force, Van der Waals (VdW) force and the experimental values expected. In green are represented the jump-to-contact and jump-out-of-contact phenomena (b) Same scheme but with the total force.

Fixing the VdW force in contact means that only the Hertzian stiffness is taken into account. Hence using Hertzian formulas (52) and (53) to retrieve the 810 N/m value of the  $k_{ts}$ , one finds a  $z' = 0.35 \text{ nm}$  indentation depth. For this indentation, the repulsive force exerted by the surface to the tip is 190 nN. This value is one order of magnitude above the VdW force found for a 0.5 nm distance: 11 nN, pointing out the model choice might be mistaken.

To resume, with the Hertz model we find an indentation depth below the lattice constants of material involved. This means that the materials can be considered rigid and interacting through a force potential without deformation, as in the Bradley model (Figure 122). This last model has a one degree freedom to fit our data:  $z_0$ , which represents the equilibrium separation of the two surface.

The Bradley model writes for a sphere-sphere interaction:

$$F_{Bradley}(z) = \frac{16\gamma\pi R^*}{3} \left[ \frac{1}{4} \left( \frac{z}{z_0} \right)^{-8} - \left( \frac{z}{z_0} \right)^{-2} \right] \quad (73)$$

$$\frac{d}{dz} F_{Bradley}(z) = \frac{32\gamma\pi R^*}{3z_0} \left[ \left( \frac{z}{z_0} \right)^{-9} - \left( \frac{z}{z_0} \right)^{-3} \right] \quad (74)$$

Where  $R^*$  is the effective radius as defined by  $1/R^* = 1/R_1 + 1/R_2$ ,  $R_1$  and  $R_2$  being the radii of the spheres involved.  $\gamma$  is the work of adhesion or total surface energy per unit area defined by  $\gamma = \gamma_1 + \gamma_2 - \gamma_{12}$ ,  $\gamma_1$ ,  $\gamma_2$  and  $\gamma_{12}$  being the surface energy of the first material, the second one and of their interface. Lastly,  $z_0$  is the position at which the force is minimal and where the sphere separates when pulling off.

Trying to fit the experimental values with the Bradley model varying  $z_0$ , we find matching orders of magnitude (Figure 122) for an equilibrium position of  $z_0 = 2 \text{ nm}$ .

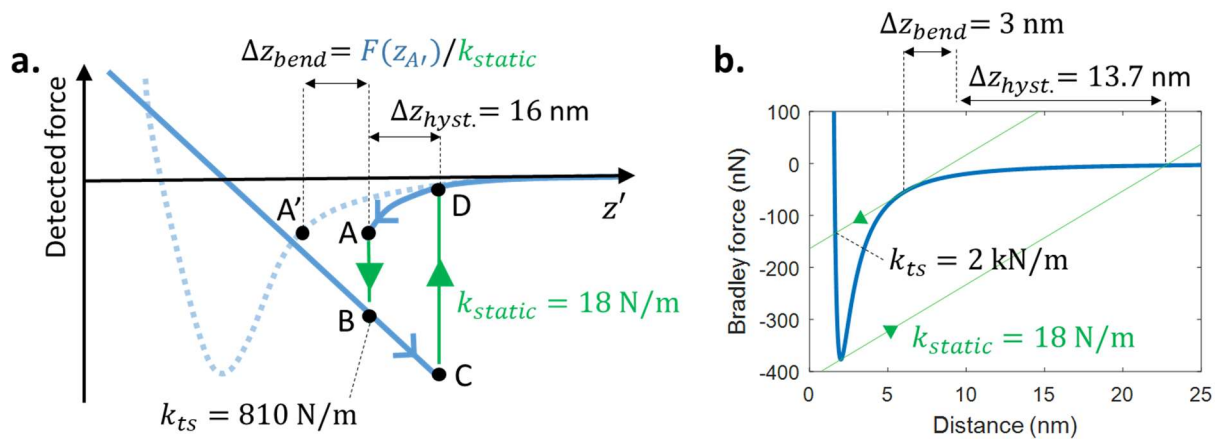


Figure 122: (a) Scheme of the force felt by the tip with experimental values from Figure 118. In green is represented the jump-to-contact. (b) Plot of the force profile given by the Bradley model, with modeled values. This model uses equation (73) with parameters  $\gamma = 0.75 \text{ J/m}^2$  (with  $\gamma_{gold} = 1.5 \text{ J/m}^2$ ,  $\gamma_{silica} = 83 \text{ mJ/m}^2$  and  $\gamma_{gold/silica} = 0.75 \text{ J/m}^2$ ),  $R^* = 40 \text{ nm}$  (with  $R_1 = 50 \text{ nm}$  and  $R_2 = 200 \text{ nm}$ ) and  $z_0 = 2 \text{ nm}$ . Compared to VdW calculations, this model implies higher attractive forces.

From this model we also understand why the attractive regime is not showing in the approach-retract curve: the jump into contact happens for  $k_{ts} > k_{static} = 18 \text{ N/m}$ , and the detection noise of the probe is higher (10 ppm which corresponds to 54 N/m).

As a note, one can observe that the attractive force of the chosen Bradley model has the same distance dependency than the VdW Hamaker formula (2) but has a magnitude approximately 100 times higher.

#### V.1.1.2 In air

The same experiment was conducted in the AFM instrument in air, with the cantilever tip facing the OM tip (Figure 123).

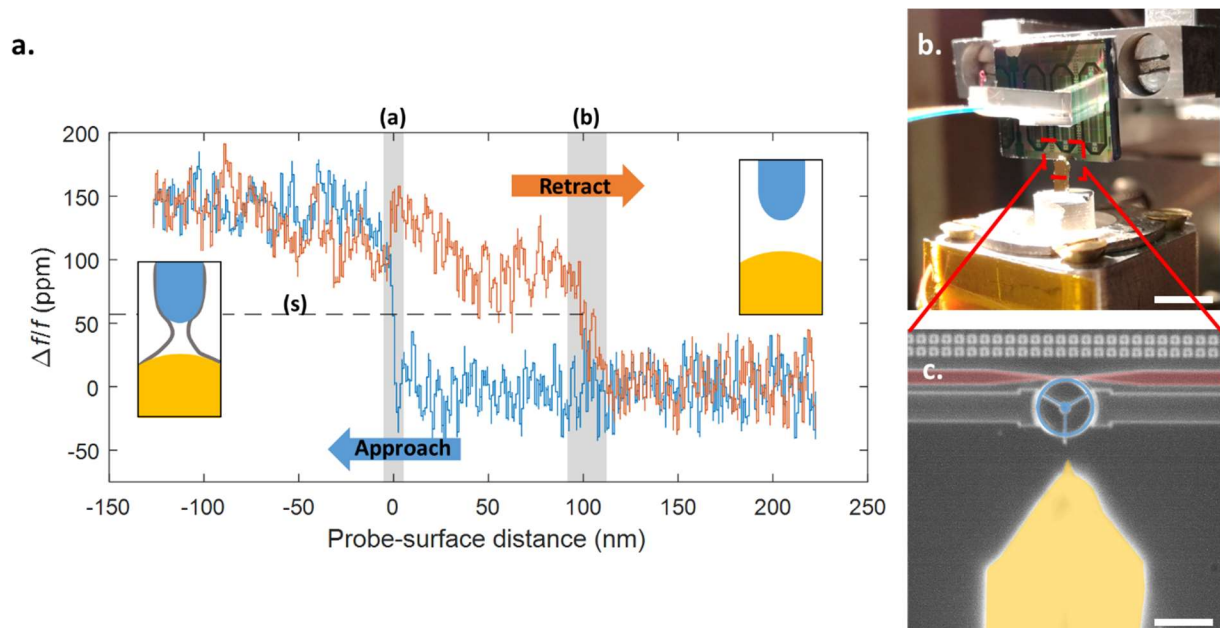


Figure 123: (a) Normalized mechanical frequency shift according to the tip-OM probe distance, this time in air. The golden tip is first approached (in blue) until the contact, indicated by abrupt frequency shift.

It is then retracted (in orange) until contact is broken and the frequency shift goes back to its rest value. Inset shows our assumption of the contact physical interaction: a water meniscus forms binding the golden tip (yellow) and the OM probe (blue). This experiment was performed with a LIA LPF bandwidth of 300 Hz. **(b)** Picture of the experiment, one can identify the fibers connectors coming from the left-hand side, onto the OM silicon chip. Underneath is the classical AFM cantilever, mounted on our High-BW Z-actuator. Scale bar: 5 mm. **(c)** Colored microscope picture of the OM probe and the classical cantilever. Scale bar: 20  $\mu\text{m}$ .<sup>77</sup>

The first value hit by the frequency shift in contact is 100 ppm. Following equation (41), the corresponding force gradient, or stiffness, is  $k_{ts} = \frac{2k_{eff}}{f_m} \Delta f_m = 8 \text{ N/m}$ , a much softer contact than in vacuum (810 N/m). The  $k_{eff}$  stiffness of this probe was simulated to be 40 kN/m and its  $k_{S\&R} = 270 \text{ N/m}$  ( $k_{S\&R}$  is the static stiffness of the probe, as defined in Figure 119). As a reminder, simulated  $k_{S\&R}$  can be found in Table 4 at page 65.

Compared to the previous experiment performed under vacuum, it shows a larger hysteresis between jump-to and jump-off contact: 100 nm in air and 15 nm in vacuum. We attribute this difference to a softer static stiffness of contact ( $k_{contact\_air} < k_{contact\_vac}$ ) and to water meniscus formation. Indeed, the former induces a smaller jump-to-contact slope; when retracting the golden tip, it will bend more, widening the hysteresis (Figure 122b). Another difference indicating the softer static contact is the slope in contact, which looks more like a plateau in this second experiment. We attribute the lower  $k_{contact\_air}$  to different position of the golden tip relative to the OM probe: as it is facing it, its  $k_C$  is closer to the one given by the datasheet  $k_C = 0.2 \text{ N/m}$ . The overall stiffness of the contact  $k_{contact\_air}$  should thus be governed by the cantilever.

We also attribute the higher hysteresis to the water meniscus formation. Indeed, there is less humidity in vacuum inducing smaller attractive force, as will be discussed in the next paragraph.

### **Additional attractive force: water meniscus**

As shown beforehand, an hysteretic effect (Figure 118) appears when attractive forces are at play, if their gradient are greater than the lowest stiffness involved in contact. To explain hysteresis over a 100 nm amplitude as experiment in air shows in Figure 123, 80 nm greater than under vacuum, one can also invoke water meniscus formation at the contact [45]. As pictured in Figure 124, the meniscus displays an attractive behavior. This meniscus effect is highly related to hydrophilicity of materials at play: silicon is hydrophobic, however the native oxide layer on it makes it hydrophilic. This meniscus effect is also highly related to humidity: another experimental fact indicating the meniscus presence is that when the experiment was first performed under vacuum, it was less stable than when performed with a preliminary nitrogen pumping in the vacuum chamber (removing the humidity of air). As a note, the size

---

<sup>77</sup> To evaluate measurements coherence, one can observe that the deviation of the normalized frequency shift values  $4 \times 10^{-5}$ , lower than the expected value  $2 \times 10^{-4}$  extracted from the Allan deviation in Sec. III.3, for  $\tau = 10^{-5} \text{ s}$  associated to the LPF bandwidth of 300 Hz. This little discrepancy is partly explained by the higher driving modulation used in this contact experiment (750 mV applied on the EOM and 100 mV in the Allan variance).

of the meniscus is limited by the dimension of the smallest tip involved, a larger meniscus will form for a larger tip and induce a more pronounced hysteretic effect.

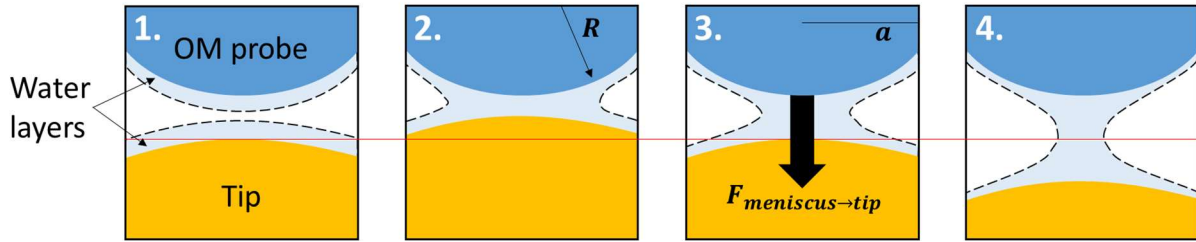


Figure 124: Schemes showing meniscus formation when the tip is brought to contact (1 and 2) and then retracted (3 and 4). Red line is present as a guide for distances appreciation. A similar JKR-simulated animation can be found in [187].

From a rough surface tension calculation, one can evaluate the added attractive force of the meniscus, integrating the surface tension on the immersion line of the OM tip:

$$F_{meniscus \rightarrow tip} = \gamma_{water/air} 2\pi a \quad (75)$$

Where  $\gamma_{water/air} = 7.2 \times 10^{-2} \text{ N/m}$  (p. 506 in [188]) is the surface tension of water/air interface and  $a$  is the radius of the cross-section of the OM tip immersed in the meniscus. From geometrical considerations, we can bound  $a$ :  $a \leq R$ , with  $R = 50 \text{ nm}$ . For  $a = 50 \text{ nm}$ , we find an added  $F_{meniscus \rightarrow tip} = 22.6 \text{ nN}$ . This value is small compared to the maximal attractive force given by the Bradley model (hundreds of nN), it however has an effect over a longer distance.

Now that we know the OM probe can detect a mechanical force with an associated frequency shift, we can test the feedback of the AFM instrument. In the next part, the frequency shift is fed back to the Z-actuator to control the tip-sample distance, stable feedback is demonstrated.

### V.1.2 Feedback control operation

The first step toward AFM imaging is to close the feedback loop (Figure 125). That is, to control sample height with the mechanical frequency shift of the OM probe.

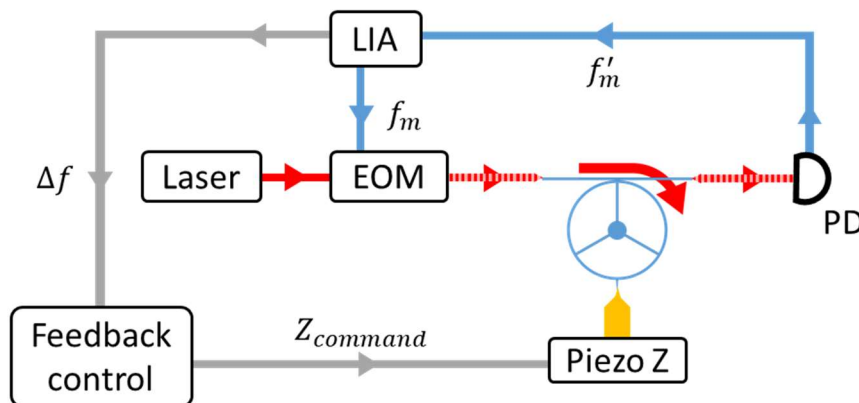


Figure 125: Scheme of the experimental set-up used for the feedback control demonstration.

The latter experiment was conducted on a single point in air. It was realized in a PM-AFM configuration. A typical behavior when closing the loop is shown in Figure 126.

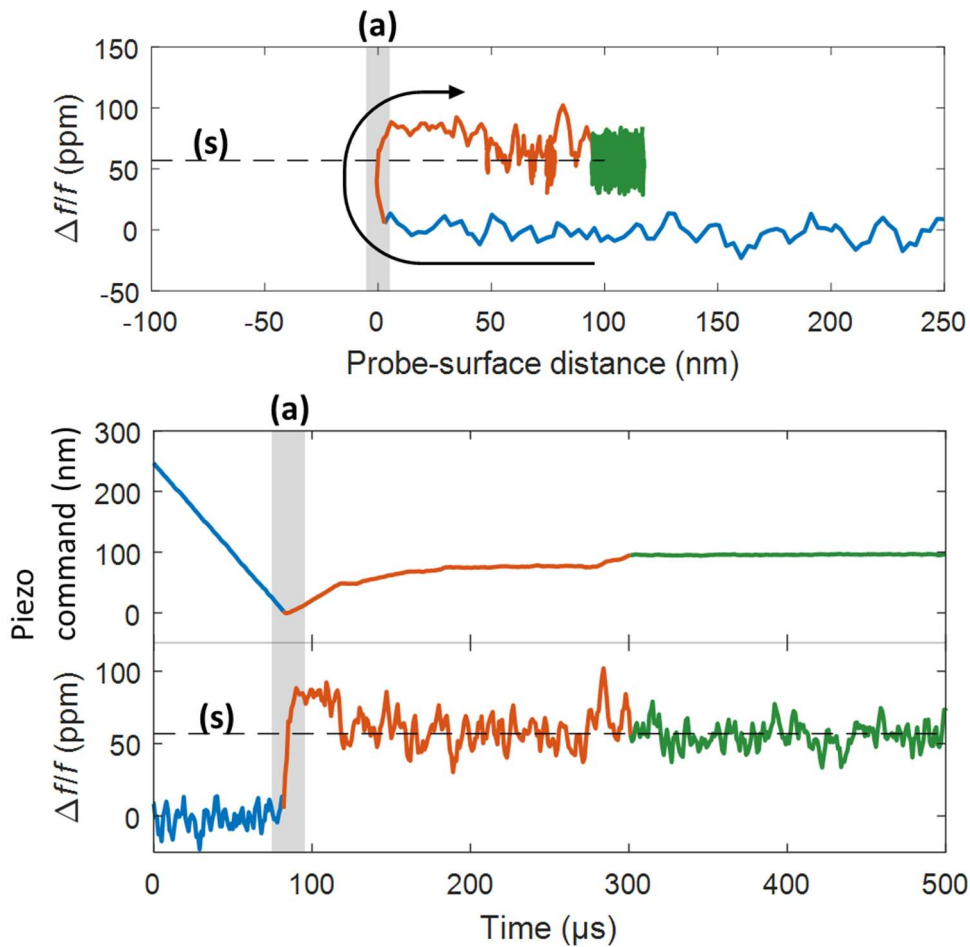


Figure 126: Dynamic behavior of feedback control of the probe to surface distance when closing the loop. **(Top)** Plot in the frequency shift – distance space. **(Bottom)** Time variation of probe-to-surface distance and frequency shift. Blue region corresponds to the probe approaching the surface before any interaction. In (a), interaction occurs with water meniscus formation. In orange region, feedback control adjusts the probe-to-surface distance in order to reach the frequency shift set-point value represented by dashed line (s). Stable close-loop operation is reached in green region. The +57 ppm set-point value corresponds a repulsive force gradient of  $4 \text{ N}\cdot\text{m}^{-1}$  between the probe-apex and surface. This trace was performed with a LIA LPF bandwidth of 300 Hz and controller gains:  $P = 4$ ,  $I = 4$  and  $D = 0$ . The data traced here has a 3 points moving average smoothing for a better readability.

This last result gives us information on the jump-to-contact and feedback loop dynamics. Looking at the  $\Delta f/f$  temporal trace in Figure 126, the jump-to-contact (orange rise in the grey zone) happens in less than  $10 \mu\text{s}$ . Looking at the orange trace, the feedback loop locks this perturbation back to the set-point in  $35 \mu\text{s}$ , giving us a time constant of about  $10 \mu\text{s}$ . This means an overall feedback-loop bandwidth of 100 kHz, reaching our 100 kHz goal. This results place our AFM instrument neck and neck with the two top-instruments in the field (RIBM Ando-type and Cypher VRS). Looking at the  $\Delta f/f$  temporal trace in green, one can also verify that our instrument stability is lower than the probe resolution as the noise is at similar levels as when not in contact (blue trace).

As a note, knowing the order-1-LPF of the LIA is at 300 Hz means that the operation regime is in the damping queue of the filter but still effective. It also means that relative frequency shifts are far more important than what is detected by the LIA.

Now that the OM probe is locked to the surface by feedback control, we can put the XY scanner to use and scan the sample, here the cantilever tip.

### V.2 Pseudo OM AFM image

Using the XY scanner present in the AFM instrument, we were able to perform an image of the cantilever tip with the feedback loop closed (Figure 127), validating the whole instrument and in particular the computer's user interface. However due to an amplifier failure on one scanning axis we were only able to trace a  $1\ \mu\text{m} \times 0.15\ \mu\text{m}$  image.

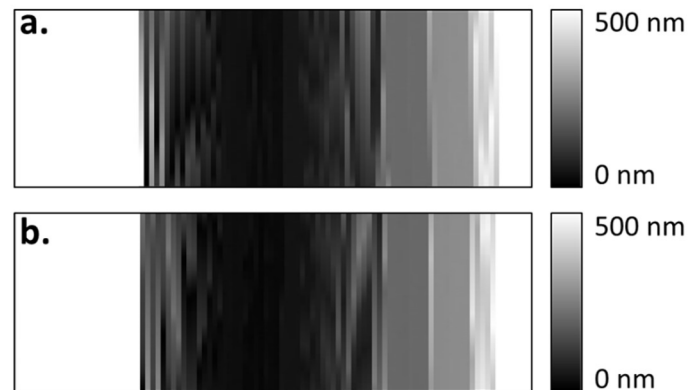


Figure 127:  $1\ \mu\text{m} \times 0.15\ \mu\text{m}$  (a) forward (left to right) and (b) backward (right to left) images<sup>78</sup> of the golden tip in terms of slow axis scanning direction. The fast axis is vertical in this image. In white is when the OM probe does not detect any mechanical stress, the fast piezo actuator is then fully extended to reach contact.

One can observe the quasi-perfect similarity of the two images, indicating that the pattern is not due to the scanning but rather geometries at play as is explained in the next scheme. Extracting a line profile of the precedent image, one can find the golden tip dimensions (Figure 128).

---

<sup>78</sup> Forward and backward traces are usually separated in AFM as they are often misaligned due to piezo hysteresis and difficult to read if parachute effect appears.

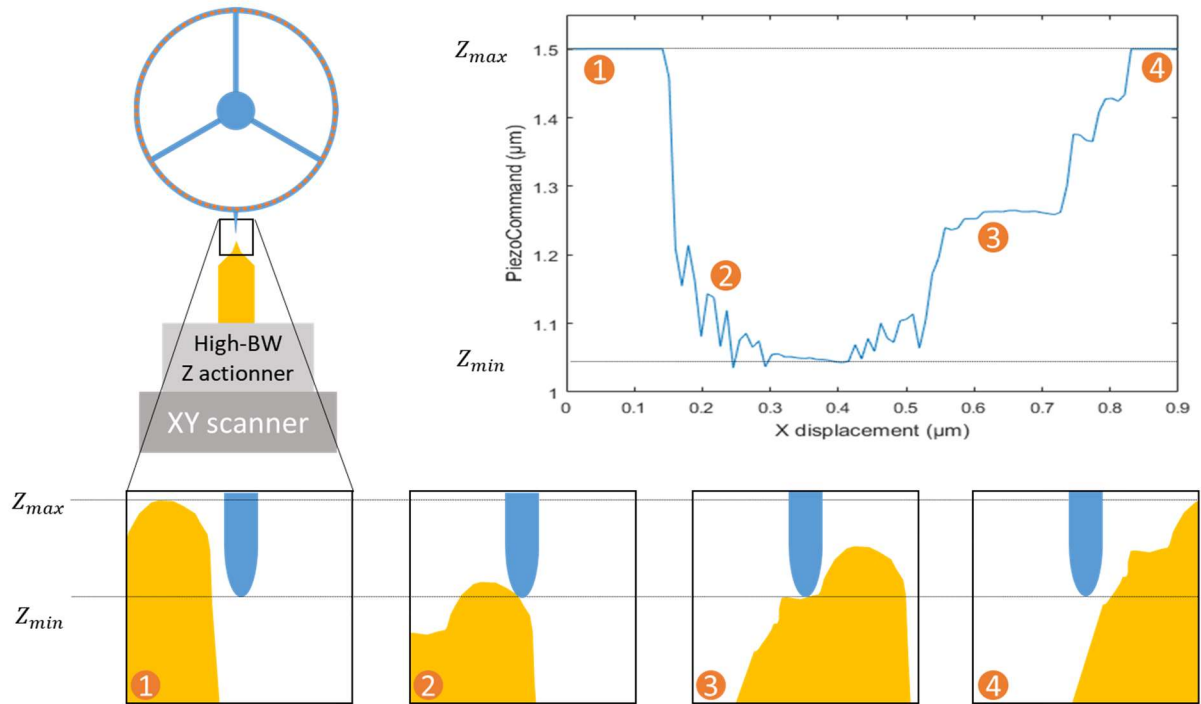


Figure 128: X-axis profile of the OM tip recorded in closed loop (PM-AFM) configuration. From the datasheet, the golden tip radius of curvature is 10 nm [169], the OM tip width at its base is 100 nm. But the part of the golden tip in contact is not the apex of it but just over it, not more than 1  $\mu\text{m}$  above. We attribute the plateau in 3 to an asperity on the outermost part of the cantilever tip, as it is present on both the forward and backward trace.

We find a cantilever radius of curvature of 200 nm, above the datasheet 50 nm, indicating that we imaged it slightly above its apex.

In this chapter, the OM probe was put in mechanical contact of another tip. It demonstrated its ability to detect mechanical force gradient down to 3 N/m in air. The behavior of the OM probe was investigated and fitted the Bradley model under vacuum. Using feedback control to lock the OM tip to a cantilever tip, the AFM instrument feedback loop bandwidth was estimated at 100 kHz, competing with the two top-instruments in the field (RIBM Ando-type and Cypher VRS). Finally, topography of a cantilever tip is investigated, with a 10 nm resolution.





## Conclusion

This thesis work towards an integrated optomechanical AFM proves the concept of the very high frequency optomechanical probe for dynamic AFM applications. Thanks to the combined work of the CEA-LETI, IEMN, Vmicro, MPQ and LAAS, we obtained the first AFM images taken with an integrated, optomechanically actuated and detected, force sensor. The over than 100 MHz vibrating OM probes demonstrated a motion limit of detection of  $4.5 \times 10^{-17} \text{m}/\sqrt{\text{Hz}}$  at room temperature, two-decades lower than any other AFM probe detection, at a frequency two-decades above the fastest cantilever. Characterization of numerous OM probes with different designs helped to find optimal designs, that is a 100 nm to 200 nm gap and spokes width below 100 nm. It also helped find subtle phenomenon as the super-mode. Among optical and capacitive actuation that were compared, the latter is the more promising. Indeed, it gets rid of the background and can *a priori* be amplified arbitrarily. Stability and noise study of the probe helped identify an additional noise source in actuation. The OM probe demonstrated its ability to detect mechanical force gradient down to 3 N/m in air. In closed loop operation, the custom AFM instrument developed to host the OM probe displayed a 100 kHz feedback-loop bandwidth, competing with the two top-instruments in the field (RIBM Ando-type and Cypher VRS). Finally, a first pseudo-image was achieved with those new OM probes, demonstrating the functioning of the whole system and validating the OM probe concept for AFM.

A general asset of the OM probe is its design versatility; its stiffnesses  $k_{static}$  and  $k_{eff}$  can be engineered to match a specific constraint. Tested ranges were  $5 \text{ kN/m} < k_{eff} < 3 \text{ MN/m}$  and  $1 \text{ N/m} < k_{static} < 1 \text{ kN/m}$ . Moreover, from experimental observations, the structure was rather resistant to shocks and bending constraints. I personally think that such a probe has a complex fabrication process but that its ultimate performances are worth the burden, allowing to test matter behavior at unprecedented frequencies. Indeed, the high-speed force spectroscopy field, for example, pushes for faster probes to explore new dynamic regimes in biomolecules [189] and experimentally confront Molecular Dynamics (MD) simulations [190].

Main locks to overcome to truly operate an OM AFM are (Figure 129):

1. Mechanical jamming as the substrate under the tip still prevents sample scanning (Figure 129 1);
2. Optical fabrication integrity as many device were cracked and had weak optical transmission (Figure 129 2);
3. Background noise due to optical feed-through, that lowers SNR of about 20 dB and which prevents the full potential of such a probe to be reached (Figure 129 3).

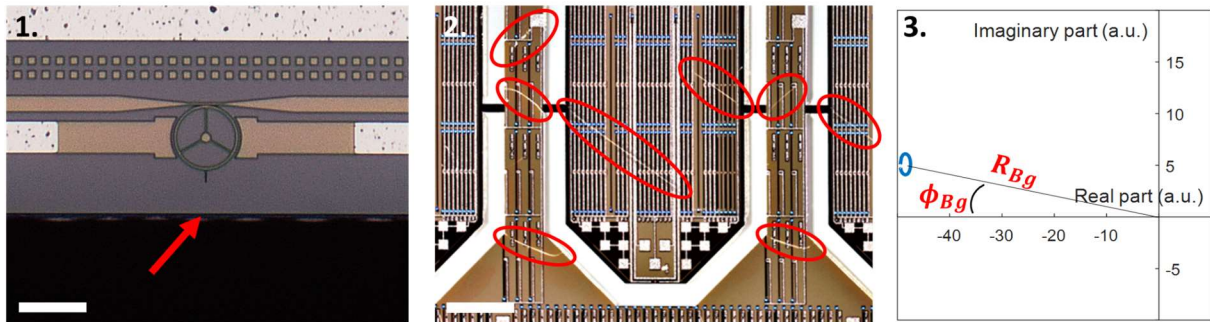


Figure 129: (1.) Close-up picture of an OM probe. (2.) Picture of an OM chip, cracks can be seen, stemming from corners. (3.) Polar plot of the optical signal of an OM probe. Scale bars from left to right respectively: 20  $\mu\text{m}$  and 700  $\mu\text{m}$ .

Solutions, to test, are:

1. To etch the substrate under the tip, developments must be made on the fabrication process. Techniques available are isotropic plasma etching, anisotropic wet etching, deep reactive ion etching (DRIE) as discussed in Sec. IV.6.1. Focused Ion Beam (FIB) etching is also an option but the former solutions are preferred as they can be applied to whole wafers.
2. The cracks were associated with the wafer thinning process, allowing DRIE chip-cutting (or dicing) and backside anisotropic etch. The thinning could be bypassed using a saw or a laser dicing technique to define the chip. It is of utmost importance as each device with cracks on its waveguide displayed no transmission and thus is unusable. Furthermore, the cracks disabled more than half of the fabricated probes. The weak transmission needs to be investigated to find their cause. It may be caused by cracks not seen on optical microscope. As it was observed only on device with a silicon top-layer of thickness 400 nm and not on 220 nm ones, another explanation is that the designs of the grating couplers/waveguides are not compatible with a 400 nm thickness. Lastly, this could have been caused by the DRIE process as this weak transmission was only observed on chips with the boat-shape.
3. Tested experimental schemes to suppress background noise are the use of 2 lasers or capacitive actuation (see Sec. III.5). The preference goes to the latter as I think it will show less non-linearity for over-than-10 pm actuation amplitudes. Another technique to get rid of the background, not tested, is the use of the device in reflection (opposed to transmission) with an optical circulator<sup>79</sup>, to benefit from the CCW mode.

<sup>79</sup> Reflection configuration was tested but with cleaved facet chips and side-injection. The reflection was thus mostly occurring on the cleaved facet of the chip. Here the idea is to use reflection inside the cavity with back-scattering (see Sec. II.2.2).

## Perspectives

As summarized in the conclusion, the optomechanical probe concept for AFM was proven. Nevertheless, to routinely image a surface, there is still developments to be made. In these paragraphs we suggest some interesting leads.

To be able to probe matter in a less invasive way in the non-contact (*i.e.* attractive) regime of AFM, the OM probe needs to have a higher static stiffness. Using the VdW formula (2), for tip with a 50 nm radius, a maximal attractive gradient of 130 N/m is felt at 0.4 nm. Designing a thinner tip or a probe with  $k_{static} = 1$  kN/m should definitively prevent jump-to-contact.

Next step is also liquid operation demonstration as many application sought for a high-bandwidth atomic force microscopy and spectroscopy are in biology. Optomechanical detection has already been demonstrated for disk (p. 149 in [142]), but not actuation. In liquid, the mechanical quality factor is expected to decrease 100-fold. This induces a similar decrease on the SNR and a higher actuation should then be needed to circumvent it. Optical actuation should still work but the higher power, needed to actuate more and retrieve the initial SNR, might trigger non-linear effects. As discussed above capacitive actuation seems a better choice (in solution 3.), to be tested in liquid.

Following the mechanical figure-of-merit in Sec. I.3.4, one would seek even higher frequencies to reach a new AFM probe performance window. A higher frequency can be obtained with a smaller ring radius or a higher azimuthal mode order. I would recommend the latter because a smaller silicon ring tends to have larger non-linear optical behavior ( $P_{st} \propto 1/R$ ), in particular larger 2PA (as seen on  $R = 5$   $\mu\text{m}$  silicon rings p. 130 in [146]). This last issue can also be worked around using other materials with less absorption and smaller non-linear coefficients as SiN. This higher frequency improvement must be done with a strong actuation, as the capacitive one, to observe atoms (able to actuate to the angström) but could also allow probing lower force fields with resolving under the angström.

For the telecommunications field will push for integration of optical circuits, the rise of integrated OM sensor will ease experiments, allowing its democratization. This means on-chip EOM, laser and PD. For example, on-chip tunable lasers with matching powers and linewidth already exist, albeit not for commercial use [191]. As fabrication reproducibility will increase, this will allow less-tunable lasers to be compatible with OM sensor, with a tunability in the 5 nm range.





## Appendix B: Electromagnetic wave propagating in a slab

From a standard electromagnetic point of view, let us consider a propagating light wave of electric field vector  $\vec{E}(\vec{r}, t)$  and magnetic field vector  $\vec{B}(\vec{r}, t)$ . From Maxwell's equations, one can show, in a d'Alembertian fashion, that a propagating wave in a material of refractive index  $n$  obeys:

$$\Delta \vec{E}(\vec{r}, t) - \frac{n^2(\vec{r})}{c^2} \frac{\partial^2 \vec{E}(\vec{r}, t)}{\partial t^2} = 0 \quad (\text{B-1})$$

If we look at a monochromatic propagating wave in the z-direction with the real (without attenuation nor gain) propagation constant  $\beta = k_0 n_{eff}$  (which could be noted  $\beta_z$ ), and writing its angular frequency  $\omega_0$ , we can write the general harmonic solution as:

$$\vec{E}(\vec{r}, t) = \text{Re}\{\vec{E}(x, y)e^{i(\omega_0 t - \beta z)}\} \quad (\text{B-2})$$

Injecting equation (B-2) in equation (B-1), one can find the Helmholtz equation:

$$\left(\frac{\partial^2}{\partial x^2} + \frac{\partial^2}{\partial y^2}\right)\vec{E}(x, y) + (k_0^2 n^2(\vec{r}) - \beta^2)\vec{E}(x, y) = 0 \quad (\text{B-3})$$

Where  $k_0 = \omega_0/c$ ,  $k_0$  is the wave vector in vacuum and  $c$  light celerity.

Let us now apply those equations in a slab waveguide structure (Figure ).

### B.1 Slab

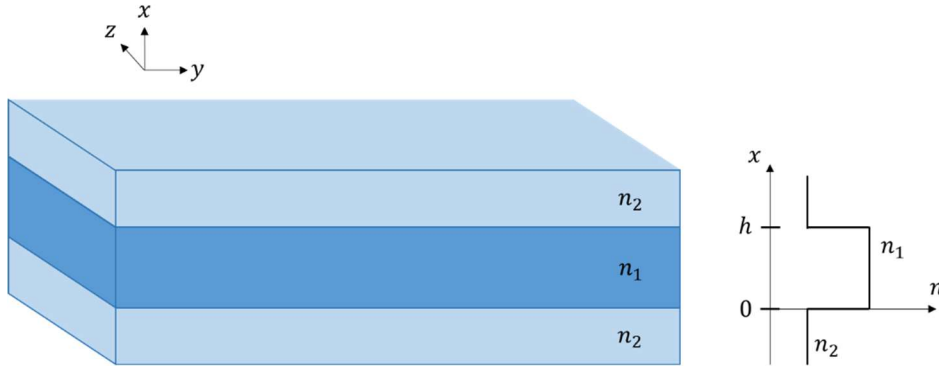


Figure B-1: Scheme of a slab waveguide, the waveguide in the Y-axis is considered infinite and the propagation is considered in the Z-direction.

A dielectric slab as in Figure B-1 is invariant by y-axis, therefore it imposes the invariance on the light wave:  $\partial E(x, y)/\partial y = 0$ . Injecting this condition in equation (B-3), one can write:

$$\frac{\partial^2 \vec{E}(x)}{\partial x^2} + (k_0^2 n^2(\vec{r}) - \beta^2)\vec{E}(x) = 0 \quad (\text{B-4})$$

The up and down boundaries impose that z-guided light has a favored electrical field component (*i.e.* fixed polarization), either in the y-direction, transverse electric mode (TE) or in the x-direction, transverse magnetic mode (TM). For the TE case, we have:

$$\frac{\partial^2 E_y(x)}{\partial x^2} + \gamma^2 E_y(x) = 0 \quad (\text{B-5})$$

Where  $\gamma^2 = (k_0^2 n^2(\vec{r}) - \beta^2)$ , we write in materials 1 and 2 respectively  $\gamma^2 = \beta_x^2 = (k_0^2 n_1^2 - \beta^2)$  and  $\gamma^2 = \alpha_x^2 = (\beta^2 - k_0^2 n_2^2)$ , assuming that the refractive index in both material is invariant.

The form of the solutions to equation (B-5) depends on the part of the slab. Since we consider that we inject light in the core only, we choose:

$$E_y(x) = \begin{cases} Ae^{-\alpha_x(x-h)} & \text{for } x \geq h \\ B\cos(\beta_x x) + C\sin(\beta_x x) & \text{for } 0 \leq x \leq h \\ De^{\alpha_x x} & \text{for } x \leq 0 \end{cases} \quad (\text{B-6})$$

As  $\beta^2 = k_0^2 n_{eff}^2$  and the guiding condition  $n_2 \leq n_{eff} \leq n_1$ , one can see that  $\beta_x$  is real and  $\alpha_x$  is imaginary. So equation (B-6) says that the electric field profile has an oscillating pattern within the waveguide and is exponentially decaying out of it in the X direction.

Now one can use the boundary conditions in  $x = 0$  and  $x = h$ : tangential electric field and its derivative are continuous at boundaries, in particular  $E_y$  and  $\partial E_y(x)/\partial x$  are. From equation (B-6), one can find:

$$D = B \quad (\text{B-7})$$

$$\alpha_x D = \beta_x C \quad (\text{B-8})$$

$$A = B\cos(\beta_x h) + C\sin(\beta_x h) \quad (\text{B-9})$$

$$-\alpha_x A = -B\beta_x \sin(\beta_x h) + C\beta_x \cos(\beta_x h) \quad (\text{B-10})$$

Mixing equations (B-7) to (B-10), one can find:

$$\tan(\beta_x h) = \frac{2\beta_x \alpha_x}{\beta_x^2 - \alpha_x^2} \quad (\text{B-11})$$

This equation can be re-written:

$$\tan(hk_0 \sqrt{n_1^2 - n_{eff}^2}) = \frac{\sqrt{(n_1^2 - n_{eff}^2)(n_{eff}^2 - n_2^2)}}{k_0(n_1^2 - n_2^2)} \quad (\text{B-12})$$



Fixing the light wave frequency, and thus its wave vector  $k_0$ , numerical calculations or drawings can then provide approached values of the effective index with equation (B-12). One can find a discrete number of solutions, corresponding to fundamental and higher modes guided. A handy online calculator can be found in [192].

## Appendix C: Instruments

In this part we present the instruments used in this manuscript (Figure C-1).

a.



b.

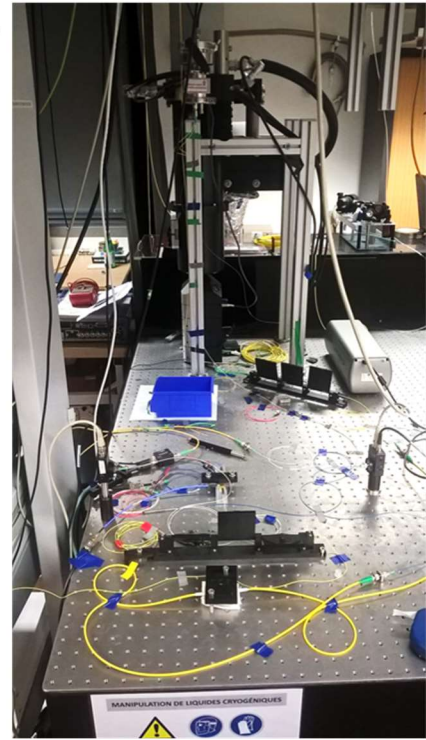


Figure C-1: Pictures of (a.) the AFM set-up at LAAS and (b.) the optical characterization set-up at MPQ.

### C.1. Optics

#### C.1.1. Laser

EXFO T100S-HP (ex Yenista Tunics, ex Photonetics) (Figure )

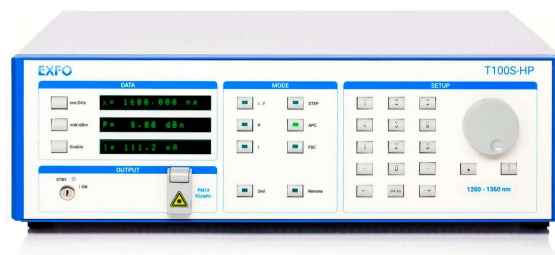


Figure C-2: Picture of an external cavity tunable laser. This particular laser is tunable between 1.5 and 1.63  $\mu\text{m}$ , has a spectral linewidth of 400 kHz (*i.e.* 3 fm in wavelength) and a maximal output of 20 mW.

The laser needs to be tunable at least in the FSR of the cavity so that it can inject in an optical mode. For a  $\varnothing=20 \mu\text{m}$  silicon cavity of  $n_{eff}=2.4$  and for a  $\lambda_0 = 1.55 \mu\text{m}$  light wave, we have  $\text{FSR} = \lambda_0^2 / 2n_{eff}L = (1.55 \times 10^{-6})^2 / 2 \times 2.4 \times 3.14 \times 20 \times 10^{-6} = 8 \text{ nm}$ . It needs to be spectrally thin enough to neglect dispersion. It has to be powerful enough to be above the photodiode noise after transmission. It has to be stable enough in wavelength and power to not add noise nor drift on the mechanical motion detection. The slow power drifts can be overcome by an EOM feedback loop, the wavelength drifts can be overcome by a PDH

technique. Its wavelength resolution needs to be under the cavity spectral width (FWHM=25 pm). It *a priori* needs a mode-hop free sweep, provided that injected power leads to thermo-optic shifting of the optical resonance.

### C.1.2. EOM

Thorlabs LN81S-FC (Figure C-3)

iXblue MXAN-LN-10



Figure C-3: Picture of an EOM. One can observe its input and output optical fibers on the left and right hand side of the picture. RF port, DC bias and photodiode pins can be seen on its edge. As a note, its integrated photodiode was sensitive to polarization so we did not use it to monitor power output.

The Electro-Optical Modulator (EOM) transmission versus applied voltage is presented in Figure C-4, to introduce its operating point.

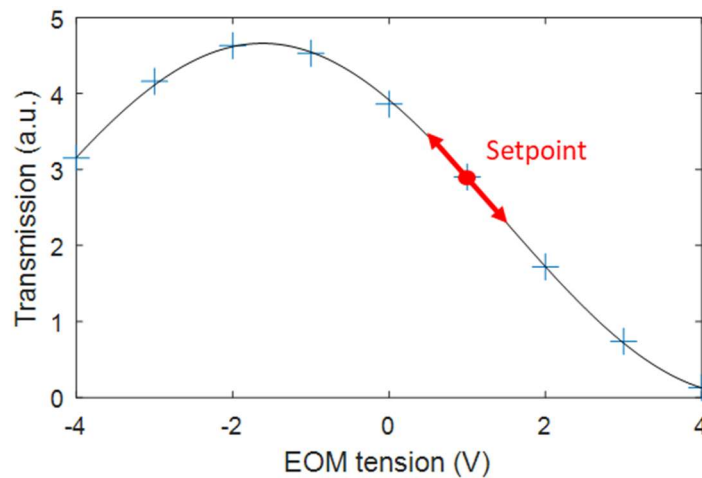


Figure C-4: Transmission (proportional to optical power) of the EOM according to the DC-voltage applied to it. The black line is a sinusoidal fit. The red dot is the DC set-point of the EOM generally just before  $V_{\pi/2}$ ,  $V_{\pi}$  being the voltage at which output is totally suppressed. It is chosen in the linear part to limit harmonics generation when modulating.

We characterized its frequency response, exciting it at a sweeping frequency on the RF-port and detecting optical modulation amplitude at the same frequency (Figure C-5).

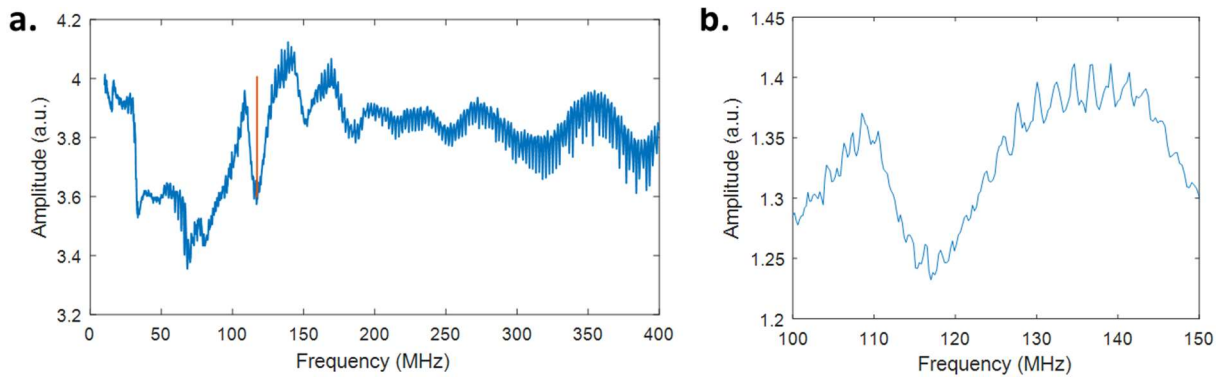


Figure C-5: (a.) Full-scale frequency response when the OM device is put in the chain. Mechanical modulation is traced in orange around 117 MHz, with a more resolved trace. On the whole spectrum, we observe a beating with a 2.3 MHz period and bigger frequency features. Those are attributed to the EOM response. (b.) Frequency response of only the EOM directly to the photodiode.

The condition on this frequency response being that it must be flat in the OM probe’s mechanical resonance frequency region.

As it depends on temperature-sensitive Lithium-Niobate Pockels cells, the EOM we used has drifts with temperature. Thus a stabilizing feedback-loop was often used, taking the EOM output power in input and the set-point voltage of the EOM in output, as shown in Figure C-6. For experiments shorter than half an hour, this can be neglected.

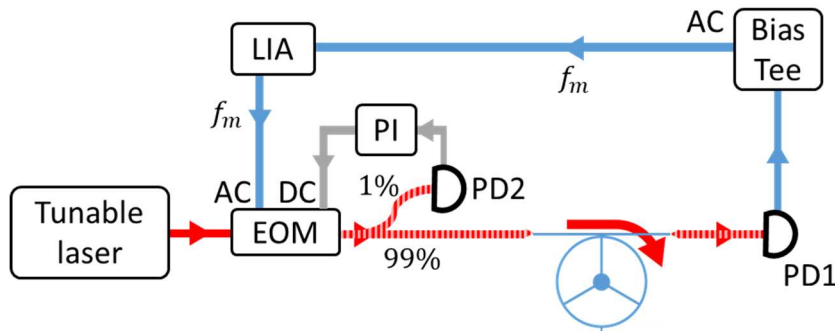


Figure C-6: Scheme of the operating set-up featuring the feedback-loop control of the EOM output. The PI block is a proportional-integral controller. Its bandwidth was usually set around 1 kHz but could have been lower.

This EOM component can *a priori* be replaced using the high frequency modulation input port integrated in our EXFO T100S-HP tunable laser (up to 200 MHz), this was not tested.

### C.1.3. Optical amplifier

EDFA: KEOPSYS CEFA-C-HG (Figure C-7)



Figure C-7: Picture of the fiber amplifier used.

To circumvent low-transmission or/and put the optical transmitted signal over the photodiode's noise floor, it can be amplified post-device by a doped-fiber amplifier.

When we sporadically used it, it displayed a 200 amplification factor for a 70 mA current supply. This optical amplifier was usually used under its normal specifications (40 dB amplification) to prevent photodiode saturation. The noise of such an amplifier comes from spontaneous emission. It thus decreases when increasing the input power: if more signal photons are amplified through stimulated emission, less excited electrons are available to amplify the spontaneous photons.

#### C.1.4. Optical tunable filter

Nano-Giga: WLTF band-pass filters (Figure C-8).

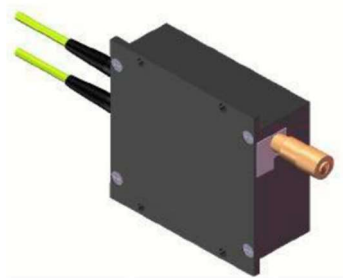


Figure C-8: 3D scheme of the manual tunable filter we used in the 2-laser configuration. Input and output fibers can be seen on the left-hand side and the tunable screw on the right hand side.

In the 2-lasers actuation/sensing technique, the pump (*i.e.* actuation) laser is filtered out with this band-pass filter of a few nanometers FWHm. A notch filter could also have been used to ease experiments. Indeed, with such a manual band-pass filter, the filter's wavelength must be changed each time the sensing laser is.

With such a filter, another noise source was brought to light: light at a different wavelength. The mechanical spectrum of an OM probe was recorded (in the 1-laser set-up) with and without the optical filter. When the optical filter is on, noise is slightly decreased (Figure C-9). This result was not carefully investigated and could be an experimental error, it however points out that a spectral investigation of the laser should be carried out to verify the laser behavior.

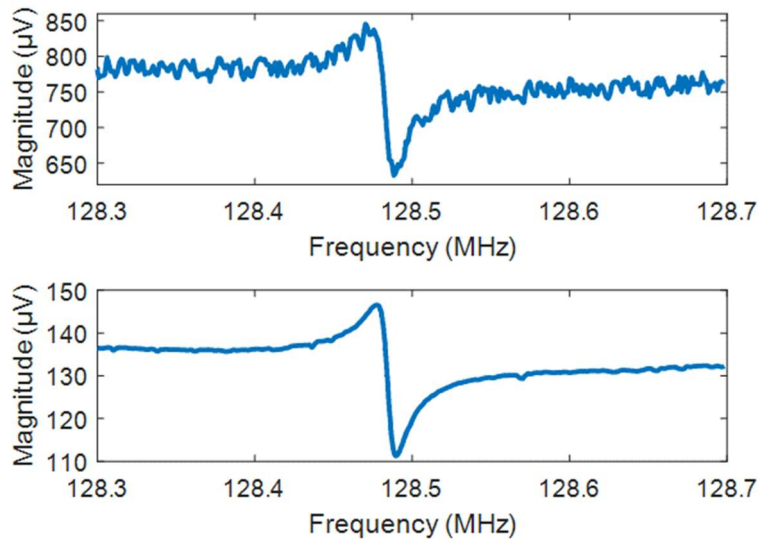


Figure C-9: Mechanical spectrum of an OM probe using the 1 laser set-up without optical filter (**top**) and with an optical filter (**bottom**).

#### C.1.5. Photodiode (PD)

Thorlabs DET01CFC: high-bandwidth PD to acquire the mechanical modulation (Figure C-10a).

Newport NewFocus 1611FC-AC: alternative high bandwidth PD but with higher NEP.

Thorlabs PDA10CS-EC: Extra photodiode to verify transmission (Figure C-10b).

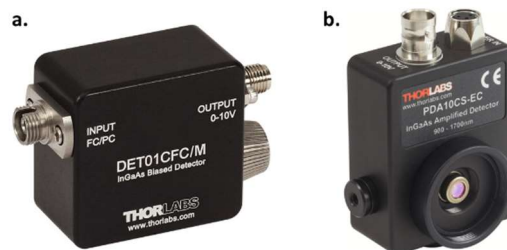


Figure C-10: Pictures of the fast (a.) and slow (b.) photodiodes used in this thesis work. The bandwidth of the left-hand side photodiode is 1.2 GHz.

The first photodiode must have a noise floor lower than the mechanical Brownian motion and a bandwidth superior to the mechanical motion frequency (around 130 MHz for our device).

#### C.1.6. Fibers, optical connectors

Couplers: Thorlabs TW1550R1A1

micro-lensed fibers: OZoptics (Figure C-11)

Circulator: Thorlabs 6015-3-APC

To connect instruments standard patchcords, APC connectorized SMF-28 fibers, are used (for C-band/telecom wavelength at 1.55  $\mu\text{m}$ ). Fiber couplers are used to probe the optical signal locally and fibered circulators are used when working in reflection. To inject light in the chip,

one can access the chip by the edge or the top. On the edge, we used tapered/micro-lensed fibers from OZoptics. On the top we used standard fibers arranged in a multi-fiber ferule.

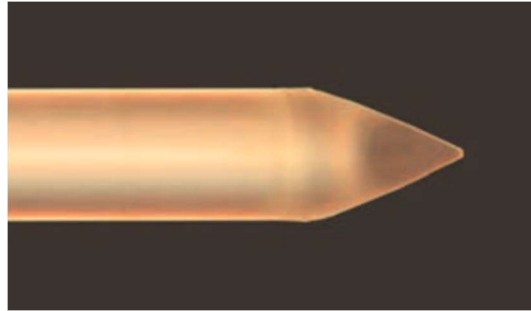


Figure C-11: Picture of a tapered fiber from OZ optics. It allows to couple light in a waveguide by the side of the silicon chip. From [193]. The end's radius of curvature is about a few micrometers.

#### *C.1.7. Polarization Controllers*

Thorlabs FPC562

### C.2. RF Electronics

#### *C.2.1. Lock-in Amplifier*

Zurich Instruments HF2LI (50 MHz-limited) and UHFLI (600 MHz-limited).

#### *C.2.2. Amplifier*

LNA: Minicircuits ZFL1000LN+ (noise factor  $NF = 3$  dB) or FEMTO HSA-X

#### *C.2.3. Bias tee*

Minicircuits ZFBT-4R2GW+

#### *C.2.4. Transposition circuit*

The global transposition circuit is presented in Figure C-12.

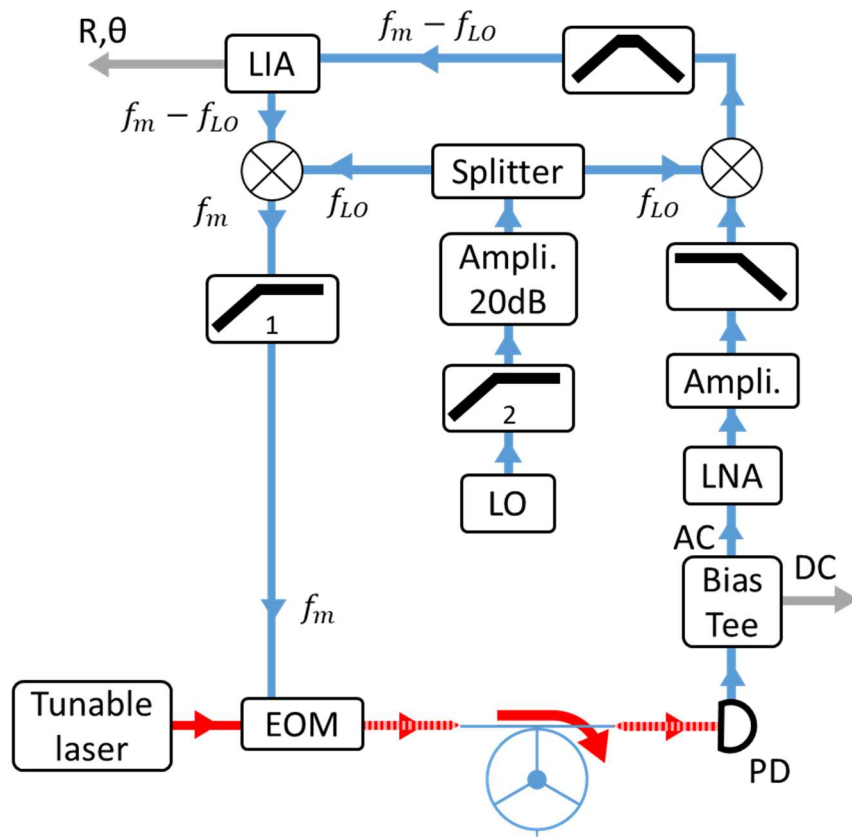


Figure C-12: Scheme of the transposition circuit used. The Minicircuits RF component are: Splitter Z99SC-62-S+, Amplifier 20dB: ZFL-1000+, Ampli. : ZFL-500HLN+, LNA: ZFL-1000LN+, High-Pass filter 1: SHP-100+, High-Pass filter 2: SHP-100A+, Band-pass filter SIF-40+.

### C.2.5. Local oscillator (LO)

Analog Device: AD9912

The local oscillator output was characterized (Figure C-13), in particular its output power to match the mixer's needs.

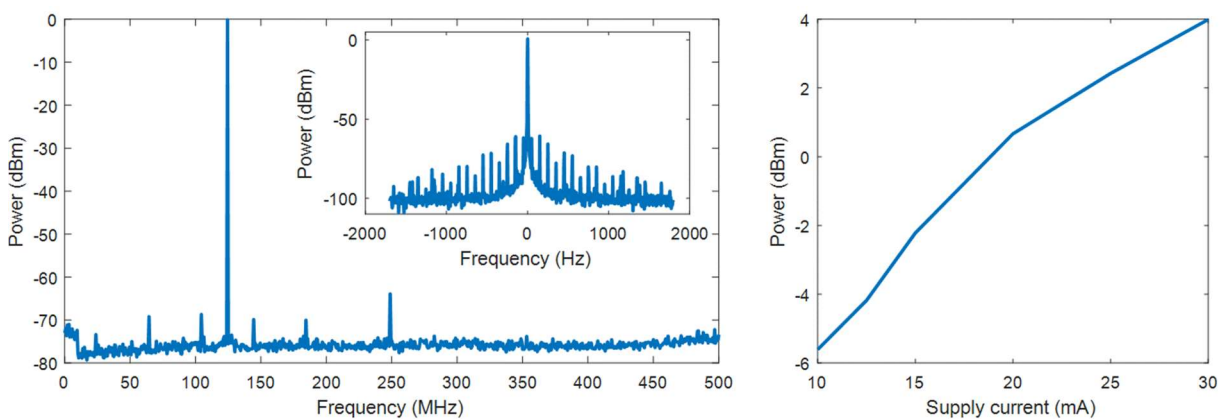


Figure C-13: (a) Spectrum of the AD9912 local oscillator. Inset shows a zoom on the peak with centered frequency at 124 MHz. (b) Peak amplitude versus supply power. For our set-up, the set point was usually chosen at 14 mA, delivering a -3 dBm LO power.



### C.3. Positioners

**Fiber positioning:** Positioning of fibers to couple from laser light through the edge of the silicon chip was done within an Attocube systems vacuum chamber with piezo-positioners controllers ACC50, ANC300 and ANC350. Positioning for experiments in air were mostly done through stages with micrometer precise screws. Characterization of many device was also performed at LETI laboratory, with an automatic prober.

**Sample positioning in AFM:** A PicoCube controller from PI was used to position the OM tip with respect to the sample.

### C.4. Miscellaneous

Visualization (back/front) was done with a NAVITAR tube and a supplementary x20 microscope objective to be able to see the OM probe and position the classical AFM cantilever.

## Appendix D: Thermomechanical noise spectrum

In this appendix, we look for the theoretical thermomechanical noise spectrum of a resonator. This is used to fit our experimental data. The outline of the calculation presented in this appendix is as follows: Fourier transform (damped harmonic oscillator) + Equipartition theorem → Thermomechanical motion spectrum [194].

Newton's 2<sup>nd</sup> law applied to a damped harmonic oscillator yields, when thermally excited:

$$m_{eff} \left[ \ddot{z}(t) + \frac{\omega_m}{Q_m} \dot{z}(t) + \omega_m^2 z(t) \right] = f_{th}(t) \quad (D-1)$$

Which gives, applying the Fourier transform:

$$m_{eff} \left[ -\omega^2 + j\omega \frac{\omega_m}{Q_m} + \omega_m^2 \right] Z(\omega) = F_{th}(\omega) \quad (D-2)$$

The complex susceptibility is then defined as (m/N):

$$\chi(\omega) = \frac{Z(\omega)}{F_{th}(\omega)} = \frac{1}{m_{eff} \left[ \omega_m^2 - \omega^2 + j\omega \frac{\omega_m}{Q_m} \right]} \quad (D-3)$$

Let us consider a broadband amplitude spectral density of thermic force (white noise):

$$F_{th}(\omega) = F_{th} \quad (D-4)$$

Equipartition theorem: «At thermal equilibrium, each liberty degree of a system contributes  $\frac{1}{2} k_B T$  to the total energy». Considering the potential energy of a spring-mass system we have (equation 2 in p. 64 in [160]):

$$\langle E_{pot}(t) \rangle = \frac{1}{2} k_{eff} \langle z^2(t) \rangle = \frac{1}{2} k_B T \quad (D-5)$$

So

$$\langle z^2(t) \rangle = \frac{k_B T}{k_{eff}} \quad (D-6)$$

Yet

$$\begin{aligned} \langle z^2(t) \rangle &= \frac{1}{2\pi} \int_0^{+\infty} |Z(\omega)|^2 d\omega = \frac{1}{2\pi} \int_0^{+\infty} |\chi(\omega) F_{th}|^2 d\omega \\ &= \frac{|F_{th}|^2}{2\pi} \int_0^{+\infty} |\chi(\omega)|^2 d\omega \end{aligned} \quad (D-7)$$

And

$$\int_0^{+\infty} |\chi(\omega)|^2 d\omega = \frac{1}{m_{eff}^2} \int_0^{+\infty} \frac{1}{(\omega_m^2 - \omega^2)^2 + \left(\omega \frac{\omega_m}{Q_m}\right)^2} d\omega \quad (D-8)$$

We consider a mechanical resonance of  $Q_m \gg 1/4$ , so (as in appendix of [195], missing a “divided by 2”):

$$\int_0^{+\infty} |\chi(\omega)|^2 d\omega = \frac{1}{m_{eff}^2} \frac{1}{2 \times \omega_m^2} \frac{Q_m \pi}{\omega_0} \quad (D-9)$$

Be  $\langle z^2(t) \rangle = \frac{|F_{th}(\omega)|^2}{2\pi} * \frac{1}{m_{eff}^2} \frac{1}{2 \times \omega_m^2} \frac{Q_m \pi}{\omega_0} = \frac{|F_{th}(\omega)|^2 Q}{4m_{eff}^2 \omega_m^3}$  (D-10)

So  $\frac{|F_{th}(\omega)|^2 Q_m}{4m_{eff}^2 \omega_m^3} = \frac{k_B T}{k_{eff}}$  (D-11)

Be  $|F_{th}(\omega)|^2 = \frac{4k_B T m_{eff}^2 \omega_m^3}{Q_m k_{eff}} = \frac{4k_B T m_{eff} \omega_m}{Q_m} = \frac{4k_B T k_{eff}}{Q_m \omega_m}$  [N<sup>2</sup>/Hz] (D-12)

Hence  $Z(\omega) = \frac{F_{th}(\omega)}{m_{eff} \left[ \omega_m^2 - \omega^2 + j\omega \frac{\omega_m}{Q_m} \right]} = \frac{\sqrt{\frac{4k_B T m_{eff} \omega_m}{Q}}}{m_{eff} \left[ \omega_m^2 - \omega^2 + j\omega \frac{\omega_m}{Q_m} \right]}$  (D-13)

$F_{th}(\omega)$  is in N/ $\sqrt{\text{Hz}}$ .

And  $|Z(\omega)|^2 = |\chi(\omega) F_{th}(\omega)|^2 = \frac{4k_B T \omega_m}{m_{eff} Q_m \left[ (\omega_m^2 - \omega^2)^2 + \left( \omega \frac{\omega_m}{Q_m} \right)^2 \right]}$  [m<sup>2</sup>/Hz] (D-14)

Evaluation at resonance:

$$|Z(\omega_m)|^2 = \frac{4k_B T Q_m}{m_{eff} \omega_m^3} = \frac{4k_B T Q_m}{k_{eff} \omega_m} = \frac{2k_B T Q_m}{\pi k_{eff} f_m} \text{ [m}^2\text{/Hz]} \quad (D-15)$$

## Appendix E: Calibration via acquisition chain

The experimental set-up used to acquire the thermomechanical motion is depicted in Figure E-1.

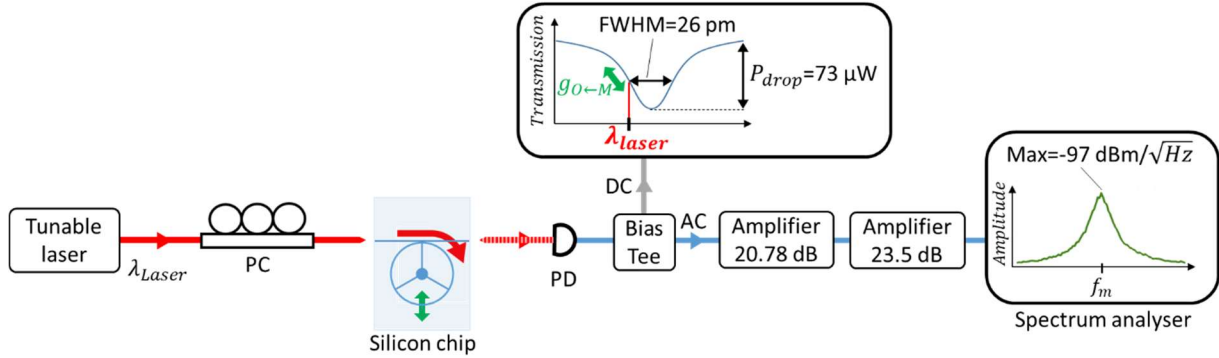


Figure E-1: Scheme of the experimental set-up used to assess the thermomechanical motion of the OM probe.

The amplitude of motion  $\Delta z$  of the cavity leads to an optical resonance pulsation shift:

$$\Delta z = \frac{1}{g_{O \leftarrow M}} \frac{\Delta \omega_{cav}}{2\pi} \quad (\text{E-1})$$

With  $\Delta \omega_{cav} = 2\pi \frac{c}{\lambda_{cav}^2} \cdot \Delta \lambda_{cav}$

The  $g_{O \leftarrow M}$  coupling factor can be decomposed in the  $g_0$  and the zero point fluctuation motion  $z_{ZPF}$ :

$$g_{O \leftarrow M} = \frac{g_0}{z_{ZPF}} \quad (\text{E-2})$$

The  $g_0$  coupling factor is FEM calculated with the COMSOL software to be  $g_0 = 1.15 \times 10^4$  Hz. The zero-point (quantum) fluctuation motion is given by:

$$z_{ZPF} = \sqrt{\frac{\hbar_p \times f_m}{k_{eff}}} \quad (\text{E-3})$$

$\hbar_p$  being the Planck constant.

Assuming the optical drop as an inversed triangle, the optical power transmission shift induced by the cavity's wavelength shifting is:

$$\Delta \lambda_{cav} = \frac{FWHM/2}{P_{drop}} \Delta P_{opt} \quad (\text{E-4})$$

Where  $FWHM$  and  $P_{drop}$  are defined in Figure E-1.

This optical power shift is transduced to a current shift  $\Delta I$  by the photodiode responsivity  $R_{esp}$ :

$$\Delta P_{opt} = \frac{\Delta I}{R_{esp}} \quad (\text{E-5})$$

For we use a DET01CFC Thorlabs photodiode, the responsivity at 1.55  $\mu\text{m}$  is  $R_{esp} = 1 \text{ A/W}$ .

For a 130 MHz signal guided in a  $r = 50 \Omega$  BNC cable, the power spectral density at 130 MHz of a sinusoidal signal of current amplitude  $\Delta I$  is  $P_{elec} = r\Delta I^2 \text{ W/Hz}$ .

The 2 RF amplifiers have a total gain  $G = 44.3 \text{ dB}$  (Figure E-1), thus:

$$P_{elec} = 10^{\frac{(P_{max}-G)-30}{10}} \quad (\text{E-6})$$

Where  $P_{max}$  is the power spectral density at resonance, measured after amplification and in dBm, as defined in Figure E-1. As a note, in this calculation, each parameter is in noise but their initial symbol is kept by abuse.

Hence we have:

$$\Delta z = \frac{1}{g_0} \sqrt{\frac{h_p \times f_m}{k_{eff}}} \times \frac{c}{\lambda_{cav}^2} \times \frac{FWHM/2}{P_{drop}} \times \frac{1}{R_{esp}} \times \frac{1}{\sqrt{r}} \sqrt{10^{\frac{(P_{max}-G)-30}{10}}} \quad (\text{E-7})$$

$$\text{So: } \Delta z = \frac{1}{1.15 \times 10^4} \sqrt{\frac{6.63 \times 10^{-3} \times 1.3 \times 10^8}{4 \times 10^4}} \times \frac{3 \times 10^8}{(1.55 \times 10^{-6})^2} \times \frac{26 \times 10^{-1} / 2}{75 \times 10^{-6}} \times \frac{1}{1} \times \frac{1}{\sqrt{50}} \sqrt{10^{\frac{(-97-44.3)-30}{10}}} = 1.2 \times 10^{-15} \text{ m}/\sqrt{\text{Hz}}.$$

The theoretical value given by the equipartition theorem is:

$$NA_{th}(\omega_m) = \sqrt{\frac{2k_B T Q_m}{\pi k_{eff} f_m}} \quad (\text{E-8})$$

$$\text{So: } NA_{th}(\omega_m) = \sqrt{\frac{2 \times 1.38 \times 10^{-23} \times 293 \times 1000}{3.14 \times 40000 \times 1.3 \times 10^8}} = 7 \times 10^{-16} \text{ m}/\sqrt{\text{Hz}}.$$

The two values  $\Delta z$  and  $NA_{th}(\omega_m)$  are in agreement via a 1.7 multiplication factor. Every numerical value in the  $\Delta z$  calculation is from experimental observation except  $k_{eff}$  and  $g_0$  that are estimated by FEM simulations. It thus provides us a verification for those FEM-calculated values.

## Appendix F: Delay line phase slope effect

When sweeping the excitation frequency around  $f_m$  with the LIA, a phase slope appears due to the delay difference accumulated in both arms of the LIA: the higher the frequency and the path difference, the higher the slope (Figure F-1).

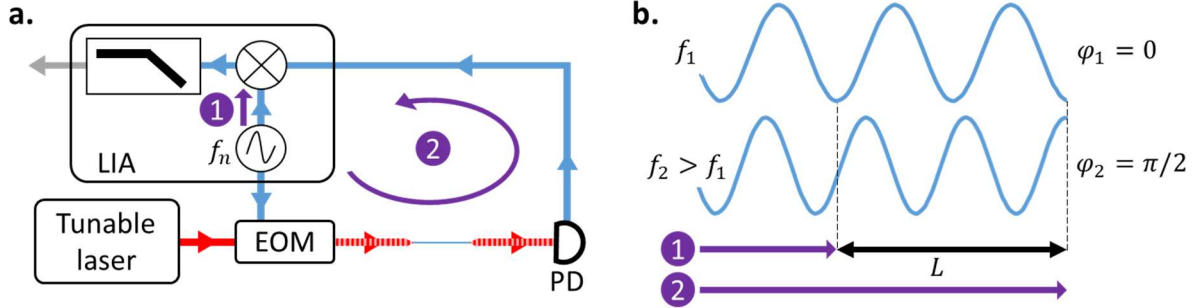


Figure F-1: (a) Scheme of the OM probe operating set-up up where the OM probe is replaced by a through line. The two paths the RF signal travels through are highlighted in purple (1) and (2). (b) Scheme of the RF signals at the LIA frequency for two different frequencies  $f_1$  and  $f_2$ . For the signal of frequency  $f_1$ , the phase-shift between the 2 paths is  $\varphi_1 = 0$ . For the chosen signal of frequency  $f_2$ , the phase-shift between the 2 paths is  $\varphi_2 = \pi/2$ . Thus for a LIA swept frequency from  $f_1$  to  $f_2$ , the phase slope will be  $\varphi_2 - \varphi_1 = \pi/2$ .

The phase delay  $\varphi_n$  accumulated by a signal passing in a path of length  $L$  depends on the signal's frequency  $f_n$ :

$$\varphi_n = \frac{2\pi f_n L}{v} \quad (\text{F-1})$$

Where  $v$  is the propagation velocity.

A slope then appears on the LIA phase when sweeping the measurement frequency:

$$\frac{\Delta\varphi}{\Delta f} = \frac{\varphi_2 - \varphi_1}{f_2 - f_1} = \frac{2\pi L}{v} \quad (\text{F-2})$$

Assuming a resonator with  $f_m = 130$  MHz and  $Q_m = 1000$ , the mechanical phase-shift is  $180^\circ$  and the frequency range over which this rotation appears is  $\Delta f = f_m/Q_m = 130$  kHz. Over this frequency range and a 10 m path difference, the phase slope effect discussed takes a value of:

$$\text{Application: } \Delta\varphi = \frac{2\pi \times 10}{3 \times 10^8} \times 130 \times 10^3 \times \frac{360}{2\pi} = 1.6^\circ$$

This value is 1% of the total phase rotation, negligible. However, for a higher frequency probe with a lower mechanical quality factor and a lower measured phase rotation (because of background for example), this value can surpass the measured phase rotation and prevent the phase-locked loop to be locked on the mechanical resonance.

Experimentally, this effect can be avoided with a delay line, a numerical delay compensation or a calibration with early traces. In this manuscript, we used the three depending on the availability of the numerical compensation in the LIA used.

## Appendix G: Cleaved facet side-injection and Fabry-Pérot effect

Some of the earlier devices we were able to assess optically were not made with grating couplers. To couple laser in and out the silicon chip, they were cleaved, letting the possibility to approach a micro-lensed fiber to the side and couple light in the waveguide. However as they are cleaved, the waveguide facets are reflective and induce Fabry-Pérot effect oscillations in the transmitted/reflected optical signal (Figure G-1).

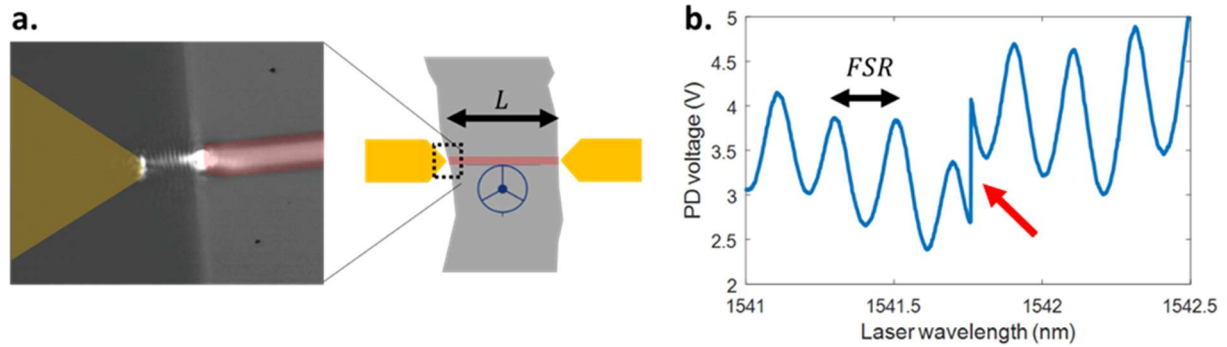


Figure G-1: (a) Scheme of the device and fibers and picture of the coupling micro-lensed fiber close to the cleaved waveguide. For scale, the waveguide highlighted in red is  $5 \mu\text{m}$  wide. (b) Optical transmission spectrum of the device. One can observe the oscillation due to the reflectivity of the device's cleaved facets. One can also observe the optical resonance of the ring resonator (red arrow) with the abrupt end of the thermo-optic shift. The  $FSR$  corresponds to the device size  $L = 5 \text{ mm}$  giving an expected  $FSR = \lambda^2/2n_{eff}L = (1541 \times 10^{-9})^2/2 \times 2.8 \times 2 \times 10^{-3} = 212 \text{ pm}$  in agreement with the experimental value of  $200 \text{ pm}$ , knowing that the silicon chip length  $L$  was roughly evaluated with a ruler. The brutal uphill slope of the transmission is associated with the end of the thermo-optic shift of the optical resonance of the OM probe.

This reflectivity allows one to operate the OM probe with only one fiber. This Fabry-Pérot effect also induces a modulation on the mechanical motion transduction (Figure G-2).

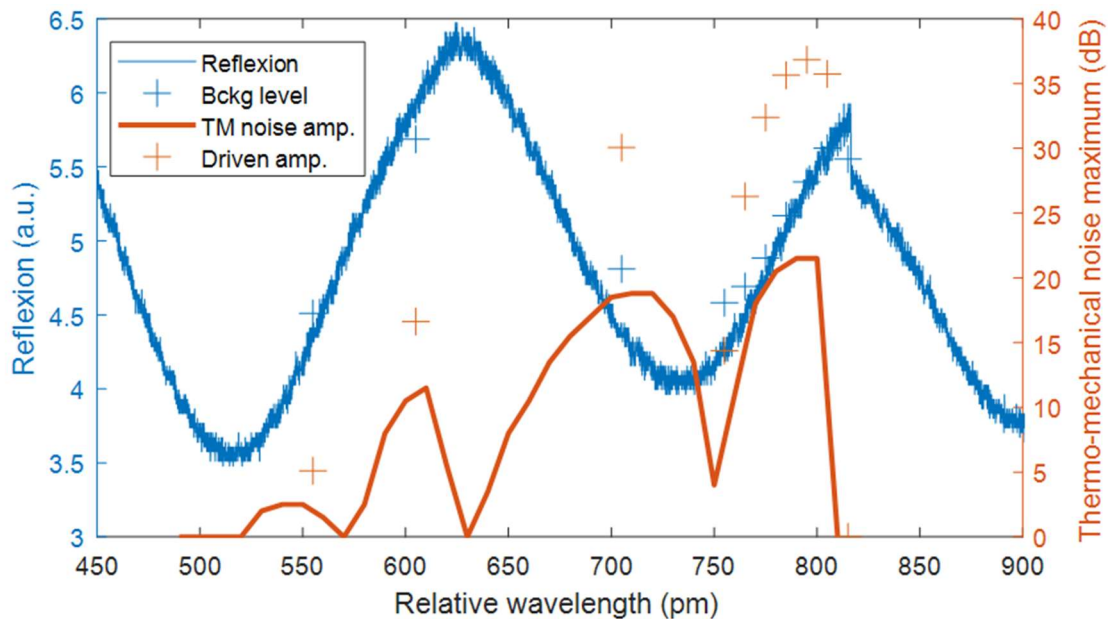


Figure G-2: Fabry-Pérot effect on the thermomechanical noise transduction. The wavelengths are relative to  $1539 \text{ nm}$  and the thermomechanical motion is taken at  $117.14 \text{ MHz}$ , relative to the noise floor of  $-98.5 \text{ dBm}$ . In plain blue is traced the reflection of the optical signal. In plain orange is traced

the thermomechanical (TM) noise maximum in dB, relative to the noise floor. The crosses are data extracted from the driven operation of the OM probe. The blue crosses are the background level and the orange crosses are the driven amplitude of the OM probe motion.

As described in Figure G-2, the plain blue trace displays a modulation corresponding to the chip cavity. One can also observe the quasi-vertical downhill at 810 pm associated with the optical resonance. Actually the laser enters the optical resonance around 520 pm and the thermo-optic effect shifts it until 810 pm. One can observe that the blue crosses fit perfectly the plain blue trace. This means that the background level is proportional to the reflection of the device as expected from the “through signal”.

The envelope of the orange curve finds its explanation in the growing slope of the optical lorentzian: as the wavelength of the laser approaches the one of the optical cavity, the thermomechanical motion is better transduced. But exceptionally, it displays a modulation. It appears that each extremum of the reflection spectrum is linked to a maximum of the thermomechanical noise transduction, indicating that power injected at those wavelength is higher inducing a better transduction. However the peaks does not match properly, in particular the first one. This could be explained by the Lorentzian shape of the optical mode, where transduction is better in the middle of the slope. This could also be explained by the fact that the reflection spectrum was taken using the continuous sweep tool of the laser. This distorts the spectrum compared to a step by step sweep (done for the thermomechanical noise maximum) where the wavelength is verified at each step. Another information on this bumpy thermomechanical noise maximum is that when the OM resonator is driven, the mechanical resonance peak reverses at each bump. It means that the phase-shift between the background and the mechanical signal changes of  $\pi$  between every bump.

The driven amplitude is higher than what the thermomechanical noise. This highlights the driving of the mechanical resonator: when more optical signal is injected, it is more actuated (the orange curve and markers fit well when the driven amplitude is divided by a linearly growing factor with respect to wavelength).



## Appendix H: Contrast and FWHm definition

From the transmission function, one can extract the contrast and the Full Width at Half Minimum (FWHm). The optical transmission  $T(\omega_{laser})$  is given by:

$$T(\omega_{laser}) = \frac{\left(\frac{\gamma_{int}}{2} - \frac{\gamma_e}{2}\right)^2 + (\omega_{cav} - \omega_{laser})^2}{\left(\frac{\gamma_e}{2} + \frac{\gamma_{int}}{2}\right)^2 + (\omega_{cav} - \omega_{laser})^2} \quad (H-1)$$

Where  $\omega_{cav}$  is the optical resonance angular frequency of the cavity and  $\omega_{laser}$  is the angular frequency of the laser.  $\gamma_{int}$  is the rate of the intrinsic optical losses of the cavity and  $\gamma_e$  of the extrinsic ones (*i.e.* coupling ones).

The transmission on resonance is straightforwardly evaluated:

$$T(\omega_{cav}) = \left(\frac{\gamma_{int} - \gamma_e}{\gamma_e + \gamma_{int}}\right)^2 \quad (H-2)$$

As the transmission is normalized, the contrast is then:

$$C = \frac{T_{max} - T(\omega_{cav})}{T_{max}} = 1 - T(\omega_{cav}) \quad (H-3)$$

To better picture the values we are talking about, they are presented in Figure H-1.

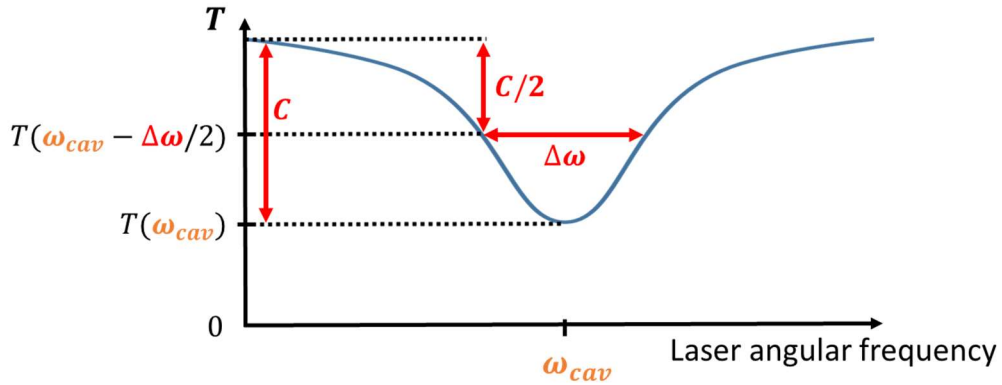


Figure H-1: Optical transmission  $T$  of an OM probe featuring its optical resonance  $\omega_{cav}$ . The contrast is actually normalized by the maximal transmission, which is taken equal to 1 in this graph.

To find the FWHm  $\Delta\omega$ , one can write the condition:

$$T\left(\omega_{cav} + \frac{\Delta\omega}{2}\right) = \frac{T(\omega_{cav}) + 1}{2} \quad (H-4)$$

Where the right side can be written:

$$\frac{T(\omega_{cav}) + 1}{2} = \frac{\gamma_e^2 + \gamma_{int}^2}{(\gamma_e + \gamma_{int})^2} \quad (H-5)$$

We have then:

$$\frac{(\gamma_{int} - \gamma_e)^2 + \Delta\omega^2}{(\gamma_e + \gamma_{int})^2 + \Delta\omega^2} = \frac{\gamma_e^2 + \gamma_{int}^2}{(\gamma_e + \gamma_{int})^2} \quad (\text{H-6})$$

So

$$[(\gamma_{int} - \gamma_e)^2 + \Delta\omega^2](\gamma_e + \gamma_{int})^2 = (\gamma_e^2 + \gamma_{int}^2)[(\gamma_e + \gamma_{int})^2 + \Delta\omega^2] \quad (\text{H-7})$$

Factorizing:

$$\Delta\omega^2 \times (2\gamma_e\gamma_{int}) = (\gamma_e + \gamma_{int})^2 \times (2\gamma_e\gamma_{int}) \quad (\text{H-8})$$

Thus:

$$\Delta\omega = \gamma_e + \gamma_{int} \quad (\text{H-9})$$

Speaking in terms of quality factor, using  $Q_{opt} = \frac{\omega_{cav}}{\Delta\omega}$  and  $Q_x = \frac{\omega_{cav}}{\gamma_x}$ , we find:

$$\frac{1}{Q_{opt}} = \frac{1}{Q_e} + \frac{1}{Q_{int}} \quad (\text{H-10})$$

Approximating the optical resonance to a triangle, one finds its slope S:

$$S = \frac{T_{max} - T(\omega_{cav})}{\Delta\omega} \quad (\text{H-11})$$

Rewriting this equation, we find:

$$S = \frac{C \times T_{max} \times Q_{opt}}{\omega_{cav}} \quad (\text{H-12})$$

To maximize the OM transduction, one has to maximize the optical resonance slope given by maximizing  $T_{max}$  and (neglecting constant terms):

$$Q_{opt}C = T_{max} \frac{\omega_{cav}}{\Delta\omega} (1 - T(\omega_{cav})) \quad (\text{H-13})$$

Giving at last:

$$Q_{opt}C = \frac{4}{Q_e Q_{int} \left( \frac{1}{Q_e} + \frac{1}{Q_{int}} \right)^3} \quad (\text{H-14})$$

One thus seeks the lowest  $\gamma_e$  and  $\gamma_{int}$  to maximize transduction. This equation also means that for a given  $Q_{int}$ , the maximum  $Q_{opt}C$  is obtained for  $Q_e = 2Q_{int}$ , i.e.  $\gamma_{int} = 2\gamma_e$ .

From the contrast and the FWHm, one can extract the  $Q_e$  and  $Q_{int}$ .

$$C = 1 - T(\omega_{cav}) = 1 - \left( \frac{\gamma_{int} - \gamma_e}{\gamma_e + \gamma_{int}} \right)^2 = \frac{4\gamma_e\gamma_{int}}{(\gamma_e + \gamma_{int})^2} = \frac{4(\Delta\omega - \gamma_e)\gamma_e}{(\Delta\omega)^2} \quad (\text{H-15})$$

Thus the  $\gamma_e$  can be found with a 2<sup>nd</sup> order formula from the contrast and FWHm:

$$4\gamma_e^2 - 4\Delta\omega\gamma_e + \Delta\omega^2 C = 0 \quad (\text{H-16})$$

With the positive discriminant  $\Delta = (4\Delta\omega)^2(1 - C)$ . The two solutions are given by:

$$\gamma_e = \frac{\Delta\omega}{2} (1 \pm \sqrt{1 - C}) \quad (\text{H-17})$$

Which gives a more handy:

$$Q_e = \frac{\lambda_{cav}}{2\Delta\lambda(1 \pm \sqrt{1 - C})} \quad (\text{H-18})$$

With  $\Delta\lambda/\lambda_{cav} = \Delta\omega/\omega_{cav}$ .

Similarly, one can find:

$$Q_{int} = \frac{\lambda_{cav}}{2\Delta\lambda(1 \pm \sqrt{1 - C})} \quad (\text{H-19})$$

The coupling regime fixes the sign of the solution. For critical coupling  $Q_e = Q_{int}$ . However for under-coupled and over-coupled regimes, the signs in the denominator are opposite, with a change in between regimes.

## Appendix I: Thermo-optical saw-tooth shift

For high powers, when the laser injected in an optical cavity is swept in the cavity towards larger wavelengths, the optical resonance appears distorted in a saw-tooth fashion (Figure I-1). The width of the tooth is proportional to injected laser power.

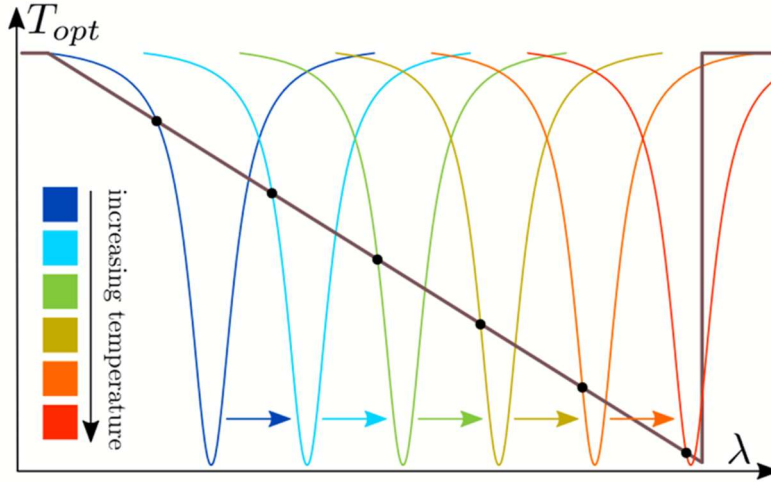


Figure I-1: Transmission (in black) of an OM ring when probing laser is swept in increasing wavelength. It displays a saw-tooth-shaped, thermo-optic distortion of the cavity. The implicit optical resonance drop is represented in colors for increasing temperature. When the laser is swept over a WGM at high power, the temperature increase in the disk gradually red-shifts the WGM resonance. As a consequence the WGM appears as a triangular profile. From p. 35 in [139].

For our  $0.22 \mu\text{m} \times 0.5 \mu\text{m}$  ring cross section featuring a  $\lambda_0 = 1.55 \mu\text{m}$  resonance, we observed a  $\Delta\lambda_{cav} = 100 \text{ pm}$  resonance wavelength shift. This shift could be explained by three phenomena:

- thermal expansion: the cavity heats up and thus deforms  $\alpha_{th\_exp} = \frac{1}{L} \frac{\partial L}{\partial T}$ ,  $L$  being the length of the cavity;
- thermo-optic effect: the cavity heats up and thus its effective index grows  $\alpha_{th\_opt} = \frac{\partial n}{\partial T}$ ;
- AC Kerr effect: effective index increase with power in cavity  $\Delta n = n_2 I = \frac{n_2 P_{circ}}{w_{ring} h}$ ,  $I$  being the optical intensity in the cavity and  $w_{ring} \times h$  being the cross-section surface of the cavity's waveguide.

Let us first compare the first two options. Assuming thermal expansion, the  $\Delta\lambda_{cav} = 100 \text{ pm}$  resonance wavelength shift would correspond to a temperature increase of, using the resonance equation  $m\lambda_0 = 2\pi R n_{eff}$ :

$$\Delta T_{thermal\_expansion} = \frac{\Delta\lambda}{\lambda_0 \alpha_{th\_exp}} \quad (I-1)$$

For  $\Delta\lambda = 100 \text{ pm}$ ,  $\lambda_0 = 1.55 \mu\text{m}$  and  $\alpha_{th\_exp} = 2.5 \times 10^{-6}$  [196], we find  $\Delta T_{thermal\_expansion} = 25 \text{ K}$ .

Or assuming thermo-optic effect, it would correspond to a temperature increase of:

$$\Delta T_{thermo\_optic} = \frac{n_{eff}\Delta\lambda}{\lambda_0\alpha_{th\_opt}} \quad (I-2)$$

For  $n_{eff} = 2.4$ ,  $\Delta\lambda = 100$  pm,  $\lambda_0 = 1.55$   $\mu\text{m}$  and  $\alpha_{th\_opt} = 1.8 \times 10^{-4}$   $\text{K}^{-1}$  [197], we find  $\Delta T_{thermo\_optic} = 0.9$  K.

The thermo-optic effect needs a 28 times lower temperature to create the same shift of wavelength. The thermal expansion effect is thus negligible over the thermo-optic one.

For the AC Kerr effect to induce such a resonance wavelength shift  $\Delta\lambda$ , the power circulating in the cavity must be:

$$P_{Kerr} = \frac{n_{eff} \times \Delta\lambda \times h \times w_{ring}}{\lambda_0 n_2} \quad (I-3)$$

For  $\Delta\lambda = 100$  pm,  $h = 220$  nm,  $w_{ring} = 500$  nm,  $\lambda_0 = 1.55$   $\mu\text{m}$ ,  $n_{eff} = 2.4$  and the AC-Kerr coefficient  $n_2 = 4.5$   $\text{nm}^2 \cdot \text{W}^{-1}$  [198], we find  $P_{Kerr} = 3.8$  W.

The optical energy stored in the cavity  $E_{stored}$  is given by:

$$E_{stored}(\omega_{laser}) = \frac{\gamma_e P_{in}}{\left(\frac{\gamma_{tot}}{2}\right)^2 + (\omega_{laser} - \omega_{cav})^2} \quad (I-4)$$

To find the circulating power, one has to divide it by  $T_0$ , the time for a photon to complete a lap in the cavity  $T_0 = \frac{m\lambda_0}{c}$ , at resonance:

$$P_{circ} = \frac{E_{stored}}{T_0} = \frac{c}{m\lambda_0} \times \frac{\gamma_e P_{in}}{\left(\frac{\gamma_{tot}}{2}\right)^2 + (\omega_{laser} - \omega_{cav})^2} = \frac{\frac{P_{in}}{2\pi Q_e m}}{\left(\frac{1}{2Q_{tot}}\right)^2 + \left(\frac{\lambda_0}{\lambda_{laser}} - 1\right)^2} \quad (I-5)$$

At resonance  $\lambda_{laser} = \lambda_0$  and assuming a critical coupling  $Q_e = Q_{int}$  so  $Q_{tot} = Q_e/2$ , one thus finds:

$$P_{circ} = \frac{P_{in} Q_{tot}}{\pi m} \quad (I-6)$$

For  $m = 100$ ,  $P_{in} = 1$  mW and  $Q_{tot} = 40\,000$ , we find  $P_{circ} = 0.13$  W.

The power needed to induce the shift is more than one order of magnitude higher than the real power, AC Kerr effect is thus negligible over thermo-optic effect. Therefore, the thermo-optic shift is a handy method to probe the temperature of the ring. For our thermo-optic shift were no wider than 1 nm, the temperature elevation due to laser in our rings was lower than 10 K.

Appendix J: Acquisition and generation digital interface

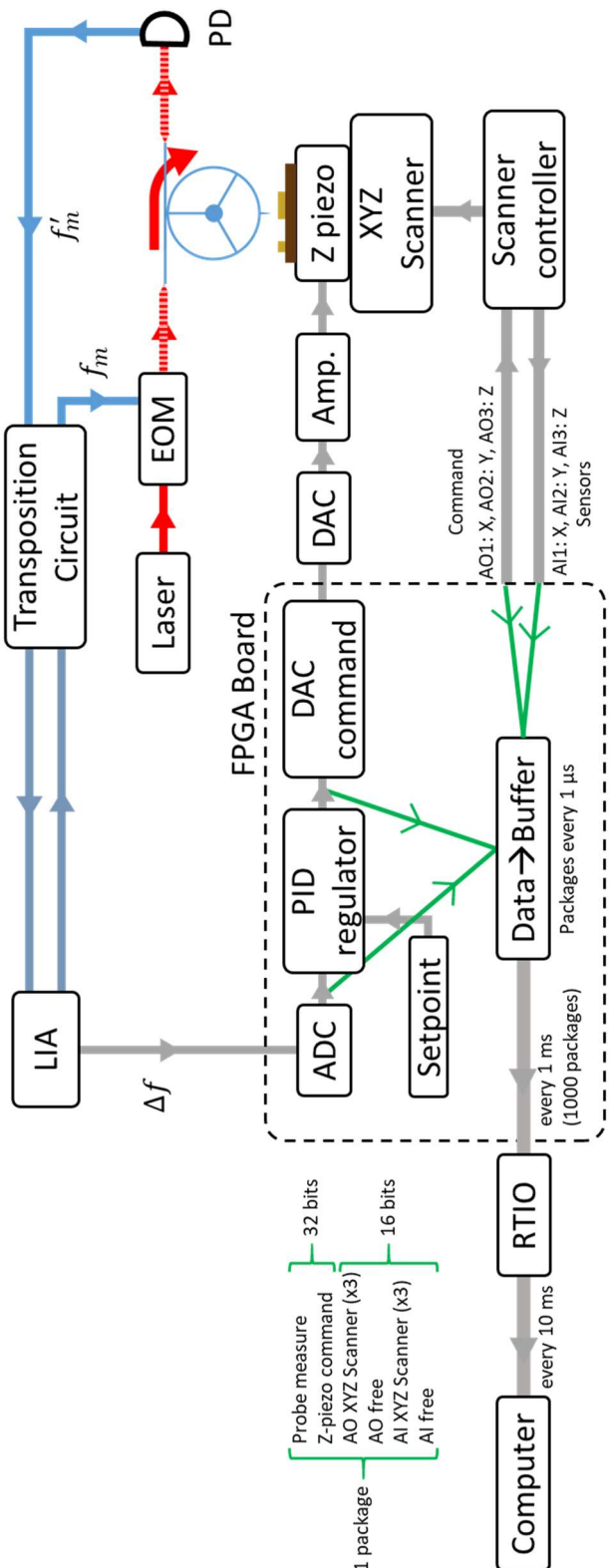


Figure J-1: Scheme of the detailed digital interface. The user interface is computed in LabVIEW. AO stands for analog output and AI stands for analog input. RTIO stands for Real-Time-Input-Output, this block consists of a National instruments Compact RIO controller with 4 modules: NI9215 (4 inputs sampling 100 kHz), NI9229 (4 inputs sampling 1 MHz), NI9253 (8 inputs sampling 50 kHz), NI9401 (4 inputs and 4 output).

## Appendix K: Effective index correction on the free spectral range

The optical resonance condition of a ring cavity of radius  $R$  writes itself:

$$m\lambda_m = 2\pi R n_{eff}(\lambda_m) \quad (K-1)$$

Using the resonance condition (K-1), one can estimate the Free Spectral Range (FSR) of the ring cavity given by  $FSR_\lambda = \lambda_{m+1} - \lambda_m$ . Considering a constant effective index  $n_{eff}$  and assuming  $m \gg 1$ , one finds:

$$FSR_\lambda = -\frac{\lambda_m}{m} \quad (K-2)$$

The  $m \gg 1$  assumption is valid for our 10  $\mu\text{m}$  radius rings with azimuthal orders  $m$  about 100. With  $\lambda_m = 1.55 \mu\text{m}$  and  $m = 100$ , one thus finds  $FSR_\lambda = -15.5 \text{ nm}$ .

This theoretical value is however about twice the experimental one, of about -9 nm. This is because one cannot neglect the variation of the effective index over the wavelength. Let us find the new free spectral range:

$$FSR_\lambda = \lambda_{m+1} - \lambda_m = \frac{2\pi R}{m} \left( \frac{n_{eff}(\lambda_{m+1})}{1 + \frac{1}{m}} - n_{eff}(\lambda_m) \right) \quad (K-3)$$

Assuming that  $m \gg 1$ , one can write:

$$FSR_\lambda = \frac{2\pi R}{m} \left( n_{eff}(\lambda_{m+1}) \times \left( 1 - \frac{1}{m} \right) - n_{eff}(\lambda_m) \right) \quad (K-4)$$

Using a first order limited development  $n_{eff}(\lambda_{m+1}) = n_{eff}(\lambda_m) + FSR_\lambda \times \frac{\partial n_{eff}}{\partial \lambda}$ :

$$FSR_\lambda = \frac{2\pi R}{m} \left( \left( n_{eff}(\lambda_m) + FSR_\lambda \times \frac{\partial n_{eff}}{\partial \lambda} \right) \times \left( 1 - \frac{1}{m} \right) - n_{eff}(\lambda_m) \right) \quad (K-5)$$

One can re-write:

$$FSR_\lambda = \frac{2\pi R}{m} \left( FSR_\lambda \times \frac{\partial n_{eff}}{\partial \lambda} \times \left( 1 - \frac{1}{m} \right) - \frac{n_{eff}(\lambda_m)}{m} \right) \quad (K-6)$$

Re-writing the pre-factor using equation (K-1) and assuming again that  $m \gg 1$ , one can write:

$$FSR_\lambda = \frac{\lambda_m}{n_{eff}(\lambda_m)} \left( FSR_\lambda \times \frac{\partial n_{eff}}{\partial \lambda} - \frac{n_{eff}(\lambda_m)}{m} \right) \quad (K-7)$$

One can thus finally write the corrected FSR:

$$FSR_\lambda = -\frac{\lambda_m}{m} \left( 1 - \frac{\lambda_m}{n_{eff}(\lambda_m)} \times \frac{\partial n_{eff}}{\partial \lambda} \right)^{-1} \quad (K-8)$$

This corrected FSR estimation gives, using  $\lambda_m = 1.55 \mu\text{m}$ ,  $m = 100$ ,  $n_{eff}(\lambda_m) = 2.4$  and  $\frac{\partial n_{eff}}{\partial \lambda} = -1.176 \mu\text{m}^{-1}$ ,  $FSR_\lambda = -8.8 \text{ nm}$ .





## Dissemination

### *International journal*

“Optomechanical resonating probe for very high frequency sensing of atomic forces”. P.E. Allain, L. Schwab, C. Mismar, M. Gély, E. Mairiaux, M. Hermouet, B. Walter, G. Leo, S. Hentz, M. Faucher, G. Jourdan, B. Legrand and I. Favero. *Nanoscale*, 12 (2020) 2939-2945 / <https://doi.org/10.1039/C9NR09690F>.

In review: “Low Latency Demodulation for High-Frequency Atomic Force Microscopy Probes”. D. Lagrange, N. Mauran, L. Schwab, B. Legrand. In review, submitted to *Transactions on Control Systems Technology*.

In preparation: “Silicon optomechanics: enabling very high frequency probes for atomic force microscopy”. L. Schwab, P.E. Allain, D. Lagrange, N. Mauran, M. Gély, M. Hermouet, G. Leo, S. Hentz, G. Jourdan, I. Favero and B. Legrand. In preparation for *Applied Physics Letters*.

### *International conference*

“Comprehensive optical losses investigation of VLSI Silicon optomechanical ring resonator sensors”. L. Schwab, P.E. Allain, L. Banniard, A. Fafin, M. Gely, O. Lemonnier, P. Grosse, M. Hermouet, S. Hentz, I. Favero, B. Legrand, and G. Jourdan. *Proceedings of 64<sup>th</sup> IEEE International Electron Devices Meeting*. IEDM 2018, San Francisco, CA, USA, December, 3-5, 2018, 4.7.1-4 (oral communication).

“130-MHz optomechanical vibrating sensor: towards high-bandwidth / ultrasensitive measurements”. L. Schwab, P.E. Allain, L. Banniard, N. Mauran, D. Lagrange, A. Fafin, M. Gely, M. Hermouet, G. Jourdan, S. Hentz, I. Favero, and B. Legrand. *Proceedings of 32<sup>nd</sup> IEEE Conference on Micro Electro Mechanical Systems*. MEMS 2019, Seoul, Korea, January 27-31, 2019, 819-822 (poster).

“Optomechanics: a key towards next-generation experiments in atomic force microscopy?”. L. Schwab, P. Allain, D. Théron, M. Faucher, B. Walter, S. Hentz, G. Jourdan, I. Favero, and B. Legrand *International Conference on Quantum Sensing and Metrology*. IQuMS 2019, Paris, France, December 9-13, 2019 (oral communication).

“MEMS-based atomic force microscopy probes: from electromechanical to optomechanical vibrating sensors”. B. Legrand, L. Schwab, P. Allain, I. Favero, M. Faucher, D. Théron, B. Walter, J.P. Salvétat, S. Hentz, and G. Jourdan. AVS 65<sup>th</sup> International Symposium & Exhibition, Long Beach, CA, USA, October 21-26, 2018 (oral communication).

“High-speed Atomic Force Microscope”. N. Mauran, D. Lagrange, X. Dollat, L. Mazenq, L. Schwab, J.P. Salvétat, B. Legrand *National Instruments Week, NI Week 2017*. Austin, Texas, USA, May 22-25, 2017 (invited oral communication).

### *Other*

“Optomechanical probe for an ultra-fast AFM”. L. Schwab, P. Allain, I. Favero, B. Legrand 11<sup>th</sup> NAMIS school, IMTEK – University of Freiburg, Freiburg, Germany, October 2-6, 2017 (poster).

“Applied cavity optomechanics: high-speed atomic force microscopy (HS-AFM)”. L. Schwab, P. Allain, I. Favero, B. Legrand. 3<sup>rd</sup> annual meeting GdR MecaQ, Paris, September 12, 2018 (oral communication).



## Bibliography

- [1] D. J. Muller, "AFM: A Nanotool in Membrane Biology," *Biochemistry*, vol. 47, no. 31, pp. 7986–7998, Aug. 2008, doi: 10.1021/bi800753x.
- [2] G. Binnig, H. Rohrer, C. Gerber, and E. Weibel, "Surface Studies by Scanning Tunneling Microscopy," *Phys. Rev. Lett.*, vol. 49, no. 1, pp. 57–61, Jul. 1982, doi: 10.1103/PhysRevLett.49.57.
- [3] G. Binnig, C. F. Quate, and C. Gerber, "Atomic Force Microscope," *Phys. Rev. Lett.*, vol. 56, no. 9, pp. 930–933, Mar. 1986, doi: 10.1103/PhysRevLett.56.930.
- [4] N. Kodera, D. Yamamoto, R. Ishikawa, and T. Ando, "Video imaging of walking myosin V by high-speed atomic force microscopy," *Nature*, vol. 468, no. 7320, pp. 72–76, Nov. 2010, doi: 10.1038/nature09450.
- [5] T. Ando, T. Uchihashi, and T. Fukuma, "High-speed atomic force microscopy for nano-visualization of dynamic biomolecular processes," *Prog. Surf. Sci.*, vol. 83, no. 7–9, pp. 337–437, Nov. 2008, doi: 10.1016/j.progsurf.2008.09.001.
- [6] F. J. Giessibl, *Noncontact Atomic Force Microscopy*. Berlin, Heidelberg: Springer Berlin Heidelberg, 2009.
- [7] R. Boubekri *et al.*, "Electrothermally driven high-frequency piezoresistive SiC cantilevers for dynamic atomic force microscopy," *J. Appl. Phys.*, vol. 116, no. 5, p. 054304, Aug. 2014, doi: 10.1063/1.4891833.
- [8] B. Walter, M. Faucher, E. Mairiaux, Z. Xiong, L. Buchaillet, and B. Legrand, "4.8 MHz AFM nanoprobe with capacitive transducers and batch-fabricated nanotips," in *2011 IEEE 24th International Conference on Micro Electro Mechanical Systems*, Jan. 2011, pp. 517–520, doi: 10.1109/MEMSYS.2011.5734475.
- [9] Sangmin An, T. Michels, Jie Zou, D. A. Westly, and V. A. Aksyuk, "Optomechanical transducer-based nanocantilever for atomic force microscopy," in *2015 International Conference on Optical MEMS and Nanophotonics (OMN)*, Aug. 2015, vol. 2, pp. 1–2, doi: 10.1109/OMN.2015.7288864.
- [10] B. P. Abbott *et al.*, "Observation of Gravitational Waves from a Binary Black Hole Merger," *Phys. Rev. Lett.*, vol. 116, no. 6, p. 061102, Feb. 2016, doi: 10.1103/PhysRevLett.116.061102.
- [11] A. Schließer, "Cavity Optomechanics and Optical Frequency Comb Generation with Silica Whispering-Gallery-Mode Microresonators," LMU Munich, 2009.
- [12] M. Aspelmeyer, P. Meystre, and K. Schwab, "Quantum optomechanics," *Phys. Today*, vol. 65, no. 7, pp. 29–35, Jul. 2012, doi: 10.1063/PT.3.1640.
- [13] A. G. Krause, M. Winger, T. D. Blasius, Q. Lin, and O. Painter, "A high-resolution microchip optomechanical accelerometer," *Nat. Photonics*, vol. 6, no. 11, pp. 768–772, Nov. 2012, doi: 10.1038/nphoton.2012.245.
- [14] J. Chae *et al.*, "Nanophotonic Atomic Force Microscope Transducers Enable Chemical Composition and Thermal Conductivity Measurements at the Nanoscale," *Nano Lett.*, vol. 17, no. 9, pp. 5587–5594, Sep. 2017, doi: 10.1021/acs.nanolett.7b02404.

- [15] S. An, J. Zou, G. Holland, J. Chae, A. Centrone, and V. Aksyuk, "Optomechanical transducer-based soft and high frequency nanoscale cantilever for atomic force microscopy," in *2016 Solid-State, Actuators, and Microsystems Workshop Technical Digest*, May 2016, vol. 2, no. c, pp. 266–269, doi: 10.31438/trf.hh2016.71.
- [16] A. van Leeuwenhoek, "Observationes microscopicae Antonii Lewenhoeck, circa particulas liquorum globosa et animalia," *Acta Erud.*, 1682.
- [17] M. Knoll and E. Ruska, "Das Elektronenmikroskop," *Zeitschrift für Phys.*, vol. 78, no. 5–6, pp. 318–339, May 1932, doi: 10.1007/BF01342199.
- [18] M. von Ardenne, "Das Elektronen-Rastermikroskop," *Zeitschrift für Phys.*, vol. 109, no. 9–10, pp. 553–572, Sep. 1938, doi: 10.1007/BF01341584.
- [19] V. A. Zworykin, J. Hillier, and R. L. Snyder, "A scanning electron microscope," *ASTM Bull*, no. 117, pp. 15–23, 1942.
- [20] D. W. Pohl, W. Denk, and M. Lanz, "Optical stethoscopy : Image recording with resolution  $\lambda / 20$ ," *Appl. Phys. Lett.*, vol. 651, no. 1984, 1984, doi: 10.1063/1.94865.
- [21] S. W. Hell and J. Wichmann, "Breaking the diffraction resolution limit by stimulated emission : stimulated-emission-depletion fluorescence microscopy," *Opt. Lett.*, vol. 19, no. 11, pp. 780–782, 1994.
- [22] F. J. Giessibl, "Atomic Resolution of the Silicon (111)-(7x7) Surface by Atomic Force Microscopy," *Science (80-. )*, vol. 267, no. 5194, pp. 68–71, Jan. 1995, doi: 10.1126/science.267.5194.68.
- [23] S. Pezzagna *et al.*, "Nanoscale Engineering and Optical Addressing of Single Spins in Diamond," *Small*, vol. 6, no. 19, pp. 2117–2121, Sep. 2010, doi: 10.1002/smll.201000902.
- [24] L. Gross, F. Mohn, N. Moll, P. Liljeroth, and G. Meyer, "The Chemical Structure of a Molecule Resolved by Atomic Force Microscopy," *Science (80-. )*, vol. 325, no. August, pp. 1110–1115, 2009.
- [25] Y. Sugimoto, Y. Nakajima, D. Sawada, K. Morita, M. Abe, and S. Morita, "Simultaneous AFM and STM measurements on the Si(111)-(7x7)," *Phys. Rev. B*, vol. 81, no. 24, p. 245322, Jun. 2010, doi: 10.1103/PhysRevB.81.245322.
- [26] Y. Seo and W. Jhe, "Atomic force microscopy and spectroscopy," *Reports Prog. Phys.*, vol. 71, no. 1, p. 016101, Jan. 2008, doi: 10.1088/0034-4885/71/1/016101.
- [27] F. Castanié, "Approches numériques et théorique du microscope à force atomique : interaction, dynamique et imagerie," Université Paul Sabatier - Toulouse III, 2012.
- [28] R. B. Bird, W. E. Stewart, and E. N. Lightfoot, *Transport Phenomena 2nd edition*. 2002.
- [29] "Bruker AFM cantilever RFESP-190 for tapping mode," 2019. <https://www.brukerafmprobes.com/p-3925-rfesp-190.aspx> (accessed May 01, 2020).
- [30] H. C. Hamaker, "The London-Van der Waals Attraction Between Spherical Particles," *Phys. 4*, no. 10, 1937.
- [31] P. E. Allain *et al.*, "Color atomic force microscopy: A method to acquire three

- independent potential parameters to generate a color image," *Appl. Phys. Lett.*, vol. 111, no. 12, p. 123104, Sep. 2017, doi: 10.1063/1.4991790.
- [32] H. Hertz, "Ueber die Berührung fester elastischer Körper.," *J. für die reine und Angew. Math. (Crelles Journal)*, vol. 1882, no. 92, pp. 156–171, Jan. 1882, doi: 10.1515/crll.1882.92.156.
- [33] K. L. Johnson, K. Kendall, and A. D. Roberts, "Surface energy and the contact of elastic solids," *Proc. R. Soc. London. A. Math. Phys. Sci.*, vol. 324, no. 1558, pp. 301–313, Sep. 1971, doi: 10.1098/rspa.1971.0141.
- [34] B. . Derjaguin, V. . Muller, and Y. . Toporov, "Effect of contact deformations on the adhesion of particles," *J. Colloid Interface Sci.*, vol. 53, no. 2, pp. 314–326, Nov. 1975, doi: 10.1016/0021-9797(75)90018-1.
- [35] R. S. Bradley, "LXXIX. The cohesive force between solid surfaces and the surface energy of solids," *London, Edinburgh, Dublin Philos. Mag. J. Sci.*, vol. 13, no. 86, pp. 853–862, Apr. 1932, doi: 10.1080/14786449209461990.
- [36] K. L. Johnson and J. A. Greenwood, "An Adhesion Map for the Contact of Elastic Spheres," *J. Colloid Interface Sci.*, vol. 192, no. 2, pp. 326–333, Aug. 1997, doi: 10.1006/jcis.1997.4984.
- [37] R. Reifenberger, *Lecture 2.5: Contact Mechanics*. nanohub.org, 2012.
- [38] K. L. Johnson, *Contact Mechanics*. Cambridge University Press, 1985.
- [39] C. J. Chen, *Introduction to Scanning Tunneling Microscopy*. Oxford University Press, 2007.
- [40] I. Morawski and B. Voigtländer, "Simultaneously measured signals in scanning probe microscopy with a needle sensor: Frequency shift and tunneling current," *Rev. Sci. Instrum.*, vol. 81, no. 3, p. 033703, Mar. 2010, doi: 10.1063/1.3321437.
- [41] B. Cappella, P. Baschieri, C. Frediani, P. Miccoli, and C. Ascoli, "Force-distance curves by AFM," *IEEE Eng. Med. Biol. Mag.*, vol. 16, no. 2, pp. 58–65, 1997, doi: 10.1109/51.582177.
- [42] F. J. Giessibl, "The qPlus sensor, a powerful core for the atomic force microscope," *Rev. Sci. Instrum.*, vol. 90, no. 1, 2019, doi: 10.1063/1.5052264.
- [43] S. Kawai, S. Kitamura, D. Kobayashi, S. Meguro, and H. Kawakatsu, "An ultrasmall amplitude operation of dynamic force microscopy with second flexural mode," *Appl. Phys. Lett.*, pp. 1–3, 2005, doi: 10.1063/1.1923200.
- [44] B. L. Weeks, M. W. Vaughn, and J. J. Deyoreo, "Direct imaging of meniscus formation in atomic force microscopy using environmental scanning electron microscopy," *Langmuir*, vol. 21, no. 18, pp. 8096–8098, 2005, doi: 10.1021/la0512087.
- [45] S. An, J. Kim, K. Lee, B. Kim, M. Lee, and W. Jhe, "Mechanical properties of the nanoscale molecular cluster of water meniscus by high-precision frequency modulation atomic force spectroscopy," *Appl. Phys. Lett.*, vol. 101, no. 5, p. 053114, Jul. 2012, doi: 10.1063/1.4740083.

- [46] B. Cappella and G. Dietler, "Force-distance curves by atomic force microscopy," *Surf. Sci. Rep.*, vol. 34, no. 1–3, pp. 1–104, Jan. 1999, doi: 10.1016/S0167-5729(99)00003-5.
- [47] F. J. Giessibl, "Advances in atomic force microscopy," *Rev. Mod. Phys.*, vol. 75, no. 3, pp. 949–983, Jul. 2003, doi: 10.1103/RevModPhys.75.949.
- [48] G. Meyer and N. M. Amer, "Novel optical approach to atomic force microscopy," *Appl. Phys. Lett.*, vol. 53, no. 12, pp. 1045–1047, Sep. 1988, doi: 10.1063/1.100061.
- [49] D. Croft, G. Shed, and S. Devasia, "Creep, Hysteresis, and Vibration Compensation for Piezoactuators: Atomic Force Microscopy Application," *J. Dyn. Syst. Meas. Control*, vol. 123, no. 1, pp. 35–43, Mar. 2001, doi: 10.1115/1.1341197.
- [50] G. R. Jayanth, Y. Jeong, and C.-H. Menq, "Direct tip-position control using magnetic actuation for achieving fast scanning in tapping mode atomic force microscopy," *Rev. Sci. Instrum.*, vol. 77, no. 5, p. 053704, May 2006, doi: 10.1063/1.2200874.
- [51] N. Sarkar, R. R. Mansour, O. Patange, and K. Trainor, "CMOS-MEMS atomic force microscope," in *2011 16th International Solid-State Sensors, Actuators and Microsystems Conference*, Jun. 2011, pp. 2610–2613, doi: 10.1109/TRANSDUCERS.2011.5969836.
- [52] P. Eaton and P. West, *Atomic Force Microscopy*. 2010.
- [53] J. G. Ziegler and N. B. Nichols, "Optimum Settings for Automatic Controllers," *J. Dyn. Syst. Meas. Control*, vol. 115, no. 2B, pp. 220–222, Jun. 1993, doi: 10.1115/1.2899060.
- [54] I. Casuso, F. Rico, and S. Scheuring, "Biological AFM: where we come from - where we are - where we may go," *J. Mol. Recognit.*, vol. 24, no. 3, pp. 406–413, May 2011, doi: 10.1002/jmr.1081.
- [55] B. Legrand, J. Salvétat, B. Walter, M. Faucher, D. Théron, and J. Aimé, "Multi-MHz micro-electro-mechanical sensors for atomic force microscopy," *Ultramicroscopy*, vol. 175, no. July 2016, pp. 46–57, Apr. 2017, doi: 10.1016/j.ultramic.2017.01.005.
- [56] T. R. Albrecht, P. Grütter, D. Horne, and D. Rugar, "Frequency modulation detection using high- Q cantilevers for enhanced force microscope sensitivity," *J. Appl. Phys.*, vol. 69, no. 2, pp. 668–673, Jan. 1991, doi: 10.1063/1.347347.
- [57] E. Rubiola, *Phase noise and frequency stability in oscillators*. Cambridge University Press, 2008.
- [58] N. Kodera, H. Yamashita, and T. Ando, "Active damping of the scanner for high-speed atomic force microscopy," *Rev. Sci. Instrum.*, vol. 76, no. 5, p. 053708, May 2005, doi: 10.1063/1.1903123.
- [59] R. Garcia and E. T. Herruzo, "The emergence of multifrequency force microscopy," *Nat. Nanotechnol.*, vol. 7, no. 4, pp. 217–226, Apr. 2012, doi: 10.1038/nnano.2012.38.
- [60] F. Rico, C. Su, and S. Scheuring, "Mechanical Mapping of Single Membrane Proteins at Submolecular Resolution," *Nano Lett.*, vol. 11, no. 9, pp. 3983–3986, Sep. 2011, doi: 10.1021/nl202351t.
- [61] A. J. Fleming, B. J. Kenton, and K. K. Leang, "Bridging the gap between conventional and

- video-speed scanning probe microscopes," *Ultramicroscopy*, vol. 110, no. 9, pp. 1205–1214, Aug. 2010, doi: 10.1016/j.ultramic.2010.04.016.
- [62] "Zurich Instruments 600 MHz Lock-in amplifier UHFLI." <https://www.zhinst.com/americas/products/uhfli-lock-amplifier> (accessed May 01, 2020).
- [63] M. Stark and R. Guckenberger, "Fast low-cost phase detection setup for tapping-mode atomic force microscopy," *Rev. Sci. Instrum.*, vol. 70, no. 9, pp. 3614–3619, Sep. 1999, doi: 10.1063/1.1149968.
- [64] Y. Suzuki *et al.*, "High-speed atomic force microscopy combined with inverted optical microscopy for studying cellular events," *Sci. Rep.*, vol. 3, no. 1, p. 2131, Dec. 2013, doi: 10.1038/srep02131.
- [65] S. C. Minne, S. R. Manalis, and C. F. Quate, "Parallel atomic force microscopy using cantilevers with integrated piezoresistive sensors and integrated piezoelectric actuators," *Appl. Phys. Lett.*, vol. 67, no. 26, pp. 3918–3920, Dec. 1995, doi: 10.1063/1.115317.
- [66] H. Sadeghian, R. Herfst, B. Dekker, J. Winters, T. Bijmagne, and R. Rijnbeek, "High-throughput atomic force microscopes operating in parallel," *Rev. Sci. Instrum.*, vol. 88, no. 3, p. 033703, Mar. 2017, doi: 10.1063/1.4978285.
- [67] H. Ximen and P. E. Russell, "Microfabrication of AFM tips using focused ion and electron beam techniques," *Ultramicroscopy*, vol. 42–44, pp. 1526–1532, Jul. 1992, doi: 10.1016/0304-3991(92)90477-2.
- [68] J. Brown, P. Kocher, C. S. Ramanujan, D. N. Sharp, K. Torimitsu, and J. F. Ryan, "Electrically conducting, ultra-sharp, high aspect-ratio probes for AFM fabricated by electron-beam-induced deposition of platinum," *Ultramicroscopy*, vol. 133, pp. 62–66, 2013, doi: 10.1016/j.ultramic.2013.05.005.
- [69] R. M. Stevens, "A new generation of Scanning Probe Technology," *IEEE Nanotechnol. Mag.*, vol. 47, no. 3, pp. 40–43, 2009.
- [70] L. Howald, E. Meyer, R. Lüthi, P. Günther, and H.-J. Güntherodt, "Scanning force microscopy on the Si ( 111 ) 7 x 7 surface reconstruction," *Zeitschrift für Phys. B*, vol. 268, pp. 267–268, 1994.
- [71] M. Schenk, M. Fütting, and R. Reichelt, "Direct visualization of the dynamic behavior of a water meniscus by scanning electron microscopy," *J. Appl. Phys.*, vol. 84, no. 9, pp. 4880–4884, Nov. 1998, doi: 10.1063/1.368731.
- [72] A. J. Weymouth, D. Wastl, and F. J. Giessibl, "Advances in AFM: Seeing Atoms in Ambient Conditions," *e-Journal Surf. Sci. Nanotechnol.*, vol. 16, no. 0, pp. 351–355, Aug. 2018, doi: 10.1380/ejssnt.2018.351.
- [73] D. S. Wastl, A. J. Weymouth, and F. J. Giessibl, "Optimizing atomic resolution of force microscopy in ambient conditions," *Phys. Rev. B*, vol. 87, no. 24, p. 245415, Jun. 2013, doi: 10.1103/PhysRevB.87.245415.
- [74] F. Ohnesorge and G. Binnig, "True Atomic Resolution by Atomic Force Microscopy



- Through Repulsive and Attractive Forces,” *Science* (80-. ), vol. 260, no. 5113, pp. 1451–1456, Jun. 1993, doi: 10.1126/science.260.5113.1451.
- [75] T. Fukuma, K. Kobayashi, K. Matsushige, and H. Yamada, “True atomic resolution in liquid by frequency-modulation atomic force microscopy,” *Appl. Phys. Lett.*, vol. 87, no. 3, p. 034101, Jul. 2005, doi: 10.1063/1.1999856.
- [76] S. Scheuring, D. Fotiadis, C. Möller, S. A. Müller, A. Engel, and D. J. Müller, “Single Proteins Observed by Atomic Force Microscopy,” *Single Mol.*, vol. 2, no. 2, pp. 59–67, Jul. 2001, doi: 10.1002/1438-5171(200107)2:2<59::AID-SIMO59>3.0.CO;2-P.
- [77] S. Morita, F. J. Giessibl, and R. Wiesendanger, *Noncontact Atomic Force Microscopy*, vol. 2. Berlin, Heidelberg: Springer Berlin Heidelberg, 2002.
- [78] T. Ando, “High-speed atomic force microscopy coming of age,” *Nanotechnology*, vol. 23, no. 6, p. 062001, Feb. 2012, doi: 10.1088/0957-4484/23/6/062001.
- [79] S. Nishida, D. Kobayashi, T. Sakurada, T. Nakazawa, Y. Hoshi, and H. Kawakatsu, “Photothermal excitation and laser Doppler velocimetry of higher cantilever vibration modes for dynamic atomic force microscopy in liquid,” *Rev. Sci. Instrum.*, vol. 79, no. 12, p. 123703, Dec. 2008, doi: 10.1063/1.3040500.
- [80] F. J. Giessibl, F. Pielmeier, T. Eguchi, T. An, and Y. Hasegawa, “Comparison of force sensors for atomic force microscopy based on quartz tuning forks and length-extensional resonators,” *Phys. Rev. B*, vol. 84, no. 12, p. 125409, Sep. 2011, doi: 10.1103/PhysRevB.84.125409.
- [81] E. Algre, Z. Xiong, M. Faucher, B. Walter, L. Buchaillot, and B. Legrand, “MEMS Ring Resonators for Laserless AFM With Sub-nanoNewton Force Resolution,” *J. Microelectromechanical Syst.*, vol. 21, no. 2, pp. 385–397, Apr. 2012, doi: 10.1109/JMEMS.2011.2179012.
- [82] K. Nieradka *et al.*, “Fabrication and characterization of electromagnetically actuated microcantilevers for biochemical sensing, parallel AFM and nanomanipulation,” *Microelectron. Eng.*, vol. 98, pp. 676–679, Oct. 2012, doi: 10.1016/j.mee.2012.06.019.
- [83] B. Lee, C. B. Prater, and W. P. King, “Lorentz force actuation of a heated atomic force microscope cantilever,” *Nanotechnology*, vol. 23, no. 5, p. 055709, Feb. 2012, doi: 10.1088/0957-4484/23/5/055709.
- [84] J. C. Doll and B. L. Pruitt, “High-bandwidth piezoresistive force probes with integrated thermal actuation,” *J. Micromechanics Microengineering*, vol. 22, no. 9, p. 095012, Sep. 2012, doi: 10.1088/0960-1317/22/9/095012.
- [85] B. Walter, E. Mairiaux, and M. Faucher, “Atomic force microscope based on vertical silicon probes,” *Appl. Phys. Lett.*, vol. 110, no. 24, p. 243101, Jun. 2017, doi: 10.1063/1.4985125.
- [86] D. Ramos, J. Tamayo, J. Mertens, and M. Calleja, “Photothermal excitation of microcantilevers in liquids,” *J. Appl. Phys.*, vol. 99, no. 12, p. 124904, Jun. 2006, doi: 10.1063/1.2205409.
- [87] M. Dukic, J. D. Adams, and G. E. Fantner, “Piezoresistive AFM cantilevers surpassing

- standard optical beam deflection in low noise topography imaging," *Sci. Rep.*, vol. 5, no. 1, p. 16393, Dec. 2015, doi: 10.1038/srep16393.
- [88] J. Brugger, R. A. Buser, and N. F. de Rooij, "Micromachined atomic force microprobe with integrated capacitive read-out," *J. Micromechanics Microengineering*, vol. 2, no. 3, pp. 218–220, Sep. 1992, doi: 10.1088/0960-1317/2/3/026.
- [89] B. Walter, E. Mairiaux, Z. Xiong, M. Faucher, L. Buchaillot, and B. Legrand, "DNA origami imaging with 10.9 MHz AFM MEMS probes," in *2012 IEEE 25th International Conference on Micro Electro Mechanical Systems (MEMS)*, Jan. 2012, no. February, pp. 555–558, doi: 10.1109/MEMSYS.2012.6170236.
- [90] A. Makky, P. Viel, S. W. Chen, T. Berthelot, J.-L. Pellequer, and J. Polesel-Maris, "Piezoelectric tuning fork probe for atomic force microscopy imaging and specific recognition force spectroscopy of an enzyme and its ligand," *J. Mol. Recognit.*, vol. 26, no. 11, pp. 521–531, Nov. 2013, doi: 10.1002/jmr.2294.
- [91] R. Erlandsson, G. M. McClelland, C. M. Mate, and S. Chiang, "Atomic force microscopy using optical interferometry," *J. Vac. Sci. Technol. A Vacuum, Surfaces, Film.*, vol. 6, no. 2, pp. 266–270, Mar. 1988, doi: 10.1116/1.575440.
- [92] D. Rugar, H. J. Mamin, and P. Guethner, "Improved fiber-optic interferometer for atomic force microscopy," *Appl. Phys. Lett.*, vol. 55, no. 25, pp. 2588–2590, Dec. 1989, doi: 10.1063/1.101987.
- [93] N. R. S. Reddy, N. B. Manson, and E. R. Krausz, "Two-laser spectral hole burning in a colour centre in diamond," *J. Lumin.*, vol. 38, no. 1–6, pp. 46–47, 1987, doi: 10.1016/0022-2313(87)90057-3.
- [94] H. Kawakatsu *et al.*, "Towards atomic force microscopy up to 100 MHz," *Rev. Sci. Instrum.*, vol. 73, no. 6, pp. 2317–2320, Jun. 2002, doi: 10.1063/1.1480459.
- [95] A. Labuda and R. Proksch, "Quantitative measurements of electromechanical response with a combined optical beam and interferometric atomic force microscope," *Appl. Phys. Lett.*, vol. 106, no. 25, p. 253103, Jun. 2015, doi: 10.1063/1.4922210.
- [96] J. D. Adams, B. W. Erickson, J. Grossenbacher, J. Brugger, A. Nievergelt, and G. E. Fantner, "Harnessing the damping properties of materials for high-speed atomic force microscopy," *Nat. Nanotechnol.*, vol. 11, no. 2, pp. 147–151, Feb. 2016, doi: 10.1038/nnano.2015.254.
- [97] "Bruker FastScan A." <https://www.brukerafmprobes.com/p-3759-fastscan-a.aspx> (accessed Apr. 26, 2020).
- [98] P. Lebedew, "Untersuchungen über die Druckkräfte des Lichtes," *Ann. Phys.*, vol. 311, no. 11, pp. 433–458, 1901, doi: 10.1002/andp.19013111102.
- [99] E. F. Nichols and G. F. Hull, "A Preliminary Communication on the Pressure of Heat and Light Radiation," *Phys. Rev. (Series I)*, vol. 13, no. 5, pp. 307–320, Nov. 1901, doi: 10.1103/PhysRevSeriesI.13.307.
- [100] NASA Space Place, "Comet tail diagram," 2009. [https://commons.wikimedia.org/wiki/File:Comet\\_tail\\_diagram.jpg](https://commons.wikimedia.org/wiki/File:Comet_tail_diagram.jpg) (accessed Jun. 02,

2020).

- [101] Timeline, “Picture of a Crookes radiometer,” 2005. [https://en.wikipedia.org/wiki/Crookes\\_radiometer#/media/File:Crookes\\_radiometer.jpg](https://en.wikipedia.org/wiki/Crookes_radiometer#/media/File:Crookes_radiometer.jpg) (accessed Jun. 02, 2020).
- [102] Science Mag, “Gravitational wave detector: VIRGO interferometer.” <https://www.sciencemag.org/news/2017/02/european-gravitational-wave-detector-falters> (accessed Jun. 02, 2020).
- [103] C. H. Metzger and K. Karrai, “Cavity cooling of a microlever,” *Nature*, vol. 432, no. 7020, pp. 1002–1005, Dec. 2004, doi: 10.1038/nature03118.
- [104] H. Rokhsari, T. J. Kippenberg, T. Carmon, and K. J. Vahala, “Radiation-pressure-driven micro-mechanical oscillator,” *Opt. Express*, vol. 13, no. 14, p. 5293, 2005, doi: 10.1364/OPEX.13.005293.
- [105] M. Eichenfield, R. Camacho, J. Chan, K. J. Vahala, and O. Painter, “A picogram- and nanometre-scale photonic-crystal optomechanical cavity,” *Nature*, vol. 459, no. 7246, pp. 550–555, May 2009, doi: 10.1038/nature08061.
- [106] M. Maldovan and E. L. Thomas, “Simultaneous localization of photons and phonons in two-dimensional periodic structures,” *Appl. Phys. Lett.*, vol. 88, no. 25, p. 251907, Jun. 2006, doi: 10.1063/1.2216885.
- [107] T. J. Kippenberg, R. Holzwarth, and S. A. Diddams, “Microresonator-Based Optical Frequency Combs,” *Science (80-. )*, vol. 332, no. 6029, pp. 555–559, Apr. 2011, doi: 10.1126/science.1193968.
- [108] A. Schliesser, P. Del’Haye, N. Nooshi, K. J. Vahala, and T. J. Kippenberg, “Radiation Pressure Cooling of a Micromechanical Oscillator Using Dynamical Backaction,” *Phys. Rev. Lett.*, vol. 97, no. 24, p. 243905, Dec. 2006, doi: 10.1103/PhysRevLett.97.243905.
- [109] A. Sawadsky *et al.*, “Observation of Generalized Optomechanical Coupling and Cooling on Cavity Resonance,” vol. 043601, no. January, pp. 1–5, 2015, doi: 10.1103/PhysRevLett.114.043601.
- [110] O. Arcizet, “Mesure optique ultrasensible et refroidissement par pression de radiation d’un micro-résonateur mécanique,” Ph. D. thesis, Université Pierre et Marie Curie - Paris VI, 2006.
- [111] I. Favero and K. Karrai, “Optomechanics of deformable optical cavities,” *Nat. Photonics*, vol. 3, no. 4, pp. 201–205, Apr. 2009, doi: 10.1038/nphoton.2009.42.
- [112] M. Aspelmeyer, T. J. Kippenberg, and F. Marquardt, “Cavity optomechanics,” *Rev. Mod. Phys.*, vol. 86, no. 4, pp. 1391–1452, Dec. 2014, doi: 10.1103/RevModPhys.86.1391.
- [113] A. Schliesser, R. Rivière, G. Anetsberger, O. Arcizet, and T. J. Kippenberg, “Resolved-sideband cooling of a micromechanical oscillator,” *Nat. Phys.*, vol. 4, no. 5, pp. 415–419, May 2008, doi: 10.1038/nphys939.
- [114] J. Chan *et al.*, “Laser cooling of a nanomechanical oscillator into its quantum ground state,” *Nature*, vol. 478, no. 7367, pp. 89–92, Oct. 2011, doi: 10.1038/nature10461.

- [115] C. Arlotti, "Conception et analyse de micro-résonateurs optiques pour la génération de peignes de fréquences," Ph. D. thesis, Université Paul Sabatier - Toulouse III, 2017.
- [116] Rahmir, "2.5 Dielectric slab waveguide," *University of Wisconsin-Madison*. <https://www.coursehero.com/file/6840310/HW2-solutions/> (accessed Apr. 11, 2020).
- [117] F. P. Kapron and T. I. Lukowski, "Monomode fiber design: power containment," *Appl. Opt.*, vol. 16, no. 6, p. 1465, Jun. 1977, doi: 10.1364/AO.16.001465.
- [118] H. H. Li, "Refractive index of silicon and germanium and its wavelength and temperature derivatives," *J. Phys. Chem. Ref. Data*, vol. 9, no. 3, pp. 561–658, Jul. 1980, doi: 10.1063/1.555624.
- [119] E. A. J. Marcatili, "Dielectric Rectangular Waveguide and Directional Coupler for Integrated Optics," *Bell Syst. Tech. J.*, vol. 48, no. 7, pp. 2071–2102, Sep. 1969, doi: 10.1002/j.1538-7305.1969.tb01166.x.
- [120] W. J. Westerveld, S. M. Leinders, K. W. A. van Dongen, H. P. Urbach, and M. Yousefi, "Extension of Marcatili's Analytical Approach for Rectangular Silicon Optical Waveguides," *J. Light. Technol.*, vol. 30, no. 14, pp. 2388–2401, Jul. 2012, doi: 10.1109/JLT.2012.2199464.
- [121] M. Hammer, "Whispering gallery modes of circular 2-D dielectric optical cavities solver." <https://www.computational-photonics.eu/wgms.html> (accessed May 01, 2020).
- [122] D. Parrain *et al.*, "Origin of optical losses in gallium arsenide disk whispering gallery resonators," *Opt. Express*, vol. 23, no. 15, p. 19656, Jul. 2015, doi: 10.1364/OE.23.019656.
- [123] D. Parrain, "Optomécanique fibrée des disques GaAs : dissipation, amplification et non-linéarités," Ph. D. thesis, Université Paris Diderot - Paris 7, 2014.
- [124] K. R. Hiremath, M. Hammer, R. Stoffer, L. Prkna, and J. Čtyroký, "Analytic approach to dielectric optical bent slab waveguides," *Opt. Quantum Electron.*, vol. 37, no. 1–3, pp. 37–61, Jan. 2005, doi: 10.1007/s11082-005-1118-3.
- [125] D. Marcuse, *Light Transmission Optics*. 1972.
- [126] B. G. Streetman and B. Sanjay, *Solid State electronic Devices (5th ed.)*. Prentice Hall, 2000.
- [127] B. Guha, "Surface-enhanced optomechanical disk resonators and force sensing," Ph. D. thesis, Université Sorbonne Paris Cité, 2017.
- [128] M. A. Green, "Self-consistent optical parameters of intrinsic silicon at 300K including temperature coefficients," *Sol. Energy Mater. Sol. Cells*, vol. 92, no. 11, pp. 1305–1310, Nov. 2008, doi: 10.1016/j.solmat.2008.06.009.
- [129] F. P. Payne and J. P. R. Lacey, "A theoretical analysis of scattering loss from planar optical waveguides," *Opt. Quantum Electron.*, vol. 26, no. 10, pp. 977–986, Oct. 1994, doi: 10.1007/BF00708339.
- [130] C. Baker, "On-chip nano-optomechanical whispering gallery resonators," Ph. D. thesis,

University Paris Diderot - Paris VII, 2014.

- [131] J. Ward and O. Benson, "WGM microresonators: sensing, lasing and fundamental optics with microspheres," *Laser Photon. Rev.*, vol. 5, no. 4, pp. 553–570, Jul. 2011, doi: 10.1002/lpor.201000025.
- [132] L. Ding, P. Senellart, A. Lemaitre, S. Ducci, G. Leo, and I. Favero, "GaAs micro-nanodisks probed by a looped fiber taper for optomechanics applications," in *Nanophotonics III*, Apr. 2010, vol. 7712, p. 771211, doi: 10.1117/12.853985.
- [133] J. Xie *et al.*, "Selective excitation of microring resonances using a pulley-coupling structure," *Appl. Opt.*, vol. 53, no. 5, p. 878, Feb. 2014, doi: 10.1364/AO.53.000878.
- [134] E. Shah Hosseini, S. Yegnanarayanan, A. H. Atabaki, M. Soltani, and A. Adibi, "Systematic design and fabrication of high-Q single-mode pulley-coupled planar silicon nitride microdisk resonators at visible wavelengths," *Opt. Express*, vol. 18, no. 3, p. 2127, Feb. 2010, doi: 10.1364/OE.18.002127.
- [135] M. Aspelmeyer, T. J. Kippenberg, and F. Marquardt, "Cavity optomechanics," *Rev. Mod. Phys.*, vol. 86, no. 4, pp. 1391–1452, Dec. 2014, doi: 10.1103/RevModPhys.86.1391.
- [136] C. W. Gardiner and M. J. Collett, "Input and output in damped quantum systems: Quantum stochastic differential equations and the master equation," *Phys. Rev. A*, vol. 31, no. 6, pp. 3761–3774, Jun. 1985, doi: 10.1103/PhysRevA.31.3761.
- [137] S. Weis *et al.*, "Optomechanically induced transparency," *Science (80-. )*, no. December, pp. 1520–1524, 2010, doi: 10.1364/sl.2011.slmb4.
- [138] H. A. Haus, "Waves and fields in optoelectronics," *Prentice-Hall, Inc., Englewood Cliffs, New Jersey 07632*. 1984.
- [139] W. Hease, "Gallium Arsenide optomechanical disks approaching the quantum regime," Ph. D. thesis, Université Paris-Diderot - Paris VII, 2013.
- [140] J. Zhu *et al.*, "On-chip single nanoparticle detection and sizing by mode splitting in an ultrahigh-Q microresonator," *Nat. Photonics*, vol. 4, no. 1, pp. 46–49, Jan. 2010, doi: 10.1038/nphoton.2009.237.
- [141] T. J. Kippenberg, "Microresonators: Particle sizing by mode splitting," *Nat. Photonics*, vol. 4, no. 1, pp. 9–10, 2010, doi: 10.1038/nphoton.2009.246.
- [142] M. Hermouet, "Optomechanical silicon microdisk resonators for biosensing in liquid," Ph. D. thesis, Université Grenoble Alpes, 2019.
- [143] D. T. Nguyen *et al.*, "Improved optomechanical disk resonator sitting on a pedestal mechanical shield," *New J. Phys.*, vol. 17, no. 2, p. 023016, Feb. 2015, doi: 10.1088/1367-2630/17/2/023016.
- [144] J. Hofer, A. Schliesser, and T. J. Kippenberg, "Cavity optomechanics with ultrahigh-Q crystalline microresonators," *Phys. Rev. A*, vol. 82, no. 3, p. 031804, Sep. 2010, doi: 10.1103/PhysRevA.82.031804.
- [145] C. Baker *et al.*, "Photoelastic coupling in gallium arsenide optomechanical disk resonators," *Opt. Express*, vol. 22, no. 12, pp. 14072–14086, 2014, doi:

10.1364/OE.22.014072.

- [146] B. Taurel, "Theoretical and experimental study of optical coupling in optomechanical systems," Ph. D. thesis, Université Grenoble Alpes, 2020.
- [147] J. Ebrahimi, "Thermal diffusivity measurement of small silicon chips," *J. Phys. D. Appl. Phys.*, vol. 3, no. 2, p. 422, Feb. 1970, doi: 10.1088/0022-3727/3/2/422.
- [148] Y. Okada and Y. Tokumaru, "Precise determination of lattice parameter and thermal expansion coefficient of silicon between 300 and 1500 K," *J. Appl. Phys.*, vol. 56, no. 2, pp. 314–320, Jul. 1984, doi: 10.1063/1.333965.
- [149] B. Guha, P. E. Allain, A. Lemaître, G. Leo, and I. Favero, "Force Sensing with an Optomechanical Self-Oscillator," *Phys. Rev. Appl.*, vol. 14, no. 2, p. 024079, Aug. 2020, doi: 10.1103/PhysRevApplied.14.024079.
- [150] P. T. Rakich, P. Davids, and Z. Wang, "Tailoring optical forces in waveguides through radiation pressure and electrostriction," in *IEEE Photonics Society Summer Topicals 2010*, Jul. 2010, vol. 18, no. 14, pp. 98–99, doi: 10.1109/PHOSST.2010.5553661.
- [151] M. L. Gorodetsky, A. Schliesser, G. Anetsberger, S. Deleglise, and T. J. Kippenberg, "Determination of the vacuum optomechanical coupling rate using frequency noise calibration," *Opt. Express*, vol. 18, no. 22, p. 23236, Oct. 2010, doi: 10.1364/OE.18.023236.
- [152] O. Arcizet, P.-F. Cohadon, T. Briant, M. Pinard, and A. Heidmann, "Radiation-pressure cooling and optomechanical instability of a micromirror," *Nature*, vol. 444, no. 7115, pp. 71–74, Nov. 2006, doi: 10.1038/nature05244.
- [153] B. S. Sheard, M. B. Gray, C. M. Mow-lowry, D. E. McClelland, and S. E. Whitcomb, "Observation and characterization of an optical spring," *Phys. Rev. A*, vol. 69, no. 051801, pp. 1–4, 2004, doi: 10.1103/PhysRevA.69.051801.
- [154] M. Hossein-Zadeh and K. J. Vahala, "Observation of optical spring effect in a microtoroidal optomechanical resonator," *Opt. Lett.*, vol. 32, no. 12, pp. 1611–1613, Jun. 2007, doi: 10.1364/OL.32.001611.
- [155] T. J. Kippenberg and K. J. Vahala, "Cavity Optomechanics: Back-Action at the Mesoscale," *Science (80-. )*, vol. 321, no. 5893, pp. 1172–1176, Aug. 2008, doi: 10.1126/science.1156032.
- [156] H. Zhu, C. Tu, G. Shan, and J. E.-Y. Lee, "Dependence of temperature coefficient of frequency (TCf) on crystallography and eigenmode in N-doped silicon contour mode micromechanical resonators," *Sensors Actuators A Phys.*, vol. 215, pp. 189–196, Aug. 2014, doi: 10.1016/j.sna.2014.04.001.
- [157] L. Schwab *et al.*, "Comprehensive optical losses investigation of VLSI Silicon optomechanical ring resonator sensors," in *2018 IEEE International Electron Devices Meeting (IEDM)*, 2018, vol. 4, no. 7, pp. 99–102, doi: 10.1109/IEDM.2018.8614508.
- [158] M. Hermouet *et al.*, "1 Million-Q Optomechanical Microdisk Resonators with Very Large Scale Integration," *Proceedings*, vol. 1, no. 4, p. 347, Aug. 2017, doi: 10.3390/proceedings1040347.

- [159] W. Chen, Ş. K. Özdemir, G. Zhao, J. Wiersig, and L. Yang, “Exceptional points enhance sensing in an optical microcavity,” *Nature*, vol. 548, no. 7666, pp. 192–195, 2017, doi: 10.1038/nature23281.
- [160] R. K. Pathria, *Statistical Mechanics*. 1972.
- [161] J. E. Sader, J. W. M. Chon, and P. Mulvaney, “Calibration of rectangular atomic force microscope cantilevers,” *Rev. Sci. Instrum.*, vol. 70, no. 10, pp. 3967–3969, Oct. 1999, doi: 10.1063/1.1150021.
- [162] L. Ding *et al.*, “High Frequency GaAs Nano-Optomechanical Disk Resonator,” *Phys. Rev. Lett.*, vol. 105, no. 26, p. 263903, Dec. 2010, doi: 10.1103/PhysRevLett.105.263903.
- [163] Y. Liu, H. Miao, V. Aksyuk, and K. Srinivasan, “Wide cantilever stiffness range cavity optomechanical sensors for atomic force microscopy,” *Opt. Express*, vol. 20, no. 16, p. 18268, Jul. 2012, doi: 10.1364/OE.20.018268.
- [164] L. Leoncino, “Optomechanical transduction applied to M / NEMS devices,” Ph. D. thesis, Université Grenoble Alpes, 2017.
- [165] D. W. Allan, “Time and Frequency (Time-Domain) Characterization, Estimation, and Prediction of Precision Clocks and Oscillators,” *IEEE Trans. Ultrason. Ferroelectr. Freq. Control*, vol. 34, no. 6, pp. 647–654, Nov. 1987, doi: 10.1109/T-UFFC.1987.26997.
- [166] M. Sansa *et al.*, “Frequency fluctuations in silicon nanoresonators,” *Nat. Nanotechnol.*, vol. 11, no. 6, pp. 552–558, Jun. 2016, doi: 10.1038/nnano.2016.19.
- [167] A. N. Cleland and M. L. Roukes, “Noise processes in nanomechanical resonators,” *J. Appl. Phys.*, vol. 92, no. 5, pp. 2758–2769, Sep. 2002, doi: 10.1063/1.1499745.
- [168] S. K. Roy, V. T. K. Sauer, J. N. Westwood-Bachman, A. Venkatasubramanian, and W. K. Hiebert, “Improving mechanical sensor performance through larger damping,” *Science (80-. )*, vol. 360, no. 6394, p. eaar5220, Jun. 2018, doi: 10.1126/science.aar5220.
- [169] “Nanosensors AFM cantilever ATEC-CONT with a tip visibility form top.” <https://store.nanoscience.com/nanosensors-atec-cont.html> (accessed May 01, 2020).
- [170] M. Stark and R. Guckenberger, “Fast low-cost phase detection setup for tapping-mode atomic force microscopy,” *Rev. Sci. Instrum.*, vol. 70, no. 9, pp. 3614–3619, Sep. 1999, doi: 10.1063/1.1149968.
- [171] D. Lagrange, N. Mauran, L. Schwab, and B. Legrand, “Low Latency Demodulation for High-Frequency Atomic Force Microscopy Probes.”
- [172] N. Kodera, M. Sakashita, and T. Ando, “Dynamic proportional-integral-differential controller for high-speed atomic force microscopy,” *Rev. Sci. Instrum.*, vol. 77, no. 8, p. 083704, Aug. 2006, doi: 10.1063/1.2336113.
- [173] “Physik Instrumente piezoelectric transducers actuators.” <https://www.physikinstrumente.co.uk/en/products/piezoelectric-transducers-actuators/linear-actuators/> (accessed Feb. 18, 2020).
- [174] Y. K. Yong, “Preloading Piezoelectric Stack Actuators in High-Speed Nanopositioning Systems,” *Front. Mech. Eng.*, vol. 2, no. October, pp. 1–9, 2016, doi:

10.3389/fmech.2016.00008.

- [175] T. Fukuma, Y. Okazaki, N. Kodera, T. Uchihashi, and T. Ando, "High resonance frequency force microscope scanner using inertia balance support," *Appl. Phys. Lett.*, vol. 92, no. 24, p. 243119, Jun. 2008, doi: 10.1063/1.2951594.
- [176] Y. Zhang, Y. Li, G. Shan, Y. Chen, Z. Wang, and J. Qian, "Real-time scan speed control of the atomic force microscopy for reducing imaging time based on sample topography," *Micron*, vol. 106, pp. 1–6, Mar. 2018, doi: 10.1016/j.micron.2017.12.004.
- [177] I. A. Mahmood and S. O. Reza Moheimani, "Fast spiral-scan atomic force microscopy," *Nanotechnology*, vol. 20, no. 36, p. 365503, Sep. 2009, doi: 10.1088/0957-4484/20/36/365503.
- [178] Minicircuits, "Frequency mixers application note." <https://www.minicircuits.com/appdoc/AN00-010.html> (accessed Dec. 05, 2019).
- [179] T. Michels, I. W. Rangelow, and V. Aksyuk, "Fabrication Process for an Optomechanical Transducer Platform with Integrated Actuation," *J. Res. Natl. Inst. Stand. Technol. Fabr.*, vol. 121, pp. 507–536, 2016.
- [180] R. d'Agostino and D. L. Flamm, "Plasma etching of Si and SiO<sub>2</sub> in SF<sub>6</sub>–O<sub>2</sub> mixtures," *J. Appl. Phys.*, vol. 52, no. 1, pp. 162–167, Jan. 1981, doi: 10.1063/1.328468.
- [181] M. Pu, L. Liu, H. Ou, K. Yvind, and J. M. Hvam, "Ultra-low-loss inverted taper coupler for silicon-on-insulator ridge waveguide," *Opt. Commun.*, vol. 283, no. 19, pp. 3678–3682, Oct. 2010, doi: 10.1016/j.optcom.2010.05.034.
- [182] S. Nambiar, P. Sethi, and S. Selvaraja, "Grating-Assisted Fiber to Chip Coupling for SOI Photonic Circuits," *Appl. Sci.*, vol. 8, no. 7, p. 1142, Jul. 2018, doi: 10.3390/app8071142.
- [183] W. Bogaerts and D. Vermeulen, "Off-Chip Coupling," 2013, pp. 97–138.
- [184] "Tyndall research packaging." <https://www.tyndall.ie/packaging/> (accessed Oct. 09, 2019).
- [185] "Specifications sheet of the SMF-28-J9 optical fiber." <https://www.thorlabs.com/thorproduct.cfm?partnumber=SMF-28-J9> (accessed May 01, 2020).
- [186] T. P. Weihs, S. Hong, J. C. Bravman, and W. D. Nix, "Measuring the Strength and Stiffness of Thin Film Materials by Mechanically Deflecting Cantilever Microbeams," *MRS Proc.*, vol. 130, no. 100, p. 87, Feb. 1988, doi: 10.1557/PROC-130-87.
- [187] "Ball contact with surface animation simulated with the JKR model." [https://en.wikipedia.org/wiki/Contact\\_mechanics#/media/File:JKR-full-cycle.gif](https://en.wikipedia.org/wiki/Contact_mechanics#/media/File:JKR-full-cycle.gif) (accessed May 01, 2020).
- [188] John A. Dean, *Lange's handbook of chemistry (15th edition)*. McGRAW-HILL, INC., 1999.
- [189] G. Hummer and A. Szabo, "Kinetics from Nonequilibrium Single-Molecule Pulling Experiments," *Biophys. J.*, vol. 85, no. 1, pp. 5–15, Jul. 2003, doi: 10.1016/S0006-3495(03)74449-X.
- [190] E. H. Lee, J. Hsin, M. Sotomayor, G. Comellas, and K. Schulten, "Discovery Through the



- Computational Microscope,” *Structure*, vol. 17, no. 10, pp. 1295–1306, Oct. 2009, doi: 10.1016/j.str.2009.09.001.
- [191] J. C. Hulme, J. K. Doyle, and J. E. Bowers, “Widely tunable Vernier ring laser on hybrid silicon,” *Opt. Express*, vol. 21, no. 17, pp. 19718–19722, Aug. 2013, doi: 10.1364/OE.21.019718.
- [192] Computational photonics, “1-D mode solver for dielectric multilayer slab waveguides.” <https://www.computational-photonics.eu/oms.html> (accessed Mar. 09, 2020).
- [193] OZoptics, “Single Mode Tapered/Lensed Fibers.” <https://shop.ozoptics.com/single-mode-taperedlensed-fibers> (accessed Jan. 29, 2020).
- [194] B. D. Hauer, C. Doolin, K. S. D. Beach, and J. P. Davis, “A general procedure for thermomechanical calibration of nano/micro-mechanical resonators,” *Ann. Phys. (N. Y.)*, vol. 339, pp. 181–207, Dec. 2013, doi: 10.1016/j.aop.2013.08.003.
- [195] M. V Salapaka, H. S. Bergh, J. Lai, A. Majumdar, and E. McFarland, “Multi-mode noise analysis of cantilevers for scanning probe microscopy,” *J. Appl. Phys.*, vol. 81, no. 6, pp. 2480–2487, Mar. 1997, doi: 10.1063/1.363955.
- [196] H. Ibach, “Thermal Expansion of Silicon and Zinc Oxide (I),” *Phys. status solidi*, vol. 31, no. 2, pp. 625–634, 1969, doi: 10.1002/pssb.19690310224.
- [197] J. Komma, C. Schwarz, G. Hofmann, D. Heinert, and R. Nawrodt, “Thermo-optic coefficient of silicon at 1550 nm and cryogenic temperatures,” *Appl. Phys. Lett.*, vol. 101, no. 4, p. 041905, Jul. 2012, doi: 10.1063/1.4738989.
- [198] A. D. Bristow, N. Rotenberg, and H. M. van Driel, “Two-photon absorption and Kerr coefficients of silicon for 850–2200nm,” *Appl. Phys. Lett.*, vol. 90, no. 19, p. 191104, May 2007, doi: 10.1063/1.2737359.
- [199] O. Arcizet *et al.*, “High-Sensitivity Optical Monitoring of a Micromechanical Resonator with a Quantum-Limited Optomechanical Sensor,” *Phys. Rev. Lett.*, vol. 97, no. 13, p. 133601, Sep. 2006, doi: 10.1103/PhysRevLett.97.133601.
- [200] “Specifications sheet of T100S-HP EXFO Laser.” [https://exfoprodstorage.blob.core.windows.net/media/9727/exfo\\_spec-sheet\\_t100s-hp\\_v3\\_en.pdf](https://exfoprodstorage.blob.core.windows.net/media/9727/exfo_spec-sheet_t100s-hp_v3_en.pdf) (accessed May 01, 2020).
- [201] D. C. Aveline, L. M. Baumgartel, G. Lin, and N. Yu, “Whispering gallery mode resonators augmented with engraved diffraction gratings,” *Opt. Lett.*, vol. 38, no. 3, p. 284, Feb. 2013, doi: 10.1364/OL.38.000284.
- [202] P. E. Allain *et al.*, “Optomechanical resonating probe for very high frequency sensing of atomic forces,” *Nanoscale*, vol. 12, no. 5, pp. 2939–2945, 2020, doi: 10.1039/C9NR09690F.
- [203] B. Dahneke, “The influence of flattening on the adhesion of particles,” *J. Colloid Interface Sci.*, vol. 40, no. 1, pp. 1–13, Jul. 1972, doi: 10.1016/0021-9797(72)90168-3.
- [204] L. Bergström, “Hamaker constants of inorganic materials,” *Adv. Colloid Interface Sci.*, vol. 70, pp. 125–169, Jul. 1997, doi: 10.1016/S0001-8686(97)00003-1.

## Résumé

Dans le domaine de la microscopie, le microscope à force atomique (AFM), inventé en 1986, est aujourd'hui toujours basé sur le même concept de sonde de force : le levier. Les performances de l'AFM, et en particulier sa vitesse d'imagerie, sont principalement limitées par ce levier, dont la fréquence de résonance plafonne à quelques MHz. Ce travail de thèse présente un nouveau concept de sonde AFM, une sonde optomécanique (OM), ainsi que les développements sur l'instrument pour exploiter ses performances. En effet, des sondes OM vibrant à plus de 100 MHz sont développées et exploitées dans ce manuscrit. Elles démontrent une limite de détection thermomécanique remarquable de  $10^{-17} \text{m}/\sqrt{\text{Hz}}$  à température ambiante, inférieure à celle de toute autre sonde AFM, permettant un fonctionnement avec une amplitude de vibration de 10 pm. Cette sonde OM est constituée d'un anneau de silicium suspendu d'un diamètre de 20  $\mu\text{m}$ , agissant à la fois comme un résonateur mécanique et un résonateur optique à mode de galerie. Les deux sont intimement couplés par la forme de l'anneau : lorsque l'anneau vibre dans un mode de respiration, la longueur de la cavité optique varie et sa longueur d'onde de résonance varie autour de la longueur d'onde centrale de 1,55  $\mu\text{m}$ . De nombreuses variantes de sondes OM sont caractérisées pour trouver la conception optimale, conduisant à un gap de couplage évanescent de 100 nm à 200 nm et une largeur de rayons de suspension inférieure à 100 nm. Grâce à une caractérisation approfondie, un phénomène singulier est également mis en évidence : le super-mode. Deux alternatives pour mettre la sonde en vibration sont comparées : l'actionnement capacitif et optique. L'étude de la stabilité et du bruit de la sonde permet d'identifier une source de bruit supplémentaire en actionnement optique. Ensuite, les sondes OM sont intégrées dans un instrument AFM dont chaque composant est spécialement développé, du scanner piézoélectrique à l'acquisition et au traitement des données. À cause d'un verrou technologique de fabrication, la pointe de la sonde OM n'a pas pu être approchée d'une surface : elle ne dépasse pas du substrat sur lequel la sonde est fabriquée. Un levier AFM classique est donc utilisé pour interagir mécaniquement avec la sonde AFM. La bande passante de l'instrument est alors caractérisée en fonctionnement, démontrant une bande passante de boucle de rétroaction de 100 kHz, à l'état de l'art. Enfin, une première pseudo-image est réalisée avec ces sondes, démontrant le fonctionnement complet de l'instrument.

Mots-clefs : Microscope à force atomique (AFM), optomécanique, résonateur, cavité.

## Abstract

In the field of microscopy, the atomic force microscope (AFM) invented in 1986 was brought little, but nonetheless impressive, incremental developments since then. This instrument's performances, and in particular imaging speed, are mainly limited by its cantilever-type force probe whose resonance frequency peaks at a few MHz. This thesis work presents a new concept of AFM probe, an optomechanical (OM) one, and custom instrument's components to exploit its performances. Indeed, the 100+ MHz vibrating OM probes tested in this manuscript demonstrate an exquisite thermomechanical limit of detection of  $10^{-17} \text{m}/\sqrt{\text{Hz}}$  at room temperature, lower than any other AFM probe detection, and an instrument-limited 10 pm vibration amplitude. This OM probe consists of a suspended silicon ring with a 10  $\mu\text{m}$  radius, acting as a mechanical resonator and a whispering-gallery-mode optical resonator. The two are intimately coupled by the ring shape: when the ring vibrates in a breathing mode, the optical cavity length varies and so does its resonance wavelength around its central value 1.55  $\mu\text{m}$ . Characterization of numerous OM probes with different designs are investigated to find optimal designs, that is a 100 nm to 200 nm evanescent-coupling-gap and spokes width below 100 nm. Through deep characterization, subtle phenomenon is also highlighted as the super-mode. Two alternatives to put the probe in vibration are compared: capacitive and optical. Stability and noise study of the probe help identify an additional noise source in optical actuation, that seem to be related to the optical background signal. Each developed component of the AFM instrument is detailed from piezoelectric scanner to data acquisition and processing. Because of a fabrication technological lock, the tip of the OM probe could not approach any surface as it did not protrude from the substrate on which the probe is made. A conventional AFM lever is therefore used to interact mechanically with the AFM probe. The instrument's bandwidth is then characterized in operation, demonstrating a state-of-the-art 100 kHz feedback-loop bandwidth. Finally, a first pseudo-image is achieved with such probes, demonstrating the whole instrument operation.

Key-words: Atomic Force Microscope (AFM), optomechanics, resonator, cavity.